*eXPRESS Polymer Letters Vol.10, No.2 (2016) 83*
*Available online at www.expresspolymlett.com*
*DOI: 10.3144/expresspolymlett.2016.9*

# Editorial corner – a personal view

## Can the standard impact tests become a true materials evaluation tool?

*P. M. Frontini*[*]

Instituto de Ciencia y Tecnología de Materiales (INTEMA), CONICET, Universidad Nacional de Mar del Plata, Juan B. Justo 4302, B7608FDQ Mar del Plata, Argentina

Impact resistance constitutes one of the most popular quality control tools for polymeric materials and plastic finished parts. There are a number of standard impact test methods devoted to evaluate the impact response of polymeric materials (e.g., tensile-impact, Charpy and Izod tests, falling weight, Gardner, etc.). Nevertheless, to the questions: which test to use? how the different toughness measurements are related between each other? straightforward answers cannot be given. The shortcomings of standardized impact tests were recognized long ago: these tests are unable to generate an 'actual material property'.

Fracture mechanics experts often criticize standard impact tests because of uncertainties about gauge length, complex three-dimensional stress states, their dependence on sample thickness, and the relationship of these factors to real situations. Indeed, to understand the true meaning of impact strength one must draw on fracture mechanics concepts. Modern instrumented devices can provide curves of high-speed stress/strain data which permit in principle the application of fracture mechanics. Even so, this approach seems to be unappealing to plastic industrialists who continue to prefer traditional impact tests. On the other hand, fracture mechanics does not take into account crack initiation in locations into the body where there are no initial sharp cracks, that is, it can't be used when the location of the failure initiation spot is not known a priori.

Nowadays, computer methods based on Finite Element Analysis (FEA) are widely used in the academia and industry for calculating forces, deformations, stresses and strains. They make possible to explore the influence of different materials and component geometries on the forces and deformations experienced in the impact event. In addition, physically based constitutive theories accounting for nonlinear and rate-dependent properties of polymers – viscoelastic and viscoplastic deformation characteristics – allow modeling the behavior of materials properly. As a consequence deeper information than that given by standard impact tests may be provided.

Future investigations should take the step forward to a full interpretation of the impact tests. Special efforts should be devoted towards understanding the existing relationship among different impact tests. This inquiry still remains as an open question which concerns polymer industry. The key lies in focusing to find the governing three-dimensional invariant-based failure criteria under impact situations. Once this goal has been achieved standard impact tests will become a true materials evaluation tool.

Prof. Dr. Patricia Maria Frontini
Member of International Advisory Board

[*]Corresponding author, e-mail: pmfronti@fi.mdp.edu.ar

*eXPRESS Polymer Letters Vol.10, No.2 (2016) 84–95*
*Available online at www.expresspolymlett.com*
*DOI: 10.3144/expresspolymlett.2016.10*

# Synthesis, kinetics of photo-dimerization/photo-cleavage and physical properties of coumarin-containing branched polyurethanes based on polycaprolactones

*R. Seoane Rivero*[1], *P. Bilbao Solaguren*[1], *K. Gondra Zubieta*[1], *L. Peponi*[2], *A. Marcos-Fernández*[2*]

[1]Gaiker Centro Tecnológico, Parque Tecnológico Edificio 202, 48170 Zamudio, Spain
[2]Instituto de Ciencia y Tecnología de Polímeros (CSIC), Juan de la Cierva 3, 28006 Madrid, Spain

*Received 2 July 2015; accepted in revised form 31 August 2015*

**Abstract.** A series of coumarin-containing branched polyurethanes based on polycaprolactones, hexamethylene diisocyanate and a monohydroxylated coumarin monomer with 5 and 10% content by weight of coumarin units were successfully prepared. Chain architecture was controlled by combination of polycaprolactone (PCL) triol or tetrol with PCL diol. Terminal coumarin units segregated from the polyurethane matrix as measured by differential scanning calorimetry (DSC). Photo-dimerization with 313 nm lamps presented an anomalous behavior in two steps with high irreversibility at high conversions. Photo-dimerization/photo-cleavage reactions showed an increase in irreversibility with the increase in cycles. It was demonstrated that conversion measured by Raman spectroscopy gave the same results than conversion measured by ultraviolet (UV) spectroscopy. Photo-dimerization produced an elastomeric material with much better mechanical properties than non-irradiated material as a consequence of the crosslinking produced. Photo-cleavage decreased the mechanical properties and repeated photo-dimerization increased mechanical properties again.

***Keywords:*** *smart polymers, coumarin, polycaprolactone, polyurethanes*

## 1. Introduction

Self-healing polymers [1–4], which are able to autonomously repair damage inflicted on them, are at the forefront of recent developments in materials chemistry and engineering. Some of them can self-repair by surface contact [5], but most need different external agents, such as heat or light. By heating, for example, a Diels-Alder reaction can take place in elastomeric polymers [6–8]. Light is used to produce reactions in light-sensitive materials such as antracenes [9, 10], coumarins [11], or cinammic acid derivatives [9, 12]. These light-sensitive materials have been used in shape memory polymers [12], hydrogels [10], surface patterning [13], drug release [14–17], and intraocular lenses [18]. Self-healing at room temperature can be achieved by light exposure of the damage if the crack surfaces contain reactive moieties that can react to form new chemical bonds under irradiation. These photo-reactive groups should be part of the polymer structure without compromising the desired properties, which often means a limited content [19, 20].

Coumarin molecules can undergo reversible photo-induced reactions; thus, when irradiated at 365 nm a [2+2] cycloaddition reaction to give rise to a cyclobutane ring takes place, and when irradiated at 254 nm a photo-cleavage reaction renders the original coumarin structures as shown in Figure 1 [11, 21–23]. Coumarin monomers have been included in the backbone of different types of polymers, including polyethers [21], poly(meth)acrylates [23, 24], polyesters [25] and polyurethanes [19].

*Corresponding author, e-mail: amarcos@ictp.csic.es

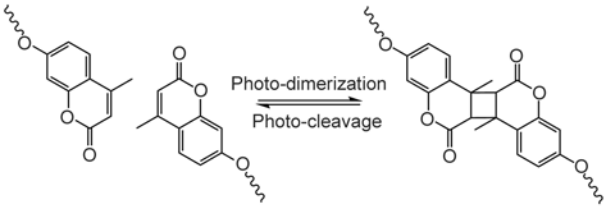


**Figure 1.** Photo-dimerization/photo-cleavage reactions of coumarin molecules

Polyurethanes are considered excellent materials because of their good physical properties. This is the reason why this material is used in different and numerous applications. Some applications of these materials are biomedical, coating and adhesive applications [26, 27]. When incorporated in a polyurethane chain, the coumarin monomer was introduced as a chain end [20, 28] or as a chain extender [19]. In both cases coumarin monomer was linked to the isocyanate monomer by a polar urethane group, and when introduced as a chain extender, coumarin units were within the hard segments.

In this work we report coumarin-based photo-reactive polyurethanes based on PCL macroglycols, hexamethylene diisocyanate and a monohydroxylated coumarin monomer. PCL macroglycols were chosen because it is well known that polyesters produce polyurethanes with better mechanical properties than polyethers. In addition, PCL polyesters are biodegradable and non-toxic and potentially could be used for biomedical applications. Short PCL were chosen to avoid crystallization as much as possible in order to obtain transparent materials where radiation could penetrate more deeply. Through the right combination of a PCL triol or tetrol with a PCL diol, branched materials with the highest possible molecular weight without reaching gelation could be obtained. In this way, these soluble materials could form films and after minimum irradiation, a network could be formed.

## 2. Experimental section

### 2.1. Materials

PCL900 triol (CAPA®3091, hydroxyl number 184.10 mgKOH/g, molecular weight 914 g/mol) and PCL1000 tetrol (CAPA®4101, hydroxyl number 224.10 mgKOH/g, molecular weight 1001 g/mol) were a gift from Perstorp (Warrington, UK), and PCL530 (molecular weight 527 g/mol) was supplied by Sigma Aldrich Química S.L (Madrid, Spain). PCLs were vacuum dried at 90 °C for 3 h and stored in a desiccator until used.

Resorcinol, ethyl acetoacetate, 2-bromoethanol, stannous octoate and hexamethylene diisocyanate were supplied by Sigma Aldrich Química S.L (Madrid, Spain) and used as received. Concentrated sulphuric acid and potassium carbonate were supplied by Panreac (Barcelona, Spain) and used as received. Dimethylformamide and 1,2-dichloroethane were supplied by Scharlau (Barcelona, Spain) and used as received.

### 2.2. Synthesis of 7-hydroxyethoxy-4-methylcoumarin (HEOMC)

7-hydroxyethoxy-4-methylcoumarin (HEOMC) was prepared as described in literature in two steps [20, 23], as shown in Figure 2.

The characterization of the molecule was made using nuclear magnetic resonance (NMR) analysis. $^1$H NMR (400 MHz, DMSO-$d_6$, ppm): 7.67 (d, 1H, $J$ = 9.6 Hz, *c*), 6.96 (dd, 1H, $J_1$ = 9.6 Hz, $J_2$ = 2.8 Hz, *d*), 6.96 (d, $J$ = 2.8 Hz, 1H, *e*), 6.19 (d, $J$ = 1.2 Hz, 1H, *a*), 4.9 (s broad, 1H, *–OH*), 4.08 (t, $J$ = 4.8 Hz, 2H, *k*), 3.74 (t, $J$ = 4.8 Hz, 2H, *l*), 2.38 (d,

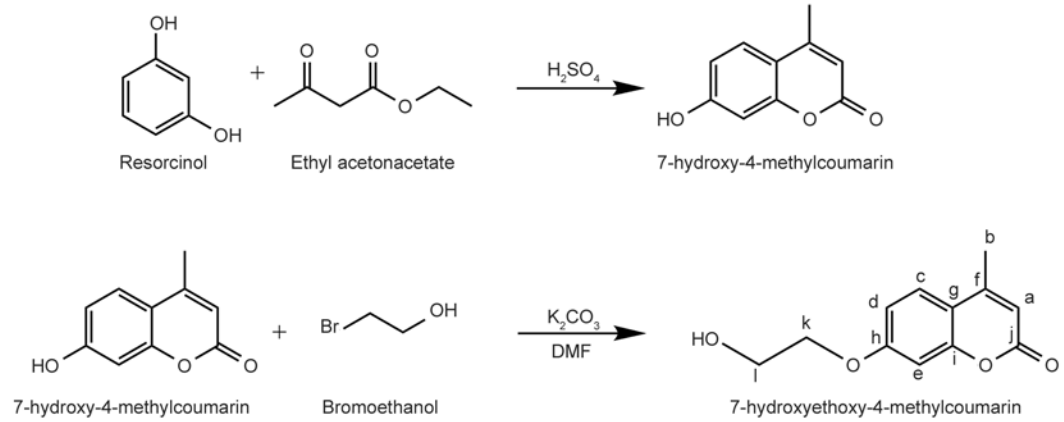


**Figure 2.** Synthesis procedure for 7-hydroxyethoxy-4-methylcoumarin (HEOMC)

$J$ = 1.2 Hz, 3H, *b*). $^{13}$C NMR (400 MHz, DMSO-$d_6$, ppm): 161.8 (*h*), 160.2 (*j*), 154.7, 153.4 (*f*, *i*), 126.3 (*c*), 113.0 (*a*), 112.4, 111.1 (*d*, *g*), 101.1 (*e*), 70.3 (*k*), 59.4 (*l*), 18.1 (*b*).

### 2.3. Synthesis of model linear polyurethanes

In a 25 mL round-bottomed flask, 1 g (1.887 mmol) of PCL530, 0.1522 g (0.692 mmol) of HEOMC and 0.3772 g (2.243 mmol) of hexamethylene diisocyanate were dissolved in 5 mL of 1,2-dichloroethane. Two drops of $SnOct_2$ catalyst were added and the stirred solution heated at 80 °C for 3 h, followed by 24 h stirring at ambient temperature. The resulting polymeric solution was cast into a Teflon mould and the solvent evaporated at room temperature for 48 h. This polymer had 10% by weight of coumarin monomer. The models with 5% by weight of coumarin monomer (1 g of PCL530, 0.0704 g of HEOMC and 0.3443 g of HDI) and without coumarin (no HEOMC was added and PCL530 and HDI were added in stoichiometric amounts) were synthesized in the same way.

### 2.4. Synthesis of branched polyurethanes

The branched coumarin-containing polymers were synthesized in the same way as the linear models, that is, one pot synthesis without prepolymerization. In Table 1, the calculated amounts of each reactant for a total of 100 g of polymer can be found. In the actual synthesis procedure, a total amount of 5 g of polymer was prepared.

### 2.5. Experimental techniques

Solution NMR spectra were recorded at room temperature in a Varian Unity Plus 400 instrument (Palo Alto, CA, USA) using deuterated dimethylsulfoxide (DMSO-$d_6$) as solvent. Spectra were referenced to the residual solvent signals at 2.50 ppm for proton spectra and 39.5 ppm for carbon spectra.

Irradiations were carried out in a crosslinker supplied by Ultra-Violet Products (Upland, CA, USA) equipped with four sets of 5×8 watts lamps with emission maxima at 313, 354, 365, and 254 nm.

UV experiments were performed in a Perkin Elmer Lambda 35 UV/Vis spectrometer (Waltham, MA, USA). Absorbance of the thin films was measured from 450 to 210 nm.

Raman spectroscopy measurements were carried out by a Renishaw inVia Laser micro-Raman Spectrometer (Wotton-under-Edge, UK). A laser beam with wavelength of 785 nm served as the excitation light. The testing area on the film was about 1 μm$^2$.

The thermal transitions of the samples were analyzed by DSC on a Mettler Toledo DSC 822e calorimeter (Schwerzenbach, Switzerland) equipped with a liquid nitrogen accessory. Disc samples cut from films weighing approximately 6 mg were sealed in aluminium pans. Samples were heated, from –90 to 80 °C at a rate of 10 °C·min$^{-1}$, cooled at 10 °C·min$^{-1}$ to –90 °C, maintained for 7 minutes at this temperature and re-heated from –90 to 80 °C at a rate of 10 °C·min$^{-1}$. Crystallization ($T_c$) and melting temperatures ($M_p$) were taken as the maximum of the exothermic or endothermic transition respectively, and glass transition temperatures ($T_g$) were taken as the midpoint of the transition. Melting ($\Delta H_m$) and crystallization ($\Delta H_c$) enthalpies were calculated by integration of the area of the peaks.

Tensile properties were measured in a MTS Synergie 200 testing machine (Eden Prairie, MN, USA) equipped with a 100 N load cell. Type 3 dumbbell test pieces (according to ISO 37) were cut from the samples. A cross-head speed of 200 mm·min$^{-1}$ was used. Strain was measured from cross-head separation and referred to 10 mm initial length. A minimum of 3 samples were tested for each material.

## 3. Results and discussion

### 3.1. Synthesis and characterization of coumarin containing polyurethanes

A series of coumarin end-capped branched polyurethanes having a content of 5 or 10% by weight of coumarin units were successfully synthesized. Also three linear polymers without coumarin and with 5 or 10% by weight of coumarin units were prepared as models. The branched polymers were designed to have the maximum possible molecular weight in order to have film forming properties. Starting PCL diol, triol and tetrol had low molecular weight to obtain amorphous or very low crystalline polymers that would be transparent and would allow penetration of UV radiation.

From Carothers equations, when monomers with functionality above 2 are used, gel point can be calculated with the Equation (1):

$$p = \frac{2}{f_{avg}} \tag{1}$$

where $p$ is the conversion at the gel point and $f_{avg}$ is the average functionality of the reactants.

To avoid gelation, $f_{avg}$ should be 2 (only at 100% conversion a gel would be obtained), and if only a PCL triol or a PCL tetrol are used to build up the branched polymer by reaction with hexamethylenediisocyanate (HDI), an equivalent ratio of HDI/PCL triol and HDI/PCL tetrol of 4/3 and 6/4 respectively has to be used. For these HDI/PCL equivalent ratios, the reaction of the free isocyanate groups with the equivalent amount of hydroxyl-coumarin (HEOMC) would produce branched polymers with a coumarin content of 15.1 and 22.6% by weight for PCL triol and PCL tetrol respectively.

Mixtures of PCL triol or tetrol with short difunctional PCL were necessary to reduce the coumarin content in the final branched polymer. Calculations by using Carothers equations allowed for the determination of the equivalent ratios of PCL triol/PCL diol and PCL tetrol/PCL diol to be reacted with HDI to obtain a final $f_{avg} = 2$ at full conversion, and the appropriate amount of free isocyanate groups to react with HEOMC giving a final coumarin content of 5 or 10% by weight in the final branched polymer, as shown in Figure 3 for the polymer based on triol PCL900, diol PCL530, HDI and 5 wt% HEOMC.

As an example, the equations used for polymer PCL1000+PCL530+HDI+HEOMC5% are given in the following. Starting from 1 mol of PCL1000 (molecular weight 1001, functionality 4), to obtain a 5 wt% of HEOMC in the final polymer we need to combine $x$ mol of PCL530 (molecular weight 527, functionality 2), $y$ mol of HDI (molecular weight 168.2, functionality 2) and $z$ mol of HEOMC (molecular weight 220.2, functionality 1), as shown in Equation (2):

$$0.05 = \frac{220.2z}{1001 \cdot 1 + 527 \cdot z + 168.2 \cdot y + 220.2 \cdot z} \quad (2)$$

For a stoichiometric reaction, the equivalents of isocyanate groups from HDI must equal the equivalents of hydroxyl groups from PCL1000, PCL530 and HEOMC, see Equation (3):

$$2 \cdot y = 4 \cdot 1 + 2 \cdot x + z \quad (3)$$

And finally, from Carothers equations for a non-stoichiometric reaction ($r \neq 1$), to obtain the maximum molecular weight in the reaction between HDI and PCL1000+PCL530, final average functionality should be 2 according to Equation (4):

$$2 = \frac{2 \cdot (4 \cdot 1 + 2 \cdot x)}{1 + x + y} \quad (4)$$

Working out the three equations the unknown amounts in mol for each reactant ($x$, $y$, $z$) are obtained, and from the mol ratio of the reactants the respective weight amounts are calculated.

In the following table, the weight amounts of each reactant, calculated for a total amount of 100 g of branched polymer are listed.

Branched polymers were prepared in 1,2-dichloroethane by mixing all reactants and using stannous

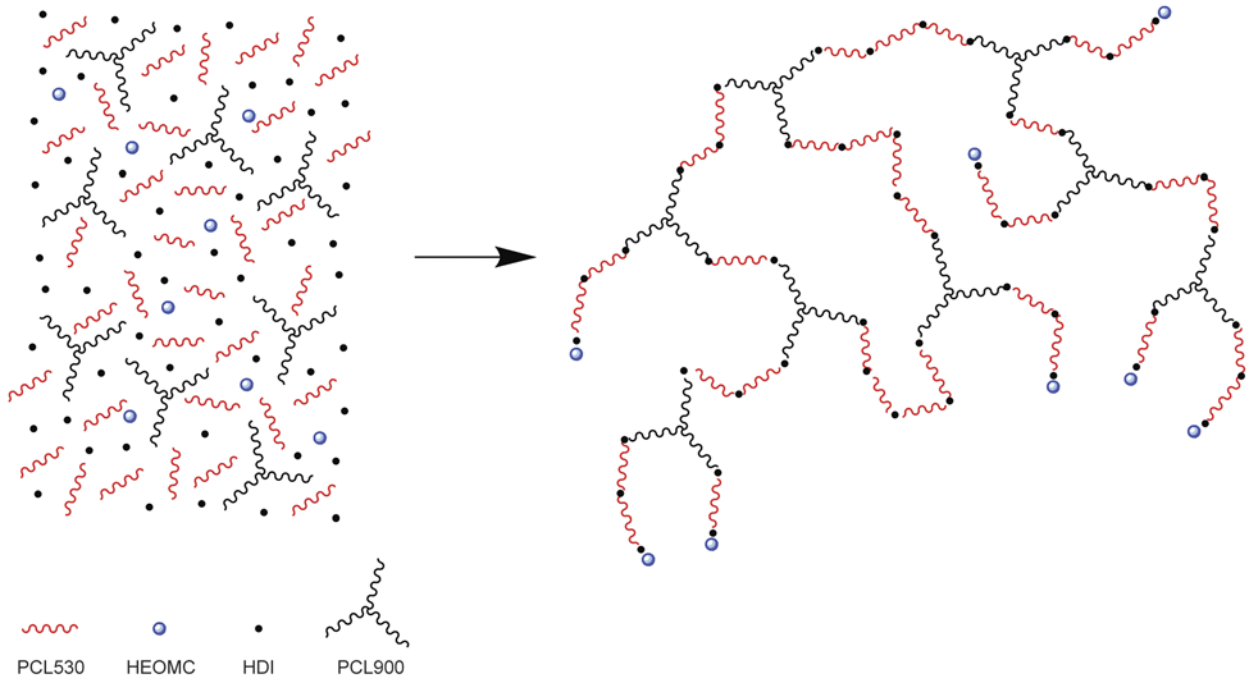


**Figure 3.** Reaction scheme for the preparation of the branched polyurethanes

**Table 1.** Amounts of reactants [g] in the synthesis of coumarin containing branched polyurethanes (calculated for 100 g of final polymer)

| POLYURETHANE | PCL900 triol | PCL1000 tetrol | PCL530 diol | HDI | HEOMC |
|---|---|---|---|---|---|
| PCL900+PCL530+HDI+HEOMC 5% | 20.43 | – | 50.76 | 23.81 | 5.00 |
| PCL900+PCL530+HDI+HEOMC 10% | 40.87 | – | 25.69 | 23.45 | 10.00 |
| PCL1000+PCL530+HDI+HEOMC 5% | – | 11.35 | 59.09 | 24.56 | 5.00 |
| PCL1000+PCL530+HDI+HEOMC10% | – | 22.70 | 42.35 | 24.94 | 10.00 |

octoate as catalyst. Films were obtained by casting directly the solution onto a Teflon mold and solvent evaporation at ambient temperature.

Similar branched polymers have been described in literature with poly(ethylene glycol) as the soft segment, a HDI trimer as the polyisocyanate and HEOMC as the coumarin monomer [20], but in that case the polymer structure was not controlled. Although not explained in that work, in a following paper by these authors [19] it was explained that some gelation occurred during synthesis as a consequence of the actual composition of the HDI trimer, in fact a mixture of compounds with some of them of higher functionality (4, 5, etc). With our synthesis procedure, no gel appeared and the final branched polymers were completely soluble with a molecular weight high enough to form films.

Thermal properties of the branched polymers as determined by DSC can be found in Table 2. The thermal properties of the linear models have been included for comparison.

In the first run from ambient temperature, an endothermic transition with several maxima was obtained, demonstrating that PCL530 chains can crystallize and, in principle, the endotermic peak could be related to PCL crystals melting. However, the maximum at higher temperature for the model linear polymer PCL530+HDI (with no coumarin) is at approximately 51 °C. And when HEOMC is introduced, the maximum at higher temperature is close or above 60 °C, that is, at significantly higher temperature. This result is unexpected, especially for branched polymers because branching points should introduce irregularities that should produce a material with lower crystallinity and smaller crystals with lower melting point. Besides, when HEOMC content increased, the relative area of the endotherm at the higher temperature side and the temperature at the higher temperature maximum increased as it is shown in Figure 4. From these results, it was deduced that coumarin end-groups were able to segregate in an ordered phase. Data from second heating run were consistent with this deduction (see Figure 5). After PCL segments glass transition, an exothermic crystallization peak due to PCL segments crystallization appeared, followed by a single endothermic peak due to PCL segments melting ending at 53 °C in the case of the linear polymer PCL530+HDI. For the polymers with coumarin end-groups, a melting endotherm with a maximum and a shoulder at higher temperature was observed for polymers PCL900+PCL530+HDI+HEOMC 5% and PCL1000+PCL530+

**Table 2.** Thermal properties of coumarin containing branched polyurethanes

| | First scan | | Second scan | | | | |
|---|---|---|---|---|---|---|---|
| POLYURETHANE | $M_p$ [°C] | $\Delta H_m$ [J/g] | $T_g$ [°C] | $T_c$ [°C] | $\Delta H_c$ [J/g] | $M_p$ [°C] | $\Delta H_m$ [J/g] |
| PCL530+HDI | 36.5<br>45.7<br>50.9 | 17.69 | –41.5 | 2.9 | –15.94 | 36.6 | 16.61 |
| PCL530+HDI+HEOMC 5% | 43.9<br>58.8 | 8.99 | –45.6 | –6.8 | –4.79 | 25.3<br>50* | 15.08 |
| PCL530+HDI+HEOMC 10% | 38.9<br>57.3 | 4.47 | –47.7 | –5.7 | –2.29 | 17<br>63.3 | 5.11 |
| PCL900+PCL530+HDI+HEOMC 5% | 48.0<br>61.9 | 4.14 | –41.9 | 3.2 | –2.81 | 31.1<br>51* | 6.43 |
| PCL900+PCL530+HDI+HEOMC 10% | 48.9<br>65.6 | 3.94 | –36.8 | 9.0 | –0.49 | 52.4 | 1.83 |
| PCL1000+PCL530 +HDI+HEOMC 5% | 46.3<br>61.0 | 4.09 | –41.3 | 2.9 | -4.17 | 31.2<br>51* | 5.75 |
| PCL1000+PCL530+HDI+HEOMC 10% | 47.7<br>66.7 | 2.49 | –35.5 | 22.5 | –1.14 | 55.5 | 1.47 |

*Shoulder. Temperature is approximate.

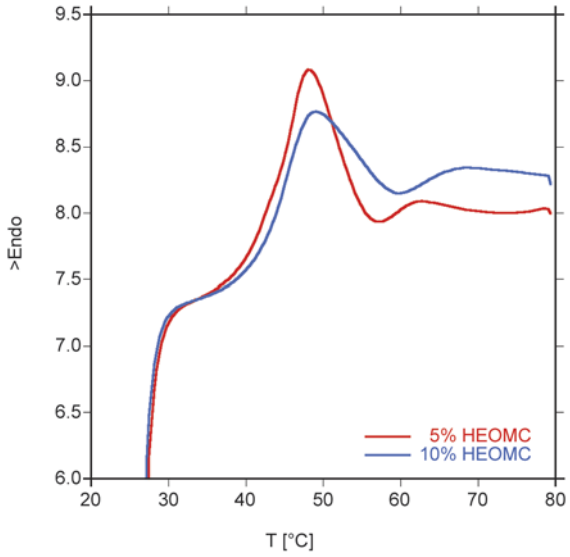


**Figure 4.** First heating curves for the polymers PCL900+PCL530+HDI+HEOMC 5% (red line) and PCL900+PCL530+HDI+HEOMC 10% (blue line)

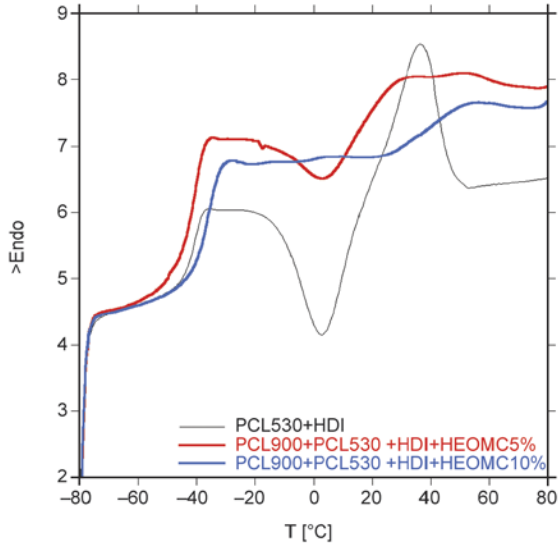


**Figure 5.** Second heating curves for the polymers PCL530+HDI (black line), PCL900+PCL530+HDI+HEOMC 5% (red line) and PCL900+PCL530+HDI+HEOMC 10% (blue line)

HDI+HEOMC 5%, the maximum at lower temperatures due to PCL segments melting and the shoulder at higher temperatures assigned to coumarin end-groups melting. For polymers PCL900+PCL530+HDI+HEOM 10% and PCL1000+PCL530+HDI+HEOMC 10% a single peak was obtained with the peak end located at 74.6 °C thus both melting endotherms (PCL and coumarin end-groups melting) are merged in a single peak (see Figure 5).

A similar peak was found in polymers prepared from PEG400-diol+HDI-trimer+HEOMC [20], with the maximum at 58.6 °C. In that work the endothermic peak was assigned to hard segment glass transition, although a glass transition should show a change in heat capacity and the authors found a broad endotherm as the ones shown in Figures 2 and 3. As already explained above, it seems more appropriate to assign the endotherm at higher temperature to the ordering of the coumarin end units.

Enthalpy values of the melting peaks ($\Delta H_m$) are very low. The highest value, as expected, is for the linear model polymer without coumarin (PCL530+HDI). Taking into account that only PCL530 segments can crystallize, after correction for the PCL530 content on the polymer (75.8% by weight) and taking 148.24 J/g as the value for the crystallization heat for a 100% crystallized pure high molecular weight PCL [29], only 15.7 wt% of the PCL530 (12 wt% respect to the total polymer weight) is able to crystallize. For the branched polyurethanes, the percentage of crystalline PCL530 is even lower. Although it cannot be calculated because the endotherm is the sum of PCL segments plus coumarin-end groups melting, the weight percentage will be even lower than for the model linear polymers, thus branched polyurethanes are almost completely amorphous. When HEOMC content is increased, the weight content of PCL530 diol in the polymer is decreased, and the enthalpy due to PCL530 segment crystallinity must decrease. However, if the enthalpy values are corrected for the PCL530 content on the polymer, it is found that despite the expected increase in the melting enthalpy due to the increase in coumarin-end groups melting, the overall value of the enthalpy decreases, thus the PCL530 segments crystallinity is decreased when HEOMC content is increased. When branched polymers based on triol PCL900 or tetrol PCL1000 are compared, for the same HEOMC content and after correcting for the PCL530 content on the polymer, it is observed that crystallinty is slightly lower for the polymers based on tetrol PCL1000.

### 3.2. Photo-dimerization/photo-cleavage kinetics in thin films

Three different set of lamps were tested for the photopolymerization of coumarin-based polymers. In Figure 6, the emission spectra of the lamps are shown. For lamp with maximum at 313 nm, emission starts at 270 nm; for lamp with maximum at 354 nm, emis-

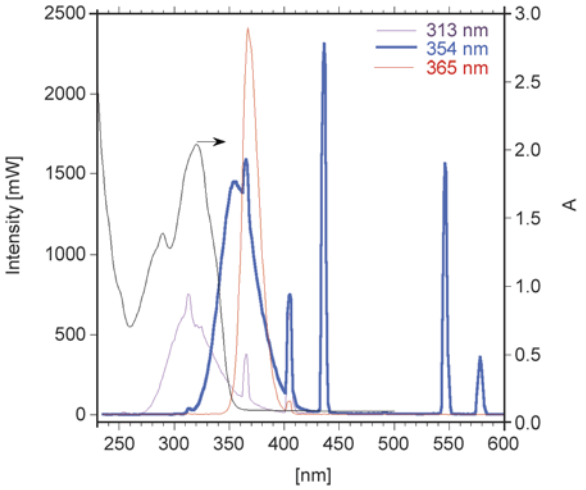


**Figure 6.** Emission spectra of the three different lamps used for photo-dimerization. Absorption spectrum of the polymer PCL530+HDI+HEOMC 10% (black line) has also been included.

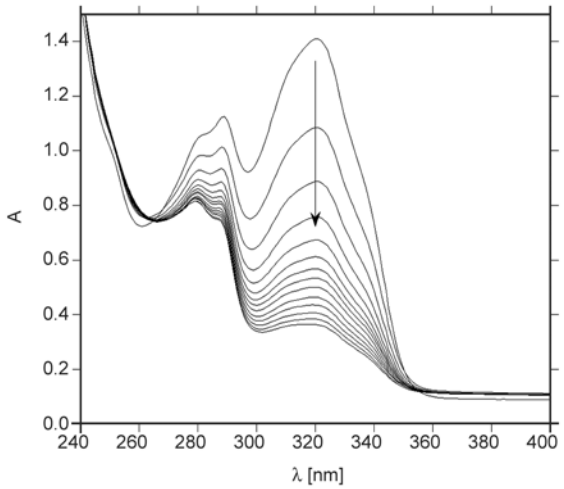


**Figure 7.** UV spectra of polymer PCL530+HDI+HEOMC 10% when irradiated at different times

sion starts at 310 nm; and for lamp with maximum at 365 nm, emission starts at 350 nm.

Photo-dimerization was followed for a film of polymer PCL530+HDI+HEOMC 10%. Film was cast from a chloroform solution of the polymer onto a side of a quartz cuvette. Final thickness of the film was approximately 2 microns.

In Figure 6, the absorption spectra of the film can be seen. Absorption of coumarin shows a π–π* transition between 260 and 300 nm attributed to electrons of the conjugated benzene nucleus and another π–π* transition between 310 and 340 nm assigned to the pyrone nucleus [20, 28].

Emission spectrum of the 313 nm lamp was almost coincident, whereas emission spectrum of the 354 nm lamp was coincident in the range 310–350 nm and emission spectrum of the 365 nm lamp barely overlapped at the very end of the absorption band of coumarin. From this graph, it was expected that lamp 313 nm would be more efficient than lamp 354 nm, and lamp 365 nm would have a very poor efficiency.

UV absorption in the maximum at approximately 320 nm was measured at different irradiation times, as seen on Figure 7. The absorption decreased because of the dimerization of the coumarin double bonds to form cyclobutane rings, which destroyed the conjugated π-system.

Conversion (or dimerization degree) was calculated from Equation (5):

$$\text{Conversion} = 1 - \frac{A_t}{A_0} \tag{5}$$

where $A_t$ and $A_0$ denote the absorbance at 320 nm at time $t$ and 0 respectively after subtraction of the baseline value at 400 nm. In Figure 8, the conversion for polymer PCL530+HDI+HEOMC 10% when irradiated at different times with lamp 313 nm can be seen.

At the beginning, dimerization was very fast, reaching 35–40% conversion within the first minute. In the following 15 minutes, conversion reached a plateau and did not change significantly with irradiation time, and afterwards, conversion increased steadily with irradiation time up to approximately 75–80% conversion at 140 minutes. In the graph, four different samples were irradiated, showing a quite good repeata-

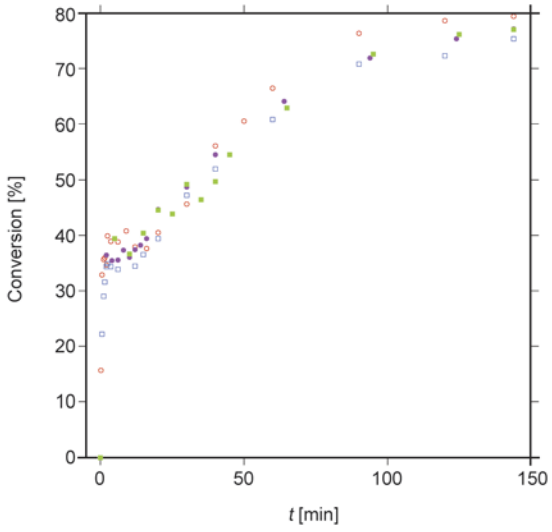


**Figure 8.** Conversion for polymer PCL530+HDI+HEOMC 10% when irradiated at different times with lamp 313 nm, for 4 different dimerization reactions

bility. This kinetic profile was unexpected, and it has not been reported in literature.

When the polymer film was irradiated with 354 or 365 nm lamps, conversion increased continuously with irradiation time until a plateau was reached, at approximately 85–90% conversion (Figure 9). This ultimate conversion is similar to the conversion found in other methylcoumarin containing polymers, for which maximum conversions reported are 77.5% [20], 81.5% [22] and approximately 80% [11]. Repeatability in conversion was as good as for the curves in Figure 6. Conversion rate was much slower for irradiation with the 365 nm lamp, but the shape of the dimerization curves was similar. When compared with the curve for irradiation with the 313 nm lamp it is clear that although within the first minute this lamp produced higher conversion, at longer times, lamp 354 nm produced higher conversions. With lamp 354 nm the plateau was reached at approximately 30 minutes, whereas for lamp 365 nm the plateau value was reached at approximately 20 hours.

Photo-cleavage of the dimerized films was carried out with the 254 nm lamps. These lamps presented a narrow irradiation band from 251 to 257 nm with a maximum at 254 nm and some other similar small narrow bands with maxima at 313 and 365 nm. Test on dimerized samples proved that 15 minutes irradiation with lamp 254 nm was enough to produce almost complete photo-cleavage.

Samples of polymer PCL530+HDI+HEOMC 10% where irradiated for certain times with lamp 313 nm

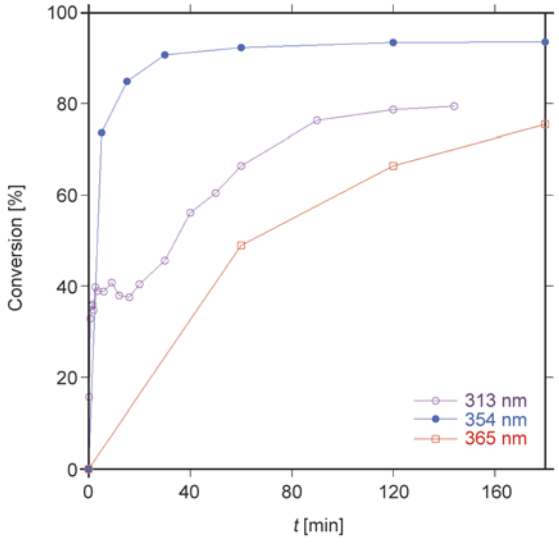


**Figure 9.** Conversion for polymer PCL530+HDI+HEOMC 10% when irradiated at different times with lamp 313 nm (purple), lamp 354 nm (blue) or lamp 365 nm (red)

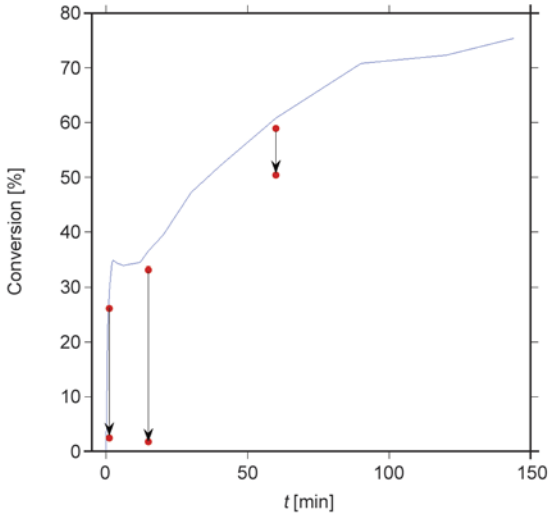


**Figure 10.** Photo-dimerization for polymer PCL530+HDI+HEOMC10% when irradiated at different times with lamp 313 nm and corresponding photo-cleavage with 354 nm lamp for 15 minutes. Line shows the complete photo-dimerization curve.

and after dimerization, where irradiated with lamp 254 nm for photo-cleavage. In Figure 10, the results are shown. It can be seen that when dimerized for up to 15 minutes, that is, during the initial fast growing part of the curve and the plateau between 1 and 15 minutes, photo-cleavage was almost complete, but for higher irradiation time photo-cleavage was strongly reduced, and for 60 minutes irradiation time photo-cleavage was only a 10%.

For 354 and 365 nm lamps, photo-cleavage was more efficient at high irradiation times. In Figure 11 for example, for irradiation with 354 nm lamp, it can be found that photo-cleavage had approximately the same efficiency at any dimerization conversion but photo-cleavage was not complete and always a dimerized material (approximately 20–25%) remained.

It has been shown extensively by other authors that photo-cleavage is never complete and is attributed to a dynamic equilibrium between photo-dimerization and photo-cleavage [11, 19–22, 25]. It was also pointed out that prolonged exposure to 254 nm light would result in an irreversible structure [20]. For 354 nm irradiation lamp it seems that the irreversibility reached a fairly constant value (20–25% dimerization) irrespective of photo-dimerization time, whereas for 313 nm lamp, irradiation time was critical respect to irradiation time, and long times led to higher irreversibility. It could be deduced that irreversibility is produced mainly by irradiation at wavelengths below 320 nm, that probably leads to irreversible structures.

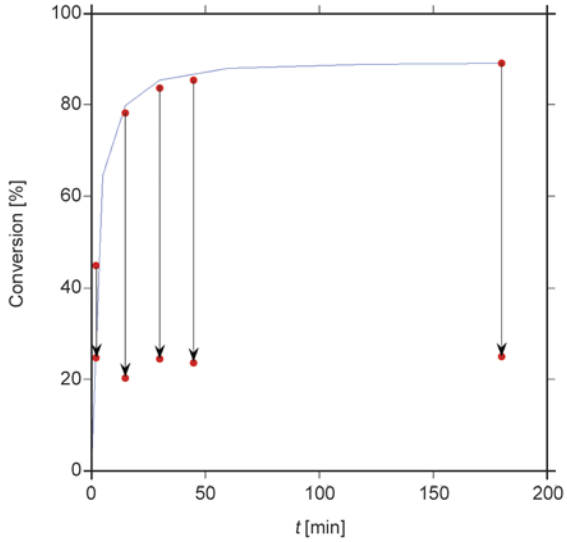


**Figure 11.** Photo-dimerization for polymer PCL530+HDI+HEOMC 10% when irradiated at different times with lamp 354 nm and corresponding photo-cleavages with lamp 354 nm for 15 minutes. Line shows the complete photo-dimerization curve.

Branched polymers were photo-dimerized and photo-cleaved with the 354 and 254 nm lamps respectively. Up to nine cycles were recorded and the curves were similar for all these polymers. In Figure 12, the cycles for polymer PCL900+PCL530+HDI+HEOMC 10% are shown as an example. As it can be seen, the photo-dimerization efficiency slightly decreased and photo-cleavage efficiency was even more reduced from cycle to cycle, showing that irreversibility increased with the number of cycles. It can

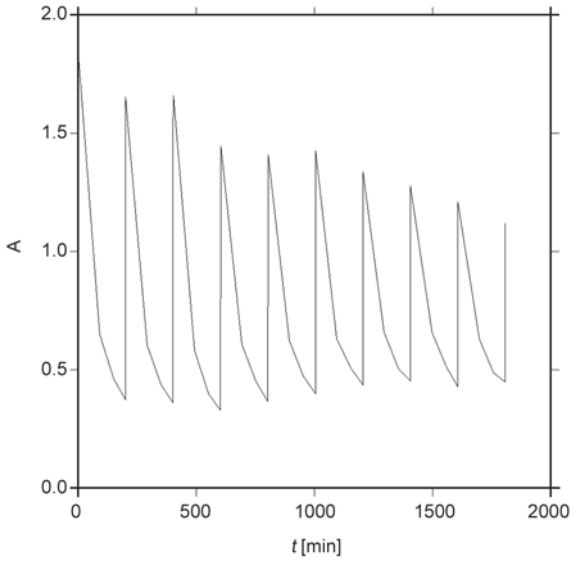


**Figure 12.** Photo-dimerization and photo-cleavage cycles for polymer PCL900+PCL530+HDI+HEOMC 10% when irradiated for 200 min at 354 nm and for 1 minute at 254 nm

be noted that the loss of efficiency is quite significant for photo-cleavage and it is much lower for photo-dimerization, as already observed by other authors [21].

### 3.3. Photo-dimerization/photo-cleavage kinetics in thick films

UV spectra were saturated in thick films and Raman spectroscopy was used for measuring photo-dimerization/photo-cleavage conversion, as already reported by other researchers [20]. Raman spectra for polymer PCL530+HDI and polymer PCL530+HDI+HEOMC 10% before irradiation and after irradiation at 354 nm are represented in Figure 13. As it can be seen, the bands related to coumarin units decreased after irradiation at 354 nm. Quantification was done by normalizing the height of the peak related to the coumarin double bond at 1614 $cm^{-1}$ and the height of the peak at 1441 $cm^{-1}$ related to methylene groups as shown in Figure 14 for non irradiated PCL530+HDI+HEOMC 10%.

Photo-dimerization kinetics was measured simultaneously by UV and by Raman in a thin film in order

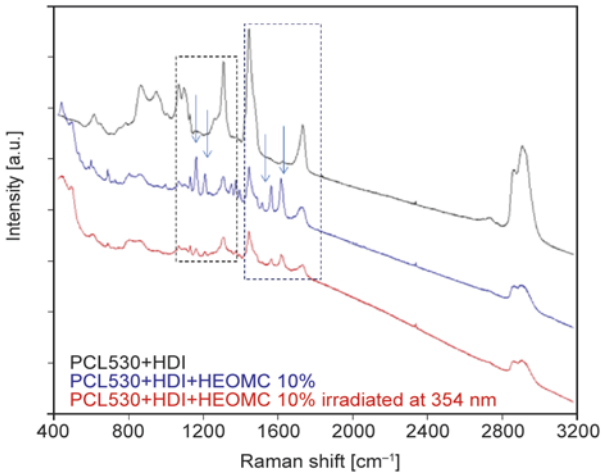


**Figure 13.** Raman spectrum of PCL530+HDI (black line), non-irradiated PCL530+HDI+HEOMC 10% (blue line) and PCL530+HDI+HEOMC 10% irradiated at 354 nm (red line)

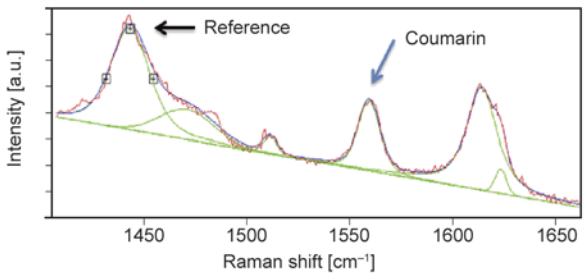


**Figure 14.** Raman bands used for conversion calculation

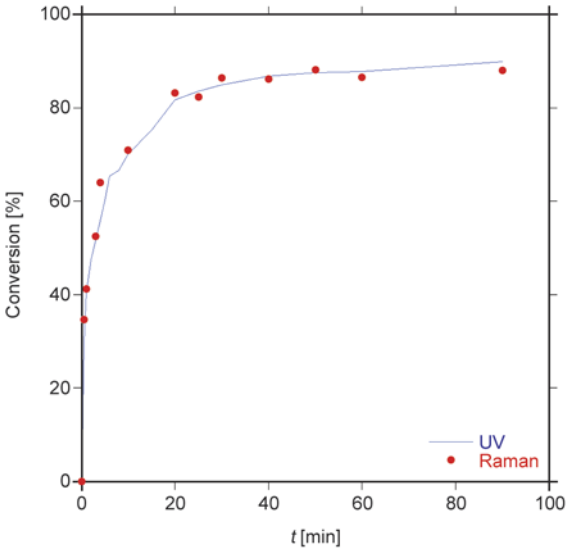


**Figure 15.** UV versus Raman conversion for polymer PCL530+ HDI+HEOMC 10%

to compare the data obtained by both techniques. As shown in Figure 15, despite the slight scattering of the Raman data, results are similar demonstrating that Raman can be used to calculate the conversion in thick films.

Raman spectra for the branched polymers (not shown) were very similar to spectra for the linear models. For the thick films prepared to measure mechanical properties Raman was used to calculate conversion.

### 3.4. Mechanical properties

Mechanical properties of linear polymers PCL530+ HDI 5% and 10% could not be measured because its films were soft and too weak due to the limited growth of the linear chains. Non irradiated branched coumarin containing polyurethanes were weak and very soft. After irradiation at 354 nm, crosslinking produced by coumarin photo-dimerization increased their properties and a soft rubbery material was finally obtained. In Table 3, the values for tensile stress and strain to failure for films of approximately 150 microns thickness of non irradiated polymers and for the polymers irradiated for 300 minutes at 354 nm are listed. Conversion measured by Raman after 300 minutes at 354 nm was approximately 70% for all the polymers.

When the monomers are reacted, PCL530 and HDI increase the chain length and HEOMC terminates the chains, and when coumarin end-groups photo-dimerize they link two different chains but do not introduce a crosslink point. Therefore, the only polyfunctionality points introduced in the final photo-crosslinked polymer come from the PCL triol or the PCL tetrol. From the data on Table 1 and supposing full conversion of the reactants during the synthesis of the branched polyurethanes and full conversion of the coumarin units during photo-dimerization, a maximum theoretical crosslink density (in moles of crosslink points·$10^4$/grams of polymer) can be calculated. The calculations give the following order of crosslink density for the polymers:

PCL1000+PCL530+HDI+HEOMC 5% (1.13) <
PCL900+PCL530+HDI+HEOMC 5% (2.23) ~
PCL1000+PCL530+HDI+HEOMC 10% (2.27) <
PCL900+PCL530+HDI+HEOMC 10% (4.47)

From the properties measured, it is clear that tetrafunctional (PCL1000) crosslinks gave better mechanical properties than trifunctional (PCL900) crosslinks for the same crosslink density. And as expected, for the same functionality of the crosslinks, when coumarin content increased the crosslink density increased and the mechanical properties increased.

Not much information is found in literature on the mechanical properties of coumarin-containing polyurethanes. For an irradiated polymer composed of PEG400-diol+HDI-trimer+HEOMC with content of 20% by weight of HEOMC, tensile strength and strain were approximately 2.25 MPa and 140% respectively [20]; and for irradiated polymers composed of PEG800-diol+IPDI+Coumarine-diol with

**Table 3.** Mechanical properties of the non-irradiated and irradiated at 354 nm for 300 minutes branched polyurethanes

| Polyurethane | Stress [MPa] | Strain [%] |
|---|---|---|
| PCL900+PCL530+HDI+HEOMC 5% non-irradiated | 0.92±0.12 | 46±2 |
| PCL900+PCL530+HDI+HEOMC 5% irradiated | 2.3±0.3 | 110±30 |
| PCL900+PCL530+HDI+HEOMC 10% non-irradiated | 1.8±0.2 | 34±10 |
| PCL900+PCL530+HDI+HEOMC 10% irradiated | 4.9±0.5 | 640±110 |
| PCL1000+PCL530+HDI+HEOMC 5% non-irradiated | 1.08±0.11 | 69±8 |
| PCL1000+PCL530+HDI+HEOMC 5% irradiated | 2.7±0.5 | 260±50 |
| PCL1000+PCL530+HDI+HEOMC 10% non-irradiated | 1.4±0.3 | 39±11 |
| PCL1000+PCL530+HDI+HEOMC 10% irradiated | 5.4±0.9 | 510±100 |

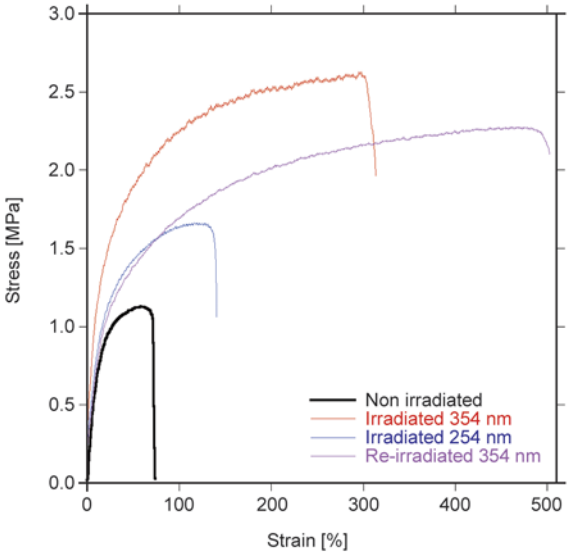


**Figure 16.** Stress-strain curves for polymer PCL1000+PCL530+HDI+HEOMC 5% non-irradiated (black line), irradiated at 354 nm (red line), irradiated at 354 nm+254 nm (blue line) and 354 nm+254 nm+354 nm (purple line)

5.5 and 13% by weight of coumarin component, with 86 and 94% of dimerization conversion respectively, values for tensile strength and strain were approximately 1.2 MPa and 650% and 3.6 MPa and 235% respectively [19]. Data on Table 3 demonstrate that PCL based materials, despite having lower coumarin content and/or lower conversion and therefore lower crosslink density, after irradiation produce polyurethanes with better mechanical properties than coumarin-containing materials based on PEG.

For all the irradiated branched materials, when irradiated at 254 nm for 12 minutes mechanical properties decreased as a consequence of photo-cleavage of coumarin units, which decreased the crosslink density of the material. Re-irradiation at 354 nm for 150 minutes increased again the crosslink density by photo-dimerization of coumarin units and mechanical properties recovered, as it can be seen in Figure 16 for the polymer PCL1000+PCL530+HDI+ HEOMC 5%.

## 4. Conclusions

A series of branched polyurethanes based on PCL with a content of 5 and 10% by weight of terminal coumarin units were successfully prepared. A mixture of short PCL triol or tetrol with a short PCL diol in the appropriate amounts was necessary to control the molecular architecture, to obtain the maximum possible molecular weight and to avoid gelation during synthesis.

The obtained branched polyurethanes presented low PCL crystallinity and segregation of the coumarin terminal units as showed by DSC measurements.

Photo-dimerization curve when irradiation was done with 313 nm lamps presented 2 distinct steps, the first one with a very fast rate and good yield for photo-cleavage and the second one with a slower rate and a very strong irreversibility respect to photo-cleavage. Optimum photo-dimerization was achieved when irradiation was done with 354 nm lamps, although some irreversibility for photo-cleavage was always present and increased with the increase on photo-dimerization/photo-cleavage cycles.

It was demonstrated that Raman spectroscopy gave the same conversion results as UV spectroscopy, and it was used to calculate conversion in thick films.

Mechanical properties of the crosslinked films by photo-dimerization were better than the properties of comparable photo-dimerized polyurethanes found in literature. Photo-cleavage decreased the mechanical properties as a consequence of the decrease in crosslinks and re-photo-dimerization increased again the properties by restoration of the crosslinks.

## Acknowledgements

The authors would like to thank the Ministry of Economy and Competitiveness (MINECO) for the financial support of this work within the framework of the Plan Nacional de I+D+I through the research projects MAT2011-25513, MAT2013-48059-C2 and MAT2014-52644-R and the INNPACTO project IPT-2012-0324-420000. Also, this work has been supported by programme Technology Centres Foundation Iñaki Goenaga.

## References

[1] Guimard N. K., Oehlenschlaeger K. K., Zhou J., Hilf S. F., Schmidt G., Barner-Kowollik C.: Current trends in the field of self-healing materials. Macromolecular Chemistry and Physics, **213**, 131–143 (2012). DOI: 10.1002/macp.201100442

[2] Binder W.: Self-healing polymers: From principles to applications. Wiley-VCH, Weinheim (2013).

[3] Billiet S., Hillewaere X. K., Teixeira R. F. A., du Prez F. E.: Chemistry of crosslinking processes for self-healing polymers. Macromolecular Rapid Communications, **34**, 290–309 (2013). DOI: 10.1002/marc.201200689

[4] Zhang M. Q., Rong M. Z.: Intrinsic self-healing of covalent polymers through bond reconnection towards strength restoration. Polymer Chemistry, **4**, 4878–4884 (2013). DOI: 10.1039/C3PY00005B

[5] Rekondo A., Martin R., de Luzuriaga A. R., Cabañero G., Grande H. J., Odriozola I.: Catalyst-free room-temperature self-healing elastomers based on aromatic disulfide metathesis. Materials Horizons, **1**, 237–240 (2014). DOI: 10.1039/c3mh00061c

[6] Pratama P. A., Sharifi M., Peterson A. M., Palmese G. R.: Room temperature self-healing thermoset based on the Diels–Alder reaction. ACS Applied Materials and Interfaces, **5**, 12425–12431 (2013). DOI: 10.1021/am403459e

[7] Liu Y-L., Chuo T-W.: Self-healing polymers based on thermally reversible Diels–Alder chemistry. Polymer Chemistry, **4**, 2194–2205 (2013). DOI: 10.1039/c2py20957h

[8] Pratama P. A., Peterson A. M., Palmese G. R.: Diffusion and reaction phenomena in solution-based healing of polymer coatings using the Diels–Alder reaction. Macromolecular Chemistry and Physics, **213**, 173–181 (2012). DOI: 10.1002/macp.201100407

[9] Bergman S. D., Wudl F.: Mendable polymers. Journal of Materials Chemistry, **18**, 41–62 (2008). DOI: 10.1039/b713953p

[10] Zheng Y., Micic M., Mello S. V., Mabrouki M., Andreopoulos F. M., Konka V., Pham S. M., Leblanc R. M.: PEG-based hydrogel synthesis via the photodimerization of anthracene groups. Macromolecules, **35**, 5228–5234 (2002). DOI: 10.1021/ma012263z

[11] Trenor S. R., Shultz A. R., Love B. J., Long T. E.: Coumarins in polymers: From light harvesting to photocross-linkable tissue scaffolds. Chemical Reviews, **104**, 3059–3077 (2004). DOI: 10.1021/cr030037c

[12] Wu L., Jin C., Sun X.: Synthesis, properties, and light-induced shape memory effect of multiblock polyesterurethanes containing biodegradable segments and pendant cinnamamide groups. Biomacromolecules, **12**, 235–241 (2011). DOI: 10.1021/bm1012162

[13] Chamsaz E. A., Sun S., Maddipatla M. V. S. N., Joy A.: Photoresponsive polyesters by incorporation of alkoxyphenacyl or coumarin chromophores along the backbone. Photochemical and Photobiological Sciences, **13**, 412–421 (2014). DOI: 10.1039/c3pp50311a

[14] Jiang J., Qi B., Lepage M., Zhao Y.: Polymer micelles stabilization on demand through reversible photo-crosslinking. Macromolecules, **40**, 790–792 (2007). DOI: 10.1021/ma062493j

[15] Kehrloesser D., Baumann R-P., Kim H. C., Hampp N.: Photochemistry of coumarin-functionalized $SiO_2$ nanoparticles. Langmuir, **27**, 4149–4155 (2011). DOI: 10.1021/la200238y

[16] Sinkel C., Greiner A., Agarwal S.: Synthesis, characterization, and properties evaluation of methylcoumarin end-functionalized poly(methyl methacrylate) for photoinduced drug release. Macromolecules, **41**, 3460–3467 (2008). DOI: 10.1021/ma702622p

[17] Jin Q., Mitschang F., Agarwal S.: Biocompatible drug delivery system for photo-triggered controlled release of 5-fluorouracil. Biomacromolecules, **12**, 3684–3691 (2011). DOI: 10.1021/bm2009125

[18] Schraub M., Kim H-C., Hampp N.: Photoinduced refractive index changes of 3-phenyl-coumarin containing polymers for ophthalmic applications. European Polymer Journal, **51**, 21–27 (2014). DOI: 10.1016/j.eurpolymj.2013.11.014

[19] Ling J., Rong M. Z., Zhang M. Q.: Photo-stimulated self-healing polyurethane containing dihydroxyl coumarin derivatives. Polymer, **53**, 2691–2698 (2012). DOI: 10.1016/j.polymer.2012.04.016

[20] Ling J., Rong M. Z., Zhang M. Q.: Coumarin imparts repeated photochemical remendability to polyurethane. Journal of Materials Chemistry, **21**, 18373–18380 (2011). DOI: 10.1039/c1jm13467a

[21] Chen Y., Jean C-S.: Polyethers containing coumarin dimer components in the main chain. II. Reversible photocleavage and photopolymerization. Journal of Applied Polymer Science, **64**, 1759–1768 (1997). DOI: 10.1002/(SICI)1097-4628(19970531)64:9<1759::AID-APP12>3.0.CO;2-T

[22] Zhao D., Ren B., Liu S., Liu X., Tong Z.: A novel photoreversible poly(ferrocenylsilane) with coumarin side group: Synthesis, characterization, and electrochemical activities. Chemical Communications, **2006**, 779–781 (2006). DOI: 10.1039/b515413h

[23] Sinkel C., Greiner A., Agarwal S.: A polymeric drug depot based on 7-(2′-methacryloyloxyethoxy)-4-methylcoumarin copolymers for photoinduced release of 5-fluorouracil designed for the treatment of secondary cataracts. Macromolecular Chemistry and Physics, **211**, 1857–1867 (2010). DOI: 10.1002/macp.201000206

[24] Chung J. S., Kim H. S., Chae K. H.: Preparation of photo-crosslinkable polymers having coumarin side groups and their properties. Korea Polymer Journal, **3**, 12–18 (1995).

[25] Nagata M., Yamamoto Y.: Photoreversible poly(ethylene glycol)s with pendent coumarin group and their hydrogels. Reactive and Functional Polymers, **68**, 915–921 (2008). DOI: 10.1016/j.reactfunctpolym.2008.01.003

[26] Szycher M.: Szycher's handbook of polyurethanes. CRC Press, New York (2012).

[27] Oertel G.: Polyurethanes handbook. Hanser, Munich (1994).

*eXPRESS Polymer Letters Vol.10, No.2 (2016) 96–110*
*Available online at www.expresspolymlett.com*
*DOI: 10.3144/expresspolymlett.2016.11*

# Electrochemical impedance and spectroscopy study of the EDC/NHS activation of the carboxyl groups on poly(ε-caprolactone)/poly(m-anthranilic acid) nanofibers

*Z. Guler*[1], *A. S. Sarac*[1,2,3*]

[1]Department of Nanoscience and Nanoengineering, Maslak, Istanbul Technical University, 34469 Istanbul, Turkey
[2]Department of Chemistry, Istanbul Technical University, Maslak, 34469 Istanbul, Turkey
[3]Department of Polymer Science and Technology, Istanbul Technical University, Maslak, 34469 Istanbul, Turkey

*Received 2 Juy 2015; accepted in revised form 2 September 2015*

**Abstract.** Electrochemical impedance spectroscopy (EIS) and spectroscopy was applied to investigate the surface activation of carboxyl group (–COOH) containing nanofibers by the reaction of 1-ethyl-3-(dimethyl-aminopropyl) carbodiimide hydrochloride (EDC)/N-hydroxyl succinimide (NHS) in different concentrations. Poly(ε-caprolactone)/poly(m-anthranilic acid) (PCL/P3ANA) nanofibers were fabricated by electrospinning and were activated with 5/0.5, 0.5/5, 5/5 and 50/50 mM of EDC/NHS. The surface activation was investigated by Attenuated Total Reflectance Fourier transform infrared spectroscopy (FTIR-ATR) and activation yield was estimated. Albumin was immobilized after surface activation and the amount of covalently immobilized protein was determined by bicinchoninic acid (BCA) assay. Morphology and composition of albumin immobilized nanofibers were characterized by Scanning Electron Microscopy/Energy-Dispersive X-ray Spectroscopy (SEM/EDX) and Atomic force microscope (AFM). EIS measurements indicated that nanofibers become resistant after albumin immobilization. The obtained data revealed that the highest amount of albumin bound to nanofibers activated with 50/50 mM of EDC/NHS which was found to be the optimum concentration for the activation of PCL/P3ANA nanofibers.

***Keywords:*** *nanomaterials, covalent immobilization, electrochemical impedance spectroscopy (EIS), poly(m-anthranilic acid)*

## 1. Introduction

Using nanostructured materials as supports for biomolecule immobilization have recently attract great interest considering their extremely high surface area to volume ratio [1]. Among these nanostructured materials, electrospun nanofibers stand out as the better alternative for immobilization of biomolecules due to the higher loading capacity and porosity compared to polymer films [2, 3].

Polymeric nanofibers allow further optimization of properties such as electrical conductivity [4] to meet different requirements in various applications. In the case of conductive polymer containing nanofibers, modification of a surface with a biomolecule can be detected by electrochemical impedance spectroscopy (EIS) [5, 6]. There other methods such as X-ray photoelectron spectroscopy (XPS), Thermal gravimetric analysis (TGA), Scanning electron microscopy (SEM) etc. can be used to investigate the surface modification [7], however EIS is a very sensitive method for the analysis of the interfacial properties such as resistance and capacitance of a surface by using very small amplitude sinusoidal voltage signals without significantly disturbing the properties being measured. Therefore, EIS is a sensitive, easy and cost effective method which allows

*Corresponding author, e-mail: sarac@itu.edu.tr

reuse of samples after EIS measurements. Poly(m-anthranilic acid) (P3ANA) is a very convenient conductive polymer for immobilization of biomolecules covalently due to the presence of carboxylic acid group –COOH on the main polyaniline backbone [8].

Covalent immobilization of the biomolecules by using reactive groups has been recognized as an attractive strategy since it provides the control of the immobilization of biological probes on the surface [9]. Covalent immobilization of biomolecules onto a –COOH group containing surface consists of preparation of a succinimidyl ester (–COOSuc)-terminated surface and its reaction with an amino ($–NH_2$) group on the biomolecule. This reaction is referred as surface 'activation' which is conducted by reacting a surface bearing carboxyl end groups with N-hydroxysuccinimide (NHS), in the presence of carbodiimide such as 1-ethyl-3-(dimethyl-aminopropyl) carbodiimide hydrochloride (EDC) [10]. EDC/NHS activation of carboxylic acids has been widely applied to various kinds of substrates of polymers [11], silicon [9], nanotubes [12] or nanoparticles [13, 14]. In these studies, the concentrations of EDC and NHS strongly vary in a wide range (from M to the mM range) from one study to another [15–17]. Voicu *et al*. [15], used 0.1 M NHS and 0.4 M EDC in order to activate silicon surface. In another study, equal amounts of EDC and NHS (100 mM) were used for activation of carboxylic acid terminated self-assembled monolayers [18]. Zander *et al*. [19] activated the surface of plasma-treated PCL nanofibers by using approximately 25 mM EDC and 43 mM NHS. Electrospun collagen or gelatin nanofibers were activated by 30 mM EDC and 6 mM of NHS [20]. Based on the EDC/NHS concentrations used in the literature, for the activation of carboxyl groups of PCL/P3ANA nanofibers, it was decided to use equal amounts of EDC/NHS (EDC/NHS = 5/5 mM and EDC/NHS = 50/50 mM), excess amount of EDC over NHS (EDC/NHS = 5/0.5 mM) and excess amount of NHS over EDC (EDC/NHS = 0.5/5 mM). These concentrations were selected since very large concentrations of EDC or NHS result the formation of the byproducts at the surface which can prevent the formation of –COOSuc surface and affect the success of the surface activation. In the case of EDC and NHS concentrations are very low, then the surface activation reaction remains incomplete [7]. Although the EDC/NHS activation has been widely used, the details of EDC/NHS activation of carboxyl groups of a semiconducting nanofiber and of the following amidation of NHS-ester for protein immobilization have not been reported. This study aims to investigate the optimum EDC/NHS concentration for surface activation of PCL/P3ANA nanofibers by spectroscopy and electrochemical impedance spectroscopy.

Poly(ε-caprolactone)/poly(m-anthranilic acid) nanofibers were fabricated by electrospinning. Figure 1 represents the chemical structure of PCL/P3ANA and shows the interaction between partial positive charges of amine groups in P3ANA [21, 22] and partially negative charges in PCL backbone [23]. The activation of carboxyl groups on the surface of PCL/P3ANA nanofibers were performed with different concentrations of EDC and NHS. Due to its low price and availability in large amounts, albumin was selected as model protein and covalently immobilized to activated nanofibers. The success of activation procedure and the amount of immobilized albumin were investigated by FTIR-ATR and the surface activation yield was estimated. The amount of covalently immobilized protein was determined by bicinchoninic acid assay. Morphology and composition of nanofibers before and after albumin immobilization were analyzed by AFM, (SEM)/(EDX). EIS analysis and equivalent circuit modeling was performed to observe the immobilized albumin depending on the EDC/NHS concentrations used in activation. The nanofibers become resistive due to albumin immobilization. The obtained data revealed that electrochemical impedance spectroscopy can be used for investigation of surface modification with biomolecule immobilization by the determina-

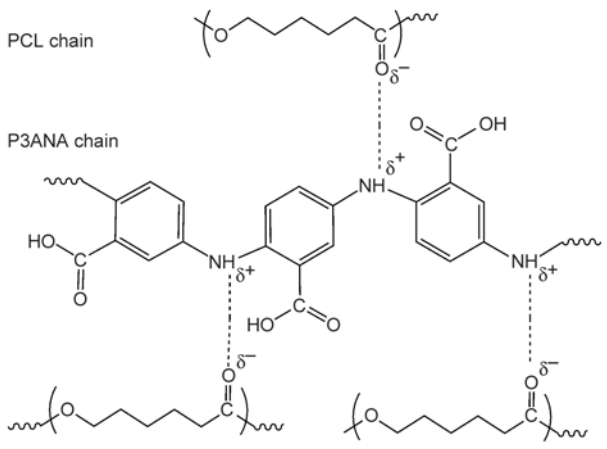


**Figure 1.** Schematic representation of the chemical structure of PCL/P3ANA

tion and quantification of the optimum and effective concentration for the activation of carboxyl group bearing polymeric nanofibers.

## 2. Experimental

### 2.1. Materials

Poly(ε-caprolactone) (440744) ($M_w$ = 80 000 g/mol), 3-aminobenzoic acid (m-anthranilic acid) (127671), albumin ($M_w$ ~ 66 kDa) (A2153), *N*-(3-dimethylaminopropyl)-*N*′-ethylcarbodiimide hydrochloride (EDC), *N*-hydroxysuccinimide (NHS), 2-morpholinoethane sulfonic acid (MES, low moisture content, ≥99) and the bicinchoninic acid (BCA) Protein Quantitation Kit were purchased from Sigma Aldrich (St Louis, MO, USA). Phosphate buffer saline (PBS) was obtained from Gibco (Carlsbad, CA). Dimethyl formamide (DMF Analytical Grade) (103034) and Tetrahydrofurane (THF Analytical Grade) (109731) were supplied from Merck (Darmstadt, Germany). Poly(m-anthranilic acid) (P3ANA) was synthesized according to our previous study [8]. Briefly, 3-aminobenzoic acid (0.043 mol) has been dissolved in 90 mL of 0.5 M NaOH. Equal mole of ammonium persulfate in water (30 mL) has been added drop wise to this solution and the mixture was stirred at room temperature for 24 h. The precipitated polymer has been collected by filtration, washed with 1.2 M HCl and water until the filtrate became colourless and dried in vacuum at 60 °C for two days. This polymer has been recovered in 70% yield as a brown powder. All of these chemicals were analytical grade and used as received.

### 2.2. Fabrication of PCL/P3ANA nanofibers by electrospinning

0.125 g of poly(m-anthranilic acid) were dissolved in 5 mL THF and DMF mixture (1/1 v/v) containing 0.5 g poly(ε-caprolactone). The obtained polymer blend was stirred for 3 h at room temperature to obtain homogeneous solution for optimum electrospinning conditions.

Electrospinning solution was placed into a syringe needle (outer diameter of 0.7 mm) which was connected to a high-voltage direct current (DC) power supply (ES 30 Model Gamma High Voltage Inc., Florida, USA). PCL/P3ANA solution was horizontally electrospun onto aluminum foil at 15 kV driving voltage with a collection distance of 15 cm. The flow rate of the solution was 1 mL/h and controlled by a syringe pump (NE-500 Model, New Era Pump Systems, Inc. New York, USA). For reproducible electrochemical measurements, nanofibers were also collected onto ITO-PET (NV Innovative Sputtering Technology, Zulte, Belgium, PET 175 lm, Coating ITO-60) substrate with dimensions of 0.5×2.5 mm, for 5 min.

### 2.3. Surface activation and covalent immobilization of albumin onto the PCL/P3ANA nanofiber mats

In order to activate the –COOH groups available on the surface of the nanofiber mat, the appropriate concentrations (5/0.5, 0.5/5, 5/5 and 50/50 mM) of EDC and NHS solutions were prepared with cold water. In order to investigate the influence of EDC and NHS concentrations during activation of carboxyl –COOH groups in nanofibers, PCL/P3ANA nanofiber mats on ITO-PET substrates were treated by shaken gently with 5 mL of the EDC/NHS solutions for 2 h at room temperature [24]. Activated mats were then washed twice with water. Activated mats were treated with 1 mL of albumin dissolved in MES buffer (pH 5.7) with the concentration of 2 mg/mL. Nanofiber mats were incubated with albumin for 2 h at +4 °C, being shaken gently. Finally, mats were taken out, washed twice again with water and dried for characterization. Initial albumin solutions as well as the residual solutions of each consecutive washing step were collected for further characterization.

### 2.4. Spectroscopic and morphological quantification of protein amount on the nanofiber mats

The activation of carboxylic acid groups on PCL/P3ANA nanofibers and the gradual change in the amount of immobilized protein depending on the EDC and NHS concentrations in the activation procedure was determined by FTIR-ATR spectrophotometer (Spectrum One, with a universal ATR attachment with a diamond and a ZnSe crystal) (Perkin Elmer, Massachusetts, USA), SEM/EDX (QUANTA 400 F) (FEI, Oregon, USA), AFM (Nanosurf Easy-Scan2) and BCA protein assay. The surface activation yield were estimated by calculation of the FTIR peak ratios of the formed succinimidyl ester and O–H stretching of carboxylic acid group by using Beer-Lambert law. All FTIR-ATR spectra were collected with 12 scans in the 600–4000 $cm^{-1}$ spectral region at 4 $cm^{-1}$ resolution. SEM/EDX analyses were performed before and after albumin immobi-

lization, with 10 kV accelerating voltage after nanofiber mats were coated with gold by Ion Sputter Metal Coating Device (MCM-100 Model). The average nanofiber diameters were determined using Image J by randomly measuring the diameters of 20 individual fibers shown in SEM images with 1 μm magnification. The influence of EDC and NHS concentrations on the structure and composition of the albumin immobilized PCL/P3ANA nanofibers were analyzed by detection of elemental concentrations for nitrogen and oxygen with EDX. The distribution of immobilized albumin on the surface of nanofiber mats was examined by EDX-mapping. The amount of immobilized albumin on the activated nanofiber mats was determined by BCA protein assay by subjecting the initial and residual solutions from albumin immobilization. As a control, albumin immobilization was carried out on non-activated PCL/P3ANA nanofibers under the same experimental conditions. The total protein content in each sample was calculated by comparing the means of absorption values with a standard curve of bovine serum dilutions (between 0 and 2 mg/mL). The samples were incubated with BCA working solution at 37 °C for 30 minutes and the absorbance was followed at 562 nm by UV-Vis spectrophotometer (Lambda 45) (Perkin Elmer, Massachusetts, USA) [25]. AFM images of PCL/P3ANA and albumin immobilized nanofibers after activation with 5/0.5, 0.5/5, 5/5 and 50/50 mM of EDC and NHS, were taken in non-contact mode using Al coated high resonance frequency silicon tips (Nanosensors NCRL tips, 40 μm width, 225 μm length). Root-mean-square (RMS) roughness values of nanofibers were calculated *via* Easy Scan 2 Software™ (version 3.0.2.4) by selecting raw data.

### 2.5. Electrochemical impedance spectroscopic measurements of albumin immobilized nanofibers

The effect of the concentrations of the EDC and NHS reactants on the activation reaction and on the amount of immobilized protein was investigated by Electrochemical Impedance Spectroscopy (EIS). EIS measurements were performed in PBS (0.1 M, pH 7.4) using potentiostat 2263 Electrochemical Analyser (Princeton Applied Research, Tennessee, USA) with frequency range between 0.01 Hz and 100 kHz and AC voltage of 10 mV. Three-electrode system, consisting of nanofiber mats after albumin immobilization as working electrode, platinum wire as counter electrode, and silver wire as pseudo reference electrode, was used. All measurements were repeated three times for confirmation. The measured impedance spectra were analyzed in terms of electrical equivalent circuits using the analysis program ZSimpWin V.3.10 (Princeton Applied Research, Tennessee, USA).

## 3. Results and discussion

### 3.1. FTIR-ATR characterization of activated PCL/P3ANA nanofibers

FTIR-ATR spectra of PCL/P3ANA nanofibers were obtained after activation procedure in order to reveal the influence of NHS and EDC concentrations (Figure 2). P3ANA in the PCL/P3ANA nanofibers displays the peaks at 2615, 1690, 1580 and 1510 $cm^{-1}$ which were attributed to O–H stretching, C=O

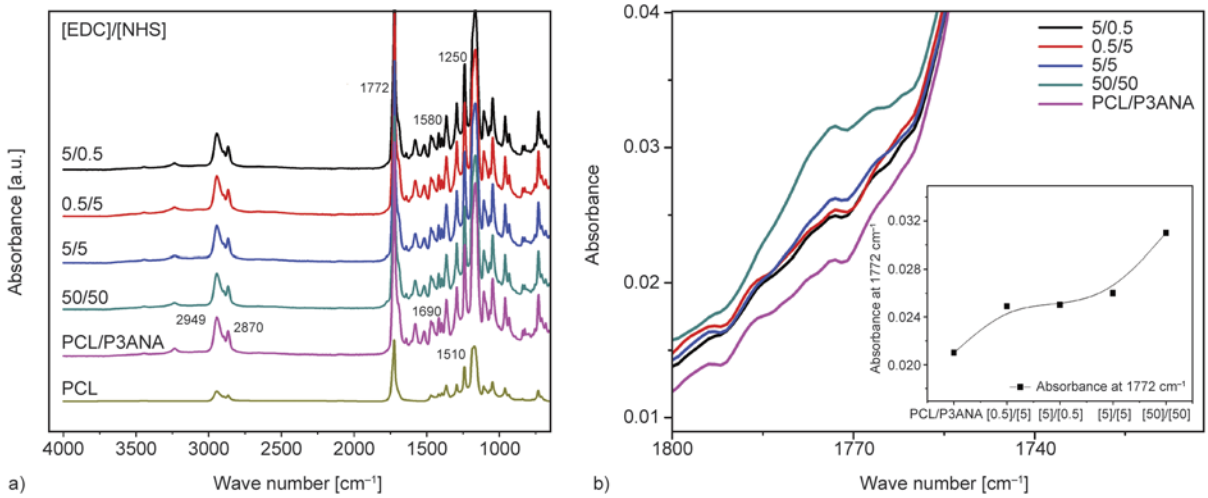


**Figure 2.** FTIR-ATR spectra of PCL, PCL/P3ANA and PCL/P3ANA nanofibers activated with EDC/NHS mixtures of various concentrations (a), succinimidyl ester absorbance (b) and the increase in absorbance (b inlet) after activation

stretching, C=C stretching and N–H stretching, respectively. The peaks at 1250 and 1070 $cm^{-1}$ were attributed to C–N stretching [8, 26]. The carboxyl groups on P3ANA provide active sites for albumin binding through forming succinimidyl ester (–COOSuc) by reacting with NHS, in the presence of EDC [7]. The attachment of a succinimidyl ester termination to PCL/P3ANA nanofibers can be evidenced by the triplet in the spectral range of the C=O stretching vibrations. The activation can be observed in some spectra by a shoulder or an asymmetry of the 1772 $cm^{-1}$ peak ascribed to the contribution of the C=O stretching mode [9]. The Figure 2b shows the C=O stretching vibrations of PCL/P3ANA nanofibers activated with different concentrations of EDC and NHS. When comparing the succinimidyl ester absorbance at 1772 $cm^{-1}$ shown in Figure 2b (inlet), at low concentrations (0.5 mM or 5 mM) of EDC and NHS, the activation reaction was incomplete. Compare to lower concentrations the activation was more successful when EDC = NHS = 50 mM, since the peak absorbance at 1772 $cm^{-1}$ was increased when the activation was performed by 50/50 mM of EDC/NHS (Figure 2b inlet).

The surface activation yield (Figure 3) was estimated by calculation of FTIR peak ratios of the formed succinimidyl ester and O–H stretching of carboxylic acid group by using Beer-Lambert law. The relative percentages of surface species can be derived from their corresponding absorption bands by means of the Beer-Lambert law ($A = \varepsilon bc$), where $A$ is the absorbance, $\varepsilon$ the extinction coefficient, $c$ the concentration and $b$ is the length of the sample layer which was the same for all nanofiber mats. For calculation, the peaks at 1772 and 2615 $cm^{-1}$ were used for succinimidyl ester and O–H stretching of carboxylic acid, respectively. Due to high absorbance of peak at 1772 $cm^{-1}$,absorbance of peak at 2615 $cm^{-1}$ was measured in an enlarged spectrum of 2000–2750 $cm^{-1}$ region.To estimate the reaction yield, peak height was measured to represent the absorbance ($A$) and the linear relationship among the individual extinction coefficients of succinimidyl ester and acid groups was 1:2 [14]. Activation yield for each PCL/P3ANA nanofibers activated with different amounts of EDC and NHS, was calculated by Equation (1):

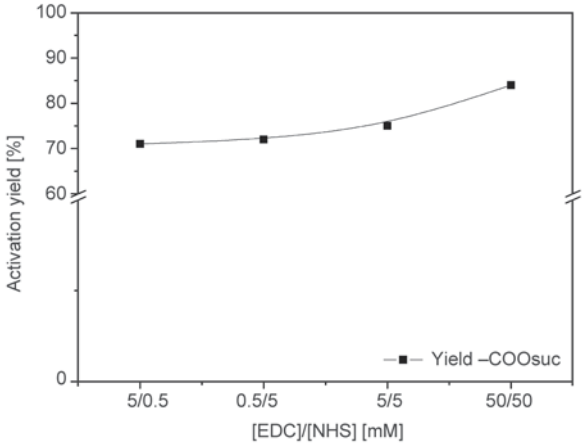


**Figure 3.** Surface activation yields of carboxylic acid groups on PCL/P3ANA nanofibers depending on the EDC/NHS concentrations used

The activation yield of carboxylic acid groups on PCL/P3ANA nanofibers activated with 5/0.5, 0.5/5, 5/5 and 50/50 mM of EDC and NHS was 71, 72, 73 and 82%.

Albumin immobilization was performed on the PCL/P3ANA nanofibers after activation with different concentrations of EDC and NHS (Figure 4). When compared to the PCL/P3ANA nanofibers which were not treated with albumin solution and nanofibers activated with lower concentration (0.5 and 5 mg) of EDC and NHS, there were no significant changes on FTIR spectra. On the contrary, after albumin immobilization onto nanofibers activated with 50/50 mM of EDC/NHS a broad peak was observed

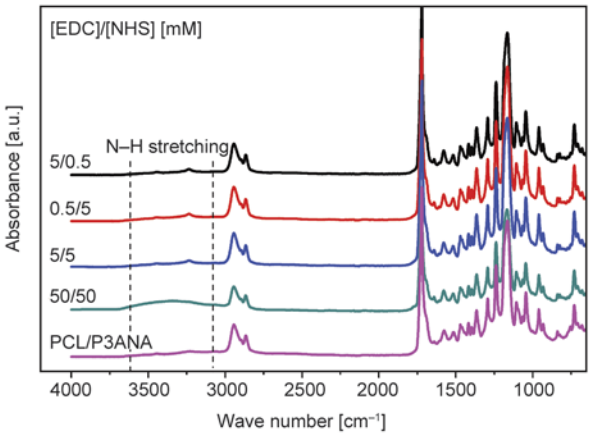


**Figure 4.** FTIR-ATR spectra of albumin immoblized PCL/P3ANA nanofibers activated with EDC/NHS mixtures of various concentrations

$$yield = \frac{A_{1772/\varepsilon_{\text{succinimidyl ester}}}}{A_{1772/\varepsilon_{\text{succinimidyl ester}}} + A_{2615/\varepsilon_{\text{carboxylic acid}}}} \cdot 100\% \quad (1)$$

between 3000 and 3600 $cm^{-1}$. The absorption in this region can be influenced by the contribution of water but in proteins the N–H groups are generally in greater numbers than O–H groups [27]. Also other albumin immobilized nanofibers showed no absorption at this region. The broad peak observed between 3000 and 3600 $cm^{-1}$ region of FTIR spectrum of nanofibers activated with 50/50 mM of EDC/NHS was attributed to the N–H stretching vibration of albumin [28]. FTIR data (Figure 4) showed that PCL/P3ANA nanofibers were activated successfully only when [EDC] = [NHS] = 50 mM, therefore covalent binding of albumin was achieved on this nanofiber mat.

### 3.2. Determination of immobilized protein amount by BCA assay

In order to determine the amount of covalently bound albumin onto nanofibers, the amount of bound protein on both non-activated and activated nanofibers was determined by BCA protein assay. After each reaction step, the nanofiber mats were taken out and washed with PBS to remove any residual albumin on the nanofiber mats. They were then reintroduced into a fresh reaction medium, and the albumin amount was detected. Figure 5 shows the amount of covalently bound albumin onto nanofibers after each immobilization step. 2 mg/mL of albumin was incubated with non-activated PCL/P3ANA nanofibers (control) and PCL/P3ANA nanofibers which were activated by EDC/NHS at different concentrations. After incubation with albumin, albumin amount of the remaining solutions (cyan) were decreased. The difference between albumin amounts of the initial solutions (2 mg/mL) and solution obtained after binding step indicates that some of the protein is attached onto nanofibers. The highest amount of albumin (~1.85 mg) was attached onto nanofibers activated with 50/50 mM of EDC/NHS. In control or other samples activated with lower concentrations of EDC and NHS, the residual albumin amounts in the solutions obtained after binding step were similar to each other. Two washing steps were applied in order to remove physically absorbed protein. The amounts of washed albumin from non-activated nanofibers or nanofibers activated with lower concentrations of EDC/NHS were higher compared to amount of albumin washed from PCL/PANA nanofibers activated by 50/50 mM of EDC/NHS. This result indicates that the attachment was mostly physical on the nanofibers activated with lower concentrations of EDC/NHS. On the other hand, there was only 0.012 mg protein in the solution remained from PCL/PANA nanofibers activated by EDC/NHS at 50/50 mM concentration after two washing steps. In correlation with the FTIR-ATR data, albumin immobilization onto PCL/P3ANA nanofibers activated with 50/50 mM of EDC/NHS was achieved with covalent binding, since the attached albumin cannot be removed with washing steps. The amount of albumin bound covalently (purple) was the highest (~1.78 mg/mL), when nanofibers were activated with 50/50 mM of EDC/NHS.

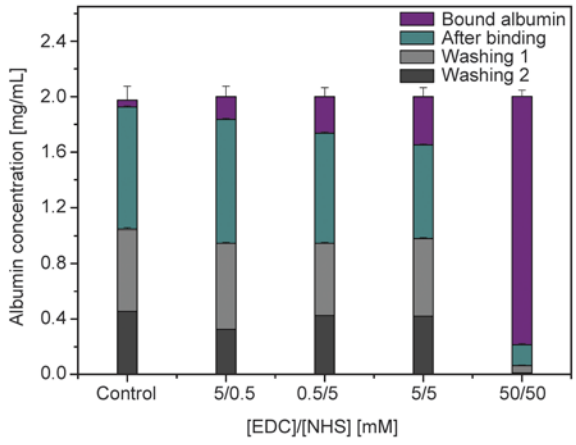


**Figure 5.** Amount of initial and residual albumin after each immobilization step

### 3.3. Morphological and elemental composition analyses of activated PCL/P3ANA nanofibers

The morphology (Figure 6, 7) and elemental composition (Figure 8, Table 1) of albumin immobilized PCL/P3ANA nanofibers activated by different concentrations of EDC/NHS were investigated. The average diameter of albumin immobilized PCL/P3ANA nanofibers activated with 5/0.5, 0.5/5, 5/5 and 50/50 mM of EDC/NHS were determined as 86±19, 75±16, 87±21 and 96±19 nm, respectively. The average fiber diameter of PCL/P3ANA before activation was determined as 89±16 nm. There is no significant change in diameter upon the binding of albumin onto PCL/P3ANA nanofibers activated with different concentration of EDC and NHS. AFM images of PCL/P3ANA and albumin immobilized nanofibers were represented in Figure 7. The surface of PCL/P3ANA nanofibers retained its topography after covalent immobilization of albumin indicating the EDC and/or NHS were not assembled or remained

on the surface after washing steps [29]. PCL/P3ANA nanofibers have RMS roughness of 150.3 nm. The surface roughness was slightly increased after albumin immobilization. The RMS roughness values of albumin immobilized nanofibers which were pre-activated with 5/0.5, 0.5/5, 5/5 and 50/50 mM of

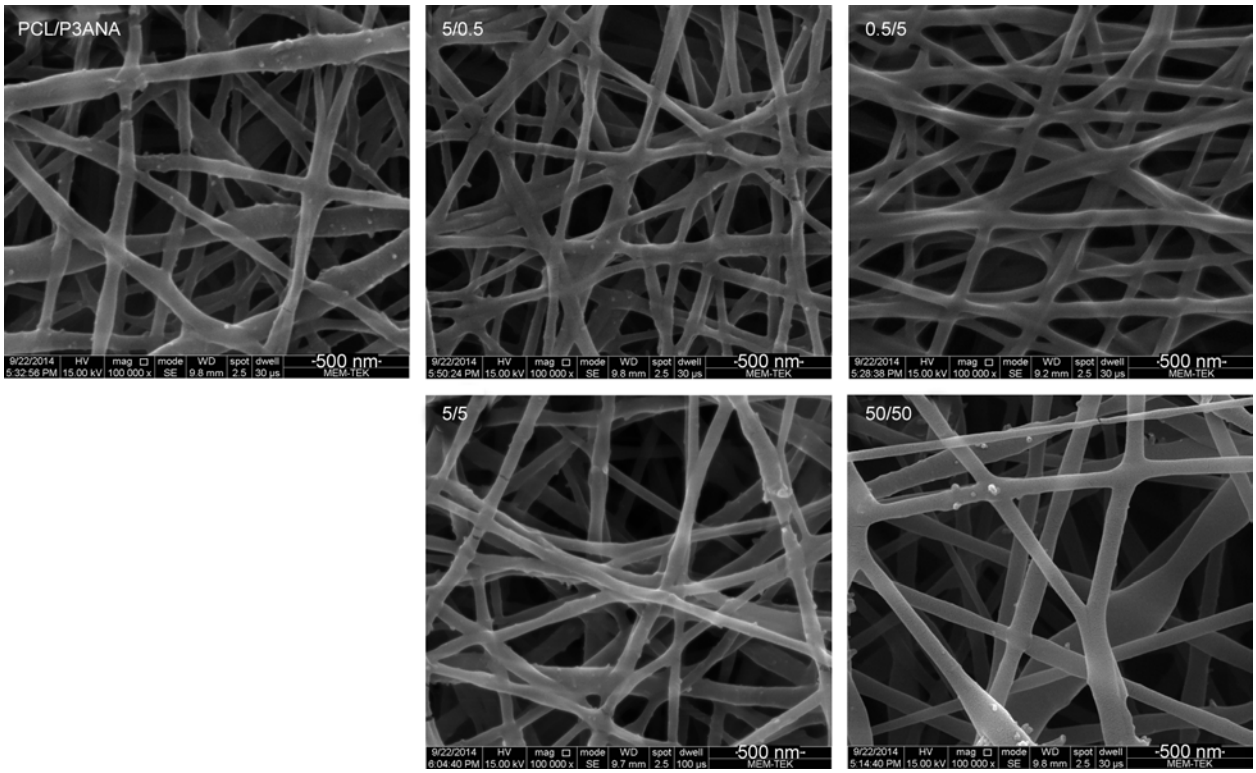


**Figure 6.** SEM images of PCL/P3ANA nanofibers and albumin immobilized PCL/P3ANA nanofibers activated with 5/0.5, 0.5/5, 5/5 and 50/50 mM of EDC/NHS

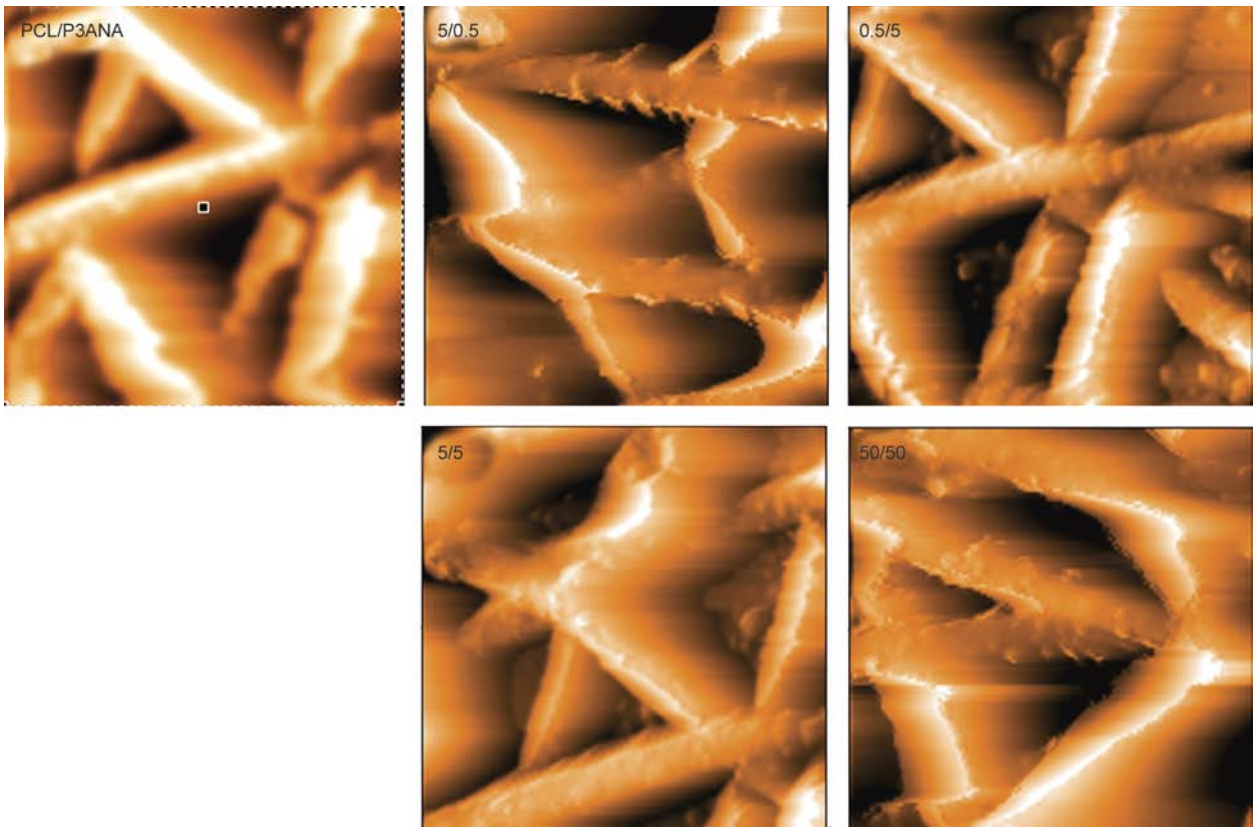


**Figure 7.** Topography AFM images (6 μm×6 μm) of PCL/P3ANA nanofibers and albumin immobilized PCL/P3ANA nanofibers activated with 5/0.5, 0.5/5, 5/5 and 50/50 mM of EDC/NHS

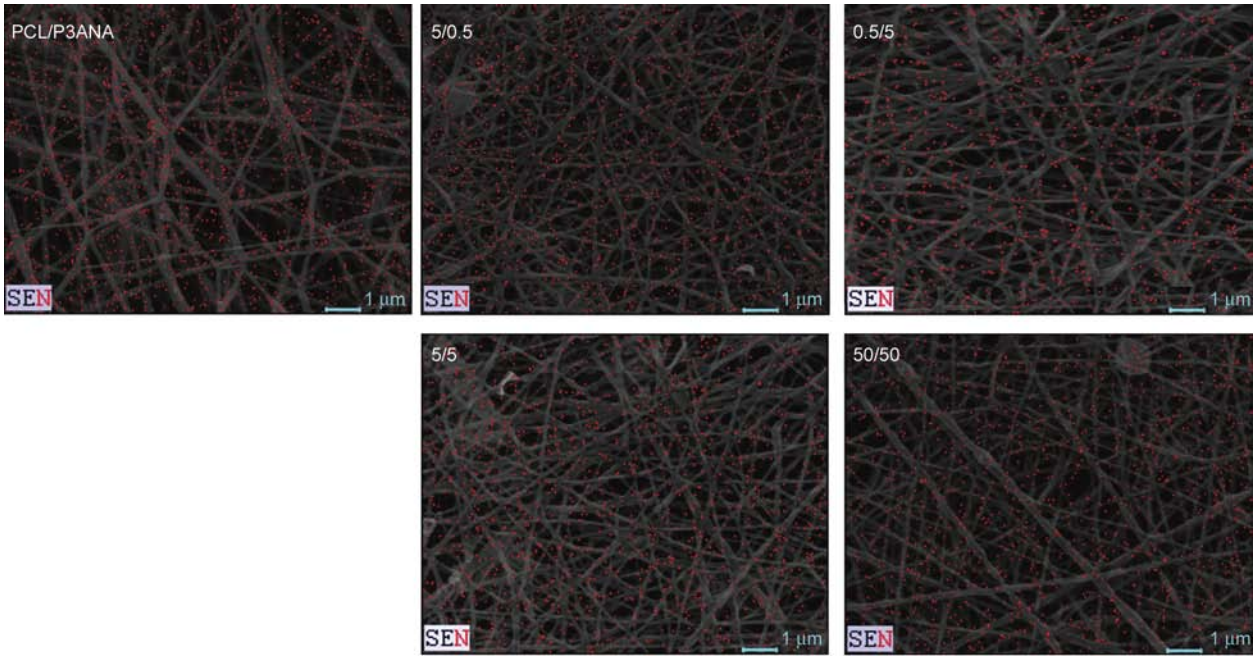


**Figure 8.** EDX-mapping of nitrogen (red) atoms on the surface of PCL/P3ANA nanofibers and albumin immobilized PCL/P3ANA nanofibers activated with 5/0.5, 0.5/5, 5/5 and 50/50 mM of EDC/NHS

**Table 1.** Elemental concentrations for nitrogen and oxygen atoms in PCL/P3ANA nanofibers and albumin immobilized nanofibers after activation with EDC/NHS

| Samples [EDC]/[NHS] [mM] | Elements [wt%] | |
|---|---|---|
| | N | O |
| PCL/P3ANA | 8.51 | 91.49 |
| [5]/[0.5] | 8.80 | 91.20 |
| [0.5]/[5] | 8.48 | 91.52 |
| [5]/[5] | 8.91 | 91.09 |
| [50]/[50] | 10.97 | 89.03 |

EDC and NHS, were 176.2, 193.2, 208.9 and 226.69 nm, respectively. This increase in roughness indicates the immobilization on albumin on the surface of activated PCL/P3ANA nanofibers [6, 30]. In correlation with FTIR-ATR, EDX and BCA, AFM images also indicates that the highest amount of albumin bound to nanofibers activated with 50/50 mM of EDC/NHS.

EDX analyses were performed to confirm the presence of the albumin onto nanofibers. The structure and composition of the albumin immobilized nanofibers were analyzed by detection of elemental concentrations for nitrogen (N) with EDX [31, 32]. Also, the distribution of immobilized albumin on the surface was investigated by EDX-mapping of PCL/P3ANA nanofiber mats (Figure 8). P3ANA has N atoms in its backbone, as well as albumin. The distribution of nitrogen atoms on PCL/P3ANA nanofiber mat seems to be random. It can be explained by the porous structure of nanofiber mat which affects the penetration depth of electrons during EDX analysis [33]. It is known that depending on the polymer chemical nature and porosity of mat, a loss of X-rays can be occurred [34]. Also, P3ANA and PCL blended in a weight ratio of 25% w/w between two polymers. Since both PCL and P3ANA contains oxygen atoms on their backbones, the amount of O atoms [wt%] was 91.49 while N atom amounts [wt%] was 8.81 on the surface of PCL/P3ANA nanofibers. The amount of N [wt%] on the surface of PCL/P3ANA and of the nanofiber mats activated with 5/0.5, 0.5/5 and 5/05 mM of EDC/NHS were approximately the same. However, when nanofibers were activated with increasing (50/50 mM) amounts of EDC and NHS, the amount of N [wt%] on the surface increased (10.97 wt%) which indicated that the N atoms were introduced to the structure of nanofibers through covalent binding of the albumin. The compositions of included atoms (nitrogen and oxygen) in the structure are given in Table 1. EDX-mapping images of albumin immobilized nanofibers showed the distribution of the immobilized albumin (Figure 8). EDX-mapping images indicate that the distribution of the albumin on the surface of nanofibers is affected by the distribution of activated functional groups –COOH of P3ANA. SEM/EDX results have been complementary with FTIR-ATR, BCA protein assay and able to verify the covalent

immobilization of albumin onto PCL/P3ANA nanofibers activated with higher and equal concentrations of EDC and NHS.

### 3.4. Electrochemical impedance spectroscopy and equivalent circuit modeling

Electrochemical impedance spectroscopy (EIS) measurements were performed on albumin immobilized PCL/P3ANA nanofibers on ITO-PET in order to understand the influence of NHS and EDC concentrations on the amount of bound albumin. The EIS data provide information about the nature of electrochemical process occurring at the electrode/electrolyte interface [35]. EIS data were obtained on PCL/P3ANA and on albumin immobilized nanofibers which were activated with different concentrations of EDC and NHS. A significant difference in the impedance spectra was observed depending on the covalent immobilization of albumin onto nanofibers and the concentrations of the EDC and NHS used in activation. In Nyquist plot (Figure 9), albumin immobilized PCL/P3ANA nanofibers exhibited a semicircle while PCL/P3ANA nanofibers showed a linear behaviour. The diameter of the semicircle of Nyquist plot represents the charge-transfer resistance ($R_{ct}$) [8] and linear line with high-slope indicates capacitive behavior [36]. Nanofibers became resistive after treated with albumin and the charge-transfer resistance of the albumin immobilized nanofibers was increased. PCL/P3ANA nanofibers activated with 50/50 mM of EDC/NHS had the largest diameter of the semicircle of the Nyquist plot indicated that the highest amount of albumin bound onto these nanofibers [37]. This result was in correlation with the data obtained from FTIR-ATR, SEM/EDX and BCA.

The measured impedance spectra were analyzed in terms of electrical equivalent circuits to evaluate the kinetics of the systems using the analysis program ZSimpWin. The circuits for PCL/P3ANA nanofibers and on albumin immobilized nanofibers which were activated with different concentrations of EDC and NHS, which describe the physical properties of the system and provide a good fit to the measured data with a reasonable number of circuit elements, were chosen. The calculated and measured data were fitted well together with the chosen equivalent circuits (Figure 9). The impedance spectra for nanofibers (PCL/P3ANA) described by the equivalent circuit of $R(CR)(QR)W$ (Figure 10) in short hand. For albumin immobilized PCL/P3ANA, the equivalent circuit of $R(CR)(CR)(QR)W$ were selected since there are additional electrical components (resistance and capacitance) arising from immobilized albumin. Table 2 represents the fitting parameters for the equivalent circuit elements by modeling of the impedance spectra.

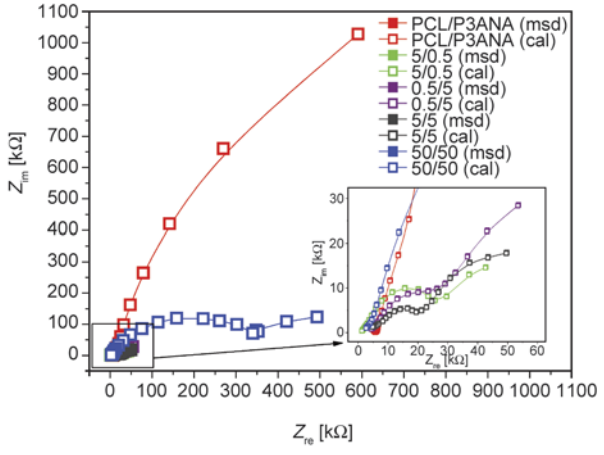


**Figure 9.** Measured (msd) and calculated (cal) Nyquist plots of PCL/P3ANA and albumin immobilized PCL/P3ANA nanofibers activated with 5/0.5, 0.5/5, 5/5 and 50/50 mM of EDC/NHS

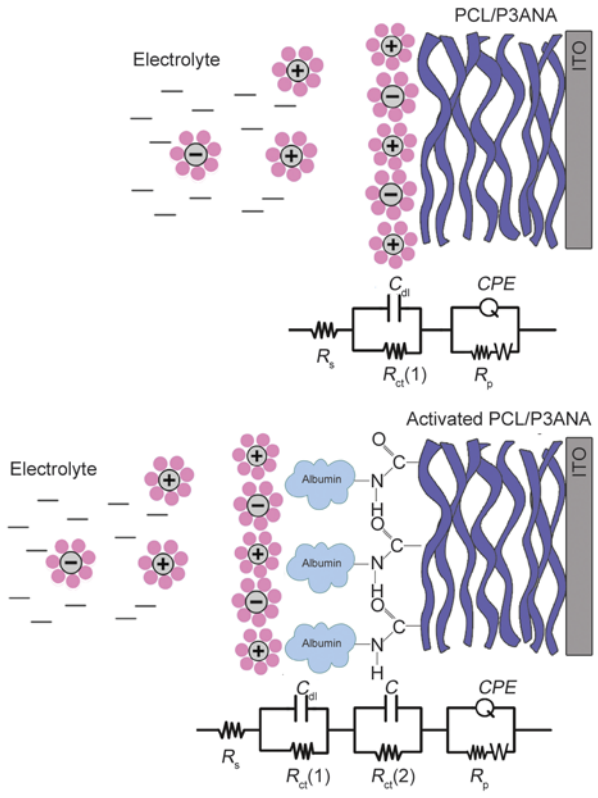


**Figure 10.** Equivalent circuits for the simulation of the EIS spectra of PCL/P3ANA (top) and albumin immobilized PCL/P3ANA nanofibers activated with EDC/NHS nanofibers (bottom)

**Table 2.** Fitting values for the equivalent circuit elements by the simulation of the impedance spectra

| [EDC]/[NHS] [mM] | $R_s$ [Ω] | $C_{dl}$ [μF] | $R_{ct}(1)$ [Ω] | $C$ [μF] | $R_{ct}(2)$ [kΩ] | $Q$(CPE) ·($10^{-7}$) [$Ω^{-1}$] | $R_p$ [kΩ] | $W$ ·($10^{-5}$) [$Ssec^5/cm^2$] | $n$ | Chi-squared error ·($10^{-4}$) |
|---|---|---|---|---|---|---|---|---|---|---|
| PCL/P3ANA R(CR)(QR)W | 2771 | 13.04 | 210 | – | – | 0.19 | 2.87 | 3.05 | 0.85 | 3.83 |
| [5]/[0.5] R(CR)(CR)(QR)W | 1108 | 0.08 | 1209 | 5.54 | 22.90 | 4.65 | 26.49 | 2.98 | 0.62 | 4.23 |
| [0.5]/[5] R(CR)(CR)(QR)W | 3403 | 0.09 | 1331 | 2.16 | 33.06 | 3.99 | 25.15 | 1.65 | 0.67 | 5.48 |
| [5]/[5] R(CR)(CR)(QR)W | 1143 | 0.08 | 4725 | 4.94 | 16.47 | 0.10 | 32.07 | 3.46 | 0.33 | 5.00 |
| [50]/[50] R(CR)(CR)(QR)W | 974 | 0.06 | 52 790 | 12.59 | 202.60 | 0.13 | 693.50 | 1.14 | 0.30 | 1.39 |

$R_s$, the first component of two circuits, represents the solution resistance of the electrolyte corresponds to the Ohmic resistance due to the presence of the electrolyte on the nanofiber and in solution [8] and of electrical contacts [38]. $R_s$ values for PCL/P3ANA nanofibers, albumin immobilized nanofibers activated with 5/0.5, 0.5/5, 5/5 and 50/50 mM of EDC and NHS were 2771, 1108, 3403, 1143 and 974 Ω, respectively. The $R_s$ values correspond to the behavior of the electrolyte, filling pores of nanofibers [39]. The second resistance in both circuits represents the charge transfer resistance ($R_{ct}$) between the solution and the surface of the PCL/P3ANA nanofibers or albumin immobilized nanofiber electrode surface. The charge transfer resistance $R_{ct}(1)$ of 210 Ω of PCL/P3ANA nanofibers increased to $R_{ct}(1)$ of 1209, 1331, 4725 and 52 790 Ω after albumin immobilization onto nanofibers activated with 5/0.5, 0.5/5, 5/5 and 50/50 mM of EDC/NHS, respectively. The increase in $R_{ct}$ value is attributed to the formation of a new layer at the interface between solution and nanofibers [26]. First $C$ in the circuits was attributed to double layer capacitance ($C_{dl}$) arise from alignment of solvated counter ions along nanofiber surface. The electron transfer through electrode occurs by overcoming activation barrier, charge transfer resistance and solution resistance [40]. Double layer capacitance ($C_{dl}$) along the surface of PCL/P3ANA nanofibers was decreased after albumin immobilization. The decrease in $C_{dl}$ is attributed to increase in thickness of electronic double layer depending on the albumin immobilization [26]. For albumin immobilized nanofibers, additional circuit elements of capacitance ($C$) and resistance ($R$) are connected in parallel to first ones in order to describe the capacitance and the charge transfer resistance between immobilized albumin molecules and PCL/P3ANA nanofibers, respectively. When PCL/P3ANA nanofibers were activated with 50/50 mM of EDC/NHS, the capacitance ($C$) occurring at the interphase between immobilized albumin and nanofibers increased as well as the charge transfer resistance of $R_{ct}(2)$. The difference between capacitance values of albumin immobilized nanofibers can be explained by the different interfacial structures, assuming different structures or sizes [41]. PCL/P3ANA nanofibers are porous electrodes and they provide large surface areas which forms interfaces between electrodes and electrolytes, resulting in high capacitances. The immobilization of albumin onto the surface of nanofibers induces higher $R_{ct}$ values [42, 43]. The increase in $R_{ct}$ values can be explained by the formation of a new layer at the interface between solution and nanofibers was formed after attachment of albumin onto surface [26]. The different interfacial structure between protein layer and nanofibers can cause higher $R_{ct}$ values. Also, EIS measurements were performed in PBS buffer at pH 7.4 where albumin become negatively charged [44]. In PBS buffer, the total positive charge concentration is greater than the total negative charge concentration [45]. After attachment of albumin on the surface, the negative charge on the surface of nanofibers was increased and this resulted in the alignment of positively charged solvated ions along the nanofiber surface and increase in $R_{ct}$ values. Moreover, negatively charged ions can be repulsed by albumin on the surface and the transfer of positively charged and relatively big ions into positively charge nanofibers become challenging [24]. $Q$ represents the constant phase element (CPE) which was applied in the equivalent circuit for the simulation of the impedance data, since CPE takes into account the non-homogeneity of the conductance [8] and the electrode [38]. The impedance of a non-ideal electrode is defined by the formula ($Z_{CPE} = T_{CPE}(jw)^{-n}$) where $T_{CPE}$ and $n$ are frequency-independent constants; $w$ is the angular frequency [35],

*n* is a parameter describing the deviation from an ideal capacitor and arises from the slope of the log*Z* versus log*f* plot. The values for *n* vary from 0 to 1. *n* = 1 belongs to an ideal capacitor, while *n* = 0 and 0.5 denotes a resistance and Warburg behavior, respectively [46]. The n value of PCL/P3ANA nanofibers was 0.85 and it is significantly reduced up to 0.30 with albumin immobilization. The values for *n* = 0 indicates a resistance while *n* = 0.5 denotes Warburg behavior. *W* represents the Warburg impedance and it is attributed to the diffusion of counterions. Once the electron transfer begins, the electrode kinetics determined by Warburg impedance (*W*) due to the mass transport [40]. $R_p$ represents the pore resistances of the nanofiber layer (Ohmic resistances of the electrolyte in the pores) [47]. $R_p$ values for PCL/P3ANA nanofibers were increased after albumin immobilization. These differences in $R_p$ can be explained by the fact that covalent immobilization of albumin by EDC/NHS activation forms a different nanofiber mat structure [48]. The highest value of 693.50 Ω of $R_p$ was observed on nanofibers activated with 50/50 mM of EDC and NHS. AFM images indicated that surface roughness increased after albumin immobilization onto nanofibers activated with 50/50 mM of EDC and NHS, the increase in pore resistance value of PCL/P3ANA nanofibers (50/50 mM of EDC/NHS) can be related with the increase in surface roughness. EIS and equivalent circuit modeling indicated that 50/50 mM of EDC/NHS were the most effective concentration on the activation of carboxylic acid groups on PCL/P3ANA nanofiber.

The activation of the carboxyl groups on the PCL/P3ANA nanofibers can be achieved in several steps. The first step is the addition of the OH group of the carboxylic acid across one of the double bonds of the carbodiimide reactant, forming an O-acylurea adduct. Then, the surface O-acylurea can be transformed into succinimidyl ester (–COOSuc) product with a nucleophilic attack by NHS. Then, this product reacts with a primary amine and yield a peptide coupling through an amide bond (Figure 11). FTIR-ATR (Figure 2) analyses of the PCL/P3ANA nanofibers which were treated with different concentrations of EDC and NHS showed that, 50/50 mM of EDC/NHS were the effective concentration to activate the nanofibers. Also, the success of covalent immobilization of the albumin is directly depending on the efficiency of the activation procedure. The subsequent analyses (FTIR-ATR, EDX, BCA and EIS) performed on albumin immobilized nanofibers indicated that the highest amount of albumin was bound onto nanofibers activated with 50/50 mM of EDC/NHS. Figure 12 represents the relationship between the surface activation and albumin immobilization. The concentrations of nitrogen (N) atoms at the surface and the charge transfer resistance of albumin immobilized nanofibers were increased as the activation of the nanofibers were achieved represented by the increase in the absorbance (1772 $cm^{-1}$) of the succinimidyl ester. During the activation pro-

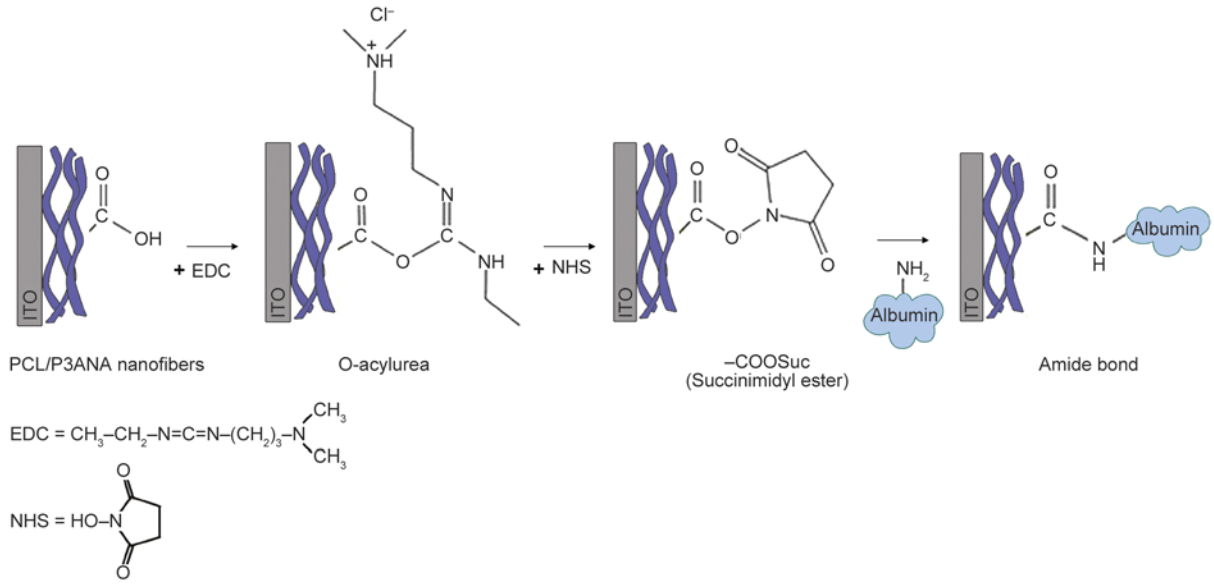


**Figure 11.** Schematic representation of covalent immobilization of protein through EDC/NHS activation

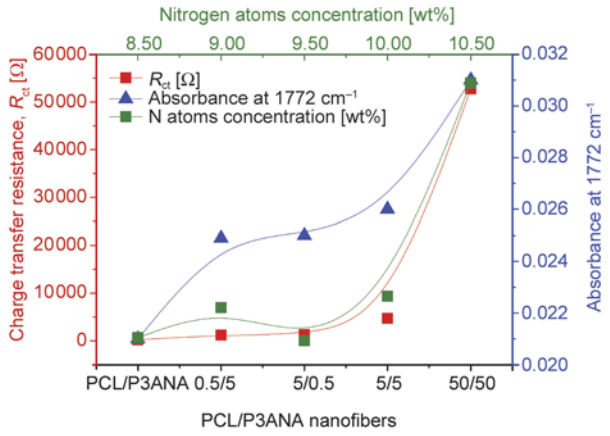


**Figure 12.** The relationship among charge transfer resitance ($R_{ct}$) from EIS, succinimidyl ester absorbance from FTIR-ATR and N atoms concentrations from EDX data of activated PCL/P3ANA nanofibers

cedure, the formation of the byproducts at the surface results a kinetic competition between different reactions [9]. In the case of EDC concentration is lower than NHS concentration (0.5/5 mM), the formation of O-acylurea become very slow resulting a slow succinimidyl ester formation. When EDC concentration is higher than NHS concentration (5/0.5 mM) O-acylurea formation become relatively fast however succinimidyl esters form very slow and byproducts of Anhydride and N-acylurea can be formed at the surface [49]. When NHS and EDC concentrations are equal to each other and both low (5/5 mM) then slow kinetics for whole reaction are expected. On contrary, when the concentrations of both EDC and NHS increased to 50 mM, great balance between formation of O-acylurea and transformation of it into succinimidyl ester product can be obtained.

## 4. Conclusions

The nanofibers of poly(ε-caprolactone)/poly(m-anthranilic acid) (PCL/P3ANA) nanofibers were fabricated by electrospinning. Carboxyl groups on the surface of PCL/P3ANA nanofibers were activated by EDC and NHS in different concentrations (5/0.5, 0.5/5, 5/5 and 50/50 mM). Albumin was covalently immobilized onto activated nanofibers. The surface activation was investigated by FTIR-ATR and activation yield was calculated. The amount of immobilized albumin was investigated by BCA assay and elemental analyses (EDX) of nanofibers. AFM images showed that surface roughness of the nanofibers was increased after albumin immobilization. The amount of bound albumin was changed depending on the activation of the carboxyl groups of P3ANA. Elemental analyses and EDX-mapping of nitrogen atoms showed that the distribution of the albumin on the surface of nanofibers is affected by the distribution of activated –COOH groups of P3ANA. Electrochemical Impedance Spectroscopy (EIS) analysis and equivalent circuit modeling was performed to observe the immobilized albumin depending on the EDC/NHS concentrations used in activation. The nanofibers become resistive due to albumin immobilization and the higher charge transfer resistance was observed for the nanofibers activated with 50/50 mM of EDC/NHS. This study showed that 50/50 mM of EDC/NHS was the most effective concentration for the activation of PCL/P3ANA nanofibers. This study indicated that Electrochemical Impedance Spectroscopic (EIS) analysis can be successfully applied for the determination of activation degree of covalent immobilization of proteins and enzymes onto polymeric substrates.

## Acknowledgements

The authors express their thanks to Scientific and Technological Research Council of Turkey (TUBITAK) for the financial support on project 213M469.

## References

[1] Ye P., Xu Z-K., Wu C., Innocent J., Seta P.: Nanofibrous poly(acrylonitrile-*co*-maleic acid) membranes functionalized with gelatin and chitosan for lipase immobilization. Biomaterials, **27**, 4169–4176 (2006). DOI: 10.1016/j.biomaterials.2006.03.027

[2] Marx S., Jose M. V., Andersen J. D., Russell A. J.: Electrospun gold nanofiber electrodes for biosensors. Biosensors and Bioelectronics, **26**, 2981–2986 (2011). DOI: 10.1016/j.bios.2010.11.050

[3] Jung M., Kim S-U., Oh B-K., Choi J-W.: Immobilization of biomaterials on nanopatterned surface using nanoporous alumina for biodevices. Current Applied Physics, **9**, e111–e114 (2009). DOI: 10.1016/j.cap.2008.12.042

[4] Wang Z-G., Wan L-S., Liu Z-M., Huang X-J., Xu Z-K.: Enzyme immobilization on electrospun polymer nanofibers: An overview. Journal of Molecular Catalysis B: Enzymatic, **56**, 189–195 (2009). DOI: 10.1016/j.molcatb.2008.05.005

[5] Llorens E., Armelin E., del Mar Pérez-Madrigal M., del Valle L. J., Alemán C., Puiggalí J.: Nanomembranes and nanofibers from biodegradable conducting polymers. Polymers, **5**, 1115–1157 (2013). DOI: 10.3390/polym5031115

[6] Guler Z., Erkoc P., Sarac A. S.: Electrochemical impedance spectroscopic study of single-stranded DNA-immobilized electroactive polypyrrole-coated electrospun poly(ε-caprolactone) nanofibers. Materials Express, **5**, 269–279 (2015).
DOI: 10.1166/mex.2015.1249

[7] Mohamad N. R., Marzuki N. H. C., Buang N. A., Huyop F., Wahab R. A.: An overview of technologies for immobilization of enzymes and surface analysis techniques for immobilized enzymes. Biotechnology and Biotechnological Equipment, **29**, 205–220 (2015).
DOI: 10.1080/13102818.2015.1008192

[8] Giray D., Balkan T., Dietzel B., Sarac A. S.: Electrochemical impedance study on nanofibers of poly(m-anthranilic acid)/polyacrylonitrile blends. European Polymer Journal, **49**, 2645–2653 (2013).
DOI: 10.1016/j.eurpolymj.2013.06.012

[9] Sam S., Touahir L., Andresa J. S., Allongue P., Chazalviel J. N., Gouget-Laemmel A. C. C., de Villeneuve C. H., Moraillon A., Ozanam F., Gabouze N., Djebbar S.: Semiquantitative study of the EDC/NHS activation of acid terminal groups at modified porous silicon surfaces. Langmuir, **26**, 809–814 (2009).
DOI: 10.1021/la902220a

[10] Staros J. V., Wright R. W., Swingle D. M.: Enhancement by *N*-hydroxysulfosuccinimide of water-soluble carbodiimide-mediated coupling reactions. Analytical Biochemistry, **156**, 220–222 (1986).
DOI: 10.1016/0003-2697(86)90176-4

[11] Dai J., Baker G. L., Bruening M. L.: Use of porous membranes modified with polyelectrolyte multilayers as substrates for protein arrays with low nonspecific adsorption. Analytical Chemistry, **78**, 135–140 (2006).
DOI: 10.1021/ac0513966

[12] Wang Z-G., Wang Y., Xu H., Li G., Xu Z-K.: Carbon nanotube-filled nanofibrous membranes electrospun from poly(acrylonitrile-*co*-acrylic acid) for glucose biosensor. The Journal of Physical Chemistry C, **113**, 2955–2960 (2009).
DOI: 10.1021/jp807047s

[13] Dahoumane S. A., Nguyen M. N., Thorel A., Boudou J-P., Chehimi M. M., Mangeney C.: Protein-functionalized hairy diamond nanoparticles. Langmuir, **25**, 9633–9638 (2009).
DOI: 10.1021/la9009509

[14] Wang C., Yan Q., Liu H-B., Zhou X-H., Xiao S-J.: Different EDC/NHS activation mechanisms between PAA and PMAA brushes and the following amidation reactions. Langmuir, **27**, 12058–12068 (2011).
DOI: 10.1021/la202267p

[15] Voicu R., Boukherroub R., Bartzoka V., Ward T., Wojtyk J. T. C., Wayner D. D. M.: Formation, characterization, and chemistry of undecanoic acid-terminated silicon surfaces: Patterning and immobilization of DNA. Langmuir, **20**, 11713–11720 (2004).
DOI: 10.1021/la047886v

[16] Wissink M. J. B., Beernink R., Pieper J. S., Poot A. A., Engbers G. H. M., Beugeling T., van Aken W. G., Feijen J.: Immobilization of heparin to EDC/NHS-cross-linked collagen. Characterization and *in vitro* evaluation. Biomaterials, **22**, 151–163 (2001).
DOI: 10.1016/S0142-9612(00)00164-2

[17] Yang Z., Wang J., Luo R., Maitz M. F., Jing F., Sun H., Huang N.: The covalent immobilization of heparin to pulsed-plasma polymeric allylamine films on 316L stainless steel and the resulting effects on hemocompatibility. Biomaterials, **31**, 2072–2083 (2010).
DOI: 10.1016/j.biomaterials.2009.11.091

[18] Ducker R. E., Montague M. T., Leggett G. J.: A comparative investigation of methods for protein immobilization on self-assembled monolayers using glutaraldehyde, carbodiimide, and anhydride reagents. Biointerphases, **3**, 59–65 (2008).
DOI: 10.1116/1.2976451

[19] Zander N. E., Orlicki J. A., Rawlett A. M., Beebe Jr T. P.: Quantification of protein incorporated into electrospun polycaprolactone tissue engineering scaffolds. ACS Applied Materials and Interfaces, **4**, 2074–2081 (2012).
DOI: 10.1021/am300045y

[20] Casper C. L., Yang W., Farach-Carson M. C., Rabolt J. F.: Coating electrospun collagen and gelatin fibers with perlecan domain I for increased growth factor binding. Biomacromolecules, **8**, 1116–1123 (2007).
DOI: 10.1021/bm061003s

[21] Benyoucef A., Huerta F., Vázquez J. L., Morallon E.: Synthesis and in situ FTIRS characterization of conducting polymers obtained from aminobenzoic acid isomers at platinum electrodes. European Polymer Journal, **41**, 843–852 (2005).
DOI: 10.1016/j.eurpolymj.2004.10.047

[22] Vacareanu L., Catargiu A-M., Grigoras M.: An electrochemical study of two self-dopable water-soluble aniline derivatives: Electrochemical deposition of copolymers. Journal of Analytical Methods in Chemistry, **2012**, 737013/1–737013/11(2012).
DOI: 10.1155/2012/737013

[23] Khandanlou R., Ahmad M. B., Shameli K., Saki E., Kalantari K.: Studies on properties of rice straw/polymer nanocomposites based on polycaprolactone and $Fe_3O_4$ nanoparticles and evaluation of antibacterial activity. International Journal of Molecular Sciences, **15**, 18466–18483 (2014).
DOI: 10.3390/ijms151018466

[24] Dagli U., Guler Z., Sarac A. S.: Covalent immobilization of tyrosinase on electrospun polyacrylonitrile/polyurethane/poly(*m*-anthranilic acid) nanofibers: An electrochemical impedance study. Polymer-Plastics Technology and Engineering, in press (2015).
DOI: 10.1080/03602559.2015.1010218

[25] Ficen S. Z., Guler Z., Mitina N., Finiuk N., Stoika R., Zaichenko A., Ceylan S. E.: Biophysical study of novel oligoelectrolyte-based nonviral gene delivery systems for mammalian cells. The Journal of Gene Medicine, **15**, 193–204 (2013).
DOI: 10.1002/jgm.2710

[26] Sophia I. A., Gopu G., Vedhi C.: Synthesis and characterization of poly anthranilic acid metal nanocomposites. Open Journal of Synthesis Theory and Applications, **1**, 1–8 (2012).
DOI: 10.4236/ojsta.2012.11001

[27] Grdadolnik J., Maréchal Y.: Bovine serum albumin observed by infrared spectrometry. I. Methodology, structural investigation, and water uptake. Biopolymers, **62**, 40–53 (2001).
DOI: 10.1002/1097-0282(2001)62:1<40::AID-BIP60>3.0.CO;2-C

[28] Bouhekka A., Bürgi T.: *In situ* ATR-IR spectroscopy study of adsorbed protein: Visible light denaturation of bovine serum albumin on $TiO_2$. Applied Surface Science, **261**, 369–374 (2012).
DOI: 10.1016/j.apsusc.2012.08.017

[29] Sargeant T. D., Rao M. S., Koh C. Y., Stupp S. I.: Covalent functionalization of NiTi surfaces with bioactive peptide amphiphile nanofibers. Biomaterials, **29**, 1085–1098 (2008).
DOI: 10.1016/j.biomaterials.2007.11.002

[30] Cho H-J., Perikamana S. K. M., Lee J-H., Lee J., Lee K-M., Shin C. S., Shin H.: Effective immobilization of BMP-2 mediated by polydopamine coating on biodegradable nanofibers for enhanced *in vivo* bone formation. ACS Applied Materials and Interfaces, **6**, 11225–11235 (2014).
DOI: 10.1021/am501391z

[31] Meng J., Song. L., Zhong J., Wang C. Y., Kong H., Xu Z. Y., Xie S. S.: Comparison of adsorption behaviour for fibrinogen and albumin on single walled carbon nanotubes nonwoven. Solid State Phenomena, **121**, 781–784 (2007).
DOI: 10.4028/www.scientific.net/SSP.121-123.781

[32] Timin A. S., Solomonov A. V., Musabirov I. I., Sergeev S. N., Ivanov S. P., Rumyantsev E. V., Goncharenko A.: Immobilization of bovine serum albumin onto porous poly(vinylpyrrolidone)-modified silicas. Industrial and Engineering Chemistry Research, **53**, 13699–13710 (2014).
DOI: 10.1021/ie501915f

[33] Rabiller-Baudry M., Gouttefangeas F., Le Lannic J., Rabiller P.: Coupling of SEM-EDX and FTIR-ATR to (quantitatively) investigate organic fouling on porous organic composite membranes. in 'Current microscopy contributions to advances in science and technology' (ed.: A. Méndez-Vilas) Formatex, Badajoz, 1066–1076 (2012).

[34] Otto T. N., Habicht W., Dinjus E., Zimmerman M.: Catalyst characterization with FESEM/EDX by the example of silver-catalyzed epoxidation of 1,3-butadiene. in 'Scanning electron microscopy' (ed.: Kazmiruk V.) InTech, Rijeka, 367–392 (2012).
DOI: 10.5772/37952

[35] Gu H., Su X. D., Loh K. P.: Electrochemical impedance sensing of DNA hybridization on conducting polymer film-modified diamond. The Journal of Physical Chemistry B, **109**, 13611–13618 (2005).
DOI: 10.1021/jp050625p

[36] Feng X., Chen N., Zhou J., Li Y., Huang Z., Zhang L., Ma Y., Wang L., Yan X.: Facile synthesis of shape-controlled graphene–polyaniline composites for high performance supercapacitor electrode materials. New Journal of Chemistry, **39**, 2261–2268 (2015).
DOI: 10.1039/C4NJ01843E

[37] Rodríguez-Sevilla E., Ramírez-Silva M-T., Romero-Romo M., Ibarra-Escutia P., Palomar-Pardavé M.: Electrochemical quantification of the antioxidant capacity of medicinal plants using biosensors. Sensors, **14**, 14423–14439 (2014).
DOI: 10.3390/s140814423

[38] Zehani N., Dzyadevych S. V., Kherrat R., Jaffrezic-Renault N. J.: Sensitive impedimetric biosensor for direct detection of diazinon based on lipases. Frontiers in Chemistry, **2**, 1–7 (2014).
DOI: 10.3389/fchem.2014.00044

[39] Radecka M., Wierzbicka M., Rekas M.: Photoelectrochemical cell studied by impedance spectroscopy. Physica B: Condensed Matter, **351**, 121–128 (2004).
DOI: 10.1016/j.physb.2004.05.020

[40] Park J-Y., Park S-M.: DNA hybridization sensors based on electrochemical impedance spectroscopy as a detection tool. Sensors, **9**, 9513–9532 (2009).
DOI: 10.3390/s91209513

[41] Kityakarn S., Pooarporn Y., Songsiriritthigul P., Worayingyong A., Robl S., Braun A. M., Wörner M.: (Photo) electrochemical characterization of nanoporous $TiO_2$ and Ce-doped $TiO_2$ sol–gel film electrodes. Electrochimica Acta, **83**, 113–124 (2012).
DOI: 10.1016/j.electacta.2012.07.129

[42] Zainudin N., Hairul A. R. M., Yusoff M. M., Tan L. L., Chong K. F.: Impedimetric graphene-based biosensor for the detection of *Escherichia coli* DNA. Analytical Methods, **6**, 7935–7941 (2014).
DOI: 10.1039/C4AY01836B

[43] Chang B-Y., Park S-M.: Electrochemical impedance spectroscopy. Annual Review of Analytical Chemistry, **3**, 207–229 (2010).
DOI: 10.1146/annurev.anchem.012809.102211

[44] Tribet C., Porcar I., Bonnefont P. A., Audebert R.: Association between hydrophobically modified polyanions and negatively charged bovine serum albumin. The Journal of Physical Chemistry B, **102** 1327–1333 (1998).
DOI: 10.1021/jp973022p

[45] Birner S., Uhl C., Bayer M., Vogl P.: Theoretical model for the detection of charged proteins with a silicon-on-insulator sensor. Journal of Physics: Conference Series, **107**, 012002/1–012002/15 (2008). DOI: 10.1088/1742-6596/107/1/012002

[46] Lu X., Dou H., Yuan C., Yang S., Hao L., Zhang F., Shen L., Zhang L., Zhang X.: Polypyrrole/carbon nanotube nanocomposite enhanced the electrochemical capacitance of flexible graphene film for supercapacitors. Journal of Power Sources, **197**, 319–324 (2012). DOI: 10.1016/j.jpowsour.2011.08.112

[47] Panić V. V., Dekanski A. B., Mišković-Stanković V. B., Nikolić B. Ž.: The study of capacitance change during electrolyte penetration through carbon-supported hydrous ruthenium oxide prepared by the sol-gel procedure. Chemical and Biochemical Engineering Quarterly, **23**, 23–30 (2009).

[48] Pauliukaite R., Ghica M. E., Fatibello-Filho O., Brett C. M. A.: Electrochemical impedance studies of chitosan-modified electrodes for application in electrochemical sensors and biosensors. Electrochimica Acta, **55**, 6239–6247 (2010). DOI: 10.1016/j.electacta.2009.09.055

[49] Douarche C., Cortès R., de Villeneuve H. C., Roser S. J., Braslau A.: DNA adsorption at functionalized Si/buffer interfaces studied by X-ray reflectivity. The Journal of Chemical Physics, **128**, 225108/1–225108/15 (2008). DOI: 10.1063/1.2927256

*eXPRESS Polymer Letters Vol.10, No.2 (2016) 111–124*
*Available online at www.expresspolymlett.com*
*DOI: 10.3144/expresspolymlett.2016.12*

# Poly(butylene cyclohexanedicarboxylate/diglycolate) random copolymers reinforced with SWCNTs for multifunctional conductive biopolymer composites

*E. Fortunati[1], M. Gigli[2], F. Luzi[1], N. Lotti[2], A. Munari[2], M. Gazzano[3], I. Armentano[1*], J. M. Kenny[1]*

[1]Materials Engineering Center, UdR INSTM, University of Perugia, Strada di Pentima 4, 05100 Terni, Italy
[2]Civil, Chemical, Environmental and Materials Engineering Dept. (DICAM), University of Bologna, Via Terracini 28, 40131 Bologna, Italy
[3]Organic Synthesis and Photoreactivity Institute (ISOF-CNR), CNR, Via Selmi 2, 40126 Bologna, Italy

*Received 14 June 2015; accepted in revised form 13 September 2015*

**Abstract.** The objective of this work was to develop a versatile strategy for preparing multifunctional composite films with tunable properties. Novel conductive composites based on the combination of single walled carbon nanotubes (SWCNTs) and biodegradable poly(butylene cyclohexanedicarboxylate/diglycolate) random copolymers (P(BCEmBDGn)) are here presented. In particular, synthesized PBCE homopolymer and two copolymers containing different amounts of ether–oxygen containing co-units, P(BCE90BDG10) and P(BCE70BDG30), have been considered as matrices of SWCNTs based composites. The effect of incorporation of different amounts of SWCNTs (0.1–0.5–0.75–1 wt%) on morphological, thermal, mechanical and electrical properties was deeply investigated. The morphology of the fracture surfaces is affected by the SWCNT presence, while the increase in the SWCNT content does not provide significant microstructure modifications. The thermal properties underlined that nanotubes can act as nucleating agents, favouring the polymer crystallization process. The mechanical behavior demonstrated that the introduction of carbon nanotubes both in the case of PBCE homopolymer and in random copolymers based formulations exerted a reinforcing effect. All composites exhibit high electrical conductivity in comparison to the neat polymers. This work demonstrates that this combinatorial approach can be used to develop materials with tunable and advanced functional properties.

***Keywords:*** *biopolymers, biocomposites, carbon nanotubes, electrical properties*

## 1. Introduction

Over the past years, much attention has been paid towards biodegradable polymeric materials, as an answer to the urgent environmental issues related to terrestrial and aquatic pollution [1]. Thus, a novel category of materials has been developed, often reported as 'environmentally-friendly'. These materials are capable to undergo hydrolytic and/or enzymatic degradation, resulting in harmless low molecular weight substances [2, 3].

Aliphatic polyesters are one of the most studied classes of biodegradable polymers, as they possess promising physical/mechanical properties and they can be synthesized at moderate costs [4]. Poly(butylene cyclohexanedicarboxylate) (PBCE), obtained by polycondensation of 1,4-butanediol and 1,4-*trans*-cyclohexanedicarboxylic acid, is undoubtedly a very interesting aliphatic polyester. As a matter of fact, the presence of the aliphatic ring along the polymer backbone enables the material to have high melting temperature above 160 °C, good thermal stability, to show interesting mechanical properties and to maintain biodegradability [5, 6]. Moreover, the monomers employed in the PBCE synthesis can be obtained

*Corresponding author, e-mail: ilaria.armentano@unipg.it

from either fossil or renewable resources. In particular, 1,4-butanediol and 1,4-cyclohexanedicarboxylic acid can be produced starting from bio-based succinic acid [7] and bio-based therephthalic acid (derived from limonene) [8], respectively.

Unfortunately, given its high crystallinity degree and hydrophobicity, PBCE displays slow biodegradation rate and poor flexibility [8].

In this view, copolymerization is an effective tool to tailor the polymer properties and to make it suitable for the desired application. In particular, the authors recently focused on the PBCE modification through the introduction of ether linkages along its macromolecular chain. This strategy permitted to improve the surface wettability and to depress the crystallinity degree as well as to decrease the glass transition temperature of the starting homopolymer. These factors play indeed a significant role in the modification of both mechanical properties and hydrolytic and enzymatic degradation rate [9–11].

Increasing demand for special materials has led to the conception of composites, since valuable properties can be combined. The chance to incorporate functional nanostructures with unique properties in a polymer matrix, is a versatile strategy to transfer and to integrate specific properties into a single material, enabling to realize multifunctional composites to be used in advanced applications like catalysis, energy storage, nanobiotechnology, etc. [12, 13]. The new designed materials might possess the unique properties offered by the synergistic interaction of the nanostructures with the polymer matrix [14, 15].

Carbon nanotubes (CNTs) have been considered as ideal reinforcing candidates for the production of multifunctional polymer composites, since they simultaneously display high aspect ratio and nanometer dimensions, and more importantly, extraordinary mechanical strength and high electrical and thermal conductivity [16–19]. However, in order to obtain the desired performance in the final composites, a tailored CNT dispersion in the polymers has to be reached and the strong Van der Waals interaction between the tubes [20, 21] has to be overcome. We have recently focused on the development of conductive composites by using carbon nanotubes, and mixing them with commercial biodegradable polymers [12, 22, 23].

On the contrary, the present research work aims to evidence the evolution and potentiality of a versatile strategy to prepare polymeric nanostructured materials combining newly synthesized biodegradable random copolymers based on 1,4-*trans*-cyclohexanedicarboxylic acid and diglycolic acid [11] with a composite approach, by using single walled carbon nanotubes (SWCNTs) as reinforcement and functional phase. The thermal, structural, electrical and dielectric properties of the novel developed film formulations were investigated and correlated to SWCNT content and polymer chain microstructure.

## 2. Experimental part

### 2.1. Materials

1,4-dimethylcyclohexanedicarboxylate (DMCE) containing 99% of *trans* isomer, dimethyldiglycolate (DMDG), 1,4-butanediol (BD), and titanium tetrabutoxide ($Ti(OBu)_4$) (Aldrich) were reagent grade products; DMCE, DMDG, and BD were used as supplied, whereas $Ti(OBu)_4$ was distilled before use. All the reagents used were purchased from Sigma Aldrich (Milan, Italy). Single walled carbon nanotubes (SWCNTs) were supplied by Thomas Swan & Co. Ltd (Elicarb™, Durham, UK), with typical nanotube dimensions of 2 nm diameter and ca. 1 μm in length. Nanotubes were morphologically characterized by field emission electron microscopy (FESEM, Supra 25-Zeiss, Germany).

### 2.2. Composite film development

Poly(butylene cyclohexanedicarboxylate/diglycolate) random copolymers (P(BCEmBDGn)) were synthesized in bulk by the usual two step melt polycondensation, as reported elsewhere [24]. Briefly, 1,4-butanediol (BD) and different molar ratios of DMCE and DMDG, were employed in the syntheses, using 20% mol in excess of glycol with respect to dimethylesters and a concentration of catalyst ($Ti(OBu)_4$) of about 150 ppm of Ti/g of polymer. Three different polyesters have been prepared: the homopolymer PBCE and two copolymers, namely P(BCE90BDG10) and P(BCE70BDG30) containing 10 and 30 mol% of BDG units, respectively.

The reactions were carried out in a 250 mL stirred glass reactor, with a thermostated silicon oil bath; temperature and torque were continuously recorded during the polymerization. The first stage was run under pure nitrogen flow at a temperature equal to 190 °C until more than 90% of the theoretical amount of methanol was distilled (about 90 min). In the second stage, the pressure was reduced to about 0.1 mbar and the temperature was increased to 250 °C; the

polymerizations were carried out until a constant torque value was measured.

Composite films were prepared by solvent casting method in chloroform ($CHCl_3$). SWCNTs were dispersed in $CHCl_3$ by using a tip sonicator (VIBRA CELL Sonics mod. VC 750, USA) for 30 min in ice bath and for further 30 min in an ultrasonic bath (Ultrasonic bath-mod.AC-5, EMMEGI). The different polymer matrices were mixed with nanotube dispersions (polymer/solvent ratio was chosen as 5% wt/v) by magnetic stirring for 5 h. After complete polymer dissolution, the mixture was cast onto a glass Petri substrate and air dried at room temperature (RT) for 24 h and for additional 48 h in vacuum. Composite samples containing 0.1, 0.5, 0.75 and 1 wt% with respect to polymer initial weight were prepared with different matrices. Sample formulations are summarized in Table 1. Composite films of 90 μm thickness were obtained. Neat PBCE, P(BCE90BDG10) and P(BCE70BDG30) polymeric films were also prepared by solvent casting for comparison. In the following P(BCE90BDG10) and P(BCE70BDG30) will be named BDG10 and BDG30, respectively.

## 2.3. Composite film characterization

### 2.3.1. Microstructure

Field emission scanning electron microscopy (FESEM, Zeiss Supra25) was used to analyze the fractured surfaces of the produced composite films. Cross-section samples were fractured after immersion in liquid nitrogen, gold sputtered and then analyzed.

### 2.3.2. Thermal analysis

Thermogravimetric analysis (TGA) was performed using a quartz rod microbalance (Seiko Exstar 6300, Japan) in the following conditions: sample weight 10 mg, nitrogen flow (250 mL·min$^{-1}$), temperature range 30–800 °C, heating rate 10 °C·min$^{-1}$.

Calorimetric measurements (Perkin Elmer DSC7) were conducted in order to determine the glass transition and the melting temperature of the samples under study. In the typical setup, the external block temperature control was set at –120 °C and weighed samples of c.a. 10 mg were heated up to 40 °C above fusion temperature at a rate of 20 °C·min$^{-1}$ (1$^{st}$ scan), held for 3 min, quenched (about 100 °C·min$^{-1}$) to –80 °C and finally reheated up to 40 °C above the melting point (heating rate of 20 °C·min$^{-1}$, 2$^{nd}$ scan).

### 2.3.3. X-ray diffraction (XRD)

X-ray diffraction (XRD) patterns of polymeric films were carried out by using a PANalytical X'PertPro diffractometer equipped with a fast solid state X'Celerator detector and a copper target ($\lambda$ = 0.15418 nm). Data were acquired at each 0.10° step for 100 s in the 5–60° 2θ interval. Crystallinity degree ($X_c$) was evaluated from the XRD profiles as the ratio between the crystalline diffraction area ($A_c$) and the total area of the diffraction profile ($A_t$), $X_c = A_c/A_t$. The crystalline diffraction area has been obtained by subtracting the amorphous halo (modelled as bell shaped peak baseline) from the total area of the diffraction profile. The non-coherent scattering was taken into consideration.

### 2.3.4. Dynamic-mechanical analysis (DMA)

Dynamic-mechanical analysis (DMA) was performed with an ARES $N_2$ instrument (Rheometric Scientific, USA) in a dynamic time sweep test, at a frequency of 1 Hz, at room temperature (RT). The strain 0.05% was chosen by means of an iso-frequency test in the elastic linear region. The reported storage elastic modulus ($G'$) is the average of tests performed on five rectangular samples (10 mm× 40 mm, about 90 μm thick).

### 2.3.5. Electrical properties

Electrical resistivity measurements were conducted (ASTM D-257) by using a Keithley 6517A electrometer and a Keithley 8009 test fixture, by applying a square wave ranging from 400 V (for pure poly-

**Table 1.** Material formulations

| Formulations | | | Polymer [wt%] | SWCNTs [wt%] |
|---|---|---|---|---|
| PBCE based formulations | P(BCE90BDG10) based formulations | P(BCE70BDG30) based formulations | | |
| PBCE | BDG10 | BDG30 | 100 | 0 |
| PBCE_0.1SWCNTs | BDG10_0.1SWCNTs | BDG30_0.1SWCNTs | 99.9 | 0.1 |
| PBCE_0.5SWCNTs | BDG10_0.5SWCNTs | BDG30_0.5SWCNTs | 99.5 | 0.5 |
| PBCE_0.75SWCNTs | BDG10_0.75SWCNTs | BDG30_0.75SWCNTs | 99.25 | 0.75 |
| PBCE_1SWCNTs | BDG10_1SWCNTs | BDG30_1SWCNTs | 99 | 1 |

mer) to 1 V (for percolated composites) with a period of 60 s in the laboratory conditions, of at least four measurements for each sample.

#### 2.3.6. Dielectric properties

The real and imaginary parts of the complex impedance ($Z$) of the different polymers and composite films were measured by Hewlett Packard 4284A Precision LCR Meter at RT, in the 20 Hz÷1 MHz frequency range. The AC conductivity of the samples as a function of frequency $\sigma(\omega)$ is calculated as: $\sigma_{AC} = d/(|Z|\cdot A)$ where $A$ is the cross-sectional area and $d$ is sample thickness. The real part of conductivity $\sigma'(\omega)$, was used to evaluate the dielectric behavior of the new systems, and it was calculated by using the Equation (1):

$$\sigma'(\omega) = \varepsilon''(\omega)\omega\varepsilon_0 \quad (1)$$

where $\omega = 2\pi f$ is the angular frequency of the signal applied to the samples, $\varepsilon''(\omega)$ is the imaginary part of the complex permittivity, and $\varepsilon_0 = 8.852\cdot10^{-14}$ F·cm$^{-1}$ is the vacuum permittivity.

## 3. Results and discussion

### 3.1. Morphological investigations

Chemical structure of the P(BCEmBDGn) copolymer, FESEM and scheme of SWCNTs and image of the polymer and composite films from PBCE, BDG10 and BDG30 are shown in Figure 1. SWCNTs were deposited on to indium thin oxide substrates, SWNT bundles of about 10 nm diameter were found in the samples.

Neat polymer and composite films with different contents of SWCNTs were successfully developed by solvent casting process. The visual observation image of all samples is shown in Figure 1. PBCE homopolymer and BDG10 neat polymers displayed a white/transparent color, while a more yellowish color was observed for BDG30 film, due to the catalyst employed in the synthesis (i.e. $Ti(OBu)_4$) [25]. The color of the composite films was dependent on the nanotube loading. Samples containing lower amount of SWCNTs were grey, while those based on higher content of SWCNTs had a completely black appearance, due to the carbon nanotubes and the interconnected microstructure. The different color in the composites with 0.1 wt% could be ascribed to the different interaction with poly(butylene cyclohexanedicarboxylate/diglycolate) copolymers. The SWCNT dispersion in the polymer plays a key role on the physical properties of composite. Figure 2 shows the FESEM micrographs of the fracture surfaces of the neat polymers (Figure 2a) and of all composites (Figure 2b), containing 0.1, 0.5, 0.75 and 1 wt% of SWCNTs, at different resolutions. Neat polymers present a porous microstructure, due to the solvent cast processing (Figure 2a). It is important to point out that the original structure of the different polymer matrix films has been completely modified by the carbon nanotubes introduction. A dense fractured structure was already observed for low SWCNT content (0.1 wt%). When higher amounts of carbon nanotubes were introduced, (i.e. 0.5, 0.75 and 1 wt%), the composites fractured surface displayed similar features to those containing 0.1 wt% of SWCNTs, indicating that a small amount of SWCNTs can disperse homogeneously in PBCE, BDG10 and BDG30 (Figure 2b). An increase of the fractured surface roughness could be observed by increasing the SWCNT content. Finally, no evidence of individual SWCNTs was found, thus a good dispersion of the nanotubes in the selected polymer matrices was achieved.

### 3.2. Thermogravimetric analysis

The results of thermogravimetric behavior of PBCE, BDG10 and BDG30 neat polymers and composites are shown in Table 2, that reports the maximum degradation temperature ($T_{max}$). On the other hand, Figure 3 shows the derivative (DTG) curves of the developed systems. All the analyzed polymeric films highlighted a single degradation peak. A similar behavior was also observed in the composite formulations. Neat PBCE, BDG10 and BDG30 displayed a thermal degradation within a relatively narrow interval centered at 413, 412 and 413 °C, respectively (Table 2), underlining that the BDG co-unit presence did not influence the thermal stability of the produced films, as well as the addition of SWCNTs as already observed [23].

### 3.3. Thermal and structural characterization

It is well established that the melting behavior of a polymer is affected by its previous thermal history. Therefore, in order to provide the same heat treatments to all samples investigated, each film was kept at room temperature for at least four weeks prior to thermal analysis. DSC traces of different samples after processing are reported in Figure 4 and the data obtained in Table 2.

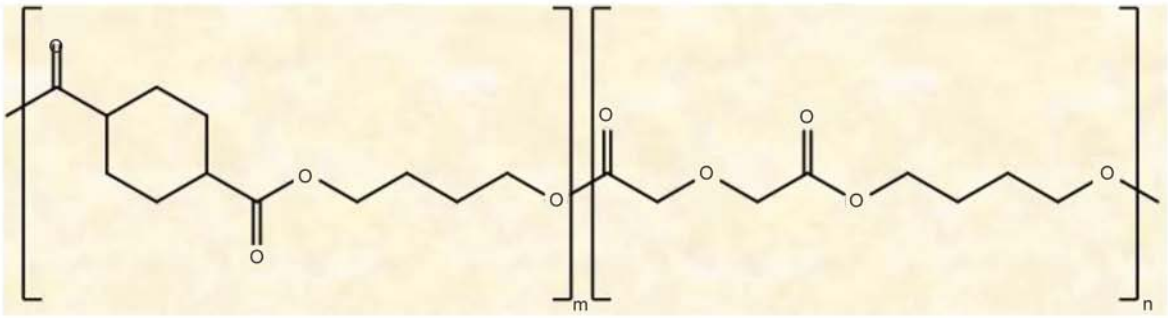


Chemical structure of the P(BCEmBDGn) copolymers

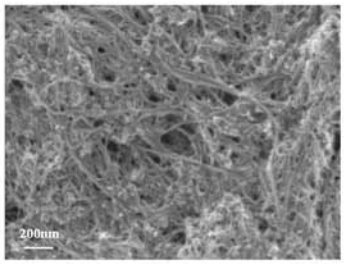


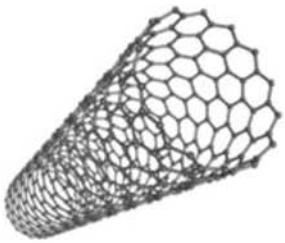

FESEM image and scheme of SWCNTs


**Figure 1.** Chemical structure of the P(BCEmBDGn) copolymers, FESEM and scheme of SWCNTs and image of the polymer and composite films. The SWCNT concentration (wt% on the polymer) is indicated.

All samples appeared as semicrystalline after the solvent casting procedure, the calorimetric traces were characterized by a conspicuous melting endotherm. The DSC data obtained from the first heating scan underlined that the melting temperature and enthalpy did not change with the increasing of the SWCNT content, in all the composites. To better understand the nature of the crystalline phase present in the polymers under investigation, the structural characterization was carried out by X-ray dif-

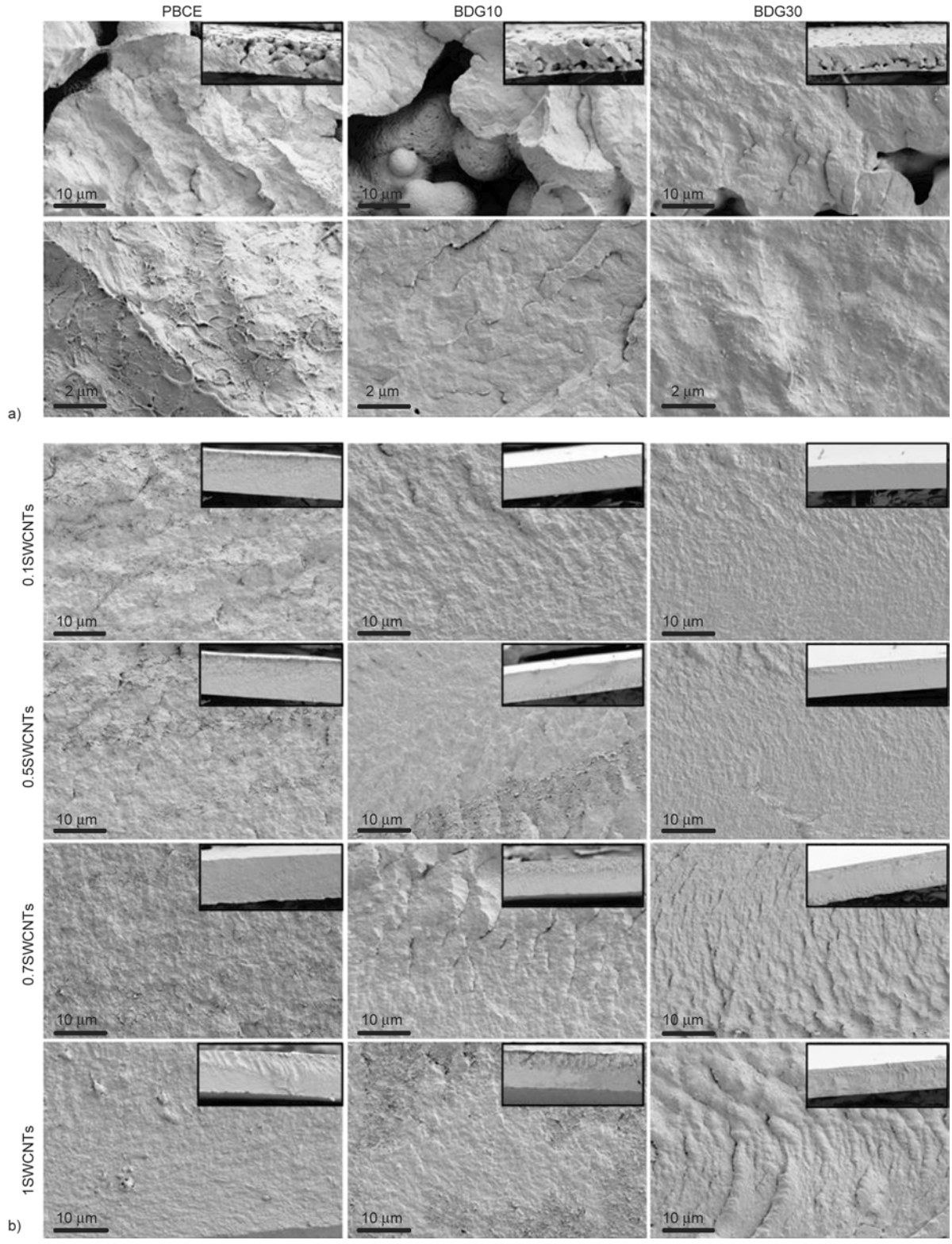


**Figure 2.** FESEM fractured surface of PBCE, BDG10 and BDG30 polymers (a) and composite formulations (b). The film sections are shown in the inserts.

**Table 2.** Thermal and mechanical properties of PBCE, BDG10 and BDG30 polymer and composite films

| Formulations | DSC results | | | | | | | XRD results | TGA results | DMA results |
|---|---|---|---|---|---|---|---|---|---|---|
| | I scan | | II scan | | | | | | | |
| | $T_m$ [°C] | $\Delta H_m$ [J/g] | $T_g$ [°C] | $\Delta C_p$ [J/(g·°C)] | $T_m$ [°C] | $\Delta H_m$ [J/g] | $T_m$ [°C] | $X_c$ [%] | $T_{max}$ [°C] | $G'_{Time\ 500}$ [Pa·10$^{10}$] |
| **PBCE** | | | | | | | | | | |
| PBCE | 167 | 45 | 15 | 0.082 | 167 | 31 | 167 | 52±3 | 413 | 1.7±0.2 |
| PBCE_0.1SWCNTs | 167 | 43 | 16 | 0.074 | 166 | 34 | 167 | 50±2 | 414 | 2.2±0.3 |
| PBCE_0.5SWCNTs | 166 | 45 | 16 | 0.073 | 166 | 36 | 166 | 48±4 | 414 | 2.0±0.3 |
| PBCE_0.75SWCNTs | 167 | 43 | 16 | 0.092 | 166 | 38 | 167 | 53±2 | 414 | 3.1±0.6 |
| PBCE_1SWCNTs | 166 | 44 | 16 | 0.087 | 166 | 39 | 166 | 51±2 | 415 | 3.8±0.5 |
| **P(BCE90BDG10)** | | | | | | | | | | |
| BDG10 | 155 | 37 | –2 | 0.091 | 155 | 29 | 155 | 45±1 | 412 | 1.6±0.2 |
| BDG10_0.1SWCNTs | 154 | 39 | –2 | 0.102 | 155 | 32 | 154 | 45±3 | 413 | 1.9±0.2 |
| BDG10_0.5SWCNTs | 154 | 36 | –3 | 0.101 | 155 | 32 | 154 | 45±3 | 414 | 1.9±0.3 |
| BDG10_0.75SWCNTs | 155 | 38 | –2 | 0.091 | 155 | 34 | 155 | 46±2 | 414 | 2.1±0.5 |
| BDG10_1SWCNTs | 155 | 41 | –3 | 0.102 | 155 | 36 | 155 | 45±2 | 415 | 2.6±0.4 |
| **P(BCE70BDG30)** | | | | | | | | | | |
| BDG30 | 120 | 27 | –17 | 0.263 | 120 | 21 | 120 | 42±1 | 413 | 1.3±0.4 |
| BDG30_0.1SWCNTs | 119 | 26 | –19 | 0.246 | 120 | 21 | 119 | 43±2 | 413 | 1.3±0.2 |
| BDG30_0.5SWCNTs | 119 | 24 | –18 | 0.250 | 120 | 23 | 119 | 43±2 | 414 | 1.4±0.2 |
| BDG30_0.75SWCNTs | 119 | 28 | –19 | 0.246 | 121 | 26 | 119 | 42±4 | 415 | 2.1±0.4 |
| BDG30_1SWCNTs | 120 | 28 | –18 | 0.258 | 120 | 27 | 120 | 43±3 | 416 | 2.3±0.3 |

fraction. The patterns are reported in Figure 5. All the samples, i.e. neat PBCE, BDG10, BDG30 and the composites, showed a well-defined diffraction pattern, whose peaks are situated at the same angular positions and displayed similar intensities (Figure 5a), suggesting the presence of the same crystal phase. The two broad peaks of the SWCNTs (at about 25 and 43°) are not detectable in the composites pattern, as the amount of nanotubes in the polymer matrix is very low. In addition, crystallinity degree evaluation by XRD confirmed the results obtained by DSC during the first heating scan. Indeed, no variation in the $X_c$ was reported with the increasing of SWCNT content for each polymer (Table 2). On the other hand, a decrease in the $X_c$ was observed with the increasing of BDG mol% (Table 2). This trend can be ascribed to the presence of increasing amount of ether-linkages in BDG10 and BDG30 with respect to PBCE. BDG co-units caused a reduction of the chain symmetry, therefore hampering the crystallization process and lowering the crystal perfection.

In order to better evidence and study the glass transition phenomenon, the samples under study were subjected to rapid cooling from the melt. The DSC curves after melt quenching are shown in Figure 4. As it can be seen from the data reported in Table 2, the glass transition temperature and $\Delta C_p$ values were not influenced by the presence of nanofillers and the results here presented are in good agreement with those previously obtained for neat polymers [24].

During the second heating scan, DSC traces of neat polymers showed multiple melting peaks, due to melt-recrystallization processes [26]. With the addition of increasing amounts of SWCNTs, this phenomenon progressively disappeared, and single melting endotherms could be observed. Moreover, an increase of the $\Delta H_m$ with the increasing of SWCNT content was highlighted. Both these effects can be explained by taking into consideration that the nanotubes can act as nucleating agents, thus favouring the sample crystallization process [23]. Higher amount of crystal phase and better crystal perfection can be therefore achieved. It is also worth noticing that the film preparation process played a role to determine the degree of crystallinity of the neat polymers, as evidenced by both DSC and WAXS measurements (Figure 5b). The compression moulding process limited the crystallization rate and crystal phase perfection, since a rapid cooling from the melt was adopted; on the other hand the solvent casting method allowed the polymer to develop a higher amount of a more perfect crystal phase. This was evidenced by the absence of the double melting peak in the 1$^{st}$ scan DSC traces, and by the absence of the small reflections at 16.2 and 19.5° in the diffraction patterns of the films obtained by solvent casting, as

well as by the $\Delta H_m$ and $X_c$ values reported in Table 2, as compared to those previously obtained [24].

### 3.4. Dynamic-mechanical characterization

The dynamic-mechanical behavior of neat PBCE, BDG10 and BDG30 polymeric films and their composites was studied in order to evaluate the effect of SWCNT introduction and content on the mechanical response of the systems. Figure 6 shows the storage $G'$ modulus as function of time for polymeric films (Figure 6a) and composites (Figure 6b–6d). All the studied formulations exhibited a linear trend [22, 27]. The $G'$ values are reported in Table 2. As it can be observed in Figure 6a, PBCE homopolymer displayed the highest $G'$ value with respect to the BDG10 and BDG30, highlighting the higher stiffness of this material due to the aliphatic ring that confers rigidity to the polymer chain [11]. Moreover, Figure 6a underlines the effect of BDG co-unit. By varying the amount of ether-linkages, it has been possible to tailor the homopolymer mechanical behavior by progressively reducing the $G'$ value and therefore the rigidity of the film. This is due to the higher flexibility of material induced by the ether–oxygen atoms. BDG30 film displayed in fact the lowest values of storage modulus.

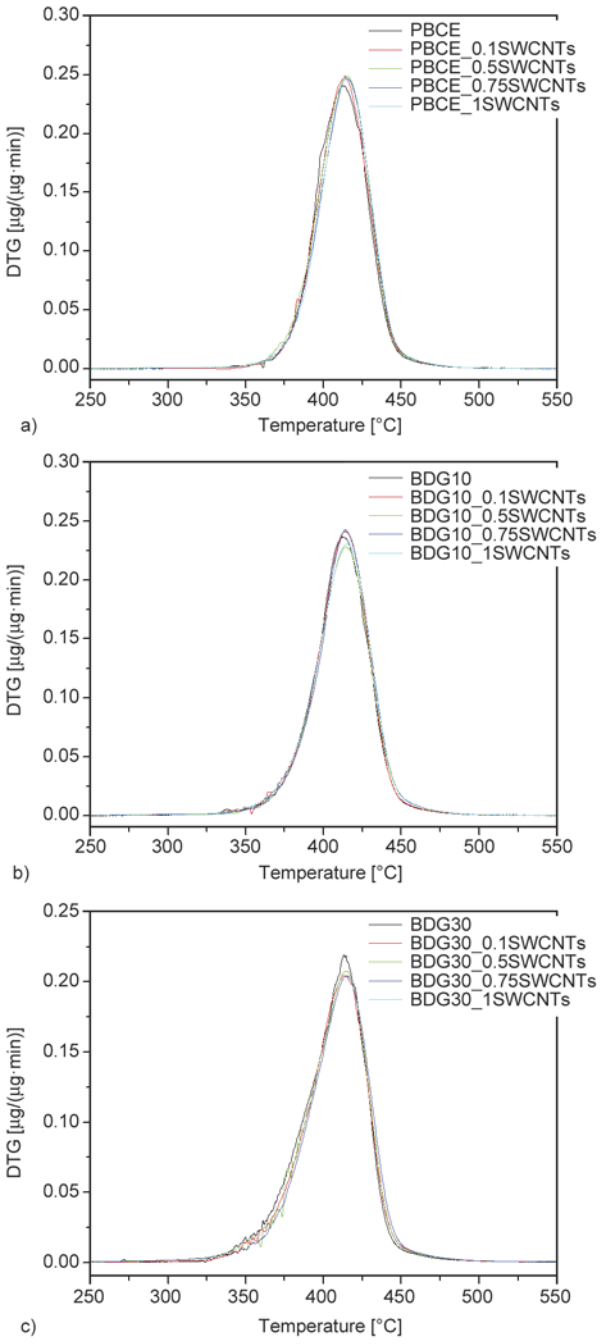


**Figure 3.** DTG graphs of neat polymer and composite films, for PBCE based fomrulations (a), BDG10 based formulations (b) and BDG30 based formulations (c)

In the composite films an increase of the $G'$ as compared to the corresponding neat polymer matrices was observed (Figure 6b–6d show the $G'$ *vs. time* dependence of different formulations, while Table 2 summarizes the $G'$ at 500 s and highlights the composition dependence of each studied polymer). This result underlines the reinforcement effect produced by SWCNTs. Figure 6b evidences also the effect of SWCNT content on the mechanical response of PBCE matrix. Comparable results were detected for 0.1–0.5 and 0.75–1 wt% formulations ($G'$ values around 2.1 Pa·$10^{10}$ for PBCE_0.1SWCNTs and PBCE_0.5SWCNTs and about 3.5 Pa·$10^{10}$ for PBCE_0.75SWCNTs and PBCE_1SWCNTs, respectively). Moreover, PBCE_0.75SWCNTs and PBCE_1SWCNTs displayed the highest values of $G'$ (increase of 106% if compared to PBCE matrix) also with respect to the other composites produced from BDG10 and BDG30, due to the brittle nature of PBCE homopolymer. On the contrary, a clearer trend was detected in the case of BDG10 based composite formulations with respect to the carbon nanotube content. Indeed, a linear increase in the $G'$ values was measured for these materials with the increase of SWCNT content (Figure 6c). BDG10_1SWCNTs displayed the highest $G'$ value, with an increase of about 63% with respect to the pristine BDG10 film. Finally, no particular effects were detected for BDG30_0.1SWCNTs and BDG30_0.5SWCNTs: in this case the $G'$ value was close to that of BDG30 matrix. Finally, a significant reinforcement effect (about 63%) was evident in the BDG30_0.75SWCNTs and BDG30_1SWCNTs due

to the higher content of SWCNTs. In conclusion, the mechanical characterization confirmed for all the studied formulations, the reinforcement effect guaranteed by the SWCNTs that act as nucleating

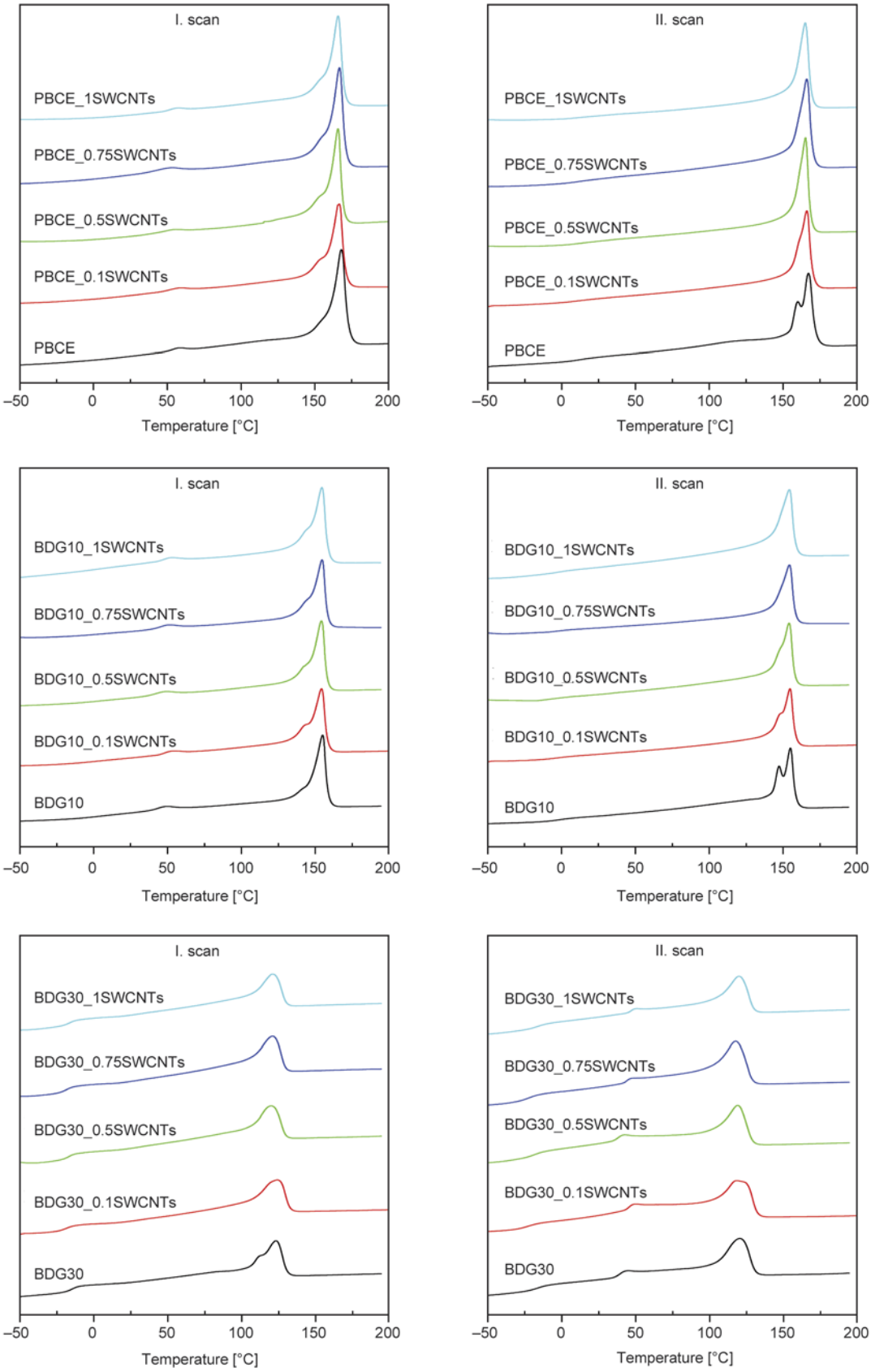


**Figure 4.** Calorimetric curves of neat polymers and composites; I scan and II scan after melt quenching

agents, in agreement with the discussion of the DSC results above reported. The obtained results evidenced that no particular effects over the time (Table 2, $G'$ at 500 s) are present also in the case of SWCNT based systems. Therefore the original mechanical properties over the time, for the different studied formulations, were maintained. This aspect is of high importance for practical applications.

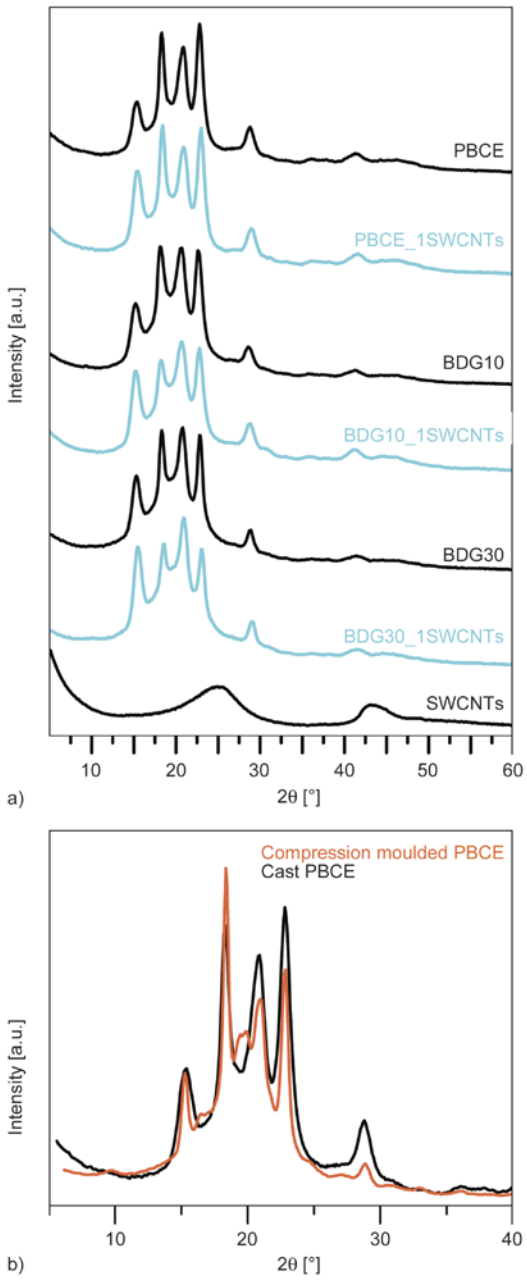


**Figure 5.** X-ray diffraction patterns of neat polymers, samples containing 1 wt% of SWCNTs and SWCNT powder (a). Comparison between the X-ray diffraction patterns of a PBCE films produced by solvent casting and by compression moulding (b).

### 3.5. Electrical and dielectric properties

DC electrical conductivity ($\sigma_{DC}$) behavior of the different samples is reported in Figure 7 as a function of the SWCNT content. The volume conductivity of neat PBCE and BDG10 was found to be about $10^{-14}$ S/m. By increasing of BDG mol% co-unit, an increased value of conductivity was measured, up to $10^{-12}$ S/m, for the BDG30 neat polymer film, probably due to the increasing chain mobility, as underlined by the glass transition values and dynamic-mechanical analysis.

A small addition of nanotubes to the polymers yielded a drastic raise in $\sigma_{DC}$. The presence of 0.1 wt% of SWCNTs resulted in an increase of 6 orders of magnitude with respect to neat polymers. Near to the electrical percolation threshold, conductivity showed a sudden rise of several orders of magnitude. In general it is possible to conclude that a conductive behavior was found for SWCNT contents higher than 0.1 wt%, and values higher than $10^{-4}$ S/m were obtained for 1 wt% of SWCNTs. Moreover, from the plotted curves it can be seen that the percolation threshold is between 0.1 and 0.50 wt% of carbon nanotubes. When these amounts are reached, nanotubes form a network which results in the formation of conductive path, causing the material to behave like a conductor. For SWCNT content lower than 0.1 wt%, the composites contained few conductive networks and/or electron tunneling and therefore acted as insulators. A step-like transition due to the percolation phenomenon could be observed when the SWCNT content increased from 0.1 to 0.50 wt%. The electrical conductivity of the composites with 0.50 wt% SWCNTs was three orders of magnitude greater than that of the composite with 0.1 wt% SWCNTs. These data are in agreement with our recent results obtained by dispersing CNT in poly (L-Lactide) polymer matrix, by using the same dispersing procedure [28].

As expected, the composites produced from the different polymers, presented the same percolation behavior with the introduction of SWCNTs, since the conductive behavior is mainly due to the SWCNT presence, content and process technology. It is clear that the main factors affecting the electrical percolation threshold are the processing conditions, equal for all the investigated polymers.

Dielectric characterization permits to investigate the frequency-dependent electrical properties of the

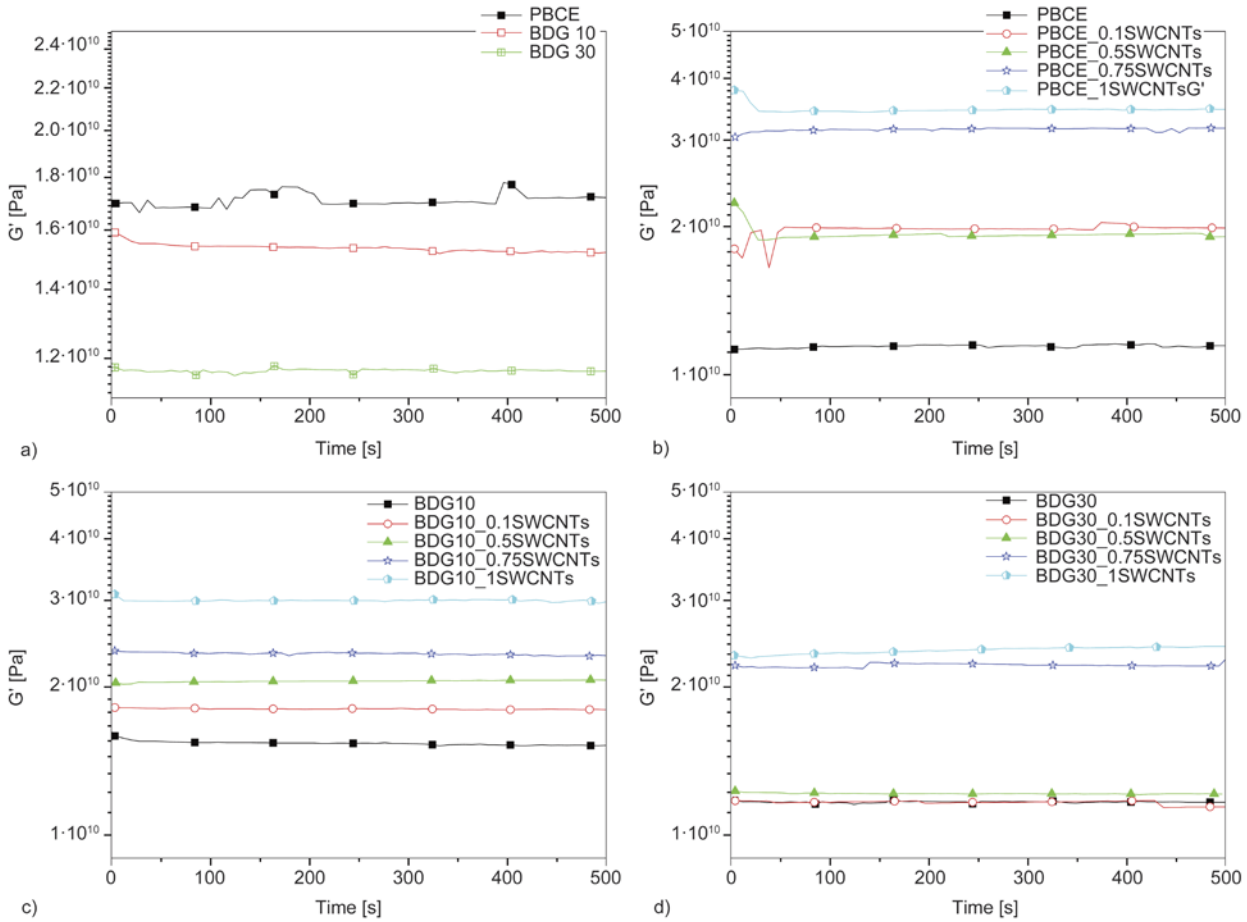


**Figure 6.** Storage $G'$ modulus behavior as function of time for PBCE, BDG10 and BDG30 polymers (a) and composite formulations (b–d)

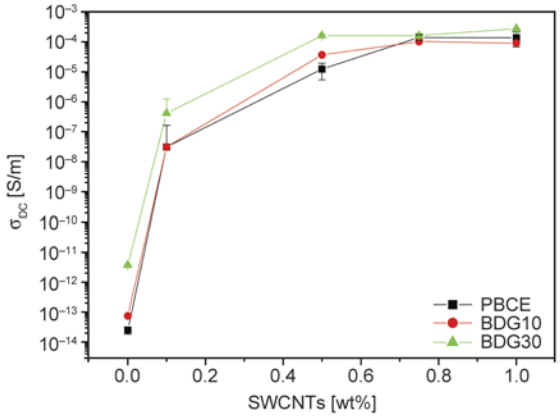


**Figure 7.** Bulk electrical conductivities of composites based on different content of SWCNTs

CNT-filled systems, identifying the dielectric behavior of SWCNT based composites, that may be masked under the DC time-domain approach previously used [29, 30]. Figure 8 shows the evolution of the real part of the electrical conductivity ($\sigma_{AC}'$) measurements (log–log scale) with the frequency: of PBCE (a), BDG10 (b) and BDG30 (c) based composites in the 20 Hz–1 MHz frequency range. The $\sigma_{AC}'$ of the neat polymer films displayed a linear behavior with respect to the frequency, while composite materials highlighted a plateau until a specific frequency value, named critical frequency ($f_c$), followed by a linear behavior. The $f_c$ shifted to high frequency with the increasing of the SWCNT content in the composites [31]. At low frequencies, for the samples over the percolation threshold a plateau in conductivity was found, corresponding to the current flowing almost exclusively through the nanotube network, which behaved as a resistive path. As the frequency rose, the capacitive parts, which can be associated to both the capacitive polymer matrix and the tube/polymer/tube structures, contributed to an increasing conductance.

## 4. Conclusions

Novel composite films based on poly(butylene cyclohexanedicarboxylate/diglycolate) random copolymer and single walled carbon nanotubes were successfully produced by solvent casting. To better understand the effect of filler shape and the ability

to build efficient conductive architecture through the composite, different amounts of carbon nanotubes were dispersed in the polymers. The presence of SWCNTs affected the morphological, thermal, dynamic-mechanical, electrical and dielectric properties of the polymer matrices. The surface structure significantly changed with the introduction of carbon nanotubes. Results underlined that SWCNTs act as nucleating agent and reinforcing phase in all the investigated polymers.

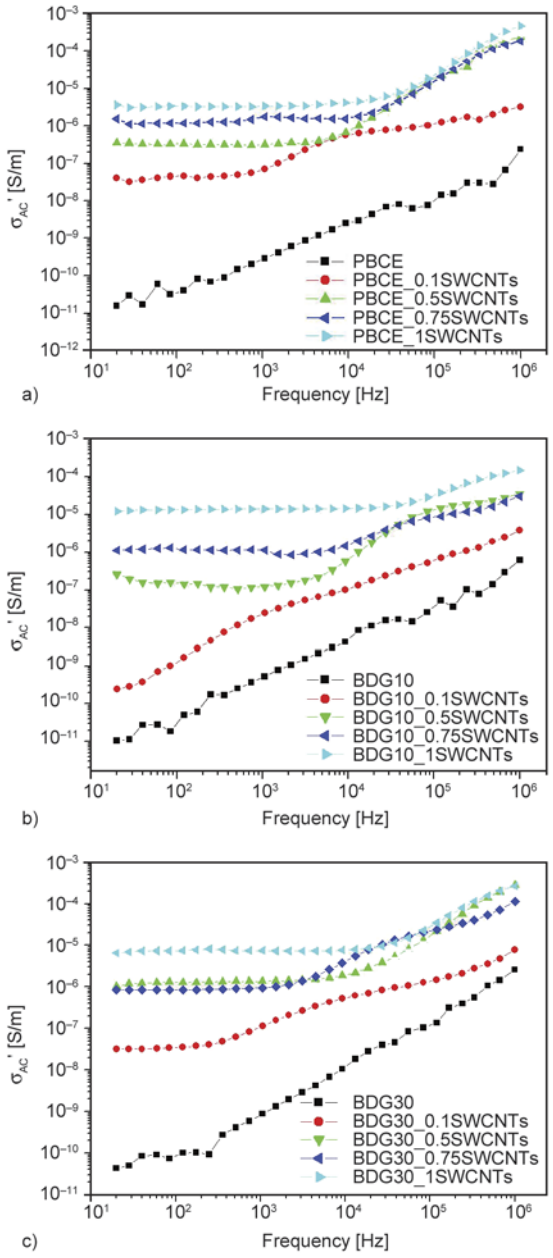


**Figure 8.** Real part of the AC Conductivity of PBCE (a), BDG10 (b) and BDG30 (c) based composite films

Moreover, SWCNTs improved the polymer electrical and dielectric conductivity already at low concentrations, with a formation of a tridimensional nanotube network in the percolated formulations. The new developed polymeric conductive composites can be considered very promising for several biomedical applications. In particular, such materials can be used to proliferate cells under electrical stimulation, and could offer significant potential benefits for the functional reconnection of damaged nerves in the peripheral and central nervous systems. The findings of this work prove that the preparation of composites represents a winning strategy to improve the final material properties and can be surely considered a valuable starting point to design other high performance conductive composites.

## Acknowledgements

The authors wish to thank Dr. Samantha Mattioli for FESEM analysis.

## References

[1] Luckachan G. E., Pillai C. K. S.: Biodegradable polymers – A review on recent trends and emerging perspectives. Journal of Polymers and the Environment, **19**, 637–676 (2011). DOI: 10.1007/s10924-011-0317-1

[2] Abdul Khalil H. P. S., Bhat A. H., Ireana Yusra A. F.: Green composites from sustainable cellulose nanofibrils: A review. Carbohydrate Polymers, **87**, 963–979 (2012). DOI: 10.1016/j.carbpol.2011.08.078

[3] Armentano I., Bitinis N., Fortunati E., Mattioli S., Rescignano N., Verdejo R., Lopez-Manchado M. A., Kenny J. M.: Multifunctional nanostructured PLA materials for packaging and tissue engineering. Progress in Polymer Science, **38**, 1720–1747 (2013). DOI: 10.1016/j.progpolymsci.2013.05.010

[4] Tserki V., Matzinos P., Pavlidou E., Vachliotis D., Panayiotou C.: Biodegradable aliphatic polyesters. Part I. Properties and biodegradation of poly(butylene succinate-*co*-butylene adipate). Polymer Degradation and Stability, **91**, 367–376 (2006). DOI: 10.1016/j.polymdegradstab.2005.04.035

[5] Berti C., Celli A., Marchese P., Marianucci E., Barbiroli G., Di Credico F.: Influence of molecular structure and stereochemistry of the 1,4-cyclohexylene ring on thermal and mechanical behavior of poly(butylene 1,4-cyclohexanedicarboxylate). Macromolecular Chemistry and Physics, **209**, 1333–1344 (2008). DOI: 10.1002/macp.200800125

[6] Berti C., Binassi E., Celli A., Colonna M., Fiorini M., Marchese P., Marianucci E., Gazzano M., Di Credico F., Brunelle D. J.: Poly(1,4-cyclohexylenedimethylene 1,4-cyclohexanedicarboxylate): Influence of stereochemistry of 1,4-cyclohexylene units on the thermal properties. Journal of Polymer Science Part B: Polymer Physics, **46**, 619–630 (2008).
DOI: 10.1002/polb.21397

[7] Bechthold I., Bretz K., Kabasci S., Kopitzky R., Springer A.: Succinic acid: A new platform chemical for biobased polymers from renewable resources. Chemical Engineering and Technology, **31**, 647–654 (2008).
DOI: 10.1002/ceat.200800063

[8] Colonna M., Berti C., Fiorini M., Binassi E., Mazzacurati M., Vannini M., Karanam S.: Synthesis and radiocarbon evidence of terephthalate polyesters completely prepared from renewable resources. Green Chemistry, **13**, 2543–2548 (2011).
DOI: 10.1039/C1GC15400A

[9] Gigli M., Lotti N., Gazzano M., Siracusa V., Finelli L., Munari A., Dalla Rosa M.: Biodegradable aliphatic copolyesters containing PEG-like sequences for sustainable food packaging applications. Polymer Degradation and Stability, **105**, 96–106 (2014).
DOI: 10.1016/j.polymdegradstab.2014.04.006

[10] Gigli M., Govoni M., Lotti N., Giordano E. D., Gazzano M., Munari A.: Biocompatible multiblock aliphatic polyesters containing ether-linkages: Influence of molecular architecture on solid-state properties and hydrolysis rate. RSC Advances, **4**, 32965–32976 (2014).
DOI: 10.1039/C4RA04248D

[11] Gigli M., Lotti N., Vercellino M., Visai L., Munari A.: Novel ether-linkages containing aliphatic copolyesters of poly(butylene 1,4-cyclohexanedicarboxylate) as promising candidates for biomedical applications. Materials Science and Engineering: C, **34**, 86–97 (2014).
DOI: 10.1016/j.msec.2013.08.013

[12] Armentano I., Dottori M., Fortunati E., Mattioli S., Kenny J. M.: Biodegradable polymer matrix nanocomposites for tissue engineering: A review. Polymer Degradation and Stability, **95**, 2126–2146 (2010).
DOI: 10.1016/j.polymdegradstab.2010.06.007

[13] Matos C. F., Galembeck F., Zarbin A. J. G.: Multifunctional and environmentally friendly nanocomposites between natural rubber and graphene or graphene oxide. Carbon, **78**, 469–479 (2014).
DOI: 10.1016/j.carbon.2014.07.028

[14] Seligra P. G., Lamanna M., Famá L.: Promising PLA-functionalized MWCNT composites to use in nanotechnology. Polymer Composites, in press (2015).
DOI: 10.1002/pc.23504

[15] Musto P., Russo P., Cimino F., Acierno D., Lupò G., Petrarca C.: Dielectric behavior of biopolymer based composites containing multi wall carbon nanotubes: Effect of filler content and aspect ratio. European Polymer Journal, **64**, 170–178 (2015).
DOI: 10.1016/j.eurpolymj.2015.01.010

[16] Lee C. J., Park J., Kang S. Y., Lee J. H.: Growth and field electron emission of vertically aligned multi-walled carbon nanotubes. Chemical Physics Letters, **326**, 175–180 (2000).
DOI: 10.1016/S0009-2614(00)00751-X

[17] Sun L. F., Liu Z. Q., Ma X. C., Zhong Z. Y., Tang S. B., Xiong Z. T., Tang D. S., Zhou W. Y., Zou X. P., Li Y. B., Tan K. L., Xie S. S., Lin J. Y.: Growth of carbon nanotube arrays using the existing array as a substrate and their Raman characterization. Chemical Physics Letters, **340**, 222–226 (2001).
DOI: 10.1016/S0009-2614(01)00417-1

[18] Dalton A. B., Collins S., Muñoz E., Razal J. M., Ebron V. H., Ferraris J. P., Coleman J. N., Kim B. G., Baughman R. H.: Super-tough carbon-nanotube fibres. Nature, **423**, 703–703 (2003).
DOI: 10.1038/423703a

[19] Saito R., Dresselhaus G., Dresselhaus M. S.: Physical properties of carbon nanotubes. Imperal College Press, London (1998).

[20] Grossiord N., Kivit P. J. J., Loos J., Meuldijk J., Kyrylyuk A. V., van der Schoot P., Koning C. E.: On the influence of the processing conditions on the performance of electrically conductive carbon nanotube/polymer nanocomposites. Polymer, **49**, 2866–2872 (2008).
DOI: 10.1016/j.polymer.2008.04.033

[21] Alig I., Pötschke P., Lellinger D., Skipa T., Pegel S., Kasaliwal G. R., Villmow T.: Establishment, morphology and properties of carbon nanotube networks in polymer melts. Polymer, **53**, 4–28 (2012).
DOI: 10.1016/j.polymer.2011.10.063

[22] Armentano I., Marinucci L., Dottori M., Balloni S., Fortunati E., Pennacchi M., Becchetti E., Locci P., Kenny J. M.: Novel poly(L-lactide) PLLA/SWNTs nanocomposites for biomedical applications: Material characterization and biocompatibility evaluation. Journal of Biomaterials Science, Polymer Edition, **22**, 541–556 (2011).
DOI: 10.1163/092050610X487873

[23] Fortunati E., D'Angelo F., Martino S., Orlacchio A., Kenny J. M., Armentano I.: Carbon nanotubes and silver nanoparticles for multifunctional conductive biopolymer composites. Carbon, **49**, 2370–2379 (2011).
DOI: 10.1016/j.carbon.2011.02.004

[24] Gigli M., Lotti N., Gazzano M., Siracusa V., Finelli L., Munari A., Dalla Rosa M.: Fully aliphatic copolyesters based on poly(butylene 1,4-cyclohexanedicarboxylate) with promising mechanical and barrier properties for food packaging applications. Industrial and Engineering Chemistry Research, **52**, 12876–12886 (2013).
DOI: 10.1021/ie401781d

[25] Chrissafis K., Paraskevopoulos K. M., Bikiaris D. N.: Thermal degradation kinetics of the biodegradable aliphatic polyester, poly(propylene succinate). Polymer Degradation and Stability, **91**, 60–68 (2006).
DOI: 10.1016/j.polymdegradstab.2005.04.028

[26] Gigli M., Lotti N., Gazzano M., Finelli L., Munari A.: Synthesis and characterization of novel poly(butylene succinate)-based copolyesters designed as potential candidates for soft tissue engineering. Polymer Engineering and Science, **53**, 491–501 (2013).
DOI: 10.1002/pen.23289

[27] Kwiatkowska M., Broza G., Schulte K., Roslaniec Z.: The *in-situ* synthesis of polybutylene terephthalate/carbon nanotubes composites. Reviews on Advanced Materials Science, **12**, 154–159 (2006).

[28] Lizundia E., Sarasua J. R., D'Angelo F., Orlacchio A., Martino S., Kenny J. M., Armentano I.: Biocompatible poly(L-lactide)/MWCNT nanocomposites: Morphological characterization, electrical properties, and stem cell interaction. Macromolecular Bioscience, **12**, 870–881 (2012).
DOI: 10.1002/mabi.201200008

[29] Pötschke P., Dudkin S. M., Alig I.: Dielectric spectroscopy on melt processed polycarbonate – Multiwalled carbon nanotube composites. Polymer, **44**, 5023–5030 (2003).
DOI: 10.1016/S0032-3861(03)00451-8

[30] Loh K. J., Lynch J. P., Shim B. S., Kotov N. A.: Tailoring piezoresistive sensitivity of multilayer carbon nanotube composite strain sensors. Journal of Intelligent Material Systems and Structures, **19**, 747–764 (2008).
DOI: 10.1177/1045389X07079872

[31] Monti M., Armentano I., Faiella G., Antonucci V., Kenny J. M., Torre L., Giordano M.: Toward the microstructure–properties relationship in MWCNT/epoxy composites: Percolation behavior and dielectric spectroscopy. Composites Science and Technology, **96**, 38–46 (2014).
DOI: 10.1016/j.compscitech.2014.03.008

*eXPRESS Polymer Letters Vol.10, No.2 (2016) 125–138*
*Available online at www.expresspolymlett.com*
*DOI: 10.3144/expresspolymlett.2016.13*

# Effects of polymerization degree on recovery behavior of PVA/PVP hydrogels as potential articular cartilage prosthesis after fatigue test

*Y. Shi*[1], *D. S. Xiong*[1,2,3*], *Y. Peng*[1], *N. Wang*[1]

[1]School of Materials Science and Engineering, Nanjing University of Science and Technology, 210094 Nanjing, Jiangsu, PR China
[2]Jiangsu Key Laboratory of Advanced Micro/nano Materials and Technology, 210094 Nanjing, Jiangsu, PR China
[3]Synergetic Research Center on Advanced Materials (SRCAM), 210094 Nanjing, Jiangsu, PR China

*Received 13 April 2015; accepted in revised form 19 September 2015*

**Abstract.** Poly (vinyl alcohol)/poly (vinyl pyrrolidone) (PVA/PVP) hydrogels with various polymerization degrees of PVA were synthesized by a repeated freezing-thawing method. The influence of polymerization degree on microstructure, water content, friction coefficient, compressive fatigue and recovery properties of PVA/PVP hydrogels were investigated. The results showed that higher polymerization degree resulted in larger compressive modulus and lower friction coefficient. The fatigue behaviors of PVA/PVP hydrogels were evaluated under sinusoidal compressive loading from 200 to 800 N at 5 Hz for up to 50 000 cycles. The unconfined uniaxial compressive tests of PVA/PVP hydrogels were performed before and after fatigue test. During the fatigue test, the height of the hydrogel rapidly decreased at first and gradually became stable with loading cycles. The compressive tangent modulus measured 0 h after fatigue was significantly larger than the values obtained before test, and then the modulus recovered to its original level for 48 h after test. However, the geometry of hydrogels could not return to the original level due to the creep effects. PVA/PVP hydrogels prepared with lower polymerization degree showed better recovery capability than that prepared with high polymerization degree.

***Keywords:*** *mechanical properties, PVA/PVP hydrogel, polymerization degree, fatigue, recovery*

## 1. Introduction

Articular cartilage, which covers the end of the long bones in the body, functions as a nearly frictionless bearing, and withstands high mechanical loads and uniformly transfers the loads on underlying bone to prevent high stress concentrations. Because of the avascular and aneural nature of articular cartilage it endows itself with poor intrinsic healing capacity for self-repair [1]. Once the articular cartilage is damaged, osteoarthritis gradually develops and finally the joint loses its function [2]. The surgical techniques, including microfracture, autologous chondrocyte implantation (ACI), osteochondral autograft transfer (OAT) etc. [3], have been widely used to ease pain and regenerate tissue function. However, all of these techniques cannot reconstruct natural function to the cartilage. Using an appropriate implant to replace the damaged cartilage is considered as a promising approach for cartilage replacement and has been of great interest to biomaterial scientists for many years [4].

Hydrogels, which are hydrophilic polymers that are swollen in water [5], are widely researched as a potential artificial articular cartilage due to their structural similarity to cartilage [6]. As present, hydrogels have been used in two forms for the pur-

*Corresponding author, e-mail: xiongds@163.com

pose of articular cartilage repair – as permanent implants to replace damaged cartilage, or as cell carrier materials to encourage tissue regeneration [7]. Hydrogels that consist of naturally derived materials, like hyaluronan [8], collagen [9], chitosan [10], alginate [11], etc, are often used as cell-seeded tissue engineering scaffold. Though these hydrogels have been successful in mimicking the morphological and biochemical appearance of hyaline cartilage, but the lack of mechanical integrity makes them inappropriate as load-bearing implants [7]. Synthetic polymers, including PVA [12, 13], poly(ethylene glycol) (PEG) [14], poly(*N*-isoproylacrylamide) (PNIPAAm) [15, 16], show mechanical similar to cartilage and allow efficient load transfer [17]. PVA hydrogel has been one of the most widely used polymer as a potential articular cartilage substitute due to its excellent biocompatibility, good load-bearing properties, and can be easily processed and modified [12, 18]. The swelling behavior [19, 20], mechanical properties [21, 22], and biotribological properties [23–25] of PVA hydrogels has been widely characterized by researchers. Tadavarthy *et al*. [26] found no adverse effects in surrounding tissue after implanting PVA gels subcutaneously or intramuscularly into rabbits. Baker *et al*. [18] summarized that PVA hydrogels could be tailored to 1–17 MPa of tensile strength and 0.0012–0.85 MPa of compressive modulus, which is close to the natural cartilage, by changing polymer concentration and the number of cycles tested.

However, pure PVA hydrogels undergo dissolution when immersed in a solvent for a long period of time. The dissolution mechanism involves the unfolding of the polymer chains of crystals in the presence of water to join the amorphous portion surrounding them [27], which leads to larger pore sizes and hence lower mechanical stiffness. PVP is another hydrogel that has been used for a variety of biomedical applications due to its good biocompatibility and hydrophilic ability properties [28, 29]. The incorporation of PVP into PVA is expected to significantly decrease degradation and stabilize the polymer network and the mechanical properties of pure PVA hydrogels through hydrogen bonding interactions between the carbonyl group on PVP and the hydroxyl group along PVA chain [30]. Leone *et al*. [31] has demonstrated the biocompatibility of PVA/PVP hydrogel. Thomas *et al*. [32] indicated that blend hydrogels prepared with 99 wt% PVA and 1 wt% PVP had the best combination of network stability and a relatively tight, stable, and crosslinked network. Our previous study showed the consistent results with Thomas' that PVA/PVP hydrogel with 1 wt% PVP had the best mechanical strength [21].

The term fatigue is used to describe the changes in properties of metallic and non-metallic materials resulting from a repeatedly applied stress or strain. If applied adequate number of times, failure may occur in the materials. During daily activities, the synovial joint is routinely subjected to static as well as dynamic loads. It has been estimated that the average person takes about 2 millions steps per year [33]. Therefore, the articular cartilage on the diarthrodial joint in the lower limbs is exposed to approximately 1 millions load cycles during this time, and each cyclic load is of several times body weight in walking condition [33, 34]. During exercise such as running, cartilage is also subjected to cyclic loading and the loads are applied at faster rates than that experienced during walking. There have been a number of researches shown that the appropriate dynamic mechanical stimulation on cell-seeded tissue-engineered constructs is beneficial to enhance extracellular matrix (ECM) synthesis, or stimulate proliferation and chondrogenesis of progenitor cells [35–38]. However, fatigue resulting from cyclic load was suggested as a failure mechanism of cartilage [39]. Weightman [40] demonstrated that the fatigue properties of human articular cartilage decreased with age, and fatigue failure could occur in life to such an extent. It was thought that the reduction in mechanical properties of cartilage with age was itself the result of fatigue [40]. Therefore, it is of high importance to study the alternative materials for cartilage replacement from a fatigue point of view attributed to the presence of cyclic stress that the materials would face in vivo after implantation. Vikingsson and coworkers [41, 42] proposed a model to assess mechanical behavior of polycaprolactone (PCL) scaffold and predict their performance '*in vivo*' during tissue regeneration, the results showed that the scaffold/gel construct was not affected after up to 100 000 compressive dynamic cycles. But this kind of scaffold would degrade gradually after implantation *in vivo*, followed by the decreasing load-bearing capacity.

When the fatigue properties of cartilage replacements were investigated, the researchers generally used dynamic loading with strain controlled, and the strain

was limited to 15%, which is considered to be the order of magnitude of physiological deformations suffered by articular cartilage [41]. 15% strain always corresponds to a very small load for hydrogels, just several N and even lower for tissue engineered hydrogels. This load is far less than the physiological load that the cartilage is subjected. And 15% strain is very close to the linear elastic region of hydrogels, so it is expected that the hydrogel would not fail for even a very long term loading cycles. To our knowledge, there are few reports about the recovery behavior of cartilage prosthesis after fatigue test under large load.

In the present study, PVA hydrogels with small amounts of PVP were synthesizes by a repeated freezing-thawing method. The effects of the incorporation of PVP and the polymerization degree of PVA on the material properties of PVA/PVP hydrogels, including microstructure, water content, compressive mechanical and friction properties, were evaluated. In order to explore the compressive fatigue properties of PVA/PVP hydrogels as cartilage prosthesis, the hydrogel samples were subjected to cyclic compressive loading from 200 to 800 N for up to 50 000 cycles at 5 Hz. The changes in height and compressive tangent modulus before and after fatigue tests, and the recovery behavior of PVA/PVP hydrogels with time after fatigue tests were investigated.

## 2. Materials and methods

### 2.1. Hydrogel preparation

PVA, saponified greater than 99% with a polymerization degree of 1750, 2099 and 2399, and PVP K-30 (40 000 g·mol$^{-1}$, Shanghai Jiuyi Chemical Reagent Co., China) were chosen as the raw materials. Both polymers were used without further purification. The required amount of polymer powders were dissolved in deionized water at 90 °C for 10 h to prepare 15 wt% polymer solution, composed of 99 wt% PVA and 1 wt% PVP. And then the polymer solution was held at a higher temperature to remove air bubbles. After that the polymer solution was then poured into moulds and subjected to 6 cycles of freezing at –20 °C for 18 h and thawing at room temperature for 6 h. 15 wt% pure PVA 1750 hydrogels were prepared as controls.

### 2.2. Microstructure

Scanning electron microscopy (SEM, JEOLJSM-6380LV, Japan) was used to evaluate the morphology and microstructure of PVA/PVP hydrogels. The samples were dried by vacuum oven at 50 °C for 60 h to remove all water, and then they were sputter-coated with a layer of gold for SEM observations. The porosity was investigated by image processing using VC++ software. Briefly, scanning electron micrographs of hydrogels were threshold analysed on the basis of different grayscale. The porosity of specimens was calculated via the ratio of black pixel area to gross. Three SEM pictures at different region for each hydrogel formulation were chosen to calculate the porosity.

### 2.3. Differential scanning calorimetry analysis

Differential scanning calorimetry (DSC, Mettler-Toledo, Switzerland, Model: DSC823e) was performed on 3 independent specimens for each hydrogel formulation to examine crystallinity. Dynamic scans were carried out from 50 to 300 °C at a heating rate of 10 °C/min, under $N_2$ atmosphere. The speed of nitrogen gas flow was 30 mL/min. Before DSC analysis, the samples were dried in vacuum for at least 48 h at 60 °C. The crystallinity degree was calculated using Equation (1) and the heat of fusion of a perfect crystal of PVA sample ($\Delta H_{f*}$ = 138.6 J/g) [43]:

$$\text{Crystallinity} = \frac{\Delta H_f}{\Delta H_{f*}} \cdot 100 \tag{1}$$

### 2.4. Water content

For all the hydrogel samples, the water content, $W$, was determined according to Equation (2):

$$\text{Water content} = \frac{M_s - M_d}{M_s} \tag{2}$$

where $M_s$ and $M_d$ represent the equilibrium swollen and completely dried sample, respectively. Five independent samples were tested for each set of hydrogels ($n$ = 5).

### 2.5. Mechanical characterization

#### 2.5.1. Compression tests

Unconfined compressive properties were carried out in a PBS solution bath at room temperature on Instron 5943 under three different strain rate (100 and 1000%·min$^{-1}$) up to 65% strain to investigate the strain rate effect on compression property. The compressive tangent modulus for each hydrogel sample was calculated at 10% increments from 10–

60% strain by the finite difference method according to the stress-strain curves obtained, and it was expressed with the Equation (3) [44]:

$$E_\varepsilon = \frac{\sigma_{\varepsilon+\Delta\varepsilon} - \sigma_{\varepsilon-\Delta\varepsilon}}{2\Delta\varepsilon} \quad (3)$$

where $E_\varepsilon$ is the compressive tangent modulus of the hydrogel at the compression strain ratio value of $\varepsilon$. The value of $\Delta\varepsilon$, the variable of strain value, is 2%. The sample size was approximately 12 mm in diameter and 4 mm in height. Three independent samples were tested for each set of hydrogels ($n$ = 3).

#### 2.5.2. Indentation creep test

The indentation creep tests were conducted in an UMT-IImulti-functional micro-friction test machine in PBS solution at room temperature. The hydrogel samples were manufactured into cylindrical disks with 20 mm in diameter and 4 mm in thickness. A stainless steel ball (Stellite 3) was used as the indenter, and its diameter was 7.9375 mm. The samples were placed between the compression plate and the spherical indenter under compression to 10 N, resulting in a nominal contact stress of about 0.6 MPa. And then this load was kept constant for 3600 s. The displacement and time were recorded. Three indentations at different region were indented for each hydrogel formulation.

#### 2.5.3. Viscoelastic measurements

Dynamic shear tests were conducted on a controlled strain dynamic mechanical thermal analysis instrument (DMTA Q800, USA), and the samples were subjected to a sinusoidal shear strain at room temperature with frequencies ranging from 0.1 to 10 Hz. The strain amplitude of 3% was used, which was within the range of linear viscoelastic region. The flat rectangular samples with 25 mm parallel plates were used. The dynamic viscoelastic functions such as $G'$ (storage modulus) and $G''$ (loss modulus) and were measured as function of frequency.

#### 2.5.4. Compressive fatigue tests

Compressive fatigue tests were performed on Instron Model 8801 test machine. The samples were placed under an impermeable compression plate, and subjected to dynamic compressive load from 200 to 800 N at 5 Hz, using a sinusoidal waveform, for up to 50 000 cycles in PBS at room temperature. The tests were run with a preload of approximately 500 N. The displacement was simultaneously recorded with 20 data point per compression cycle during the whole fatigue test, which presented the relative position of the press head, and reflected the deformation of the hydrogel in the process of fatigue test. The samples were immersed back in fresh PBS at room temperature for up to 14 days, with height and mass measured every day. Compression tests were carried out on an electronic universal material testing machine (CSS-44300, China) on each hydrogel sample before fatigue test, and 0 h (immediately after the test), 24, 48 h and 14 days after fatigue test under a strain rate of 100%·min$^{-1}$. The compressive tangent modulus was calculated at 10, 20, and 30% strain. The hydrogel samples were manufactured into rectangle with the size of 21 mm×15 mm×9 mm. As the hydrogel is slippery due to its very smooth surface, the hydrogels were packed with ultra-high molecular weight polyethylene (UHMWPE) fiber cloth, and the cloth would limit the lateral expansion of hydrogels and raised the load-bearing capacity. Three independent samples were tested for each hydrogel formulation ($n$ = 3).

### 2.6. Friction tests

The friction property was evaluated by sliding against CoCrMo ball with a diameter of 8 mm on a ball-on-plate reciprocating sliding tribometer (CETR-UMT2, USA). Tests were conducted at room temperature lubricated by PBS solution. The applied normal load, reciprocating sliding frequency and stroke length were kept constant at 5 N, 1 Hz and 8 mm, respectively. Test duration was typically 30 min, and the friction coefficient evolution was continuously monitored during the tests. Each of test was repeated three times ($n$ = 3).

### 2.7. Statistical analysis

All values were reported as means of standard deviation. Statistical analysis was performed using a one-way analysis of variance (ANOVA). Comparison between the two means was made by the Tukey test with statistical significance evaluated at $p < 0.05$.

## 3. Results

### 3.1. Microstructure

Investigation of PVA hydrogel microstructure indicates that the hydrogel shows an internal three-dimensional network structure with lots of micropores on the surface (Figure 1a), which is similar to

SEM micrographs of the natural cartilage dried under the same condition [45]. As demonstrated by researchers, phase separation into a PVA-rich phase and a water-rich phase is the crucial and unique mechanism that occurs in the process of freeze-thawed PVA hydrogel gelation [46]. During freezing process, water froze, while the polymers were expelled to form regions of concentrated polymer. The polymer chains in polymer-rich regions were pushed into close contact with each other, facilitating the formation of hydrogen bonding and crystallite. During the thawing process, the crystals of frozen water, which performed as a pore-forming agent, left pores filled with water. These processes repeated with each cycle, microstructural remodeling of the polymer phase occurred, decreasing the distance between the polymer chains further and promoting crosslinking; water crystals grew and even met the facets of other crystals during freezing, and then interconnected pores arose within the hydrogel after thawing. Finally a three-dimensional and porous and interconnected hydrogel structure was created. When blended with PVP, the internal structure of PVA/PVP hydrogels becomes denser and less porosity (Figure 1b) due to the interpolymer complexation between PVA and PVP. With the increase of polymerization degree of PVA, the network becomes denser, and the porosity decreases, as shown in Table 1. For long PVA molecular chains, it is believed to provide more physical crosslinking points, encouraging the formation of more hydrogen bonding and hence a denser network structure.

### 3.2. Crystallinity

The degrees of crystallinity of PVA hydrogels were listed in Table 1. The incorporation of PVP increased the crystallinity of PVA hydrogels, while the crystallinity decreased with the increase of PVA polymerization degree. That is because the higher polymerization degree results in greater crosslinking,

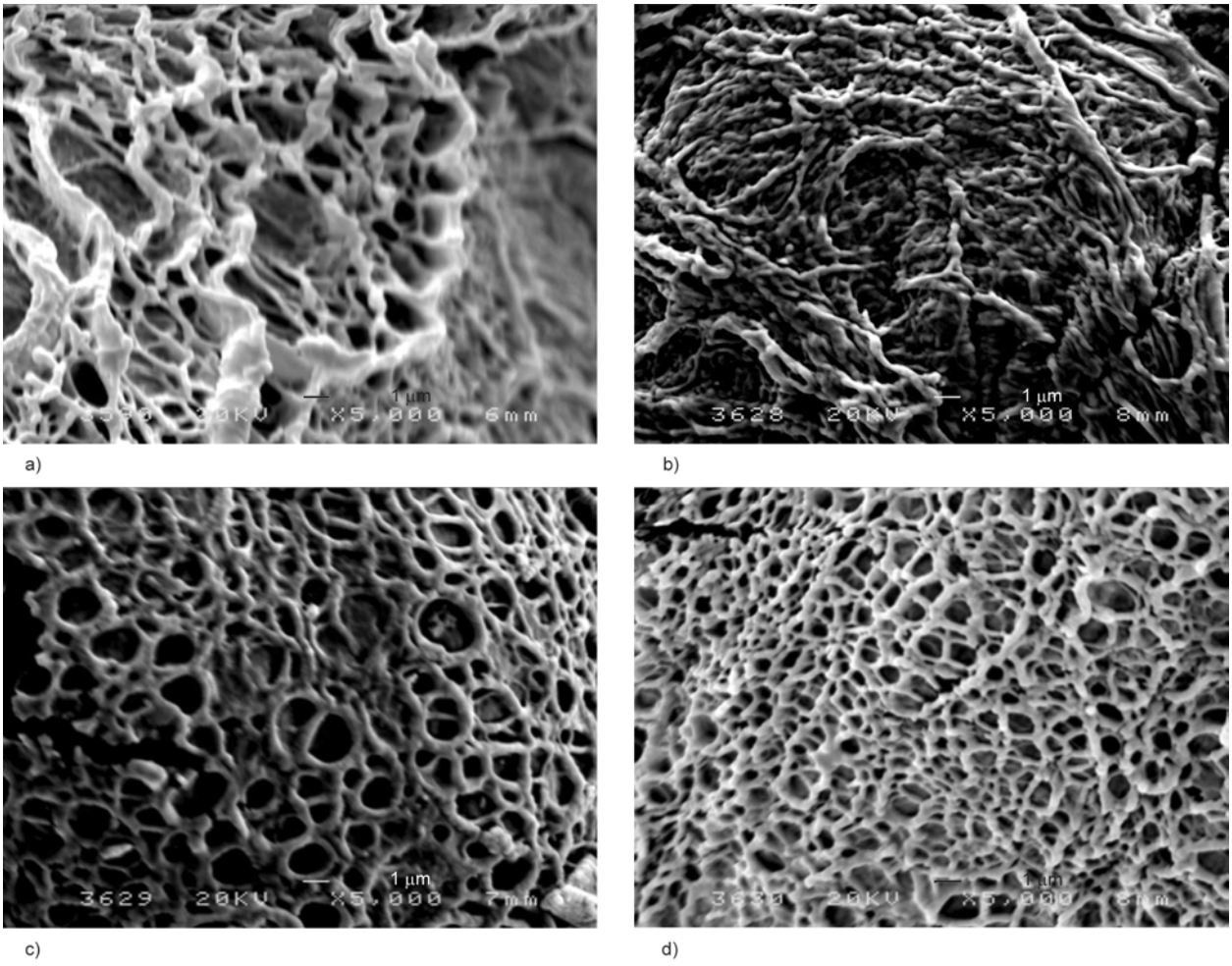


**Figure 1.** Micrographs of pure PVA hydrogel and PVA/PVP hydrogels prepared with various polymerization degree of PVA. (a) Pure PVA1750 hydrogel, (b) PVA1750/PVP hydrogel, (c) PVA2099/PVP hydrogel, (d) PVA2399/PVP hydrogel.

**Table 1.** Porosity, crystallinity, water content, and friction coefficient of PVA/PVP hydrogels

| Sample | Porosity [%] | Crystallinity [%] | Water content [%] | Friction coefficient |
|---|---|---|---|---|
| Pure PVA1750 | 79.39±5.52 | 35.1±1.2 | 81.3±1.5 | 0.261 |
| PVA1750/PVP | 72.69±4.63 | 36.2±1.8 | 84.6±1.2 | 0.193 |
| PVA2099/PVP | 65.32±5.21 | 28.1±1.7 | 82.2±1.0 | 0.182 |
| PVA2399/PVP | 56.76±3.68 | 21.5±2.1 | 80.8±0.7 | 0.139 |

which may break the symmetry and regularity of the polymer chains, and the resulting denser structure limits the activities of polymer chains, and then the crystallinity of the hydrogel decreases significantly ($p < 0.05$).

### 3.3. Water content

The values of water content of different PVA hydrogels are summarized in Table 1. It is shown that the addition of PVP into PVA hydrogel resulted in the increase of water content of the pure hydrogel, because the amide group on PVP showed stronger hydrophilicity than the hydroxyl group on PVA [21]. The polymerization degree of PVA showed a significant influence on water content of hydrogels. The water content decreased significantly ($p < 0.05$) with the increasing polymerization degree attributed to the denser network structure, which left less space for water molecules to inhabit.

### 3.4. Compressive mechanical properties

#### 3.4.1. Unconfined uniaxial compression tests

As shown in Figure 2, the unconfined uniaxial compressive properties of PVA/PVP hydrogels were found to be significantly influenced by strain level, which demonstrated the typically nonlinear and viscoelastic behavior. The addition of PVP enhanced the mechanical property of pure PVA hydrogel. The tangent modulus significantly increased with the increasing polymerization degree of PVA. But the differences of the tangent modulus value between PVA1750/PVP and PVA2099/PVP hydrogels were not significant when the strain level was below 30%. The compressive tangent modulus increased about tenfold from 30 to 60% strain. At low strain level, the hydrogels exhibited small tangent modulus and were prone to deformation, so that the pressure presented on the materials could be uniformly distributed by the enlarged contact area. While at high strain level, the larger tangent modulus of the materials led to the ability to withstand larger stress and resist the deformation. These are consistent with the important functions of natural cartilage to support and distribute large mechanical loads [47]. The compressive tangent modulus shows strong dependence on strain rate (Figure 2b). For each hydrogel formulation, the high strain rate resulted in a significant increase of the tangent modulus at the same strain level. It is because the interstitial water had no time to migrate out from the pores under large strain rate, resulting in higher instantaneous pressurization to sustain higher stress, and hence the compressive tangent modulus at the same strain level increased.

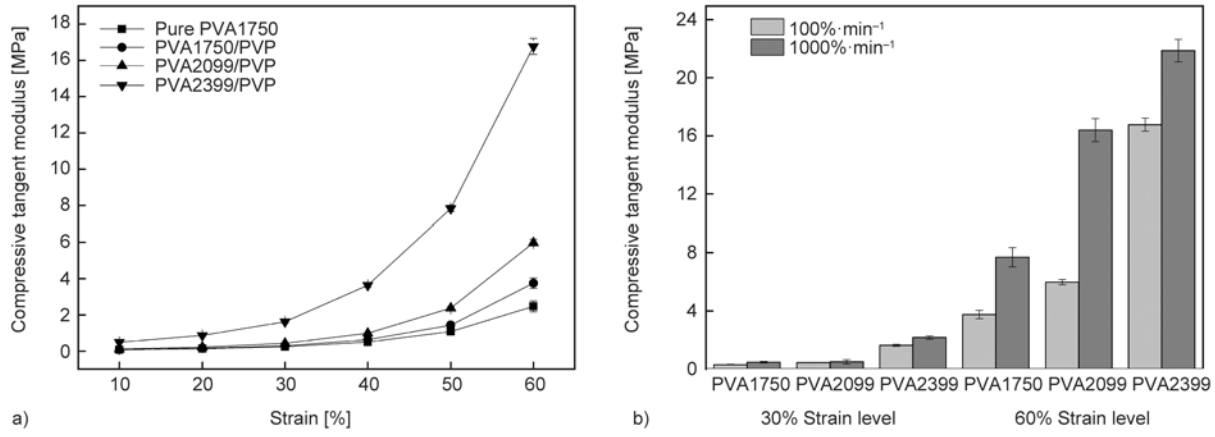


**Figure 2.** Effects of (a) strain magnitude (100%·min$^{-1}$) and (b) the strain rate on the compressive tangent modulus of various hydrogel formulations

### 3.4.2. Indentation creep test

Figure 3 demonstrates the indentation creep properties of various PVA/PVP hydrogel formulations. It was found that under constant compressive stress, the deformation rate of all hydrogel samples rapidly increased at first, and then became slow with time, and it may infer from the deformation-time curves that the deformation would reach equilibrium state eventually. The incorporate of PVP and higher polymerization degree of PVA resulted in less deformation of the hydrogels due to the resulting increased compressive modulus ($p < 0.05$). In the end of the test, the deformation of pure PVA1750, PVA1750/PVP, PVA2099/PVP and PVA2399/PVP hydrogel samples were 0.4897±0.021, 0.435±0.016, 0.403±0.011 and 0.358±0.012mm, respectively.

### 3.5. Viscoelastic behavior

Figure 4 displays the shear storage modulus ($G'$) and loss modulus ($G''$) as a function of frequency for each hydrogel tested. It can be seen that for all hydrogel formulations, $G'$ was always much higher than $G''$ over the whole frequency range, which was a characteristic feature of a 'strong' hydrogel [48]. $G'$ values of all hydrogel samples increased slowly with the increasing test frequency, implying the hydrogels maintain a strong network structure [49]. The similar tendency of $G''$ varying with the frequency was found, but $G''$ showed weak dependency of frequency.

Storage modulus ($G'$) is a good measure of material stiffness [50], the larger $G'$ reflects the larger strength of the material [51, 52]. Figure 4a showed that the incorporation of PVP increased the $G'$ much when compared with pure PVA hydrogels. With the increase of polymerization degree of PVA, the values of $G'$ increased significantly due to the increasing crosslinking density. The results indicate that hydrogels incorporated with PVP and prepared with larger polymerization degree have larger mechanical strength compared to the pure PVA hydrogels, which is consistent with the results obtained in unconfined compression tests. $G''$ increased with the increase of polymerization degree, indicating the increasing of viscosity.

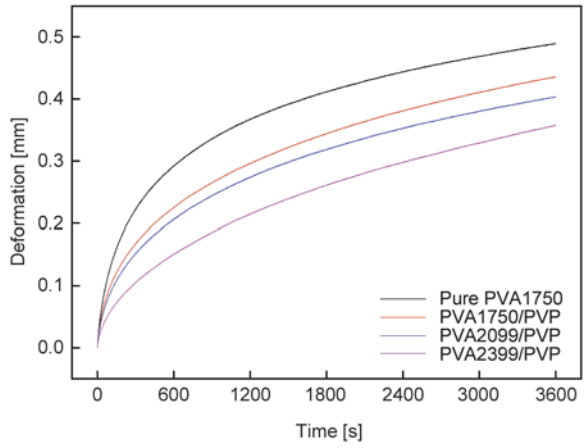


**Figure 3.** Effect of polymerization degree of PVA on indentation creep characteristics of PVA/PVP hydrogels

### 3.6. Compressive fatigue properties

The compressive fatigue tests of PVA/PVP hydrogels were carried out with a sinusoidal compressive loading mode from 200 to 800 N for up to 50, 000 cycles at 5 Hz, and the height of hydrogels changed constantly with the sinusoidal compressive loads. The amount of deformation of different hydrogel formulations during a single loading cycle at the initial, medium and later stage of fatigue tests are summarized in Table 2. It demonstrates that the amount of deformation during a single cycle decreased gradually with loading cycles. Hydrogels prepared with

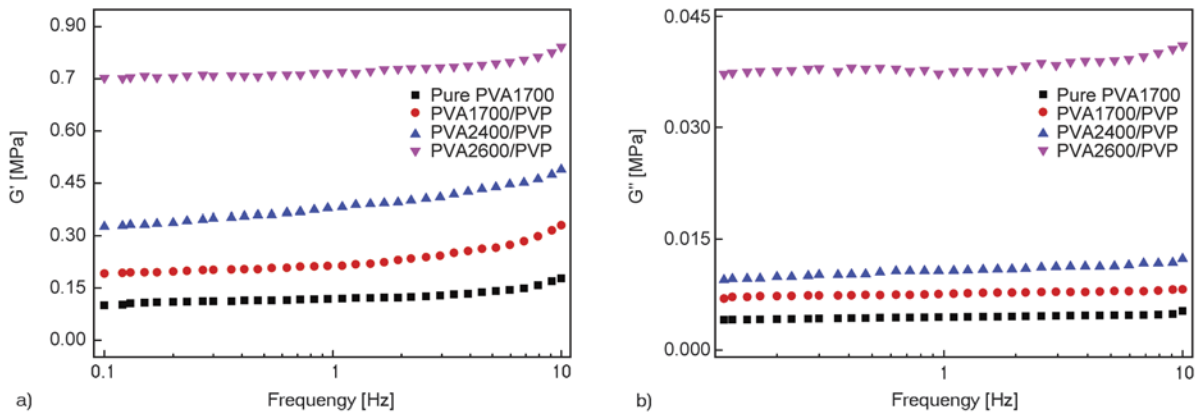


**Figure 4.** (a) Storage and (b) loss modulus of the hydrogels as function of frequency

**Table 2.** The amount of deformation under load during a single loading cycle for PVA/PVP hydrogels at various fatigue test stage

| Samples | $D_I$ [mm] | $D_M$ [mm] | $D_L$ [mm] |
|---|---|---|---|
| PVA1750/PVP | 0.194±0.007 | 0.138±0.004 | 0.083±0.003 |
| PVA2099/PVP | 0.235±0.011 | 0.189±0.009 | 0.124±0.012 |
| PVA2399/PVP | 0.339±0.019 | 0.297±0.015 | 0.201±0.009 |

*$D_I$ – the amount of deformation at the initial stage (1750 cycle),
$D_M$ – the amount of deformation at the medium stage (25 000 cycle),
$D_L$ – the amount of deformation at the later stage (50 000 cycle).

higher polymerization degree showed larger deformation during the same loading cycle. All the pure PVA hydrogels samples failed after 34 000 cycles, so the relevant experimental data were not given here.

The change in normalized deformation of hydrogels under 200 N with fatigue cycles is given in Figure 5. The deformation increased rapidly at first, and then increased slowly as function of loading cycles, implying a tendence toward the stability. And the final deformation was smaller for hydrogels prepared with higher polymerization degree ($p < 0.05$). The normalized deformation of the three hydrogels after fatigue were 29.3±1.2, 27.0±0.9, and 24.9±0.6%,

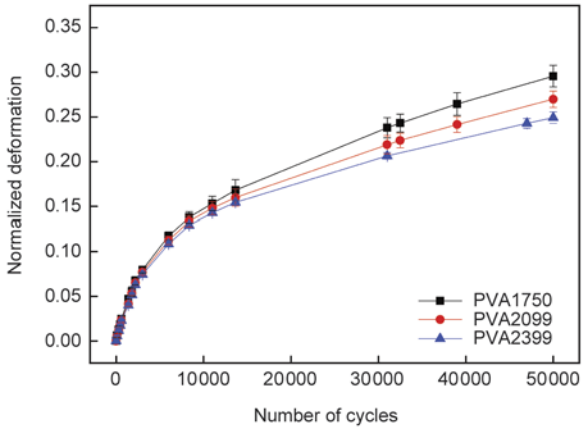


**Figure 5.** The normalized deformation of various hydrogel formulations as function of fatigue cycles under the load of 200 N

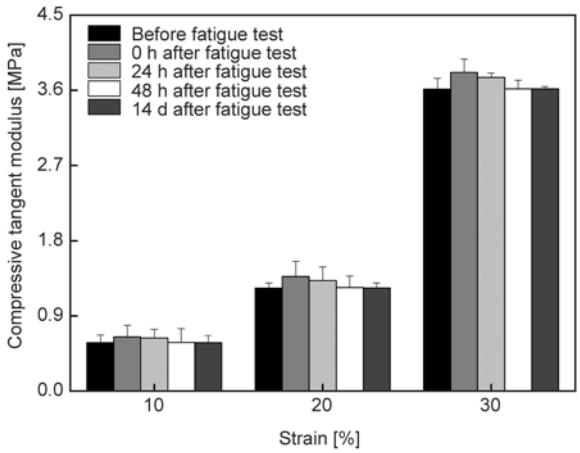


**Figure 6.** The compressive modulus at 10, 20 and 30% strain before fatigue and after fatigue test (PVA1750/PVP)

respectively, with the increase of polymerization degree.

The values of compressive tangent modulus of PVA/PVP hydrogels were calculated at 10, 20 and 30% strain before fatigue test and 0, 24, 48 h, and 14 days after test. After subjected to 50 000 fatigue cycles, as clearly shown in Figure 6, the tangent modulus of PVA1750/PVP hydrogels showed a significant increase, and then the modulus was recovered to the level before fatigue for 48 h, regardless of the strain level. Table 3 summaries the compressive tangent modulus of the three hydrogel formulations before and 48 h after fatigue test. The differences between the compressive tangent modulus measured pro-fatigue and post-fatigue were very small for each formulation at each strain level, indicating good recovery capacity for the mechanical property of hydrogels that subjected to 50 000 fatigue cycles.

Figure 7 describes the change of normalized height and mass with time for PVA/PVP hydrogels after fatigue tests. All the hydrogel samples that had been subjected to 50 000 fatigue cycles showed large deformation and mass loss. And it is obvious that

**Table 3.** Summary of the compressive modulus of PVA/PVP hydrogels fabricated with various polymerization degree of PVA before fatigue and 48 h after fatigue tests

| Samples | $\varepsilon_{10\%}$ [MPa] | $\varepsilon_{20\%}$ [MPa] | $\varepsilon_{30\%}$ [MPa] |
|---|---|---|---|
| PVA1750 (before fatigues) | 0.583±0.006 | 1.235±0.012 | 3.612±0.019 |
| PVA1750 (after fatigues) | 0.588±0.011 | 1.242±0.020 | 3.618±0.017 |
| PVA2099 (before fatigues) | 0.654±0.004 | 1.457±0.007 | 5.183±0.013 |
| PVA2099 (after fatigues) | 0.659±0.017 | 1.458±0.015 | 5.185±0.012 |
| PVA2399 (before fatigues) | 0.752±0.014 | 1.982±0.018 | 5.813±0.018 |
| PVA2399 (after fatigues) | 0.765±0.016 | 1.983±0.021 | 5.815±0.020 |

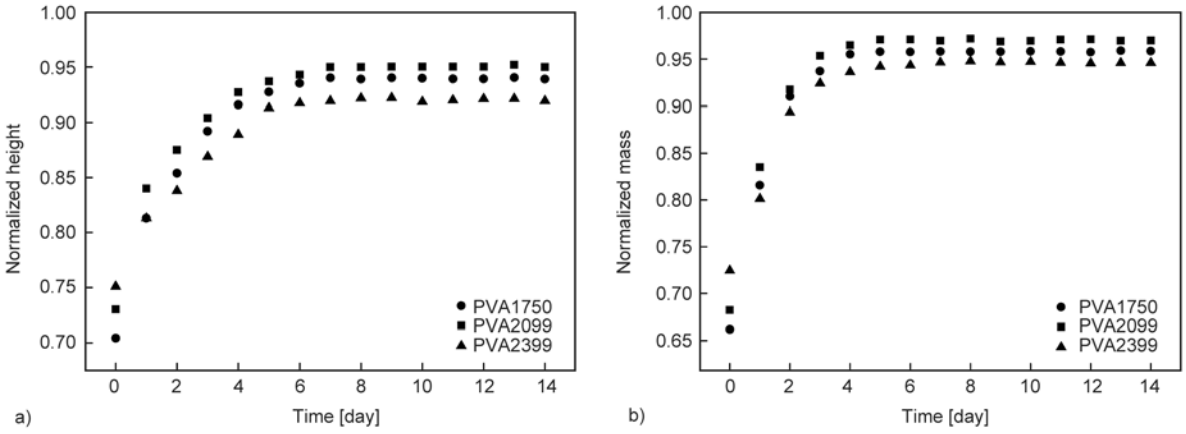


**Figure 7.** The change of normalized (a) height and (b) mass over time for various PVA/PVP hydrogel formulations after fatigue tests

both height and mass of each hydrogel formulation recovered rapidly within the first 2 days of unrestrained recovery in PBS solution, followed by a slow recovery rate, and then reached a plateau value within one week. It is notable that though both height and mass finally recovered to more than 90% of their initial values, they could not reach to their original state completely. It is shown from Figure 7 that hydrogels prepared with low polymerization degree experienced more deformation and mass loss during fatigues, but showed better recovery capacity after fatigues than hydrogels fabricated with high polymerization degree.

### 3.7. Friction property

Figure 8 gives the friction coefficient evolution over time during sliding. It is shown that the friction coefficient of PVA/PVP hydrogels was low at the initial stage, and then the friction coefficient increased gradually as time prolonging and tended to stable. The three-dimensional porous biphasic structure of hydrogels accounted for this. When the applied normal load was applied to the hydrogel, most of the load was supported by the fluid phase, leading to the relatively low friction coefficient. As the time going, more interstitial water within the porous structure of hydrogels was squeezed out away the contact area, while there was insufficient time for the non-contact area to rehydration. Thus the proportion of load supported by the solid phase was continuously increased, which enlarged the solid-to-solid contact and increased the friction coefficient, and then reached to a relatively stable level [23, 53]. As shown in Figure 8, the friction coefficient of the pure PVA hydrogel increased rapidly, and the samples were worn out within 800 s. After blended with PVP, the hydrogel was kept relatively low level of friction during the entire friction tests, which was due to the higher hydrophilcity of PVP and the resulting improved lubricity. The friction coefficient of hydrogels decreased with the increasing polymerization degree, as the hydrogel prepared with high polymerization degree showed better load-bearing capacity and then less contact area during sliding.

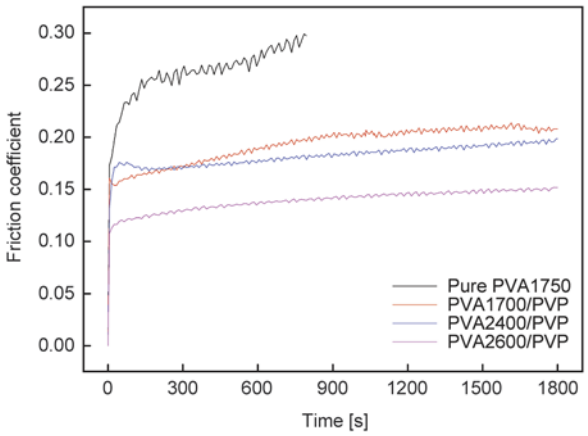


**Figure 8.** Friction coefficient evolution of pure PVA and PVA/PVP hydrogels during sliding

## 4. Discussion

During daily activities, the synovial joint is routinely subjected to static as well as dynamic loads. Dynamic loading, which causes intra-tissue fluid flow and dynamic tissue deformation, can stimulate the synthesis of matrix molecular at certain amplitudes and frequencies [54], but can also lead to cartilage failure [39]. Researchers always investigated the fatigue behavior of cartilage replacements by

using the dynamic loading with strain controlled, and the strain was limited to 15%. In general, 15% strain corresponds to a very small load for hydrogels, and this load would far less than the physiological load that the cartilage is subjected, which is of several times body weight. 15% strain is very close to the linear elastic region of hydrogels, so it is expected that the hydrogel would not be failure for even a very long term loading cycles. In addition, the reports about the recovery behavior of cartilage prosthesis after fatigue test under large load are few. So in the present study, we were interested in characterizing the compressive fatigue behavior of PVA/PVP hydrogels as cartilage prosthesis under dynamic loading from 200 to 800 N for up to 50 000 cycles at 5 Hz and their recovery behavior after fatigue failure.

PVA/PVP hydrogels show the creep phenomenon under static loading for a period of time, called the static creep here. The consecutive sinusoidal loading for up to 50 000 cycles at 5 Hz could have produced creep effects as well [55], defined as the dynamic creep. The same tendency of deformation varying with time (or the cycles) was found in both static and dynamic creep (Figure 3 and 6). The rapid deformation at first is attributed to the fast effusion of interstitial water from the loading zone. The extrusion rate of the water decreased with time, and the slow motion of molecular chains was dragged by large internal friction [56], resulting in the decreased deformation rate. The deformation would reach to a stable level eventually. This deformation tendency with time under load is similar to the natural articular cartilage [57]. The deformation of the natural cartilage tissue could achieve a cyclic steady state faster than under a static load [58, 59]. However, there seems to be a contradiction between the experimental results and the expectation in the present study. That is primarily because the differences between the local deformation resulting from the indentation creep with a spherical indenter and the block deformation caused by the compression plate. The creep rate of cartilage was dependent on its permeability [60], and its equilibrium time of creep was demonstrated to be approximately 60 min [57]. While the deformation of both static and dynamic creep for PVA/PVP hydrogels was increasing during the entire testing time, instead of reaching an equilibrium value. The thicker sample delays the equilibrium time of creep may account for this [61].

Considering the movement of the interstitial water during the sinusoidal loading can lead to an explanation of the recovery behavior during fatigue. Figure 9 provides a visual picture for the microstructural change of a PVA/PVP hydrogel sample during a single sinusoidal loading cycle. During loading phase, the polymer network deforms, and the interstitial water migrated from the loaded region to the unloaded region due to the pressure gradient caused by the differences between the applied stress and the hydrogel swelling pressure (Figure 9b to 9c). While during the uploading phase, the flow direction of interstitial water changed to the reverse direction, resulting in the re-swelling of the hydrogel; but the flow was driven under the action of a much lower pressure gradient, because the swelling pressure, which would govern the recovery rate, was far lower than the stress resulting from the loads acting. So it was impossible for the hydrogel sample to fully recover during such a very short period of time (0.1 s), that is, $h'_{200}$ was less than $h_{200}$. This result is consistent with Maroudas's predictions [62]. Barker and Seedhom [63] has demonstrated that the contact between the flat-ended indenter and the natural cartilage, even under a small tare load of about 0.014 MPa, has almost blocked the path of the fluid being imbibed by the cartilage matrix during the recovery phase of the loading cycle. In the present experiment, the large normal load was maintained on the hydrogel surface throughout the test, which significantly decreased the permeability of the hydrogel surface. As a result, the fluid path was further restricted, and the recovery was greatly restrained during the loading cycle.

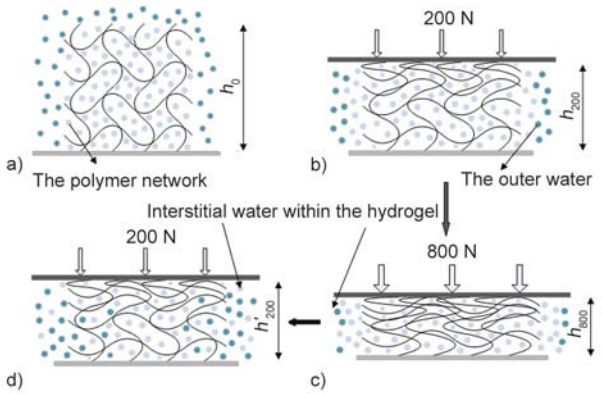


**Figure 9.** The diagrams of microstructure of PVA/PVP hydrogel during a single loading cycle. (a) represents the unloaded hydrogel. (b), (c) and (d) denote the state of hydrogels loaded from 200 to 800 N, and then unloaded to 200 N, respectively.

After unrestrained recovery in fresh PBS solution after fatigue test, there was no change in compressive tangent modulus of samples before and after fatigue tests for 48 h after fatigue tests, indicating intact and structurally unchanged for the hydrogel samples. Height and mass of hydrogels presented greater recovery at the first 2 days, after that the recovery of all hydrogel formulations reached a plateau value gradually. Both height and mass finally recovered to more than 90% of their initial values. That is the permanent deformation, due to the creep effect caused by the cumulative fatigue, prevented the complete recovery of the tested hydrogel. In the present experiment it was observed that hydrogel prepared with lower polymerization degree of PVA showed faster recovery rate and less permanent deformation than the one prepared with higher polymerization degree. Under the same loading condition, hydrogels with lower polymerization degree is subjected to larger strains, and the swelling pressure during the recovery phase after fatigue test must be higher than that of hydrogels with higher polymerization degree. The less porosity and the lower permeability resulting from the denser network structure also account for the slower recovery of hydrogel with higher polymerization degree. Hydrogel prepared with higher polymerization degree shows larger permanent deformation, it is attributed to the excessive viscous losses (Figure 4b).

In the present study, PVA/PVP hydrogel sustains dynamic compressive load from 200 to 800 N for up to 50 000 cycles with structurally unchanged, and shows good recovery capacity after fatigue test, indicating its potential to be used as articular cartilage prosthesis. More detailed studies are still needed in the following researches, including longer fatigue cycles, multiple fatigue recovery. Combining the micro-properties with the bulk mechanical properties via techniques such as nanoindentation to explore the fatigue failure mechanism of hydrogels in depth is also another important research direction. The compressive fatigue properties of the natural articular cartilage would be evaluated and then make comparisons with that of replacement materials for better material design.

## 5. Conclusions

In this study, PVA/PVP hydrogel were synthesized by a repeated freezing-thawing method. The incorporation of PVP into PVA hydrogel stabilized its mechanical property and improves the lubricity. Higher compressive modulus was observed for hydrogel prepared with higher polymerization degree, and the friction coefficient decreased with the increase of polymerization degree. In order to explore the compressive fatigue properties of PVA/PVP hydrogels as cartilage prosthesis, the hydrogel samples were subjected to cyclic compressive loading from 200 to 800 N at 5 Hz for up to 50 000 cycles, and their recovery behavior after fatigue test was evaluated. The result showed that the height of the hydrogel rapidly decreased at first and gradually became stable with loading cycles. After unrestrained recovery in fresh PBS solution after fatigue test, the compressive tangent modulus recovered to its original level within 48 h, but the geometry of samples could not regain their original state completely due to the creep effects. Hydrogels prepared with lower polymerization degree of PVA showed better recovery capacity from cyclic loading.

## Acknowledgements

This project is supported by the National Natural Science Foundation of China (Grant nos. 11172142 and 51575278), and the Priority Academic Program Development of Jiangsu Higher Education Institutions (PAPD).

## References

[1] Schulz R. M., Bader A.: Cartilage tissue engineering and bioreactor systems for the cultivation and stimulation of chondrocytes. European Biophysics Journal, **36**, 539–568 (2007). DOI: 10.1007/s00249-007-0139-1

[2] Rawal B. R., Ribeiro R., Chouksey M., Tripathi K.: Biomaterials for cartilage repair: A review. Journal of Medical Sciences, **13**, 615–620 (2013). DOI: 10.3923/jms.2013.615.620

[3] Peretti G. M., Pozzi A., Ballis R., Deponti D., Pellacci F.: Current surgical options for articular cartilage repair. Advances in Minimally Invasive Surgery and Therapy for Spine and Nerves, **108**, 213–219 (2011). DOI: 10.1007/978-3-211-99370-5_33

[4] Hoffman A. S.: Hydrogels for biomedical applications. Advanced Drug Delivery Reviews, **54**, 3–12 (2002). DOI: 10.1016/S0169-409X(01)00239-3

[5] Peppas N. A., Hilt J. Z., Khademhosseini A., Langer R.: Hydrogels in biology and medicine: From molecular principles to bionanotechnology. Advanced Materials, **18**, 1345–1360 (2006). DOI: 10.1002/adma.200501612

[6] Gonzalez J. S., Alvarez V. A.: Mechanical properties of polyvinylalcohol/hydroxyapatite cryogel as potential artificial cartilage. Journal of the Mechanical Behavior of Biomedical Materials, **34**, 47–56 (2014). DOI: 10.1016/j.jmbbm.2014.01.019

[7] Spiller K. L., Maher S. A., Lowman A. M.: Hydrogels for the repair of articular cartilage defects. Tissue Engineering Part B, **17**, 281–299 (2011). DOI: 10.1089/ten.teb.2011.0077

[8] Toh W. S., Lee E. H., Guo X-M., Chan J. K., Yeow C. H., Choo A. B., Cao T.: Cartilage repair using hyaluronan hydrogel-encapsulated human embryonic stem cell-derived chondrogenic cells. Biomaterials, **31**, 6968–6980 (2010). DOI: 10.1016/j.biomaterials.2010.05.064

[9] Lee C. R., Grodzinsky A. J., Spector M.: The effects of cross-linking of collagen-glycosaminoglycan scaffolds on compressive stiffness, chondrocyte-mediated contraction, proliferation and biosynthesis. Biomaterials, **22**, 3145–3154 (2001). DOI: 10.1016/S0142-9612(01)00067-9

[10] Hao T., Wen N., Cao J-K., Wang H-B., Lü S-H., Liu T., Lin Q-X., Duan C-M., Wang C-Y.: The support of matrix accumulation and the promotion of sheep articular cartilage defects repair *in vivo* by chitosan hydrogels. Osteoarthritis and Cartilage, **18**, 257–265 (2010). DOI: 10.1016/j.joca.2009.08.007

[11] Ho S. T., Cool S. M., Hui J. H., Hutmacher D. W.: The influence of fibrin based hydrogels on the chondrogenic differentiation of human bone marrow stromal cells. Biomaterials, **31**, 38–47 (2010). DOI: 10.1016/j.biomaterials.2009.09.021

[12] Bray J. C., Merrill E. W.: Poly(vinyl alcohol) hydrogels for synthetic articular cartilage material. Journal of Biomedical Materials Research, **7**, 431–443 (1973). DOI: 10.1002/jbm.820070506

[13] Hassan C. M., Peppas N. A.: Structure and applications of poly(vinyl alcohol) hydrogels produced by conventional crosslinking or by freezing/thawing methods. Advances in Polymer Science, **153**, 37-65 (2000). DOI: 10.1007/3-540-46414-X_2

[14] Bryant S. J., Arthur J. A., Anseth K. S.: Incorporation of tissue-specific molecules alters chondrocyte metabolism and gene expression in photocrosslinked hydrogels. Acta Biomaterialia, **1**, 243–252 (2005). DOI: 10.1016/j.actbio.2004.11.003

[15] Cho J. H., Kim S-H., Park K. D., Jung M. C., Yang W. I., Han S. W., Noh J. Y., Lee J. W.: Chondrogenic differentiation of human mesenchymal stem cells using a thermosensitive poly(*N*-isopropylacrylamide) and water-soluble chitosan copolymer. Biomaterials, **25**, 5743–5751 (2004). DOI: 10.1016/j.biomaterials.2004.01.051

[16] Gong J. P., Katsuyama Y., Kurokawa T., Osada Y.: Double-network hydrogels with extremely high mechanical strength. Advanced Materials, **15**, 1155–1158 (2003). DOI: 10.1002/adma.200304907

[17] Stammen J. A., Williams S., Ku D. N., Guldberg R. E.: Mechanical properties of a novel PVA hydrogel in shear and unconfined compression. Biomaterials, **22**, 799–806 (2001). DOI: 10.1016/S0142-9612(00)00242-8

[18] Baker M. I., Walsh S. P., Schwartz Z., Boyan B. D.: A review of polyvinyl alcohol and its uses in cartilage and orthopedic applications. Journal of Biomedical Materials Research Part B: Applied Biomaterials, **100**, 1451–1457 (2012). DOI: 10.1002/jbm.b.32694

[19] Pan Y-S., Xiong D-S., Ma R-Y.: Preparation and swelling behavior of polyvinyl alcohol physiological saline gel. Journal of Central South University of Technology, **13**, 27–31 (2006). DOI: 10.1007/s11771-006-0101-x

[20] Xie L., Jiang M., Dong X., Bai X., Tong J., Zhou J.: Controlled mechanical and swelling properties of poly (vinyl alcohol)/sodium alginate blend hydrogels prepared by freeze–thaw followed by $Ca^{2+}$ crosslinking. Journal of Applied Polymer Science, **124**, 823–831 (2012). DOI: 10.1002/app.35083

[21] Ma R., Xiong D., Miao F., Zhang J., Peng Y.: Novel PVP/PVA hydrogels for articular cartilage replacement. Materials Science and Engineering: C, **29**, 1979–1983 (2009). DOI: 10.1016/j.msec.2009.03.010

[22] Zhang L., Wang Z. P., Xu C., Li Y., Gao J. P., Wang W., Liu Y.: High strength graphene oxide/polyvinyl alcohol composite hydrogels. Journal of Materials Chemistry, **21**, 10399-10406 (2011). DOI: 10.1039/C0JM04043F

[23] Shi Y., Xiong D.: Microstructure and friction properties of PVA/PVP hydrogels for articular cartilage repair as function of polymerization degree and polymer concentration. Wear, **305**, 280–285 (2013). DOI: 10.1016/j.wear.2012.12.020

[24] Dunn A. C., Sawyer W. G., Angelini T. E.: Gemini interfaces in aqueous lubrication with hydrogels. Tribology Letters, **54**, 59–66 (2014). DOI: 10.1007/s11249-014-0308-1

[25] Chen K., Zhang D., Wang S.: Start-up friction properties of poly(vinyl alcohol)/nano-hydroxyapatite/silk composite hydrogel. Materials Express, **3**, 265–272 (2013). DOI: 10.1166/mex.2013.1127

[26] Tadavarthy S. M., Moller J. H., Amplatz K.: Polyvinyl alcohol (Ivalon) – A new embolic material. The American Journal of Roentgenology, Radium Therapy, and Nuclear Medicine, **125**, 609–616 (1975).

[27] Mallapragada S. K., Peppas N. A.: Dissolution mechanism of semicrystalline poly(vinyl alcohol) in water. Journal of Polymer Science Part B: Polymer Physics, **34**, 1339–1346 (1996). DOI: 10.1002/(SICI)1099-0488(199605)34:7<1339::AID-POLB15>3.0.CO;2-B

[28] Maolin Z., Hongfei H., Yoshii F., Makuuchi K.: Effect of kappa-carrageenan on the properties of poly(*N*-vinyl pyrrolidone)/kappa-carrageenan blend hydrogel synthesized by γ-radiation technology. Radiation Physics and Chemistry, **57**, 459–464 (2000).
DOI: 10.1016/S0969-806X(99)00415-6

[29] Wagner D. H.: Nanocomposites: Paving the way to stronger materials. Nature Nanotechnology, **2**, 742–744 (2007).
DOI: 10.1038/nnano.2007.401

[30] Abd El-Mohdy H. L., Ghanem S.: Biodegradability, antimicrobial activity and properties of PVA/PVP hydrogels prepared by γ-irradiation. Journal of Polymer Research, **16**, 1–10 (2009).
DOI: 10.1007/s10965-008-9196-0

[31] Leone G., Consumi M., Greco G., Bonechi C., Lamponi S., Rossi C., Magnani A.: A PVA/PVP hydrogel for human lens substitution: Synthesis, rheological characterization, and *in vitro* biocompatibility. Journal of Biomedical Materials Research Part B: Applied Biomaterials, **97**, 278–288 (2011).
DOI: 10.1002/jbm.b.31813

[32] Thomas J., Lowman A., Marcolongo M.: Novel associated hydrogels for nucleus pulposus replacement. Journal of Biomedical Materials Research Part A, **67**, 1329–1337 (2003).
DOI: 10.1002/jbm.a.10119

[33] Bellucci G., Seedhom B. B.: Mechanical behaviour of articular cartilage under tensile cyclic load. Rheumatology, **40**, 1337–1345 (2001).
DOI: 10.1093/rheumatology/40.12.1337

[34] Sakai N., Hagihara Y., Furusawa T., Hosoda N., Sawae Y., Murakami T.: Analysis of biphasic lubrication of articular cartilage loaded by cylindrical indenter. Tribology International, **46**, 225–236 (2012).
DOI: 10.1016/j.triboint.2011.03.016

[35] Mauck R. L., Seyhan S. L., Ateshian G. A., Hung C. T.: Influence of seeding density and dynamic deformational loading on the developing structure/function relationships of chondrocyte-seeded agarose hydrogels. Annals of Biomedical Engineering, **30**, 1046–1056 (2002).
DOI: 10.1114/1.1512676

[36] Bryant S. J., Chowdhury T. T., Lee D. A., Bader D. L., Anseth K. S.: Crosslinking density influences chondrocyte metabolism in dynamically loaded photocrosslinked poly(ethylene glycol) hydrogels. Annals of Biomedical Engineering, **32**, 407–417 (2004).
DOI: 10.1023/B:ABME.0000017535.00602.ca

[37] Huang A. H., Farrell M. J., Kim M., Mauck R. L.: Long-term dynamic loading improves the mechanical properties of chondrogenic mesenchymal stem cell-laden hydrogels. European Cells and Materials, **19**, 72–85 (2010).

[38] Mauck R. L., Soltz M. A., Wang C. B., Wong D. D., Chao P-H. G., Valhmu W. B., Hung C. T., Ateshian G. A.: Functional tissue engineering of articular cartilage through dynamic loading of chondrocyte-seeded agarose gels. Journal of Biomechanical Engineering, **122**, 252–260 (2000).
DOI: 10.1115/1.429656

[39] Weightman B. O., Freeman M. A. R., Swanson S. A. V.: Fatigue of articular cartilage. Nature, **244**, 303–304 (1973).
DOI: 10.1038/244303a0

[40] Weightman B.: Tensile fatigue of human articular cartilage. Journal of Biomechanics, **9**, 193–200 (1976).
DOI: 10.1016/0021-9290(76)90004-X

[41] Vikingsson L., Gómez-Tejedor J. A., Ferrer G. G., Gómez Ribelles J. L.: An experimental fatigue study of a porous scaffold for the regeneration of articular cartilage. Journal of Biomechanics, **48**, 1310–1317 (2015).
DOI: 10.1016/j.jbiomech.2015.02.013

[42] Vikingsson L., Ferrer G. G., Gómez-Tejedor J. A., Ribelles J. L.: An '*in vitro*' experimental model to predict the mechanical behavior of macroporous scaffolds implanted in articular cartilage. Journal of the Mechanical Behavior of Biomedical Materials, **32**, 125–131 (2014).
DOI: 10.1016/j.jmbbm.2013.12.024

[43] Peppas N. A., Merrill E. W.: Differential scanning calorimetry of crystallized PVA hydrogels. Journal of Applied Polymer Science, **20**, 1457–1465 (1976).
DOI: 10.1002/app.1976.070200604

[44] Pan Y., Xiong D.: Study on compressive mechanical properties of nanohydroxyapatite reinforced poly(vinyl alcohol) gel composites as biomaterial. Journal of Materials Science: Materials in Medicine, **20**, 1291–1297 (2009).
DOI: 10.1007/s10856-008-3679-8

[45] Clark J. M.: Variation of collagen fiber alignment in a joint surface: A scanning electron microscope study of the tibial plateau in dog, rabbit, and man. Journal of Orthopaedic Research, **9**, 246–257 (1991).
DOI: 10.1002/jor.1100090213

[46] Holloway J. L., Lowman A. M., Palmese G. R.: The role of crystallization and phase separation in the formation of physically cross-linked PVA hydrogels. Soft Matter, **9**, 826–833 (2013).
DOI: 10.1039/c2sm26763b

[47] McNary S. M., Athanasiou K. A., Reddi A. H.: Engineering lubrication in articular cartilage. Tissue Engineering Part B: Reviews, **18**, 88–100 (2012).
DOI: 10.1089/ten.teb.2011.0394

[48] Calvet D., Wong J. Y., Giasson S.: Rheological monitoring of polyacrylamide gelation: Importance of cross-link density and temperature. Macromolecules, **37**, 7762–7771 (2004).
DOI: 10.1021/ma049072r

[49] Michailova V., Titeva S., Kotsilkova R., Krusteva E., Minkov E.: Influence of aqueous medium on viscoelastic properties of carboxymethylcellulose sodium, hydroxypropyimethyl cellulose, and thermally pregelatinized starch gels. Colloids and Surfaces A: Physicochemical and Engineering Aspects, **149**, 515–520 (1999).
DOI: 10.1016/S0927-7757(98)00608-6

[50] Ricciardi R., Gaillet C., Ducouret G., Lafuma F., Lauprêtre F.: Investigation of the relationships between the chain organization and rheological properties of atactic poly(vinyl alcohol) hydrogels. Polymer, **44**, 3375–3380 (2003).
DOI: 10.1016/S0032-3861(03)00246-5

[51] Sosnik A., Sefton M. V.: Semi-synthetic collagen/poloxamine matrices for tissue engineering. Biomaterials, **26**, 7425–7435 (2005).
DOI: 10.1016/j.biomaterials.2005.05.086

[52] Haines L. A., Rajagopal K., Ozbas B., Salick D. A., Pochan D. J., Schneider J. P.: Light-activated hydrogel formation via the triggered folding and self-assembly of a designed peptide. Journal of the American Chemical Society, **127**, 17025–17029 (2005).
DOI: 10.1021/ja054719o

[53] Katta J., Jin Z., Ingham E., Fisher J.: Effect of nominal stress on the long term friction, deformation and wear of native and glycosaminoglycan deficient articular cartilage. Osteoarthritis and Cartilage, **17**, 662–668 (2009).
DOI: 10.1016/j.joca.2008.10.008

[54] Davisson T., Kunig S., Chen A., Sah R., Ratcliffe A.: Static and dynamic compression modulate matrix metabolism in tissue engineered cartilage. Journal of Orthopaedic Research, **20**, 842–848 (2002).
DOI: 10.1016/S0736-0266(01)00160-7

[55] Joshi A., Fussell G., Thomas J., Hsuan A., Lowman A., Karduna A., Vresilovic E., Marcolongo M.: Functional compressive mechanics of a PVA/PVP nucleus pulposus replacement. Biomaterials, **27**, 176–184 (2006).
DOI: 10.1016/j.biomaterials.2005.06.003

[56] Reynaud B., Quinn T. M.: Tensorial electrokinetics in articular cartilage. Biophysical Journal, **91**, 2349–2355 (2006).
DOI: 10.1529/biophysj.106.082263

[57] Meng W-C., Dong Q-R.: The experiment study on the compression properties of articular cartilage. Journal of Medical Biomechanics, **18**, 28–33 (2003).

[58] Linn F. C.: Lubrication of animal joints. I. The arthrotripsometer. Journal of Bone and Joint Surgery, **49**, 1079–1098 (1967).

[59] Simon W. H.: Scale effects in animal joints. I. Articular cartilage thickness and compressive stress. Arthritis and Rheumatism, **13**, 244–255 (1970).
DOI: 10.1002/art.1780130305

[60] Li L. P., Korhonen R. K., Iivarinen J., Jurvelin J. S., Herzog W.: Fluid pressure driven fibril reinforcement in creep and relaxation tests of articular cartilage. Medical Engineering and Physics, **30**, 182–189 (2008).
DOI: 10.1016/j.medengphy.2007.03.001

[61] Mow V. C., Holmes M. H., Lai W. M.: Fluid transport and mechanical properties of articular cartilage: A review. Journal of Biomechanics, **17**, 377–394 (1984).
DOI: 10.1016/0021-9290(84)90031-9

[62] Maroudas A.: Physico-chemical properties of articular cartilage. Pitman Medical, London (1973).

[63] Barker M. K., Seedhom B. B.: The relationship of the compressive modulus of articular cartilage with its deformation response to cyclic loading: Does cartilage optimize its modulus so as to minimize the strains arising in it due to the prevalent loading regime? Rheumatology, **40**, 274–284 (2001).
DOI: 10.1093/rheumatology/40.3.274

*eXPRESS Polymer Letters Vol.10, No.2 (2016) 139–159*
*Available online at www.expresspolymlett.com*
*DOI: 10.3144/expresspolymlett.2016.14*

# High performance unsaturated polyester based nanocomposites: Effect of vinyl modified nanosilica on mechanical properties

*J. D. Rusmirović*[1*], *K. T. Trifković*[2], *B. Bugarski*[2], *V. B. Pavlović*[3], *J. Džunuzović*[4], *M. Tomić*[5], *A. D. Marinković*[6]

[1]Innovation Center, Faculty of Technology and Metallurgy, University of Belgrade, 11120 Belgrade, Serbia
[2]Faculty of Technology and Metallurgy, Department of Chemical Engineering, University of Belgrade, Karnegijeva 4, 11120 Belgrade, Serbia
[3]Faculty of Agriculture, Department of Mathematics and Physics, University of Belgrade, Nemanjina 6, 11080 Belgrade-Zemun, Serbia
[4]Institute of Chemistry, Technology and Metallurgy (ICTM) – Center of Chemistry, University of Belgrade, Studentski trg 12–16, 11000 Belgrade, Serbia
[5]Faculty of Technology and Metallurgy, Department of General and Inorganic Chemistry, University of Belgrade, Karnegijeva 4, 11120 Belgrade, Serbia
[6]Faculty of Technology and Metallurgy, Department of Organic Chemistry, University of Belgrade, Karnegijeva 4, 11120 Belgrade, Serbia

*Received 22 June 2015; accepted in revised form 19 September 2015*

**Abstract.** Influences of the vinyl modified nanosilica Aerosil® 380, *i.e.*, vinyl and methacryloyl silane coupling agent and linseed oil fatty acids (BD) reactive residues, on the mechanical properties of the unsaturated polyester resins (UPes) based nanocomposites, was studied. The polycondensation of maleic anhydride and products of poly(ethylene terephthalate) (PET) depolymerization with propylene glycol, with and without separation of ethylene glycol, yields UPe1 and UPe2 resin, respectively. The hydroxyl terminated PET depolymerization products (glycolyzates) and UPes were characterized by acid and hydroxyl values, Fourier Transform Infrared (FTIR) and nuclear magneti resonance (NMR) spectroscopies. Transmission electron microscopy (TEM) confirmed that silica nanoparticles formed domains of aggregates in the polymer matrix. An increase from 195 to 247% of stress at break ($\sigma_b$), and from 109 to 131% of impact strength ($\sigma_i$) of UPes based nanocomposites was obtained for 1 wt% addition of vinyl modified silica. Flexural strength ($\sigma_f$) increase from 106 to 156% for both UPes based nanocomposites with 1 wt% addition of BD modified silica. Cross-linking density ($\nu$), storage modulus ($G'$), tanδ and $T_g$ of the nanocomposite were determined from the dynamic mechanical testing and discussed in relation to the structure of silica modification.

***Keywords:*** *nanocomposites, material testing, poly(ethylene terephthalate) recycling, unsaturated polyester resin*

## 1. Introduction

Poly(ethylene terephthalate) (PET), as one of the most used engineering thermoplastic, has wide application in automobile industry, electrics, food packaging, bottle containers and textile industry, causing the increase of the world consumption of PET twice in a period of ten years [1]. The widespread use of PET imposes solution of the plastic waste problem through recycling and reprocessing method classified as primary, secondary, tertiary and quaternary recycling [2]. The products of tertiary PET recycling, especially glycolytic PET depolymerization

*Corresponding author, e-mail: jrusmirovic@tmf.bg.ac.rs

products, can be used as raw materials for production of new ones, such as different oligomers [3, 4], unsaturated polyester and vinyl ester resins [5, 6] and alkyd resins [7, 8].

The increased need for multifunctional materials with improved properties, such as high strength performance, good thermal, mechanical and physical properties, gas barrier, transparency and safety induced the development of various polymer-inorganic nanocomposites for different applications [9, 10]. By incorporation of modified inorganic nanoparticles in polymer matrices, new reinforced materials with integrated polymer matrix functionalities were obtained, such as low weight and easy processing, and unique features of the nanoparticles, such as high surface area and energy [11]. One of the reinforced materials, with a wide range of industrial applications, is unsaturated polyester resin (UPe) loaded with nanofillers such as titanium oxide [12], organo-chemically modified silicone oxide particles [13–15] or inorganic/organic modified multi-walled carbon nanotubes [16]. A significant improvement of mechanical and thermal properties of nanocomposite materials, obtained by the addition of silica in polymer [17–19], is caused by strong interactions between silica nanoparticles and strong filler cross-linking [20]. The main application problem of bare silica is hydrophilic surface which reduces compatibility with polymer matrix causing agglomeration, and thus it is recommended to perform appropriate modification of the silica nanoparticles [21]. A good filler dispersion, stability and compatibility with the polymer matrix can be obtained by chemical surface modification of hydroxyl groups with organosilanes [20, 22], which provides enormous possibility for new functionalities introduction. Kim and White [23] used organosilanes having different aliphatic chain lengths for silica surface chemical treatment. By organo-chemical silica modification, hybrid nanoparticles (spherical brushes) with reduced chains steric crowding were obtained [24]. The strong interaction between reinforcements and the polymer matrix distinguishes the modified silica particles from other nanoparticles [25, 26]. Luo and co-workers [27] have studied the mechanical and thermal properties of the 3-methacryloyloxypropyl trimethoxy silane modified silica nanoparticles reinforced polyurethane (PU) coatings. Their results showed that the mechanical and thermal properties of PU coatings reinforced by modified silica nanoparticles were enhanced remarkably and the tensile strength ($\delta$) and Young's modulus ($E$) of PU films containing 1.5 wt% modified silica were increased up to 64.2 and 2535.9 MPa, respectively [27].

In this work, mechanical properties of hybrid composite materials prepared by using UPes, based on glycolyzates and chemically modified silica nanoparticles with vinyl reactive functionalities: vinyl, methacryloyl and linseed oil fatty acids reactive residues, were investigated. UPe1 and UPe2 were synthesized from hydroxyl functionalized products, obtained by catalytic PET glycolysis with propylene glycol with and without azeotropic removal of ethylene glycol, respectively, and maleic anhydride. The mechanical and dynamic-mechanical properties of the obtained nanocomposites were determined, and obtained results were discussed in relation to properties of used UPes, modified silica content and structural properties and reactivity of vinyl based functionalities introduced at nanosilica surface.

## 2. Experimental section

### 2.1. Materials and sample preparation

#### 2.1.1. Materials

Waste PET, used for unsaturated polyester resin production, was collected from soft beverage bottles. PET bottles were crushed into small pieces (app. 0.5×0.5 cm) and washed with ethanol and dichloromethane to remove impurities and residual adhesives. Propylene glycol (1,2-propanediol) and ethylene glycol were purchased from Riedel-de Haën Seelze-Hannover (Sigma-Aldrich, Darmstadt, Germany). Xylenes (mixture of 1,2-, 1,3- and 1,4-dimethyl-benzene), tetrabutyl titanate (TBT), dichloromethane (DCM), (3-aminopropyl)trimethoxysilane 97% (APTMS), 3-(trimethoxysilyl) propyl methacrylate (TMSPM) and tris(2-methoxyethoxy)(vinyl)silane (TMEVS) were purchased from Fluka (Sigma-Aldrich, Darmstadt, Germany). Styrene, toluene, pyridine, 2-butanone peroxide (methyl ethyl ketone peroxide; MEKP), cobalt octoate (Co-oct), maleic anhydride (MA), hydroquinone (HQ), methanol, absolute ethanol, terephthaloyl dichoride and tetrahydrofuran (THF) were obtained from Sigma-Aldrich (Sigma-Aldrich Darmstadt, Germany). Fumed silica, with trade name Aerosil® 380, was kindly provided by Evonik (Evonik industries, Essen, Germany). Aerosil® 380 is hydrophilic fumed silica with a specific surface area of 380 $m^2/g$.

### 2.1.2. Glycolysis of PET

*a) Classical method*

The classical method for PET glycolysis have recently been described elsewhere [15]. Molar ratio of waste PET and PG used for glycolysis was 1.0:1.5.

*b) Ethylene glycol (EG) removal method*

Following the procedure of classical method for PET glycolysis (2.1.2. a)), new synthesis of PET glycolyzate was done with the succeeding modification by EG azeotropic removal method [15]. Continual monitoring, by the use of gas chromatography method (GC), of the EG/PG content in the bottom layer of Dean-Stark was used for quantification of time-dependent removal of PG. Azeotropically separated PG was compensated by addition appropriate quantity of PG into reaction mixture to maintain approximately 1.0/1.5 PG/PET initial molar ratio according to the calculated extent of reaction. Continual decreases of EG was observed from GC chromatogram, and when no more EG was found (app. 91% extent of reaction), excess of PG was azeotropically removed, placed in a vacuum oven (100 °C/ 2000 Pa) and then the obtained reaction product was hot filtered.

By application of both glycolysis methods, products of various compositions were obtained. In the case 2.1.2. a) glycolyzate consisted of a mixture of PG symmetrical and asymmetrical glycol esters of terephthalic acid: *bis*(2-hydroxylpropyl) terephthalate and *bis*(1-hydroxypropan-2-yl) terephthalate, as well as (2-hydroxyethyl) (2-hydroxypropyl) terephthalate (main component)) and free glycols, EG and PG. Product obtained by method 2.1.2. b) is mainly composed of PG symmetrical and asymmetrical glycol esters of terephthalic acid.

### 2.1.3. Synthesis of EG ester of terephthalic acid – *bis*(2-hydroxyethyl)terephthalic acid

For synthesis of terephthalic acid ester, previously described in detail [15], was used 3.7 g, (0.06 mol) of EG dry solution, 1.58 g, (0.02 mol) of dry pyridine in 50 mL of dry THF and a solution of terephthaloyl dichoride (2.03 g, 0.01 mol) in 50 mL of dry THF.

The *bis*(2-hydroxy propyl)terephthalate was synthesized analogously to *bis*(2-hydroxy-ethyl)terephthalate. The characterization of the obtained products of glycolysis was performed by FTIR, $^{1}$H and $^{13}$C NMR, and elemental analysis [28], and used as standard for HPLC analysis.

### 2.1.4. Synthesis of unsaturated polyesters resin (UPeN) based on PET glycolyzates

*a) UPe1*

After completion of the glycolysis reaction (product obtained by classical method – 2.1.2. a)), keeping inert atmosphere, mixture was cooled down to 90 °C and the Dean-Stark separator was assembled. MA (123 g, 1.25 mol) and half of the required amount of HQ (0.03 g dissolved in 2 mLof ethanol) were charged into glass reactor, whereupon the mixture was heated to 115 °C at constant temperature for 1 h. Afterwards, continuous temperature increase was achieved at a heating rate of 15 °C/h until 150 °C, when the toluene (6 wt%) was added as the agent for azeotropic removal of water. The temperature increase was continued until 210 °C. The reaction was conducted until the acid number value decreased below 30 mg KOH/g, after which the resin obtained was cooled down to 120 °C and a solution of the 0.03 g HQ in 2 mL of methanol was added. After the completion of the reaction, the low boiling compounds were removed from the reaction product by vacuum distillation. The vacuum distillation was carefully applied for 1 hour, and the obtained resin was cooled down to 100 °C and dissolved in styrene (40 wt%) containing equivalent amount of inhibitor.

*b) UPe2*

The synthesis of unsaturated polyester resin (UPe2) from the glycolysis product obtained by ethylene glycol azeotropic removal method was performed in an analogous manner as described in method 2.1.4. a).

### 2.1.5. Synthesis of methyl ester of linseed oil fatty acid (biodiesel – BD)

In a four-necked glass reactor of 2 l, equipped with a reflux condenser, mechanical stirrer, thermometer and dropping funnel, 929 g (3.3 mol) of linseed oil, dissolved in 85 mL of methanol, was added. The potassium hydroxide solution in methanol (0.12 mol of KOH in 102 mL of methanol) was added drop wise. Afterward, the reaction mixture was heated at 58–62 °C for 3 hours, and left to cool down. Bottom layer, *i.e.* mainly raw glycerin, was separated, and upper layer was treated with active charcoal and filtered

through diatomaceous earth. After drying with sodium sulfate, the obtained linseed oil methyl ester (biodiesel) was purified by vacuum distillation under nitrogen. Characteristics of methyl ester of linseed oil fatty acid mixture, named BD: acid value (*AV*) 5 mg KOH/g; ester content 97%; iodine value 152.

### 2.1.6. Chemical modification of Aerosil® 380

Three types of silane coupling agents containing vinyl, methacryloxy and unsaturated fatty acid residues were used for silica functionalization in order to study the influence of silica modification on the mechanical properties of the UPe based nanocomposites. It was proved that modified nanoparticles behave beneficially within polymer matrices in comparison to unmodified ones, *e.g.*, the modified nanoparticles show comparatively better dispersion in polymer, accompanied with covalent bonding, which could significantly improve nanocomposite properties [20, 22]. In order to achieve these goals, modification of Aerosil® 380 was performed by covalent bonding with unsaturated fatty acid residues to silica surface by a two-step method:

*a) First step; modification with (3-aminopropyl)trimethoxysilane*

In a dry three-necked glass reactor, equipped with a magnetic stirrer, reflux condenser, thermometer and a nitrogen inlet tube, 1.0 g of silica (Aerosil® 380) and 120 mL of dry toluene were charged. After dispersion of silica in toluene under ultrasound for 5 min, 3.97 g of (3-aminopropyl)trimethoxysilane was added and the modification reaction was continued for 48 hours at 25 °C under the nitrogen atmosphere. Ultrasonic bath (Bandelin electronic, Berlin, Germany, power 120 W, frequency 35 kHz) was thermostated by circulating water through the jacket, and used for silane modification as well as for preparation of nanocomposite. The modified silica was separated from solution by vacuum filtration, and the filter cake was washed twice with the toluene, and then dispersed in 120 mL of toluene using ultrasonic bath.

*Second step of silica modification with BD*

The modified silica with terminal amino group, from the first step of silica modification, was dispersed in 50 mL THF and 1.56 g of methyl ester of linseed oil fatty acids were charged in a three-necked glass reactor, equipped with a magnetic stirrer, thermometer, reflux condenser and calcium chloride protection tube. The reaction took place for 12 h at 25 °C, whereupon the mixture was heated to 60 °C and maintained for 2 hours. The obtained product, named R380BD, was filtered under the vacuum, two times re-dispersed in THF and filtered, washed with absolute ethanol and dried at 40 °C for 12 h.

*b) Silica modification with 3-(trimethoxysilyl)propyl methacrylate*

The modification of fumed silica nanoparticles with TMSPM was done in an analogues manner to the procedure 2.1.6. a). Obtained product was named R380MA.

*c) Silica modification with tris(2-methoxyethoxy)(vinyl)silane*

In an analogues manner to the procedure 2.1.6. b), the modification of fumed silica nanoparticles with TMEVS was performed. Obtained product was named R380V.

### 2.1.7. Preparation of nanocomposites based on UPeN and chemically modified silica by solution dispersion (blending) method

Nanocomposites based on UPeN and chemically modified silica nanoparticles were prepared using solution blending method. The UPes were used as the polymeric matrix and the modified silica nanoparticles, dispersed in styrene, were used as filler for nanocomposite preparation. The nanocomposites, UPeN/R(n), were obtained by processing of appropriate amounts of binder, UPeN resin, and dispersed nanofillers, modified silica nanoparticles. Index N designates UPe resin (described in exp. 2.1.4.)), index R designates the silica modification (R380BD, R380MA and R380V designates APTMS-BD, TMSPM and TMEVS modification of Aerosil® R380, respectively); index (n) designates the percent of the addition of modified silica nanoparticles: 0.1 (a), 0.5 (b), 1.0 (c) and 2.0 (d) [wt%] in nanocomposites. The homogenization of fumed silica with UPeN (60 wt% in styrene) was achieved by using modified laboratory homogenizer and an ultrasonic bath. The pure UPeN (60 wt% in styrene) and nanocomposites UPeN/R(n) were cured using MEKP (1 wt%) as the initiator and Co-oct (0.5 wt%) as the accelerator. Schematic illustration of the preparation and intermolecular interactions in cross-linked UPeN/R nanocomposites is given in Figure 1.

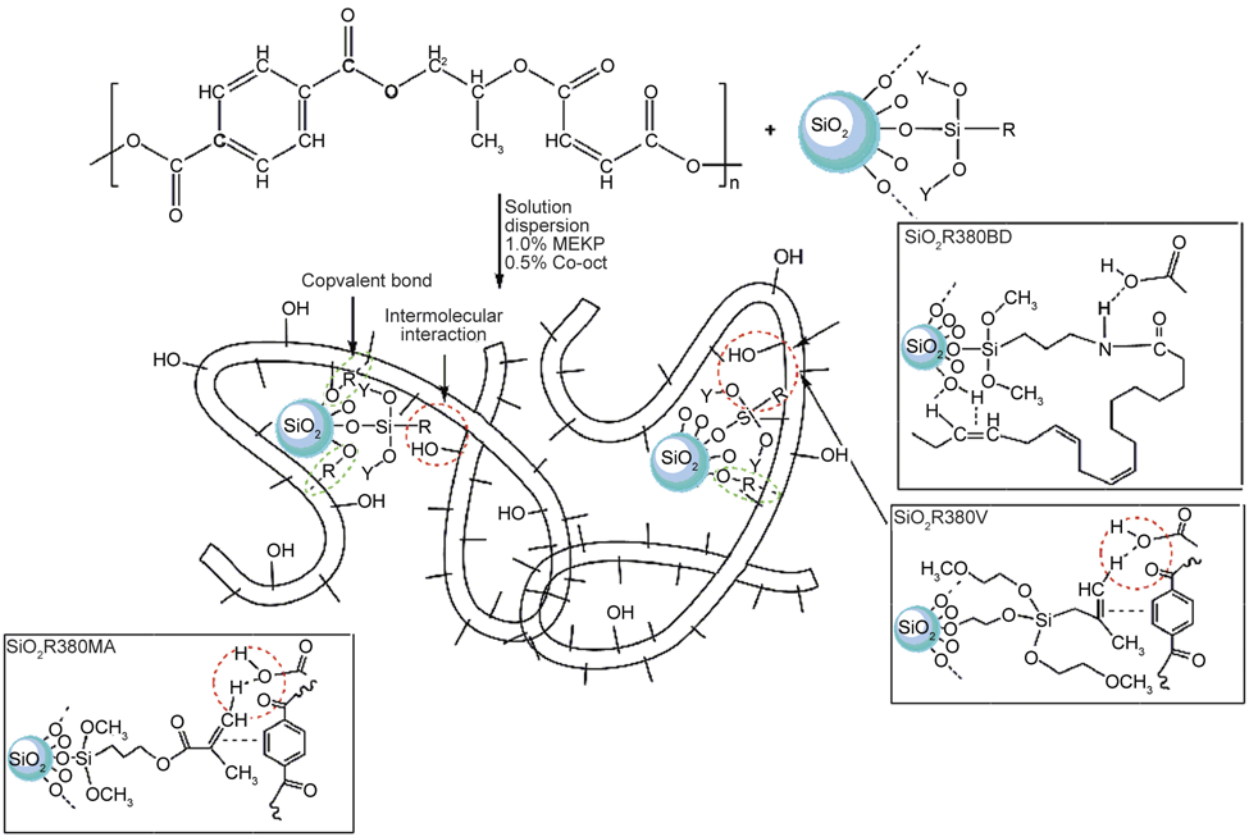


**Figure 1.** Preparation of nanocomposites with proposed reinforcing interactions between modified silica nanofiller and UPe matrix

Hydrophylicity of Aerosil® 380 surface, due to coverage by hydroxyl groups, contributes to the lower silica compatibility with UPe matrix and small reinforcing effect in the nanocomposite. The design of silica surface involved modification with vinyl based silane coupling agents and BD reactive residues, to achieve better nanofiller dispersibility and reinforcement of prepared nanocomposite. Vinyl containing surface moieties provide, in addition to the cross-linking reactivity during curing, compatibility and physical reinforcing due to the existence of different intermolecular interactions: π,π-stacking, dipolar and hydrogen bonding interactions (Figure 1). Also, spatial conformations of the fatty acid residue, due to pronounced flexibility could form spherical wrapped structure stabilized by hydrogen like bonding interactions, and in that way influence availability of ethylene groups to participate in cross-linking reaction during nanocomposite curing.

## 2.2. Experimental techniques

The structural analysis of the obtained glycolyzed product and synthesized polyesters was performed by Fourier transform infrared (FTIR) (Bomem MB-102) spectroscopy, within a range of 400–4000 $cm^{-1}$, at a resolution of 4 $cm^{-1}$. $^{1}H$ and $^{13}C$ nuclear magnetic resonance (NMR) spectra of UPeN were recorded in deuterated chloroform ($CDCl_3$), using a Varian-Gemini 2000 spectrometer at 200 MHz for the $^{1}H$ NMR and 50 MHz for the $^{13}C$ NMR spectra. Varian 3400 gas chromatography with DB5 column and flame ionization detector was used for analysis of EG/PG mixture. Evaluation of the composition of glycolysis products was performed by high performance liquid chromatography using Spectra System P4000, column Zorbax SB-C8 and mobile phase acetonitrile/methanol (60/40) (isocratic mode).

The hydroxyl value (*HV*) was determined using a conventional acetic anhydride/pyridine method (ISO 4326:1992) [29]. The acid value (*AV*) was determined using a standard method ASTM D3644 [30]. Ester value (*EV*) was determined using European quality standard for fatty acid methyl esters E14103 [31]. Number average molecular weight was calculated according to the Equation (1):

$$M_n = \frac{2 \cdot 56100}{AV + HV} \quad (1)$$

Iodine value was determined by the Wijs method. Elemental analyses were performed using a VARIO EL III Elemental analyzer.

The viscosity measurement of the UPeN, 60 wt% styrene solution, was carried out at 25 °C, using Ford viscosity cup 4 (ASTM D1200) [32]. The gel time of the samples was determined from the cure exotherm which was measured according to ASTM D2471-99 [33].

Microstructural (morphological) characterization of the UPeN/R(n) nanocomposites was performed on a transmission electron microscope (TEM) JEM–1400.

Uniaxial tensile measurements of standard cured samples (ASTM D882) [34] were performed using an AG–X plus Universal testing machine, Shimadzu. All tests were performed at room temperature adjusted at crosshead speed of 0.5 mm/min. The flexural properties were measured by the Instron (Model 1332) as per ASTM D 790 [35]. The support span length was set at 45 mm. The testing speed was set at 1.5 mm/min. The impact strength was measured by Karl Frank GMBH Weinheim – Birkenau; Type 5330, Werk – Nr 29680 as per ASTM D 256 [36].

Thermogravimetric analysis (TGA) was performed using a Seteram Setsys Evolution-1750 instrument. The TGA experiments were run in a nitrogen atmosphere (flow rate 25 $cm^3$/min) from 30 to 800 °C, with a heating rate of 10 °C/min.

The mechanical properties and glass transition temperature ($T_g$) of unsaturated polyester composites were obtained using dynamic-mechanical analysis, which was performed on a Discovery Hybrid Rheometer HR2 (TA Instruments). The dynamic-mechanical analysis was conducted in a torsion rectangular mode (dimensions: 6/1/0.2) from 25 to 120 °C at fixed strain amplitude of 0.1% and angular frequency of 1 Hz. The results are presented as mechanical spectra by monitoring the dependence of the storage ($G'$) and loss ($G''$) shear modulus and loss or damping factor $\tan\delta$ ($G''/G'$) on temperature. Differential scanning calorimetric (DSC) measurements were performed using Setaram151 R instrument in the temperature range 30–200 °C.

## 3. Results and discussion

### 3.1. Glycolysis of PET with PG

Various oligoesters (glycolysis products) can be obtained by PET de-polymerization using different glycols like ethylene glycol, diethylene glycol, propylene glycol, polyethylene glycol, 1,4-butanediol, hexylene glycol, *etc*. [37]. Güclü *et al*. [38] have investigated glycolysis of waste PET with PET/EG or PET/ PG molar ratio of 1.0:0.5 to 1.0:3.0 in xylene. They have found that the PET glycolysis in xylene was a multiphase reaction in which formed oligomers transferred from PET/glycol dispersion to xylene medium at elevated temperature. The best glycolysis monomer/dimer ratio was found at 220 °C.

The glycolysis reaction of waste PET with PG was catalyzed with TBT and the hydroxy-terminated products of glycolysis PET were obtained. Table 1 displays *HV*, *AV* values and results of elemental analysis of the glycolyzed products obtained by methods 2.1.2. a) and 2.1.2. b).

The higher oxygen content of the product obtained by method 2.1.2. a), found from elemental analysis and *HV* values (Table 1), confirms that the glycolysis products in the case 2.1.2. a) consisted of the mixture of glycol esters of terephthalic acid: *bis*(2-hydroxylpropyl) terephthalate, (2-hydroxyethyl)(2-hydroxypropyl)terephthalate (main product – 55–60%) and free glycols. Due to the azeotropic removal of excess of PG and liberated EG, product of glycolysis, obtained by method 2.1.2. b), contains mainly *bis*(2-hydroxylpropyl)terephthalate and minor (less than 5%) fraction of (2-hydroxyethyl)(2-hydroxypropyl)terephthalate. These results were evaluated from HPLC analysis of glycolysis products obtained by methods 2.1.2. a) and b). Characterization of the products of glycolysis was essential for understand-

**Table 1.** *HV*, *AV* values and results of elemental analysis of glycolyzed products (PG ester of terephthalic acid)

| Method | $HV^*_{theor.}$ [mg KOH/g] | $HV_{exp.}$ [mg KOH/g] | $AV_{exp.}$ [mg KOH/g] | | %C | %H | %O** |
|---|---|---|---|---|---|---|---|
| 2.1.2. a) | 418 | 302 | 5 | Exp. | 57.85 | 6.16 | 35.98 |
| | | | | Calc. | 58.20 | 6.01 | 35.78 |
| 2.1.2. b) | 397 | 274 | 4 | Exp. | 59.04 | 6.70 | 34.26 |
| | | | | Calc. | 59.57 | 6.43 | 34.00 |

*Theoretical *HV* value was calculated in relation to the theoretical number of hydroxyl groups of PG, recalculated to the molar mass of the product of glycolysis; **Oxygen percent was calculated as subtraction

ing/establishing the structure/properties (reactivity) relationships of the obtained UPeN and nanocomposites.

### 3.2. FTIR analysis of glycolysis product, fumed silica, UPeN and composite materials

The FTIR spectra of the product of PET glycolysis, obtained by method 2.1.2. b), the unmodified and modified fumed silica, and the UPeN (method 2.1.4. a) and b)) are shown in Figure 2a.

The broad peak at about 3382 $cm^{-1}$ and the low intensity peak at 701 $cm^{-1}$ originate from hydroxyl (OH) groups stretching vibrations. Aromatic C–H stretching vibrations are observed at around 2961 $cm^{-1}$. Overlapped symmetric and asymmetric vibrations of methyl ($CH_3$) and methylene ($CH_2$) groups are observed at 2952 and 2854 $cm^{-1}$, while their bending vibrations are observed at about 1452 and 1366 $cm^{-1}$. The band at 1725 $cm^{-1}$ originates from carbonyl (C=O) groups present in ester terephthalic acid. Ester C–O stretching vibrations, asymmetric and symmetric, are observed at about 1360 and 1107 $cm^{-1}$, respectively.

Characteristic adsorption peak for modified and unmodified silica nanoparticles appears at 1099 $cm^{-1}$ and represents the stretching vibration of Si–O–Si bonds (Figure 2a). The OH stretching vibrations are observed at about 3433 $cm^{-1}$ and 1636, 801 and 694 $cm^{-1}$. In the FTIR spectra of different modified silica nanoparticles (methods 2.1.6. a)– c)), the adsorption peaks around 2961, 2923 and 2861 $cm^{-1}$ originate from $CH_3$ and $CH_2$ stretching vibrations, and peaks between 1560 and 1411 $cm^{-1}$ from their bending vibrations, respectively. The bands at around 1748 and 1693 $cm^{-1}$ are due to the C=O functional groups present in the modified silica nanoparticles. The stretching $\nu$(N–H) vibrations are observed at about 800 $cm^{-1}$, and are overlapped with hydroxyl group stretching vibrations (characteristic peak for APTMS modification). The C=C stretching vibrations are observed at around 1366 $cm^{-1}$ (characteristic adsorption peak for TMSPM and TMEVS silica modification).

Qualitative estimations of the differences in the spectra of the UPeN before and after the nanofiller loading indicate the types and intensity of interactions between the matrix (functional groups at polymer chains) and the nanofiller surface functional groups. FTIR spectra of UPeN (Figure 2a) and nanocomposites based on UPeN and modified silica are similar (Figure 2b). The broad band at >3000 $cm^{-1}$ originates from hydroxyl group stretching vibrations. The narrow peaks between 2985 and 2852 $cm^{-1}$ come from $CH_3$ and $CH_2$ stretching vibrations, respectively, and corresponding $CH_3$ and $CH_2$ bending vibrations appeared at 1452 and 1364 $cm^{-1}$ for UPe1 and UPe2. These peaks, for nanocomposites UPeN/R(d), are shifted to higher values (~1455 and ~1384 $cm^{-1}$). The intensive peak at 1721 $cm^{-1}$ is due to the stretching vibration of ester C=O groups present in terephthaloyl moiety, and it is shifted to higher value in UPeN/R(d) (1725 $cm^{-1}$). The bands

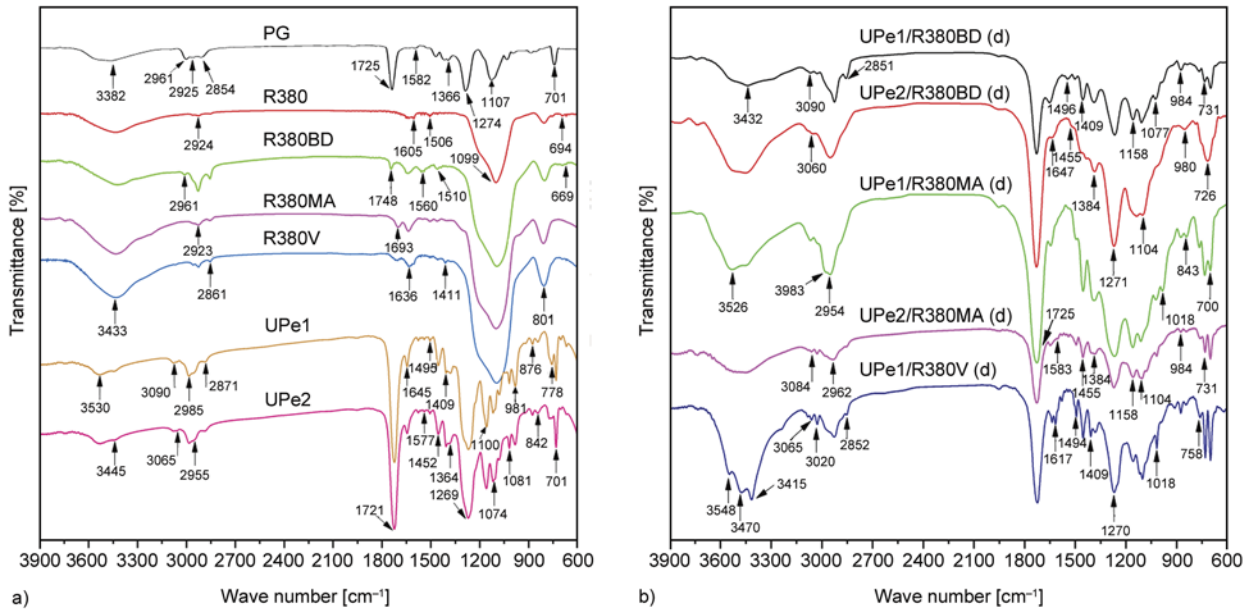


**Figure 2.** FTIR spectra of the glycolyzed product (marked as PG; method 2.1.2. b)), unmodified and modified silica, and UPe resins (a), and UPe1/and UPe2/R(d) nanocomposites (b)

in the region 3090–3020 $cm^{-1}$ correspond to the valence C–H stretching vibrations. Skeletal C=C double bond vibrations observed at 1647–1617 $cm^{-1}$ correspond to the phenyl core. Two narrow adsorption peaks identified at about 731 and 700 $cm^{-1}$ are assigned to the skeletal $\gamma$(CH) vibrations of benzene ring, and these peaks are shifted to higher value for UPeN (778 and 701 $cm^{-1}$). Similar results with smaller differences in FTIR spectra were found for other UPeN nanocomposites at lower nanofiller loading, and that is the reason why these results are not presented in this section.

### 3.3. Thermal properties of silica nanoparticles

The thermal properties of silica nanoparticles were examined by thermogravimetric analysis performed in a nitrogen atmosphere. The TGA and differential thermo-gravimetric (DTG) curves of unmodified Aerosil® 380 (R380) and modified nanosilica R380BD, R380MA and R380V are shown in Figure 3. From the TGA curves (Figure 3a)) it can be seen that the unmodified Aerosil® 380 is stable at temperatures below 800 °C with 1.7% weight loss. Significant difference in thermal stability between bare and modified silica nanoparticles could be observed from TGA and DTG curves.

TGA curves of modified silica nanoparticles are very similar, and the thermal degradation of all samples took place in two stages. The weight loss of all samples, in the range from room temperature to 150 °C, originates mainly from the moisture adsorbed on the surface. The further weight loss in the range 150–230 °C was due to the dehydration/thermal transformation of the surface organic functionalities attached via silanol groups [39]. The weight loss between 390 and 500 °C, observed on TGA curves of R380BD, R380MA and R380V samples, originates from thermal decomposition/condensation of silica surface functionalities. Consequently, two peaks on DTG curves (Figure 3b)) are observed for all tested samples. Peak at 205.1 °C originates from the partial and peak at 449.6 °C corresponds to the complete thermal degradation of modifying agent.

A difference in the weight loss of modified silica nanoparticles originates from the differences in thermal stability/reactivity of the molecular structure at silica surface. The highest weight loss was observed for the R380BD (32.9%) which contains long unsaturated aliphatic chain from linseed oil methyl ester, and structure highly sensitive to thermal treatment.

The TGA profile in the range 200–500 °C is fairly similar for modified silica indicating that weight loss is of low dependence on molecular structure and their thermal degradation process. However, in the range 500–800 °C appropriate influences of structural differences could be observed, mostly arising from the chain length of linseed oil fatty acid and less from structural diversity of methacryloxy and vinyl structure. Degradation/reactivity of unsaturated aliphatic chain is best understood on the basis of the easily abstractable hydrogens present in trienoate structure, resulting in allyl radicals formation, capable for reactivity transfer and formation of condensed structure. Thermal dehydration/transformation at lower temperatures caused formation of

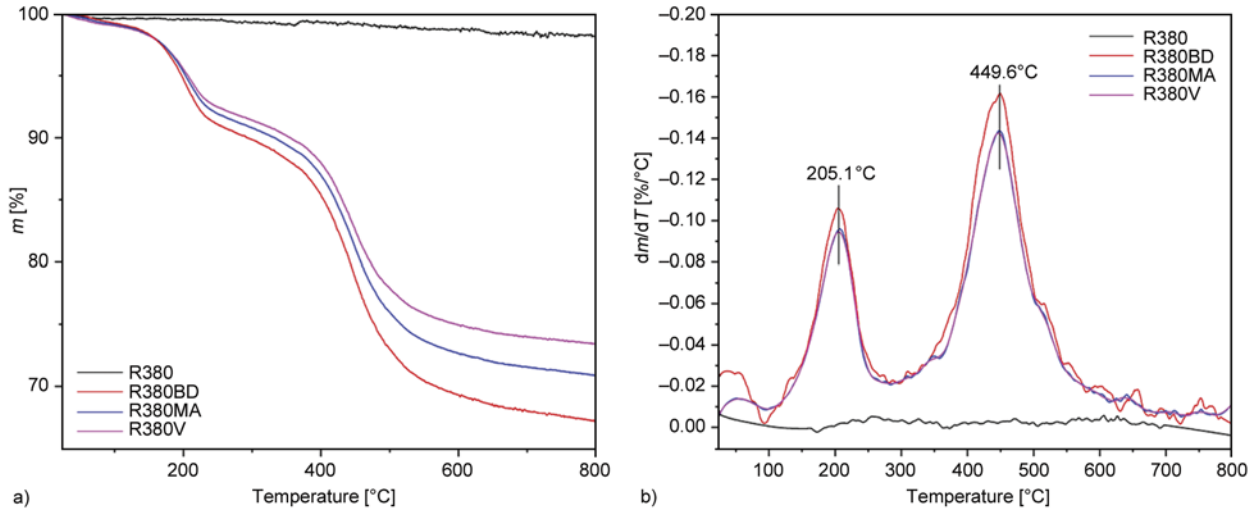


**Figure 3.** TGA (a) and DTG (b) curves of unmodified Aerosil® 380 silica nanoparticles (R380) and modified nanosilica R380BD, R380MA and R380V

stable condensed surface structures which thermally decompose at higher temperatures. On the other hand, the R380MA has a greater weight loss of 29.9% than R380V sample, 26.6%, due to the obvious difference in structure of attached fragment at silica surface.

### 3.4. NMR characterization of UPeN resin

Results of NMR analysis confirm successful synthesis of UPe1 and UPe2 resins, and together with results of $M_n$ calculation (Table 2), indicate that unsaturated polyester resin contains mostly fumaric moiety in polymeric chain, which is necessary prerequisite to achieve high cross-linking reactivity during molding/specimen formation.

Results of $^1H$ and $^{13}C$ NMR analysis (Figure 4) of UPe1 are as follow:

$^1H$ NMR ($CDCl_3$): 1.23–1.51 (*m*, 6H, 2×C$\underline{H}_3$), 4.20–4.58 (*m*, 6H, 2×C$\underline{H}_2$C$\underline{H}$–), 4.25–4.70 (*m*, 4H, –O–C$\underline{H}_2$C$\underline{H}_2$–O–), 5.21–5.79 (*m*, 2H, PhCH=C$\underline{H}_2$, styrene moiety), 6.65–6.79 (*m*, 1H, PhC$\underline{H}$=CH$_2$, styrene moiety), 6.86–6.96 (*m*, 2H, fumaric moiety), 7.43 (*s*, 4H, $H_{Ph}$, styrene moiety), 8.05 (*s*, 4H, $H_{Ph}$-terephthaloyl moiety);

$^{13}C$ NMR ($CDCl_3$): 16.22 and 19.08 (2×C$\underline{H}_3$), 62.7, 66.70–69.21, 70.19–70.30, 76.40–77.63 ($CH_2$ carbons in PG moiety), 113.70 (4×$C_{Ph}$ in styrene moiety), 126.12–128.43 (4×$C_{Ph}$), 134.00 (O=C–H$\underline{C}$=$\underline{C}$H–C=O), 133.57 (2×Ph($\underline{C}$)–COO), 164.08 and 164.39 (O=$\underline{C}$–HC=CH–$\underline{C}$=O), 164.99 and 165.28 (2×Ph$\underline{C}$OO). Similar results were found for UPe2 resin.

From the $^1H$ and $^{13}C$ NMR spectra of the synthesized UPeN resins it can be concluded that the PET glycolysis method has no effect on polycondensation reaction with maleic anhydride, and dominant products were glycol esters of terephthalic acid: *bis*(2-hydroxylpropyl) terephthalate, (2-hydroxyethyl)(2-hydroxypropyl) terephthalate and glycols. From the technical-economical aspect of UPes synthesis based on waste PET/PG glycolysis product, the classical method was selected as better alternative for the industrial level of synthesis due to the technological simplicity of synthesis method, in case when the high mechanical properties are not crucial for the application.

### 3.5. The *AV*, *HV*, $M_n$, iodine value, viscosity, gel time and maximum curing temperature of the synthesized UPeN and UPe2/R(c) nanocomposites

The products obtained by waste PET glycolysis were used for synthesis of UPes. Zahedi *et al*. [40] investigated effects of the reaction time, volume of glycol and catalyst contents on the yield of the glycolysis products and after obtaining a suitable glycolysates, the polyesterification of obtained intermediary products and MA was studied. Also, authors determined the optimal reaction time and temperature for the polyesterification of PET glycolizate with MA.

The *AV*, *HV*, $M_n$, iodine value and viscosity of UPeN are given in Table 2. From these results it could be observed that synthesized UPeN have similar viscosity, *AV*, *HV*, $M_n$, and iodine value and different glycolysis products showed no significant effect on these properties of the obtained resins. Generally, the UPe2, based on the glycolized product obtained by EG azeotropic removal method (2.1.2. b)) contributed to the higher *AV* and *HV*, while opposite is true for $M_n$, iodine value and viscosity of the obtained products.

The gel time values of UPeN and UPe2/R(c) nanocomposites, determined from the cure exotherm, are given in Table 3.

The results from Table 3 indicate that presence of $SiO_2$ nanoparticles had different influence on the gel time and the maximum curing temperature ($T_{max}$) of

**Table 3.** The gel time and maximum curing temperature ($T_{max}$) of the synthesized UPeN and UPe2/R(c) nanocomposites

| Sample | Gel time [min] | $T_{max}$ [°C] |
|---|---|---|
| UPe1 | 19.20 | 145.7 |
| UPe2 | 14.50 | 172.9 |
| UPe2/R380BD(c) | 20.00 | 112.9 |
| UPe2/R380MA(c) | 15.75 | 110.3 |
| UPe2/R380V(c) | 9.50 | 127.7 |

**Table 2.** The *AV*, *HV*, $M_n$, iodine value and viscosity of the synthesized UPeN

| Sample | *AV* [mg KOH/g] | *HV* [mg KOH/g] | $M_n$* [g/mol] | Iodine value | Viscosity [s] |
|---|---|---|---|---|---|
| UPe1 | 13.0 | 29.6 | 2634 | 47 | 105 |
| UPe2 | 13.4 | 30.7 | 2544 | 51 | 90 |

*$M_n$ values were calculated according to the Equation (1).

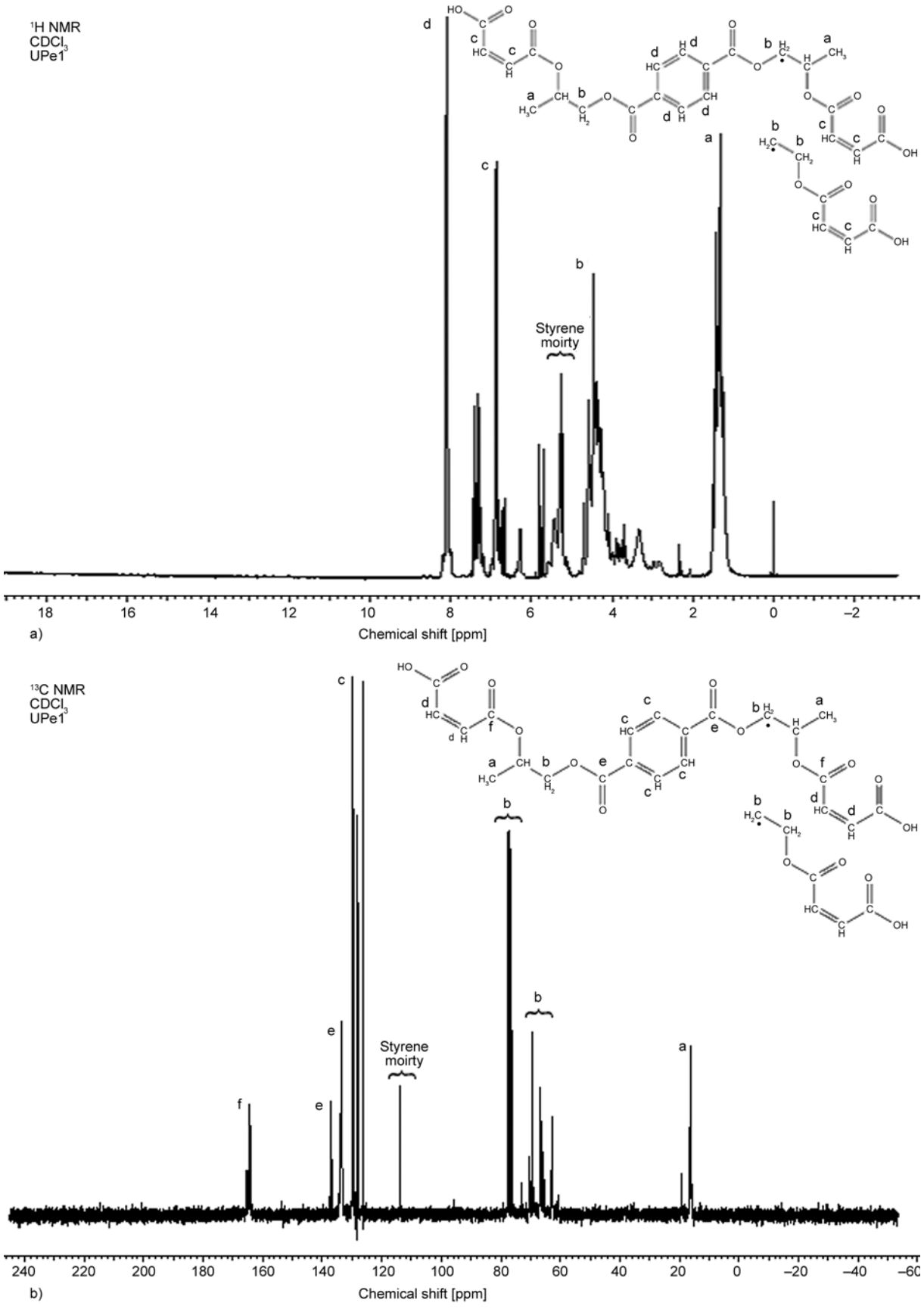


**Figure 4.** $^{1}$H NMR (a) and $^{13}$C NMR (b) spectra of UPe1 obtained according to method 2.1.4. a)

nanocomposite, depending on the type of silica modification. The shorter gel time of UPe2 in comparison to UPe1, 14.50 min *versus* 19.20 min, and higher maximum curing temperature, 172.9 °C *versus* 145.7 °C, indicate higher reactivity of UPe2 resin. The gel time of UPe2/R380BD(c) was increased slightly, 14.50 to 20.00 min, compared to the UPe2, while $T_{max}$ was decreased from 172.9 °C, for UPe2, to 112.9 °C for UPe2/R380BD(c). Silica surface modification with TMSPM and TMEVS caused reduction in the $T_{max}$ from 172.9 to 110.3 °C and 127.7 °C, respectively, while the gel time was shorter than for pure UPe2. Gel time was slightly higher for UPe2/R380MA(c), 15.75 min, and significantly lower value was found for UPe2/R380V(c), 9.50 min.

Incorporation of modified silica nanoparticles in initial UPe polymer matrix influenced cross-linking reaction due to the appropriate contribution of physical interactions and covalent bonding to reactivity/energetic effect of the curing system. Intermolecular interactions between present functionalities at nanofiller surface and polymeric chain segment prevent, to some extent, favorable approach of vinyl moieties (propagation reaction), causing in that way decrease of $T_{max}$. Higher reactivity, *i.e.* mobility of polymeric chain segments in pure UPe, contributes to higher $T_{max}$, while for UPe2 higher $T_{max}$ is also affected by better system compatibility. The long unsaturated chain of methyl esters of linseed oil fatty acid in the APTMS-BD structure provides steric hindrance of reactive vinyl group due to high flexibility, in relation to TMSPM and TMEVS modifiers, causing longer reaction period to reach $T_{max}$. APTMS-BD molecules can be randomly oriented and could therefore obscure the reactive sites, and accordingly require a longer gel time to increase the viscosity of the nanocomposites during cross-linking. TMEVS modifier has shortest alkyl chains with the most reactive vinyl group of limited flexibility, which provides the highest reactivity of UPe2/R380V(c) sample, *i.e.* the shortest gel time was obtained. Appropriate steric repulsion of methyl group present in the TMSPM causes lower accessibility of reacting species to exert reaction with double bond.

### 3.6. TEM analysis of UPe2/R(c) nanocomposite materials

Examination of the influence of the silane coupling agent on the silica dispersion in the UPe matrix of the cured UPe2/R(c) nanocomposites was per-

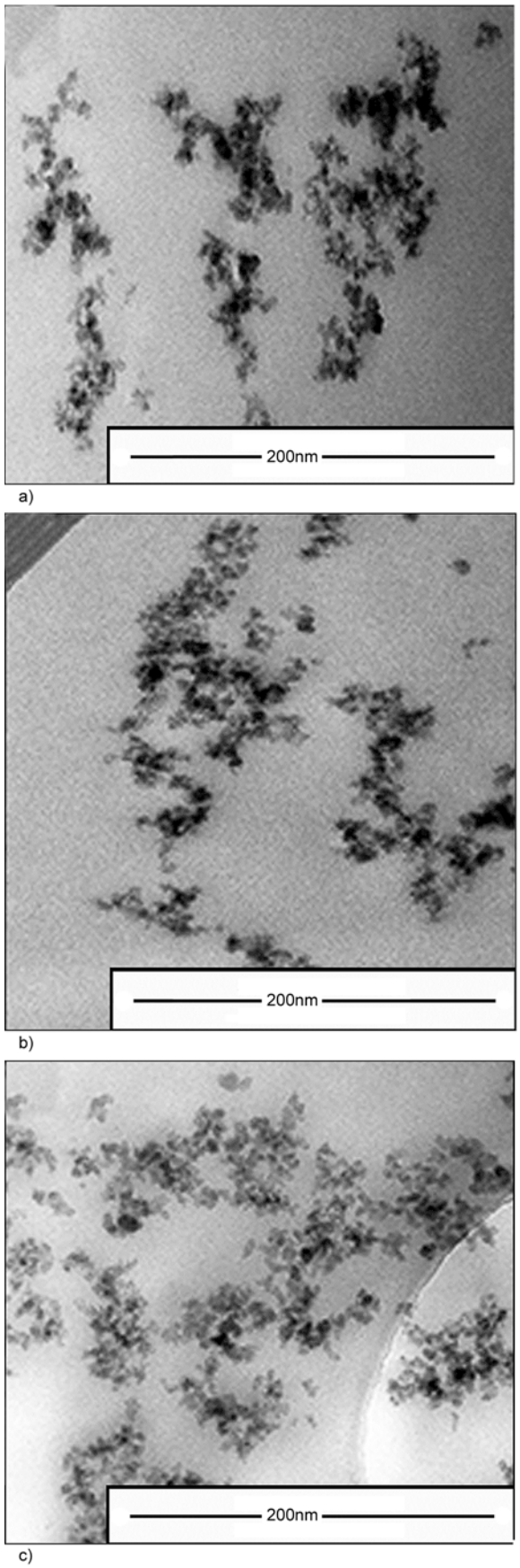


**Figure 5.** TEM micrographs of (a) UPe2/R380BD(c), (b) UPe2/ R380MA(c) and (c) UPe2/R380V(c) nanocomposites

formed by TEM technique. Figure 5 shows TEM micrographs of UPe2/R380BD(c), UPe2/R380MA(c) and UPe2/R380V(c) nanocomposites. From the TEM micrographs of all samples it can be observed that the spherical primary particles of silica nanofiller are to some extent aggregated depending on the properties of silica surface. The primary particles formed irregular chains-like structure with more intensive domain of aggregated nanofiller in UPe2/R380BD(c) nanocomposite (Figure 5a), less in UPe2/R380MA(c) (Figure 5b), and the best dispersion was found for UPe2/R380V(c) nanocomposite (Figure 5c)).

The TEM analysis of samples UPe2/R380BD(c) and UPe2/R380MA(c) (Figure 5a and 5b) shows somewhat lower uniformity of the formed aggregates due to the balanced intermolecular interactions between the nanofiller and the nanofiller/cross-linked polymer. In TEM micrograph of UPe2/R380BD(c) an irregular imperfect three-dimensional network of randomly distributed aggregates of modified silica in the polymer matrix was observed. The presence of long linseed oil fatty acid residue on the silica surface led to weakening of the interfacial interaction, due to the lower physical interaction of unsaturated acid residue/UPe matrix. In a similar study, Ou *et al*. [41] studied effects of alkylation of silica on interfacial interaction, determination, vulcanization swelling procedure, and tensile retraction of modified silica reinforcement of natural, styrene-butadiene and acrylonitrile-butadiene rubber. They have found that the type of the activities of the silica surfaces, methyl, especially hexadecyl alcohol, has influence on the relaxation process weakening interfacial interaction. Analogously, besides to the presence of reactive vinyl groups, the long unsaturated fatty acid chain created spatial barrier between primary spherical nanoparticles and polymeric chain, and the consequence of that was the lowest uniformity of UPe2/R380BD(c). The aggregates found in UPe2/R380BD(c) sample are the largest, indicating that the highest extent of cohesive interaction between nanofiller exists. The TEM analysis of sample UPe2/R380MA(c) showed similar phase dispersion in the cross-linked polymer/nanofiller as in UPe2/R380BD(c). It was caused by moderate repulsive steric interaction of methyl group present in methacryloxy fragment at silica surface. The aggregates observed in sample UPe2/R8380V(c) (Figure 5c) are present in the smallest amount, showing good dispersion of nanoparticles in polymer matrix when TMEVS was used as a modifying agent. Intensive π,π-stacking and different intermolecular interactions at the nanofiller/cross-linked polymeric network interface between terephthaloyl moieties contributed to the better distribution and higher uniformity of the nanofiller (Figure 1). The vinyl group present on silica surface caused the lowest extent of steric interference and the highest reactivity, which provided the highest level of dispersibility. Similar morphological properties were found for other UPeN/R(n) nanocomposites.

### 3.7. Mechanical testing of UPeN based nanocomposites

With the aim to investigate influence of different modification type and content of incorporated silica nanoparticles on the mechanical properties of the synthesized nanocomposites based on UPe, the mechanical testing has been done. The stress-strain curves of the examined cured UPeN and UPeN/R380BD(n) samples are shown in Figure 6, and the values of stress at break ($\sigma_b$), elongation at break ($\varepsilon_b$), and tensile modulus ($E$) are given in Table 4.

Differences in $\sigma_b$ and $\varepsilon_b$ value of pure UPeN are mainly caused by properties of the products of PET glycolysis. Higher stress and elongation at break, found for UPe2, is due to the higher structural homogeneity of cross-linked polymeric network, in comparison to UPe1. PET glycolysis product, obtained by method 2.1.2. b) mainly contains *bis*(2-hydroxypropyl) terephthalate, while the product of glycolysis used in UPe1 synthesis also includes asymmetrical terephthalic ester containing ethylene glycol residue, which contributed to segmental structure of polyester chain. Also, difference in the transfer of reactivity, *i.e.* rate of propagation reaction during cross-linking, could be of appropriate significance.

Results of mechanical testing indicate that $\sigma_b$ and $E$ increase with increasing silica content in nanocomposite samples, while $\varepsilon_b$ is slightly higher for nanocomposite samples than for the pure UPeN. The presence of long BD chain in APTMS-BD on the silica surface, which represents the soft-elastic segment in nanofiller/cross-linked polymer, contributes to higher $\varepsilon_b$ values than for pure UPeN. Also, in accordance with its structure, APTMS-BD can have a plasticizing effect in cross-linking process. With increasing silica content in UPeN/R380BD(a–c)

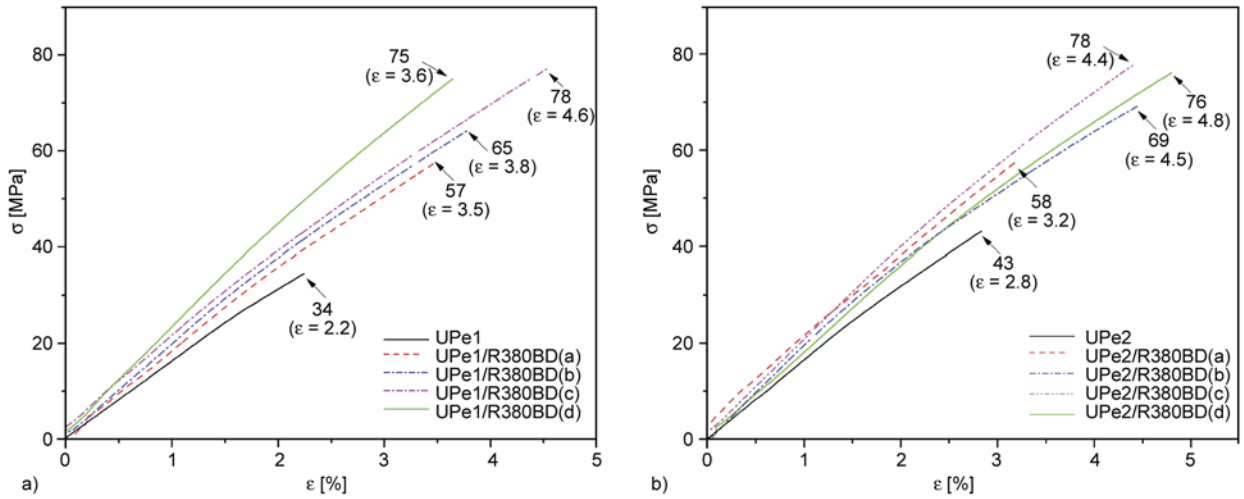


**Figure 6.** The stress-strain curves of the cured (a) UPe1 and UPe1/R380BD(n) and (b) UPe2 and UPe2/R380BD(n) nanocomposites

**Table 4.** Stress at break ($\sigma_b$), elongation at break ($\varepsilon_b$) and tensile modulus ($E$) of cured UPe1/R380BD(n) and UPe2/R380BD(n) nanocomposites

| Sample | $\sigma_b$ [MPa] | $\varepsilon_b$ [%] | $E$ [GPa] | Sample | $\sigma_b$ [MPa] | $\varepsilon_b$ [%] | $E$ [GPa] |
|---|---|---|---|---|---|---|---|
| UPe1 | 34±1.0 | 2.2 | 1.5 | UPe2 | 43±1.4 | 2.8 | 1.8 |
| UPe1/R380BD(a) | 57±1.7 | 3.5 | 2.2 | UPe2/R380BD(a) | 58±1.3 | 3.2 | 2.3 |
| UPe1/R380BD(b) | 65±1.3 | 3.8 | 2.7 | UPe2/R380BD(b) | 69±1.9 | 4.5 | 2.4 |
| UPe1/R380BD(c) | 78±1.9 | 4.6 | 2.9 | UPe2/R380BD(c) | 78±1.7 | 4.4 | 2.2 |
| UPe1/R380BD(d) | 75±1.7 | 3.6 | 1.6 | UPe2/R380BD(d) | 76±1.6 | 4.8 | 1.9 |

nanocomposite samples, prevalence of soft-elastic segments increases, as well as elongation at break. Stress at break increases with increasing silica content, and the highest $\sigma_b$ value have the UPeN/R380BD(c) samples with aggregates formed of spherical APTMS-BD modified silica nanoparticles.

Figure 7 shows stress-strain curves of the cured UPeN and UPeN/R380MA(n) nanocomposites and appropriate values of stress at break, elongation at break and tensile modulus are given in Table 5.

The results of mechanical testing of UPeN/R380MA(n) nanocomposites based on UPeN and TMSPM modified silica show similar trend as UPeN/R380BD(n) samples. With increasing silica content in UPeN/R380MA(a–c) nanocomposites, increase of elongation at break and stress at break was observed.

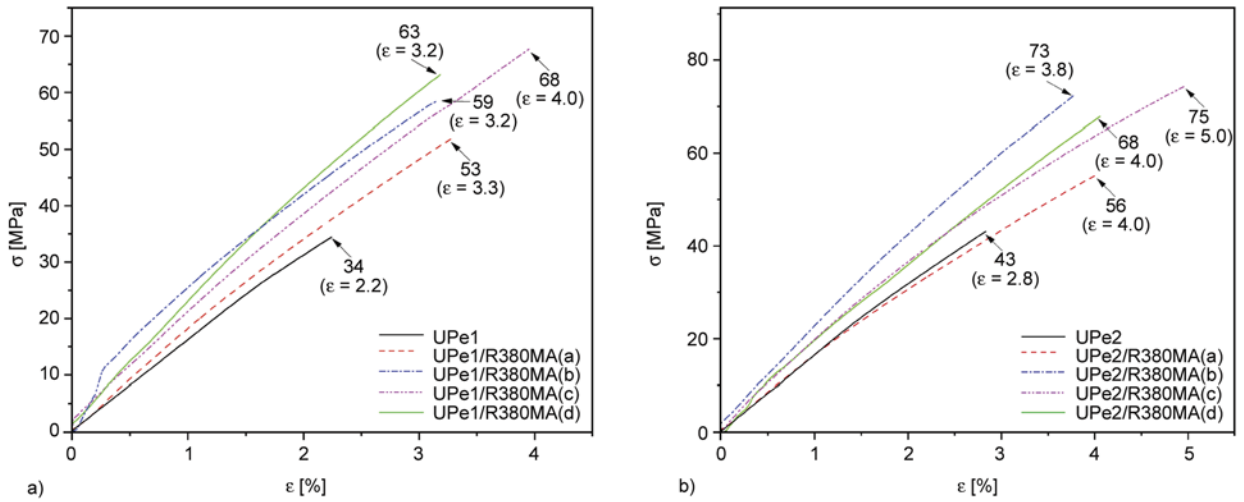


**Figure 7.** The stress-strain curves of the cured (a) UPe1 and UPe1/R380MA(n) and (b) UPe2 and UPe2/R380MA(n) nanocomposites

**Table 5.** Stress at break ($\sigma_b$), elongation at break ($\varepsilon_b$) and tensile modulus ($E$) of cured UPe1/R380MA(n) and UPe2/R380MA(n) nanocomposites

| Sample | $\sigma_b$ [MPa] | $\varepsilon_b$ [%] | $E$ [GPa] | Sample | $\sigma_b$ [MPa] | $\varepsilon_b$ [%] | $E$ [GPa] |
|---|---|---|---|---|---|---|---|
| UPe1/R380MA(a) | 53±1.3 | 3.3 | 1.8 | UPe2/R380MA(a) | 56±1.3 | 4.0 | 1.9 |
| UPe1/R380MA(b) | 59±1.2 | 3.2 | 2.0 | UPe2/R380MA(b) | 73±1.6 | 3.8 | 2.1 |
| UPe1/R380MA(c) | 68±1.7 | 4.0 | 1.9 | UPe2/R380MA(c) | 75±2.0 | 5.0 | 2.0 |
| UPe1/R380MA(d) | 63±1.7 | 3.2 | 2.4 | UPe2/R380MA(d) | 68±1.5 | 4.0 | 2.0 |

The highest stress at break was observed for UPeN/R380MA(c). By incorporation of more than 1.0 wt% of silica nanoparticles in cross-linked polymer/nanofiller, elongation at break and stress at break decrease due to the deterioration of the homogeneity of nanocomposite with the increase of silica addition, *i.e.* phase mixing/dispersing of nanofiller is not satisfactory. Guo *et al*. [42] investigated mechanical properties of polymeric nanocomposites based on TMSPM surface functionalized alumina nanoparticle and vinyl ester resin. They have found that modified alumina nanoparticles formed particle/matrix interfacial bonding, which allowed larger local plastic deformation in the matrix and resulted in significant increase in both modulus and strength, from 2.75 GPa (pure resin) to 3.25 GPa and 52.4 MPa to 63.3 MPa for 1 wt% modified alumina nanoparticles, respectively [42].

Figure 8 shows stress-strain curves of the cured UPe1 and UPe1/R380V(n) nanocomposites and determined values of stress at break, elongation at break and tensile modulus are given in Table 6.

In the case of UPe1/R380V(n) composite materials, the highest values of elongation at break and stress at break with regard to the pure cross-linked UPe1 are recorded. These results are associated with TMEVS configuration. The side chains with 1,2-dimethoxyethyl groups are short and oriented so that they cannot cause steric hindrance and hide the active sites on the modified silica surface. Kanimozhi *et al*. [43] proved vinyl silane functionalized rice husk ash reinforcing effect on unsaturated polyester nanocomposites. They confirmed that the reinforced composites exhibited higher thermal and mechanical properties than neat UPe. Modifiers, APTMS-BD and TMSPM, can occupy twisted conformation, due to the flexibility of unsaturated fatty acid residue, and due to the interaction with surface functional groups by forming closed structure which prevent availability of vinyl active sites (Figure 1).

In order to determine the effect of the organic structure of the surface coupling agent on the flexural and impact strength of the cured UPeN/R(c) composites, the flexural strength and Charpy impact testing was performed. Determined values of impact ($\sigma_i$) and flexural strength ($\sigma_f$) are given in Table 7.

Obtained results indicate that impact and flexural properties increase with 1.0 wt% filler loading for both UPeN based nanocomposites [43]. The impact strength increase from 109 to 131% and from 108 to 113% for UPe1 and UPe2 based nanocomposites, while the flexural strength increase from 108 to 156%

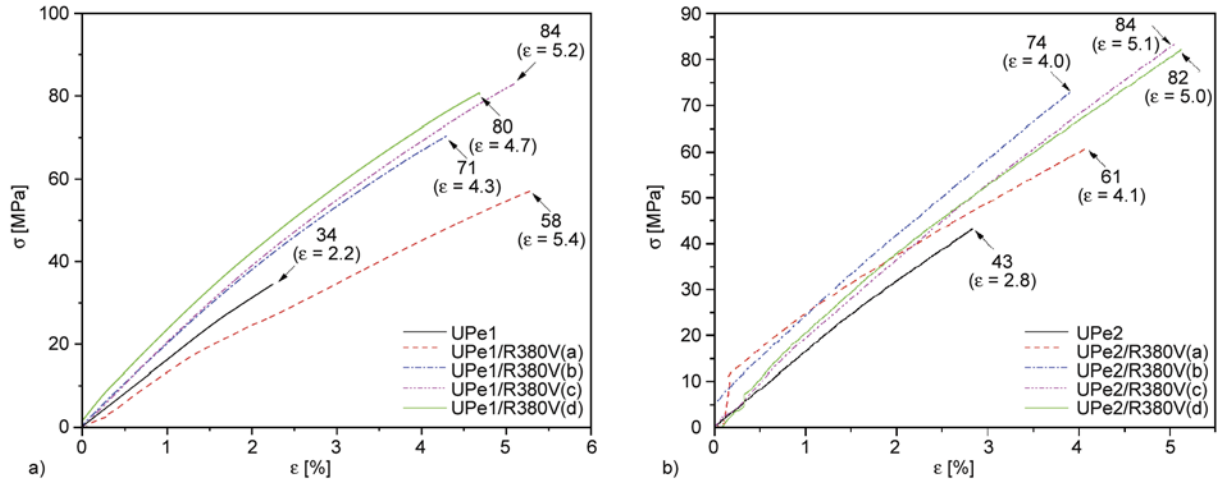


**Figure 8.** The stress-strain curves of the cured (a) UPe1 and UPe1/R380V(n) and (b) UPe2 and UPe2/R380V(n)

**Table 6.** Stress at break ($\sigma_b$), elongation at break ($\varepsilon_b$) and tensile modulus ($E$) of cured UPe1/R380V(n) and UPe2/R380V(n) nanocomposites

| Sample | $\sigma_b$ [MPa] | $\varepsilon_b$ [%] | $E$ [GPa] | Sample | $\sigma_b$ [MPa] | $\varepsilon_b$ [%] | $E$ [GPa] |
|---|---|---|---|---|---|---|---|
| UPe1/R380V(a) | 58±1.3 | 5.4 | 1.7 | UPe2/R380V(a) | 61±1.4 | 4.1 | 1.6 |
| UPe1/R380V(b) | 71±1.5 | 4.3 | 1.7 | UPe2/R380V(b) | 74±1.5 | 4.0 | 1.9 |
| UPe1/R380V(c) | 84±2.0 | 5.2 | 1.9 | UPe2/R380V(c) | 84±1.9 | 5.1 | 1.8 |
| UPe1/R380V(d) | 80±1.9 | 4.7 | 1.6 | UPe2/R380V(d) | 82±1.9 | 5.0 | 1.8 |

**Table 7.** Values of impact and flexural strength of cured UPeN/R(c

| Sample | $\sigma_i$ [J·m$^{-1}$] | $\sigma_f$ [MPa] | Sample | $\sigma_i$ [J·m$^{-1}$] | $\sigma_f$ [MPa] |
|---|---|---|---|---|---|
| UPe1 | 145.6±4.6 | 66.7±1.7 | UPe2 | 109.2±3.4 | 61.7±1.6 |
| UPe1/R380BD(c) | 159.2±4.3 | 103.9±3.0 | UPe2/R380BD(c) | 118.3±3.2 | 81.0±2.4 |
| UPe1/R380MA(c) | 158.6±4.6 | 81.6±2.3 | UPe2/R380MA(c) | 113.7±2.9 | 68.5±1.9 |
| UPe1/R380V(c) | 191.1±6.1 | 72.0±2.3 | UPe2/R380V(c) | 122.8±3.4 | 65.6±1.6 |

and from 106 to 133% for UPe1 and UPe2 based composites, respectively. Lower values of impact and flexural strength of UPe2 based nanocomposites indicate that those materials absorb lower amount of energy and have brittle transition. Also, the highest values of flexural strength of UPeN/R380BD(c) are due to best interfacial adhesion between filler and polymer matrix and indicate that the plasticizing effect of APTMS-BD moiety. The UPe2/R380MA(c) has higher values of $\sigma_f$ than UPe2/R380V(c) [44].

The influence of $SiO_2$ nanofiller content on the stress at break of UPeN/R is shown in Figure 9.

Obtained results, given in Figure 9, indicate that stress at break of all UPeN/R nanocomposites increased with increasing R content up to the 1 wt%, and after that it is constant or slightly decreased. Incorporating of more than 2 wt% of modified silica nanoparticles caused formation of larger aggregates which represent vulnerabilities/weak point in cross-linked polymer-nanofiller composite. The larger diameter of the silica cluster, larger for higher percent of added nanofiller, indicates balanced contribution of both silica/matrix and silica/silica interactions where contribution of later one increases with silica content increase.

It was evident that the content and the type of modification of silica nanoparticles had an appropriate influence on the mechanical properties of the obtained nanocomposites. Modified silica reinforced composites exhibit higher mechanical properties than neat cured UPe matrix due to the hydrophobicity of the silica surface, *i.e.* improved compatibility with UPe matrix, and thus higher reactivity contributes to higher cross-linking density. The stress at break of UPeN/R (Figure 9) reflects influence of vinyl based $SiO_2$ modification on the nanofiller dispersibility (Figure 5), extent of intermolecular interactions (Figure 1) and steric interference to vinyl group reactiv-

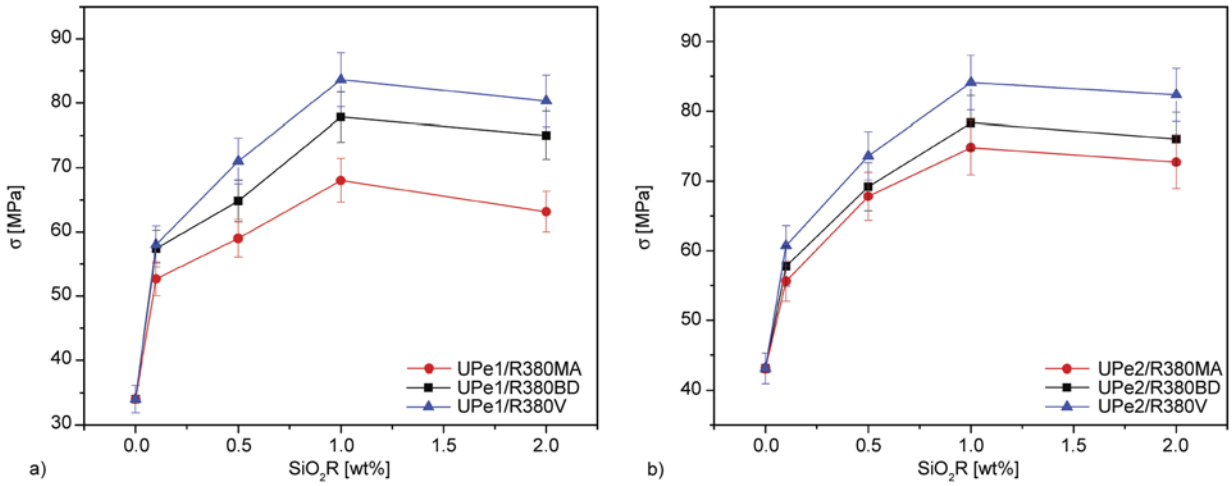


**Figure 9.** The influence of $SiO_2$ nanofiller content on the stress at break of (a) UPe1/R and (b) UPe2/R materials

ity. Lower values of stress at break for R380MA and R380BD are influenced by electronic and steric/conformational effect. The UPeN/R380BD nanocomposites have higher values of $\sigma_b$, compared to UPeN/R380MA, due to the presence of allylic hydrogen and number of ethylenic in flexible structure more likely to be involved in cross-linking process. Also, structural differences between UPe1 and UPe2 resin, due to the different EG/PG ratio in polyester chain and higher flexibility of PG moiety, influences nanocomposites properties. Extent of the interactions depends on the nature of the functional groups present on the surface of the fumed silica and UPe chain: high intensity π,π-stacking attractive interaction between vinyl and terephthaloyl moieties contribute to effective networking of the obtained system. On the other hand, low intensity non-covalent interactions: London dispersive forces, Van der Waals and different dipolar interactions had a smaller contribution to orderliness and physical cross-linking, influence lower extent on the mechanical properties of the obtained nanocomposites (Figure 1).

### 3.8. DMA and DSC analysis of cured UPeN and UPeN/R(n) nanocomposites

Chemical composition and configuration of the synthesized macromolecules, interaction between polymer chains and filler nanoparticles have influence on material crystallinity, phase formation, and dynamic-mechanical properties of composite materials.

The temperature dependences of storage modulus ($G'$), which reflects elastic behavior, loss modulus ($G''$), which reflects viscous behavior of pure UPeN and UPeN/R(c) nanocomposites are given in Figure 10. Results of the dynamic-mechanical analysis (DMA) of the investigated samples, presented in Figure 10, show that there is no significant difference in $G'$ and $G''$ values between samples of the same nanocomposite group, indicating that different modification type of applied silica nanoparticles has a minor influence on the dynamic-mechanical properties of the prepared nanocomposites. On the other hand, pure UPe2 and UPe2/R(c) nanocomposites have significantly higher $G'$ values than pure UPe1 and UPe1/R(c) in the whole investigated temperature region, as can also be observed from the values of the storage modulus in the glassy state ($G'_{GS}$), at 50 °C, and in the rubbery state ($G'_{RP}$) (Table 8). Furthermore, rubbery plateau region of samples prepared with UPe2 as polymer matrix appears at higher temperatures ($T > 180$ °C) than rubbery plateau region of samples based on UPe1 ($T > 120$ °C). $G'_{RP}$ values of UPe2/R(c) are more than one order of magnitude higher than $G'_{RP}$ values of UPe1/R(c), indicating large difference in the cross-linking density between these two nanocomposite groups, caused by the presence of different polymer matrix. The same trend was observed for the pure UPe1 and UPe2. Smaller difference between $G'$ values in the glassy and rubbery states for pure UPe2 and UPe2/R(c) nanocomposites in comparison to the samples based on UPe1 is also related to the higher cross-linking density of UPe2-based samples [45]. The trend of the $G''$ values change for two groups of samples depends on the temperature, *i.e.* up to the approximately 110 °C pure UPe1 and UPe1/R(c) nanocomposites have higher $G''$ values than pure UPe2 and UPe2/R(c) nanocomposites. Opposite is true at higher temperatures.

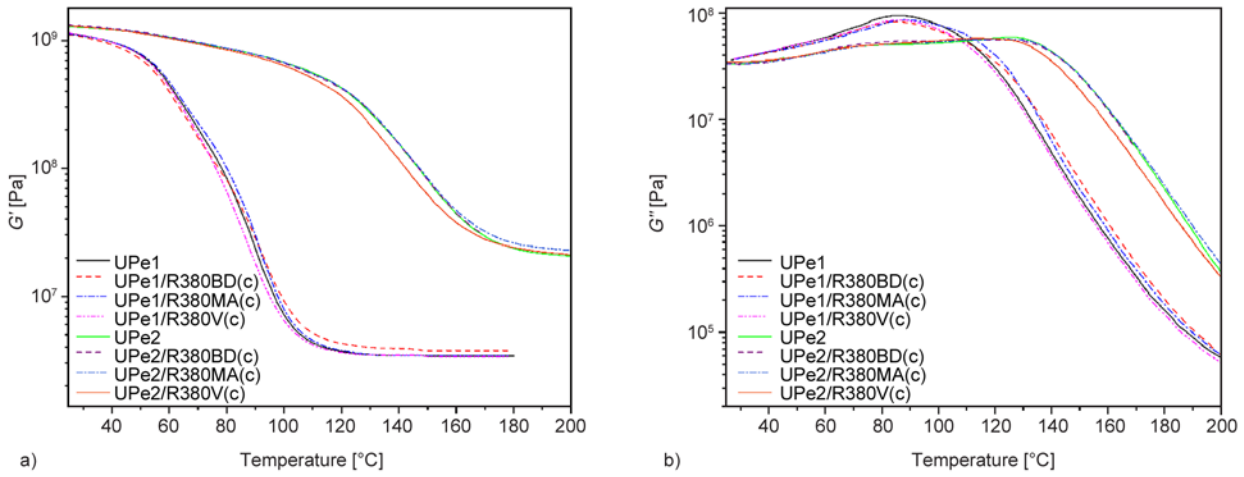


**Figure 10.** Temperature dependence of (a) storage modulus ($G'$) and (b) loss modulus ($G''$) of pure UPeN and UPeN/R(c) nanocomposites

**Table 8.** Results of DMA and DSC analysis of the UPeN and UPeN/R(c)

| Sample | $G'_{GS}$ [MPa] | $G'_{RP}$ [MPa] | $T_{g(\tan\delta\ peak)}$ [°C] | tan $\delta$ height | $T_{g(DSC)}$ [°C] | $\nu \cdot 10^3$ [mol/cm$^3$] |
|---|---|---|---|---|---|---|
| UPe1 | 780 | 3.4 | 92.4 | 0.96 | 92.0 | 3.4 |
| UPe1/R380BD(c) | 720 | 3.7 | 95.1 | 0.92 | 94.1 | 3.5 |
| UPe1/R380MA(c) | 790 | 3.4 | 93.8 | 0.96 | 93.1 | 3.4 |
| UPe1/R380V(c) | 760 | 3.4 | 91.3 | 0.95 | 90.0 | 3.4 |
| UPe2 | 1100 | 23.6 | 151.3 | 0.32 | 141.1 | 5.4 |
| UPe2/R380BD(c) | 1200 | 24.0 | 151.3 | 0.32 | 145.2 | 5.4 |
| UPe2/R380MA(c) | 1100 | 26.0 | 151.3 | 0.32 | 146.3 | 5.5 |
| UPe2/R380V(c) | 1100 | 24.0 | 145.0 | 0.31 | 145.2 | 4.3 |

In the temperature dependence of the mechanical loss factor of pure UPeN and the prepared composites given in Figure 11, only one peak in the range 91.3–95.1 °C for UPe1 and nanocomposites based on UPe1 and in the range 145.0–151.3 °C for UPe2 and nanocomposites based on UPe2 can be seen. The temperature associated with loss factor peak corresponds to the glass transition temperature ($T_g$) of the investigated samples. The $T_g$ values of pure UPeN and prepared nanocomposites determined from the tan $\delta$ temperature dependence are listed in Table 8. $T_{g(\tan\delta\ peak)}$ values of UPe1/R380(c) nanocomposites prepared using R380BD and R380MA nanoparticles are higher than $T_g$ of pure UPe1, which implies that the presence of these surface modified $SiO_2$ nanoparticles restricted molecular mobility of polymer chains at the interface between UPe1 and nanoparticles, due to the presence of the attractive interactions between nanoparticles and polymer matrix. The opposite was obtained for UPe1/R380V(c) nanocomposite. When UPe2 was used as polymer matrix, R380BD and R380MA nanoparticles showed no influence on the $T_g$ of UPe2, while $T_g$ of UPe2/R380V(c) nanocomposite was lower than $T_g$ of pure UPe2. Furthermore, $T_g$ of cured UPe1 and UPe1/R(c) samples is lower than $T_g$ of UPe2 and UPe2/R(c), due to the higher cross-linking density of the samples based on UPe2. This is also evidenced by the maximum values of tan $\delta$ (tan $\delta$ height) listed in Table 8, since it is known that samples with higher tanδ values have lower cross-linking density, *i.e.* higher mobility of the chain segments between cross-links [46]. It is also interesting to notice that tanδ peaks of UPe2 and UPe2/R(c) nanocomposites are broader than tan $\delta$ peaks of UPe1 and UPe1/R(c) samples, indicating higher cross-link non-uniformity, *i.e.* more heterogeneous polymer network and broad distribution of relaxation times in samples based on UPe2 [47, 48].

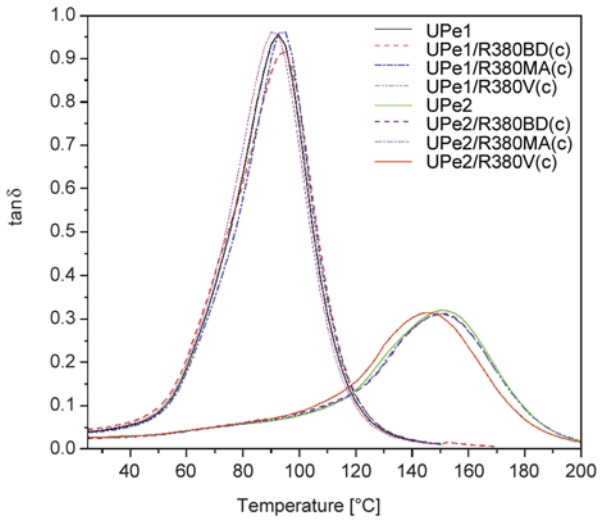


**Figure 11.** Temperature dependence of tan $\delta$ of pure UPeN and UPeN/R(c) nanocomposites

Values of the cross-linking density ($\nu$) of the prepared samples were calculated from $G'_{RP}$ following the Equation (2):

$$\nu = \frac{(G'_{RP})}{RT} \tag{2}$$

where $R$ is the universal gas constant and $T$ is $T_g$+30 °C. Determined values of the cross-linking density of the investigated samples are summarized in Table 8. It can be observed that different modification type of $SiO_2$ had no influence on the cross-linking density of pure UPe1 and UPe1/R(c) nanocomposites. Similar trend was observed for pure UPe2 and UPe2/R(c) nanocomposites, except for UPe2/R380V(c) which has slightly lower ν than pure UPe2 and other UPe2/R(c) nanocomposites, which is in accordance with determined $T_g$ values and investigated mechanical properties. Obtained DMA results revealed that type of the UPe used as polymer matrix has more pronounced influence on the dynamic-mechanical properties of the investigated nanocomposites has than the type of $SiO_2$ nanoparticles used for modification. Samples based on unsaturated polyester prepared using PET glycolysis product obtained by ethylene glycol azeotropic removal

method have higher cross-linking density and consequently lower molecular weight between cross-links than samples based on UPe1, synthesized using product obtained by classical method of PET glycolysis.

In order to determine the thermal properties of the cured UPeN and UPeN/R(n) nanocomposites, differential scanning calorimetry was performed, whereby two heating runs, as well as a cooling run between them were recorded. From the results of DSC analysis (Figure 12) similar values of $T_g$ to ones determined by DMA analysis, and no significant differences between $T_g$ of pure cured UPeN and UPeN/R(c) nanocomposites were found. Generally, the $T_g$ values of cured UPe1 and corresponding nanocomposites are in the range 92.0–94.1 °C, and of cured UPe2 and corresponding nanocomposites are in the range 141.1–146.2 °C.

In a similar manner to the present work, nanocomposites based on UPe and fumed silica Aerosil® R812S, R805 and R816, and R200 modified with phenyl terminal group, R200NPh were investigated [15]. Aerosil® R812S, R805, and R816 are a hydrophobic fumed silica obtained by treating of Aerosil® 200 with hexamethyldisilazane, octylsilane, and hexadecylsilane, respectively. Different length of aliphatic chain provided low cohesive intermolecular interactions between polymeric chain and functionalities at silica surface, which contributed to the low reinforcement effect in appropriate nanocomposites. Due to this, the best mechanical and rheological properties were found for composites with R200NPh nanofiller. High intensity π,π-stacking attractive intermolecular interaction between *N*-phenyl and terephthaloyl moieties provided effective physical cross-linking, and thus high reinforcing effect was found similar to the ones obtained in this work. However, reinforcing effect of R200NPh could not be achieved in UPe with EG and PG glycol, synthesized in this work, as for dipropylene glycol (DPG) based UPe [15]. Preliminary results indicate that lower flexibility of EG/PG fragments could not provide favorable conformational adaption to attain maximum intermolecular interactions in UPe2/R200NPh nanocomposite. Compared with the results presented in this work, with vinyl modified fumed silica Aerosil® 380 (R380BD, R380MA and R380V), the best mechanical and rheological properties was found in composites with R380V, *i.e.* UPe1/R380V and UPe2/R380V at all nanofiller loading. By incorporation of 1.0 wt% of silica R380V stress at break increase for 195–247% for UPeN/R380V(c) cross-linked nanocomposite. Presented results indicate that high performances nanocomposites based on UPe could be obtained by designing modification of nanofiller with preferably mono vinyl moiety, which could exert the lowest possible steric interference with polymeric chain.

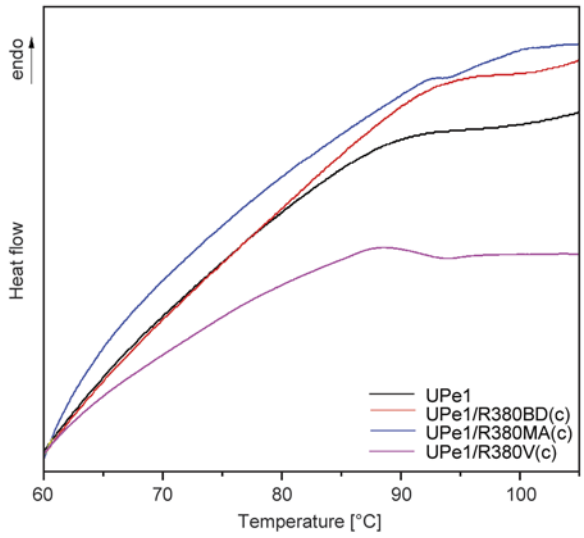


**Figure 12.** DSC curves obtained during heating at 10°C/min of pure UPe1 and UPe1/R(c) nanocomposites

Besides, in a previous work it was explained that comparison of the mechanical properties of the PET based UPes and nanocomposites with literature ones was difficult, due to the different experimental conditions, applied reinforcement materials, molecular weight of the UPe and styrene amount [15]. Commercial UPe resins with different styrene contents (60, 50, and 40 wt%) exhibited reasonably lower stress at break value (11 MPa for cured UPe resin with 60 wt%; 24 MPa for cured UPe resin with 50 wt% and 37 MPa for cured UPe resin with 40 wt%) compared with UPes prepared in this work [49]. Comparing the silica content influence on the rheological and mechanical properties of the PET based nanocomposites with, for example, influence of fiber-glass content, the fiber-glass polyester resin composites showed higher values for stress at break and tensile modulus [50]. Presented results show that UPe resins obtained by polycondensation of maleic anhydride and products of PET glycolysis and nanocomposites are materials of comparable performance to the ones published in the literature, and thus presented methodology offers an applicable alternative for large scale production.

## 4. Conclusions

In this work UPeN resins were used as polymer matrices, while surface modified fumed silica nanoparticles were used as nanofillers for the preparation of UPeN/R nanocomposites. The gel time of pure cured UPe2, obtained by EG azeotropic removal method, was shorter compared with UPe1 (*classical method*), while the maximum curing temperature was higher for UPe2 (172.9 °C). The lower gel time and maximum curing temperature were found for corresponding nanocomposites based on UPe2.

Mechanical testing results indicate that stress at break of all cured nanocomposites is higher than for pure UPeN, and increases with increasing modified silica content up to the 1 wt% in UPeN/R380(n), and after that small changes in mechanical properties was found. This result indicate that incorporation more than 2 wt% of modified silica contribute to lower dispersibility in polymeric matrix, *i.e.* strong cohesive force between nanofiller particles prevail. TEM analysis revealed that silica nanofiller formed chain-like aggregates which provided different extent of intermolecular interaction with cross-linked polymer network. Exceptional mechanical properties were obtained for UPe2/R380V(c): the value of stress at break and tensile modulus were 84 MPa and 1.8 GPa, respectively. Similar results was obtained for impact strength testing, *i.e.* highest value of $\sigma_i$ was obtained for both UPeN/R380V(c), while higher values of $\sigma_f$ was obtained for UPeN/R380BD(c). In both case UPe1 resin showed higher value of impact and flexural strength.

Obtained DMA results indicated that the synthesis method of the UPe has more pronounced influence on the dynamic mechanical properties than type of $SiO_2$ nanoparticles surface modification. Higher cross-linking density was observed for samples based on UPe2. The trend of glass transition temperature values obtained by DMA corresponds to $T_g$ values obtained by DSC analysis.

## Acknowledgements

The authors acknowledge financial support from Ministry of Education, Science and Technological development of Serbia, Project Nos. OI 172057. The authors would also like to pay special thanks to the Shimadzu Branch Belgrade (Shimadzu Corporation Japan) and Center for electron microscopy Faculty of Biology for the technical support.

## References

[1] Karayannidis G. P., Achilias D. S.: Chemical recycling of poly(ethylene terephthalate). Macromolecular Materials and Engineering, **292**, 128–146 (2007). DOI: 10.1002/mame.200600341

[2] Mendes L. C., Dias M. L., Rodrigues T. C.: Chemical recycling of PET waste with multifunctional pentaerythrytol in the melt state. Journal of Polymers and the Environment, **19**, 254–262 (2011). DOI: 10.1007/s10924-010-0276-y

[3] Zahedi A. R., Rafizadeh M., Taromi A. F.: Recycling of off-grade PET *via* partial alcoholysis to synthesize functionalized PET oligomer nanocomposites. Polymer Composites, **33**, 1832–1839 (2012). DOI: 10.1002/pc.22312

[4] Geyer B., Röhner S., Lorenz G., Kandelbauer A.: Improved thermostability and interfacial matching of nanoclay filler and ethylene vinyl alcohol matrix by silane-modification. Journal of Applied Polymer Science, **132**, 41227/1–41227/11 (2015). DOI: 10.1002/app.41227

[5] Atta A. M., Abdel-Raouf M. E., Elsaeed S. M., Abdel-Azim A-A. A.: Mechanical characterization and chemical resistances of cured unsaturated polyester resins modified with vinyl ester resins based on recycled poly (ethylene terephthalate). Journal of Applied Polymer Science, **103**, 3175–3182 (2007). DOI: 10.1002/app.25196

[6] Ahmed N. M., Tawfik M. E., Ward A. A: Characterization of a polymer composite from treated kaolin and unsaturated polyester based on PET waste. Polymer Composites, **34**, 1223–1234 (2013). DOI: 10.1002/pc.22529

[7] Torlakoğlu A., Güçlü G.: Alkyd–amino resins based on waste PET for coating applications. Waste Management, **29**, 350–354 (2009). DOI: 10.1016/j.wasman.2008.02.018

[8] Güçlü G.: Alkyd resins based on waste PET for water-reducible coating applications. Polymer Bulletin, **64**, 739–748 (2010). DOI: 10.1007/s00289-009-0166-4

[9] Klonos P., Panagopoulou A., Bokobza L., Kyritsis A., Peoglos V., Pissis P.: Comparative studies on effects of silica and titania nanoparticles on crystallization and complex segmental dynamics in poly(dimethylsiloxane). Polymer, **51**, 5490–5499 (2010). DOI: 10.1016/j.polymer.2010.09.054

[10] Dabrowska I., Fambri L., Pegoretti A., Slouf M., Vackova T., Kolarik J.: Spinning, drawing and physical properties of polypropylene nanocomposite fibers with fumed nanosilica. Express Polymer Letters, **9**, 277–290 (2015). DOI: 10.3144/expresspolymlett.2015.25

[11] Kango S., Kalia S., Celli A., Njuguna J., Habibi Y., Kumar R.: Surface modification of inorganic nanoparticles for development of organic–inorganic nanocomposites – A review. Progress in Polymer Science, **38**, 1232–1261 (2013). DOI: 10.1016/j.progpolymsci.2013.02.003

[12] Srinivasa Moorthy S., Manonmani K.: Research on sliding wear behavior of $TiO_2$ filled glass fiber reinforced polymer composite. Research Journal of Applied Sciences, Engineering and Technology, **7**, 3356–3361 (2014).

[13] Jastrzêbska M., Janik H., Paukszta D.: The investigation of polyester composites filled by modified bentonite. Polimery, **59**, 656–661 (2014). DOI: 10.14314/polimery.2014.656

[14] Wang Y-Q., Guo Y., Cui R-X., Wang Z-M., Wu Y-L.: Preparation and mechanical properties of nano-silica/UPR polymer composite. Science and Engineering of Composite Materials, **21**, 471–477 (2014). DOI: 10.1515/secm-2013-0051

[15] Rusmirović J. D., Radoman T., Džunuzović E. S., Džunuzović J. V., Markovski J., Spasojević P., Marinković A. D.: Effect of the modified silica nanofiller on the mechanical properties of unsaturated polyester resins based on recycled polyethylene terephthalate. Polymer Composites, in press (2015). DOI: 10.1002/pc.23613

[16] May-Pat A., Avilés F., Toro P., Yazdani-Pedram M., Cauich-Rodríguez J. V.: Mechanical properties of Pet composites using multiwalled carbon nanotubes functionalized by inorganic and itaconic acids. Express Polymer Letters, **6**, 96–106 (2012). DOI: 10.3144/expresspolymlett.2012.11

[17] Guo L., Xu X., Zhang Y., Zhang Z.: Effect of functionalized nanosilica on properties of polyoxymethylene-matrix nanocomposites. Polymer Composites, **35**, 127–136 (2014). DOI: 10.1002/pc.22642

[18] Tong L., Pu Z., Chen Z., Huang X., Liu X.: Effect of nanosilica on the thermal, mechanical, and dielectric properties of polyarylene ether nitriles terminated with phthalonitrile. Polymer Composites, **35**, 344–350 (2014). DOI: 10.1002/pc.22667

[19] Li Y., Han C., Zhang X., Bian J., Han L.: Rheology, mechanical properties, and biodegradation of poly(ε-caprolactone)/silica nanocomposites. Polymer Composites, **34**, 1620–1628 (2013). DOI: 10.1002/pc.22562

[20] Castellano M., Turturro A., Marsano E., Conzatti L., Vicini S.: Hydrophobation of silica surface by silylation with new organo-silanes bearing a polybutadiene oligomer tail. Polymer Composites, **35**, 1603–1613 (2014). DOI: 10.1002/pc.22813

[21] Hong R. Y., Fu H. P., Zhang Y. J., Liu L., Wang J., Li H. Z., Zheng Y.: Surface-modified silica nanoparticles for reinforcement of PMMA. Journal of Applied Polymer Science, **105**, 2176–2184 (2007). DOI: 10.1002/app.26164

[22] Spange S.: Silica surface modification by cationic polymerization and carbenium intermediates. Progress in Polymer Science, **25**, 781–849 (2000). DOI: 10.1016/S0079-6700(00)00014-9

[23] Kim K-J., White J. L.: Silica surface modification using different aliphatic chain length silane coupling agents and their effects on silica agglomerate size and processability. Composite Interfaces, **9**, 541–556 (2002). DOI: 10.1163/15685540260494119

[24] Savin D. A., Pyun J., Patterson G. D., Kowalewski T., Matyjaszewski K.: Synthesis and characterization of silica-graft-polystyrene hybrid nanoparticles: Effect of constraint on the glass-transition temperature of spherical polymer brushes. Journal of Polymer Science Part B: Polymer Physics, **40**, 2667–2676 (2002). DOI: 10.1002/polb.10329

[25] Li N., Luo P., Liu K., Chen L., Wang K., Chen F., Fu Q.: Preparation and properties of poly(ethylene terephthalate)/inorganic whiskers composites. Journal of Applied Polymer Science, **121**, 604–611 (2011). DOI: 10.1002/app.33729

[26] Zhand Y., Lv F., Ke S., Yu L., Huang H., Chan H. L. W.: Effect of hollow structure and covalent bonding on the mechanical properties of core–shell silica nanoparticles modified poly(methyl acrylate) composites. Materials Chemistry and Physics, **129**, 77–82 (2011). DOI: 10.1016/j.matchemphys.2011.03.057

[27] Luo Z., Hong R. Y., Xie H. D., Feng W G.: One-step synthesis of functional silica nanoparticles for reinforcement of polyurethane coatings. Powder Technology, **218**, 23–30 (2012). DOI: 10.1016/j.powtec.2011.11.023

[28] Hamad A.: Preparation and characterization of some unsaturated polyester alkyds based on terephthalic and isophthalic acids. PhD Thesis, Loughborough University Institutional Repository (1980).

[29] ISO 4326:1992: Non-ionic surface active agents – Polyethoxylated derivatives – Determination of hydroxyl value – Acetic anhydride method (1992).

[30] ASTM D3644: Standard test method for acid number of styrene-maleic anhydride resins (2012).

[31] EN 14103: Fat and oil derivatives – Fatty acid methyl esters (fame) – Determination of ester and linolenic acid methyl ester contents (2003).

[32] ASTM D1200: Standard test method for viscosity by ford viscosity cup (2014).

[33] ASTM D2471-99: Standard test method for gel time and peak exothermic temperature of reacting thermosetting resins (2008).

[34] ASTM D882: Standard test method for tensile properties of thin plastic sheeting (2009).

[35] ASTM D790: Standard test methods for flexural properties of unreinforced and reinforced plastics and electrical insulating materials (2010).

[36] ASTM D256: Standard test methods for determining the izod pendulum impact resistance of plastics (2006).

[37] Patel M. R., Patel J. V., Sinha V. K.: Polymeric precursors from PET waste and their application in polyurethane coatings. Polymer Degradation and Stability, **90**, 111–115 (2005).
DOI: 10.1016/j.polymdegradstab.2005.02.017

[38] Güçlü G., Kaşgöz A., Özbudak S., Özgümüs S., Orbay M.: Glycolysis of poly(ethylene terephthalate) wastes in xylene. Journal of Applied Polymer Science, **69**, 2311–2319 (1998).
DOI: 10.1002/(SICI)1097-4628(19980919)69:12<2311::AID-APP2>3.0.CO;2-B

[39] Stojanović D., Orlović A., Marković S., Radmilović V., Uskoković P. S., Aleksić R.: Nanosilica/PMMA composites obtained by the modification of silica nanoparticles in a supercritical carbon dioxide–ethanol mixture. Journal of Materials Science, **44**, 6223–6232 (2009).
DOI: 10.1007/s10853-009-3842-8

[40] Zahedi A. R., Rafizadeh M., Ghafarian S. R.: Unsaturated polyester resin via chemical recycling of off-grade poly(ethylene terephthalate). Polymer International, **58**, 1084–1091 (2009).
DOI: 10.1002/pi.2637

[41] Ou Y-C., Yu Z-Z., Vidal A., Donnet J. B.: Effects of alkylation of silicas on interfacial interaction and molecular motions between silicas and rubbers. Journal of Applied Polymer Science, **59**, 1321–1328 (1996).
DOI: 10.1002/(SICI)1097-4628(19960222)59:8<1321::AID-APP16>3.0.CO;2-8

[42] Guo Z., Pereira T., Choi O., Wang Y., Hahn H. T.: Surface functionalized alumina nanoparticle filled polymeric nanocomposites with enhanced mechanical properties. Journal of Materials Chemistry, **16**, 2800–2808 (2006).
DOI: 10.1039/B603020C

[43] Kanimozhi K., Prabunathan P., Selvaraj V., Alagar M.: Vinyl silane-functionalized rice husk ash-reinforced unsaturated polyester nanocomposites. RSC Advances, **4**, 18157–18163 (2014).
DOI: 10.1039/c4ra01125b

[44] Kutz M.: Applied plastics engineering handbook: Processing and materials. Elsevier, Waltham (2011).

[45] Crawford D. M., Escarsega J. A.: Dynamic mechanical analysis of novel polyurethane coating for military applications. Thermochimica Acta, **357–358**, 161–168 (2000).
DOI: 10.1016/S0040-6031(00)00385-3

[46] Džunuzović E., Tasić S., Božić B., Jeremić K., Dunjic B.: Photoreactive hyperbranched urethane acrylates modified with a branched saturated fatty acid. Reactive and Functional Polymers, **66**, 1097–1105 (2006).
DOI: 10.1016/j.reactfunctpolym.2006.01.016

[47] Kannurpatti A. R., Anseth J. W., Bowman C. N.: A study of the evolution of mechanical properties and structural heterogeneity of polymer networks formed by photopolymerizations of multifunctional (meth)acrylates. Polymer, **39**, 2507–2513 (1998).
DOI: 10.1016/S0032-3861(97)00585-5

[48] Worzakowska M.: Studies on the cure reaction and relationship between network structure/thermal properties of styrene copolymers based on adypic/sebacic acid modified unsaturated (epoxy) polyesters. Macromolecular Symposia, **296**, 254–264 (2010).
DOI: 10.1002/masy.201051036

[49] Osman E., Vakhguelt A., Sbarski I., Mutasher S.: Curing behaviour and tensile properties of unsaturated polyester containing various styrene concentrations. Malaysian Polymer Journal, **7**, 46–55 (2012).

[50] Pepper T.: Polyester resin. Ashland Chemical Company, Lexington (2003).

*eXPRESS Polymer Letters Vol.10, No.2 (2016) 160–175*
*Available online at www.expresspolymlett.com*
*DOI: 10.3144/expresspolymlett.2016.15*

# Reactive microencapsulation of carbon allotropes in polyamide shell-core structures and their transformation in hybrid composites with tailored electrical properties

*F. Oliveira[1], N. Dencheva[1], P. Martins[2], S. Lanceros-Méndez[2], Z. Denchev[1*]*

[1]i3N – Institute for Polymers and Composites, University of Minho, 4800-058 Guimarães, Portugal
[2]Center/Department of Physics, University of Minho, 4710-057 Braga, Portugal

*Received 14 July 2015; accepted in revised form 21 September 2015*

**Abstract.** Polyamide 6 microcapsules (PAMC) loaded with 2–10 wt% of different carbon allotropes: carbon black, multi-walled carbon nanotubes, carbon nanofibers and graphite were synthesized via activated anionic polymerization (AAROP) of ε-caprolactam in solution performed in the presence of the respective micro- or nanosized loads. The forming high-molecular weight microporous PAMC showed typical diameters of 15–35 μm, the filler particles being entrapped in the core as proven by microscopy methods. The melt processing of the loaded microcapsules produced PA6/C-filler hybrid thermoplastic composites with homogeneous distribution of one or two C-fillers even at loads of up to 10% without any functionalization. The crystalline structure of all PAMC and molded composites was studied by thermal and X-ray diffraction methods focusing on possible structure modification during the transition from PAMC to molded plates. Mechanical tests in tension and electrical conductivity measurements showed that transforming loaded PAMC into composites by melt processing could be a facile and rapid method to fabricate polyamide composites with improved mechanical performance and tailored electrical and dielectric properties.

***Keywords:*** *tailor-made polymers, polymer composites, activated anionic polymerization, microcapsules, carbon allotropes*

## 1. Introduction

Due to the huge increase of the use of polymer materials in electronics, automotive and aerospace industries, the demand for thermoplastic polymers with dissipative or conductive properties is constantly growing. The necessary enhancement of electric conductivity can be achieved in two ways: (i) by using inherently conductive polymers or (ii) by adding electrical conductive fillers to an insulating polymer matrix [1]. In the first approach, polymers with conjugated π-electron system *e.g.*, polyaniline, polypyrrole or polythiophene are among those widely used, for example, in organic solar cells as transparent electrical conductive polymer films [2]. The main shortcomings of the inherently conductive polymers are their high prices and the difficulties in their melt processing due to non-meltability combined with degradation and poor long-term stability.

In the second approach, conductive fillers are dispersed in a polymer matrix, the most frequently employed being those based on $sp^2$-carbon, *e.g.*, carbon black (CB), carbon nanofibres (CNF), and carbon nanotubes (CNT) [3], as well as exfoliated graphite (GR), graphene, fullerenes and their derivatives [4]. All these carbon materials differ significantly in the shape and morphology of their primary particles: from nanometer-size spheres (for CB and fullerenes), through medium-to-high aspect ratio tubes with diameters of several nanometers (CNF, CNT), to stacks of graphene sheets with different

*Corresponding author, e-mail: denchev@dep.uminho.pt

degrees of exfoliation (GR, graphite oxide, functionalized graphene). Due to the strong van der Waals interactions between the single spheres, tubes or sheets, formation of agglomerates is very common for those carbon fillers. Thus, it is difficult to disperse them in polymer matrices by means of conventional melt-processing techniques, affecting negatively the mechanical and conductive properties of the final composite article. Dispersion can be enhanced by surface modification, covalent or non-covalent functionalization of the carbon filler [5–7]. Such treatments result in better adhesion of the filler to the host polymer [8], however they often create surface defects on the filler particles' surface and decrease their inherent conductivity [9, 10]. The relatively complex chemistry and/or costly reagents of most functionalization procedures additionally impede a cost-effective scale-up to industrial production of the CNT-containing composites and limit their use for high price applications only [3].

A number of polymers have been tested as matrices for carbon allotrope/ thermoplastic hybrid composites, including polyamides, polyesters, aromatic polyethers, and polyolefins [11]. Among them, aliphatic polyamides are quite frequently employed since they possess a unique balance between price, processability, chemical properties and mechanical resistance. Thus, polyamide 6 (PA6), polyamide 12 (PA12) and polyamide 6.6 (PA66) have been melt-mixed with different grades of CNT for studying the structure, morphology, mechanical and electrical properties of the resulting hybrid composites [3, 12–20]. It seems that the extremely high stiffness, electrical and thermal conductivity combined with their high aspect ratio makes CNT suitable fillers for conductive polyamide nanocomposites with prospective applications in electronics, packaging and automotive industries. Polyamide-CB composites have also been prepared and studied [21–23]. CB powders are much cheaper than CNT which is important for industrial applications, however their percolation thresholds are significantly higher – 0.7–2.1 wt% for CNT against 4.3 wt% for CB introduced into PA12 matrix [24]. Exfoliated GR-containing polyamides have been prepared and investigated predominantly in terms of increasing the mechanical properties [25] or thermal diffusivity [26] of the matrix material, whereby the larger the GR stacks size and their exfoliation ratio, the more effective the formation of 3-dimensional conductive pathways and high thermal diffusivity. A clear trend toward GR filler chemical modification is observed mainly by oxidation and polymer grafting in order to increase the miscibility with the polyamide matrix [27, 28].

In all the polyamide/carbon allotrope composites mentioned so far melt mixing was used as dispersion method, whereby frequently the reported percolation thresholds in CNT-modified hybrids were found to be much higher than the theoretical ones [15]. Studies on shaping of PA6/CNT composites by injection molding revealed that high conductivity values (measured both in-line and in the finished part) can only be achieved at maximum melt temperature and minimum injection speed [29]. These findings together with the necessity of functionalization could be limiting factors for the large scale use of carbon allotrope conductive fillers in thermoplastic PA6 composites.

An alternative to overcome the limitations related to melt compounding would be to synthesize the polymer matrix *in-situ*, *i.e.*, by initially mixing the filler with the monomer and then polymerizing this system. Such reactive processing in the case of polyamides can be achieved by either hydrolytic or activated anionic ring-opening polymerization (AAROP) of lactams. Thus, O'Neill *et al*. [30] studied the effect on the *in-situ* hydrolytic polymerization of ε-caprolactam (ECL) on the structure and properties of GR oxide and found that the separate graphene sheets may be grafted with PA6 chains propagating from their surface, hence increasing the matrix-filler miscibility. No data on the electrical conductivity were presented. Kelar [31] performed AAROP of ECL containing up to 0.3 wt% of a $C_{60}/C_{70}$ fullerene mixture proving that fullerenes do not inhibit the polymerization to PA6. Zuev and Ivanova [32] studied the effect of various fulleroid fillers ($C_{60}$, mixture of $C_{60}/C_{70}$ and fulleroid soot) on the mechanical, tribological and electrical properties of PA6-based nanocomposites prepared by *in-situ* AAROP. Both tensile modulus and strength of the polymer nanocomposites were found to improve with up to 15% upon the addition of 0.001–0.1 wt% of fulleroid materials. Electrical volume resistivity decreased with filler loading reaching about $10^7$ Ω·cm at 0.1 wt% load. Functionalized $C_{60}$ fullerene introduced in concentrations of up to 3 wt% in PA6 matrix by AAROP produced similar volume resistivity values and presented strong evidence for grafting of polyamide links onto the $C_{60}$ sphere leading to extensive cross-

linking [33]. The effect of $C_{60}$ on the mechanical and dielectric properties of nanocomposites based on PA12, prepared by *in-situ* AAROP has also been studied [34, 35].

A common limitation of the bulk AAROP process carried out in solid state is that no mixing is possible at the final stages of the process which results in a gradient of the filler, if the AAROP is not fast enough [33]. Therefore, all issues of the melt-processing techniques and the necessity of fillers' functionalization, although in a lesser extent, are still present. Recently, a possible solution of these problems in PA6 hybrid composites was found by means of AAROP in solution. The process can be carried out in a way to produce micro- or nanosized capsules whose polyamide core entraps well-dispersed filler particles. The loaded capsules are further subjected to melt-processing to shape the final composite [36, 37]. This novel method is characterized by short polymerization times of ca. 60 min, low polymerization temperatures (~135 °C) and up to 75% conversion to high molecular weight polyamide microcapsules (PAMC). It can introduce up to 30% of load into the PAMC without any functionalization and is suitable for scale-up to industrial production.

The present work reports on the *in-situ* synthesis of PAMC loaded with CB, CNT, GR, CNF or mixtures of them by AAROP in solution. The effect of the content and type of the filler on the structure, morphology and thermal properties of the loaded PAMC is assessed. After transforming PAMC into PA6 hybrids by compression molding, the electrical conductivity and mechanical properties were evaluated as a function of composition, structure and preparation conditions.

## 2. Experimental

### 2.1. Materials and preparation

The ECL monomer with reduced moisture content for AAROP (AP-Nylon® caprolactam) was delivered from Brüggermann Chemical, Germany. Before use, it was kept under vacuum for 1 h at 23 °C. As polymerization activator, Bruggolen C20® from Brüggermann Chemical, Germany (C20) was used. According to the manufacturer, it contains 80 wt% of blocked di-isocyanate in ECL. The supposed chemical structure of C20 is presented in Figure 1. The initiator sodium dicaprolactamato-bis-(2-methoxyethoxo)-aluminate (Dilactamate®, DL) was purchased from Katchem, Czech Republic, and used without further

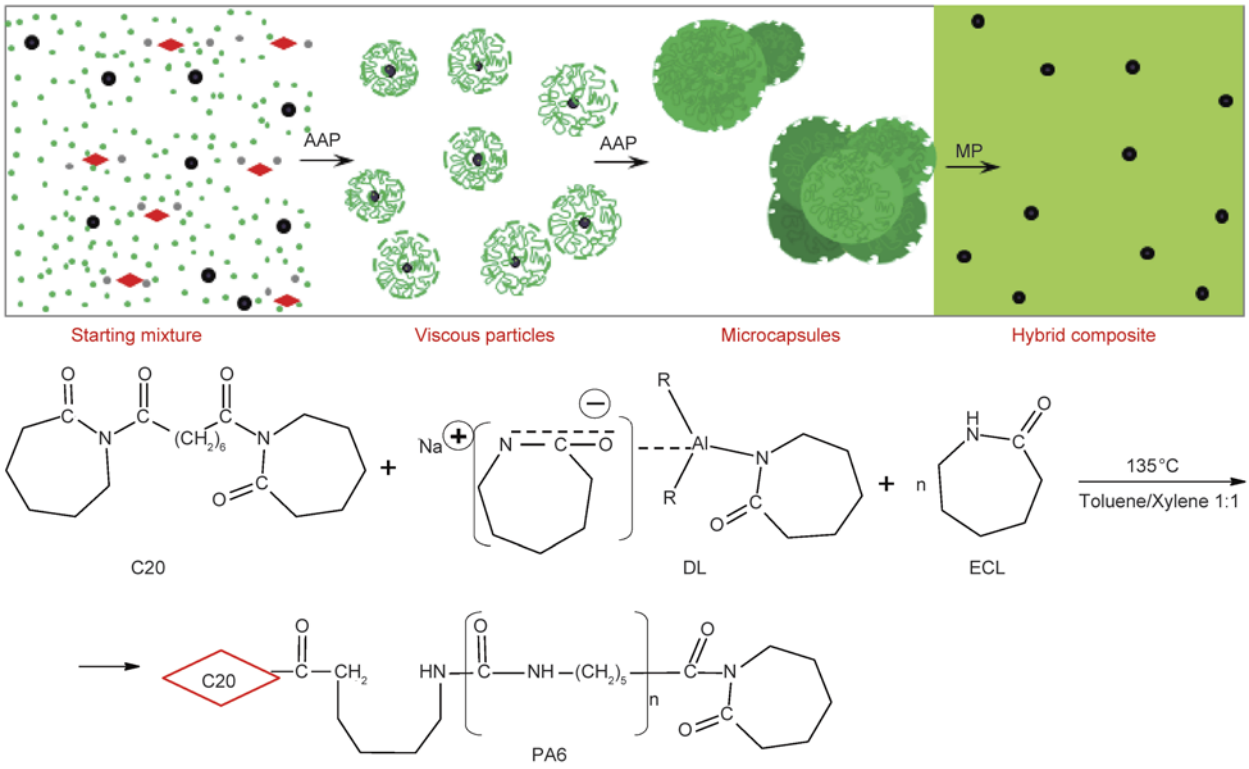


**Figure 1.** Chemical reactions occurring during AAP: C20 – Bruggolen C20 (activator) ◆; DL – dicaprolactamato-bis-(2-methoxyethoxo)-aluminate, R = $OCH_2CH_2OCH_3$ (initiator); ECL – ε-caprolactam ●; PA6 – anionic polyamide 6; Carbon allotrope powder component ●; AAP = activated anionic polymerization; MP = melt processing (compression molding)

treatment. The multi-walled CNT and GR powder (platelet size < 1 μm) were purchased from Sigma Aldrich; the acetylene CB is a product of S.E.A. Tudor, Spain and the CNF were purchased from Grupo Antolin, Spain. Methanol and other solvents are of 'puriss' grade purchased from Sigma-Aldrich and were used as received.

The AAROP was carried out in a 250 mL glass flask fitted with thermometer, magnetic stirrer, a Dean-Stark attachment for azeotropic distillation with reflux condenser, and inlet for dry nitrogen. In a typical synthesis, about 0.5 mol of ECL and the desired amount of each carbon allotrope (2, 6 or 10 wt% in respect to ECL) were added to 100 mL of 1:1 toluene/xylene mixture while stirring, under nitrogen atmosphere refluxing the reaction mixture for 10–15 min. Subsequently, 3 mol% of DL and 1.5 mol% of C20 were added at once. The reaction time was always 1 hour (from the point of catalytic system addition), the temperature being maintained in the 125–135 °C range at a constant stirring of ca. 800 rpm. The carbon-loaded PAMC formed as fine dark grey powder and were separated from the reaction mixture by hot vacuum filtration, washed several times with methanol and dried for 30 min at 100 °C in a vacuum oven. After 1 hour of polymerization the yields of PA6 in respect to ECL were 56% (empty PA6 microcapsules) and 44–60% for the loaded PAMC (Table 1).

Compression molding of PAMC to plates was performed in a 25 ton Moore hydraulic hot press, England using a rectangular mold with dimensions 85×75×1 mm, pressing for 5–7 min at 230 °C and a pressure of 5 MPa. The control samples of hydrolytic PA6 (HPA6) were produced analogously by compression molding of a medium-viscosity, general purpose commercial grade PA6 (Durethan B30S, Lanxess, USA).

## 2.2. Characterization

Bright field optical measurements of PAMC sizes, roundness and their distributions were performed in an BH-2 microscope (Olympus Corp., Tokyo, Japan) equipped with a DFC200 (Leica Microsystems, Manheim, Germany) digital camera using the Leica Application Suite 4.4 software for image processing. The scanning electron microscopy (SEM) studies were performed in a NanoSEM-200 apparatus of FEI Nova (Hillsboro, USA) using mixed secondary electron/back-scattered electron in-lens detection. The microcapsule samples were observed after sputter-coating with Au/Pd alloy in a 208 HR equipment of Cressington Scientific Instruments (Watford, UK) with high-resolution thickness control. The molded samples were observed after cryofracture.

The average viscometric molecular weight $M_v$ of the neat PA6 was determined by intrinsic viscosity measurements in 97% sulfuric acid at a concentration of 0.2 g/dL with a suspended level Ubbelohde viscometer thermostatted at 25 °C. The Mark-Houwink equation for PA6 was used with $K = 5.066 \cdot 10^{-4}$ and $\alpha = 0.74$ [38]. Flow times are recorded as an average of

**Table 1.** PAMC: sample designation, composition, polymerization yield and granulometry

| Sample designation | Load [wt%][a)] | PAMC yield [wt%][a)] | Real load, *RL* [wt%][b)] | $d_{max}$ [μm] | Roundness, $d_{max}/d_{min}$ |
|---|---|---|---|---|---|
| PA6 | – | 56 | – | 25–35 | 1.2 |
| PA6/CB | 2 | 60 | – | 25–35 | 1.2–1.3 |
| | 6 | 47 | 6.30 | 20–30 | 1.2 |
| | 10 | 57 | – | 15–30 | 1.2–1.4 |
| PA6/CNT | 2 | 45 | 1.97 | 30–40 | 1.2–1.3 |
| | 6 | 52 | 5.33 | 25–35 | 1.2 |
| | 10 | 54 | 8.00 | 20–35 | 1.2 |
| PA6/GR | 2 | 44 | – | 20–30 | 1.2–1.3 |
| | 6 | 46 | 6.09 | 20–25 | 1.2 |
| | 10 | 48 | – | 15–30 | 1.2–1.3 |
| PA6/CNF | 2 | 45 | – | 30–35 | 1.3 |
| | 6 | 48 | 5.77 | 30–35 | 1.2–1.3 |
| | 10 | 54 | – | 20–35 | 1.2–1.3 |
| PA6/CNT-GR | 5 + 5 | 51 | 8.85 | 25–30 | 1.2–1.3 |
| PA6/CNT-CB | 5 + 5 | 49 | 9.49 | 15–20 | 1.3 |
| PA6/GR-CB | 5 + 5 | 50 | 8.67 | 25–30 | 1.2–1.3 |

[a)]As introduced during AAROP, in respect to the starting monomer content;
[b)]Determined according to Equation (1).

five runs. The differential scanning calorimetry (DSC) measurements were carried out in a 200 F3 equipment of Netzsch (Selb, Germany) at a heating rate of 10 °C/min under nitrogen purge. The typical sample weights were in the 10–15 mg range. The effective inorganic load in PAMC was established by means of thermogravimetric analysis (TGA) in a Q500 gravimetric balance (TA Instruments, New Castle, USA) heating the samples to 600 °C at 10 °C/min in nitrogen atmosphere. The real load *RL* of filler in PAMC was calculated according to Equation (1):

$$RL = R_i - R_{PA6}\ [\%] \tag{1}$$

where $R_{PA6}$ is the carbonized residue at 600 °C of empty PAMC and $R_i$ – that of the respective loaded PAMC measured by TGA.

The tensile tests were performed on an Instron 4505 testing machine (Norwood, USA) at 23±2ºC with a standard load cell of 50 kN at a constant crosshead speed of 50 mm/min. From the different composite plates prepared by compression molding of PAMC, standard specimens were cut out according to DIN 53504-S3. At least five specimens of each sample were studied to calculate the average values and their standard deviation. The engineering stress $\sigma$ was determined as the ratio of the tensile force to the initial cross-section of the sample. The engineering strain $\varepsilon$ was determined as the ratio of the sample gauge length at any time during drawing to that before drawing. The Young modulus *E* values were obtained from the initial slope of the strain–stress curves (until 1% strain). In all cases conditioned samples stored for ca. 30 days at 23 °C and 65% relative humidity were tested. The improvement factor *IF* for *E* and σbr values were calculated according to Equation (2):

$$IF = \frac{P_i - P_{PA6}}{P_{PA6}} \cdot 100\ [\%] \tag{2}$$

where $P_i$ is the respective parameter of the composite material and $P_{PA6}$ – the same parameter of the neat PA6 matrix.

Synchrotron X-ray diffraction (XRD) measurements were performed in the P03 MINAXS mircofocus beamline at PETRA III, the German Synchrotron Source DESY in Hamburg, Germany. A Pilatus 300 two-dimensional detector (DECTRIS Ltd, Baden, Switzerland) was used, the sample-to-detector distance being 115 mm, and $\lambda$ = 0.969 Å. Linear XRD profiles were obtained by radial integration of the 2D XRD images by means of the Fit2D software.

Electrical current/voltage measurements were performed in a Keithley 487 pico-ampermeter/voltage source (Keithley Instruments Inc., Cleveland, USA) between –10 and +10 V using increasing and/or decreasing modes. To rule out interferences due to external electric field, all measurements were performed in a Faraday cage. The dielectric permittivity $\varepsilon'$ was obtained from the geometry of the samples in the shape of a parallel plate capacitor (circular electrodes of 5 mm diameter and sample average thickness of 600 μm). The measurement of the capacity and the loss factor $\tan\delta$ with a QuadTech (Marlborough, USA) model 1920 precision LCR meter at room temperature and pressure, at frequencies between 100 Hz and 1 MHz. The permittivity $\varepsilon'$ of the samples was thus determined according to Equation (3):

$$C = \varepsilon' \cdot \varepsilon_0 \cdot \frac{A}{d} \tag{3}$$

where *A* is the area of the capacitor plates and *d* – the sample thickness.

The electrical d.c. conductivity $\sigma$, the permittivity $\varepsilon'$, and the dielectric loss $\varepsilon''$ ($\tan\delta = \varepsilon''/\varepsilon'$) were obtained for all composites produced from compression molded PAMC. A standard procedure was followed in which the I–V dependences for all materials were determined and analyzed. From the slope of the graphs (straight lines for Ohmic materials) the resistance *R* [Ω] was determined, from which the resistivity $\rho$ [Ω·m] and conductivity $\sigma$ [S/m] were calculated according to Equation (4):

$$\sigma = \frac{1}{\rho} = \frac{1}{R} \cdot \frac{d}{A} \tag{4}$$

where *A* is the area and *d* the thickness of the gold electrodes (5 mm in diameter) deposited by sputtering on both free surfaces of each sample. Four measurements in different parts of each molded samples were performed taking the arithmetical mean as a final value of conductivity.

## 3. Results and discussion

The polymerization of ECL to PAMC is performed in a 1:1 toluene/hydrocarbon mixed solvent boiling in the 120–135 °C range that is able to dissolve the lactam monomer, the anionic initiator and the activator (Figure 1). The carbon payloads used without

functionalization are insoluble in the reaction medium. As known from detailed earlier studies [39], the initiation and propagation of lactam AAROP require an anionic initiator and an activator comprising imide links C(O)–N–C(O)–. It is important that this catalyst system should remain active in the presence of the carbon payloads and the solvent employed. These requirements determine the selection of the initiator DL and the commercial activator C20. As indicated in a series of previous studies on AAROP of neat lactams, without any payload, in solution [40–42], the growing PA6 chains form initially viscous, low molecular weight particles that upon additional propagation, coalescence and crystallization produce the final empty PAMC. It can be hypothesized that the carbon loads dispersed in the constantly stirred reaction medium will be entrapped into the viscous particles and can possibly nucleate their crystallization thus forming the loaded PAMC. The present study showed that the transformation of the viscous particles into loaded microcapsules without formation of lumps requires an optimized stirring rate (600–800 rpm), maintaining the molar ratio DL/C20 = 2 and keeping the temperature of AAROP below 135 °C.

Table 1 shows the designations of the PAMC samples prepared, the respective polymerization yields and the theoretical carbon filler content. For selected samples the real filler concentration was determined by TGA according to Equation (1). It can be seen that deviations between the real and intended filler content of up to –2% are observed only for the higher loads of 10 wt%, while for the rest of the samples the two values are almost identical.

The viscometric average molecular weight $M_v$ of empty PAMC and PAMC loaded with 2% of CB are 33 700 and 37 500 g/mol, respectively. After compression molding of PAMC to plates the $M_v$ values remain unchanged being comparable to the $M_v$ of commercial granulated hydrolytic PA6 with $M_v$ = 37 200 g/mol and, at the same time, significantly lower than the anionic PA6 ($M_v$ = 88 500 g/mol) produced with the same initiator/activator system in the bulk at 165 °C [43, 44]. The higher $M_v$ in the latter case is because the bulk AAROP takes place at higher temperature, in the polar molten ECL and in strongly basic medium. These conditions favor complex side reactions leading to partially cross-linked PA6 characterized by increased molecular inhomogeneity [39].

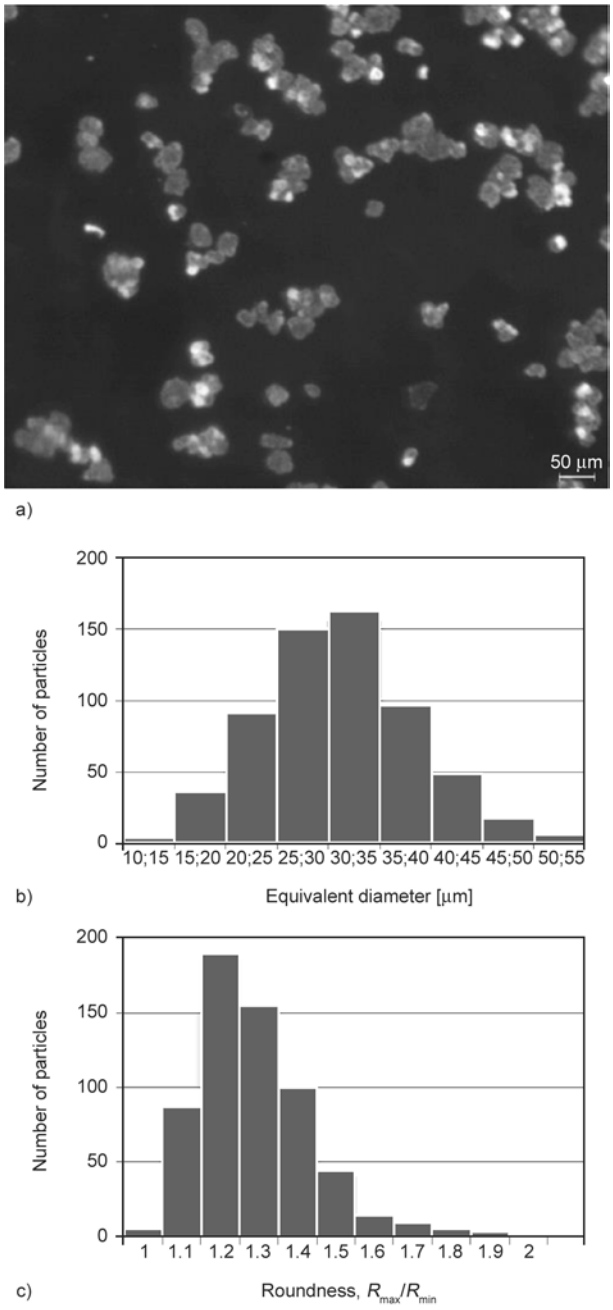


**Figure 2.** Light microscopy image of PA6/CNT-6% sample (a), from which the distributions of sizes (b) and shape (c) are determined.

Figure 2 exemplifies the estimation of the granulometry, including the histograms of size distribution of $d_{max}$ and roundness (*i.e.*, the relation $d_{max}/d_{min}$ of the microcapsules) of a selected PAMC sample (PA6/CNT-6%) by means of light microscopy. Table 1 summarizes these two values for all samples in this study. For the majority of samples obtained at the same AAROP temperature, catalytic system composition and stirring rates, the distributions of both $d_{max}$ and $d_{max}/d_{min}$ are monomodal and close to Gaussian. The most typical PAMC sizes vary

between 20–35 μm with roundness values of 1.2–1.3. Increasing the load broadens slightly both distributions. The type of the C-fillers or their combination reaching an effective load of 9.5% does not affect significantly the granulometry, which is an indication of good control of the PAMC synthesis.

A deeper insight on the morphology of PAMC samples can be obtained by SEM (Figure 3). SEM micrographs show the porosity of the PAMC samples and a scaffold-like morphology, the pores sizes being typically in the 250–500 nm range. Each microcapsule seems to be formed by the coalescence of several PA6 spheres. This finding is in good agreement with the supposed coalescence-crystallization-precipitation mechanism of AAROP in the presence of the load particles whereby the latter are entrapped into the PAMC– closer to the surface, or deeper in the core. The effect can be observed in Figure 3c and 3d displaying a CB domain with sizes 1.0×0.5 μm on the surface of a microcapsule. Figure 3e and 3f show some GR platelets on the PAMC surface as well as incrusted deeper into the pores. PAMC containing CNT (Figure 3h) display more extended morphology, most probably related to the high aspect ratio of this carbon filler. Having in mind the entrapment of the C-load within PAMC, the term 'microcapsule' was used in this work instead of 'microparticle'.

The morphological changes of loaded PAMC after their compression molding into PA6 hybrid composites are shown in Figure 4. As seen from Figure 4b–4d, even at the high load of 6 wt%, the CNT, CB and CNF fillers are finely dispersed within the PA6 matrix, their visible cross-sections being in the nanometer range. Even with the micron-sized GR platelets, a homogeneous distribution is observed (Figure 4e, 4f). These observations confirm the utility of the transformation of loaded PAMC into hybrid composites, proving that this new concept does not need chemical functionalization of the C-filler to avoid agglomeration. Figure 4g and 4h show the possibility to create homogeneous distribution of two different co-existing carbon fillers: CNT-CB and CNT-GR, respectively.

The results from the DSC measurements with loaded PAMC samples and the respective compression molded plates are presented in Table 2. Figure 5 displays the DSC traces of differently loaded PAMC during the first scan (a), cooling (b) and the second DSC scan (c). All loaded PAMC melt during the first scan at slightly lower temperatures and crystallize at significantly higher temperatures during the cooling after melting, as compared to the neat PA6 microcapsules. For some PAMC samples this difference in the crystallization temperatures can reach 20–23 °C (Table 1, PA6/CB-6, PA6/CNT-CB, Figure 5b) and can be explained with the nucleation effect of the C-filler. The cooling after melting in the presence of CNT and CB fillers) result in double crys-

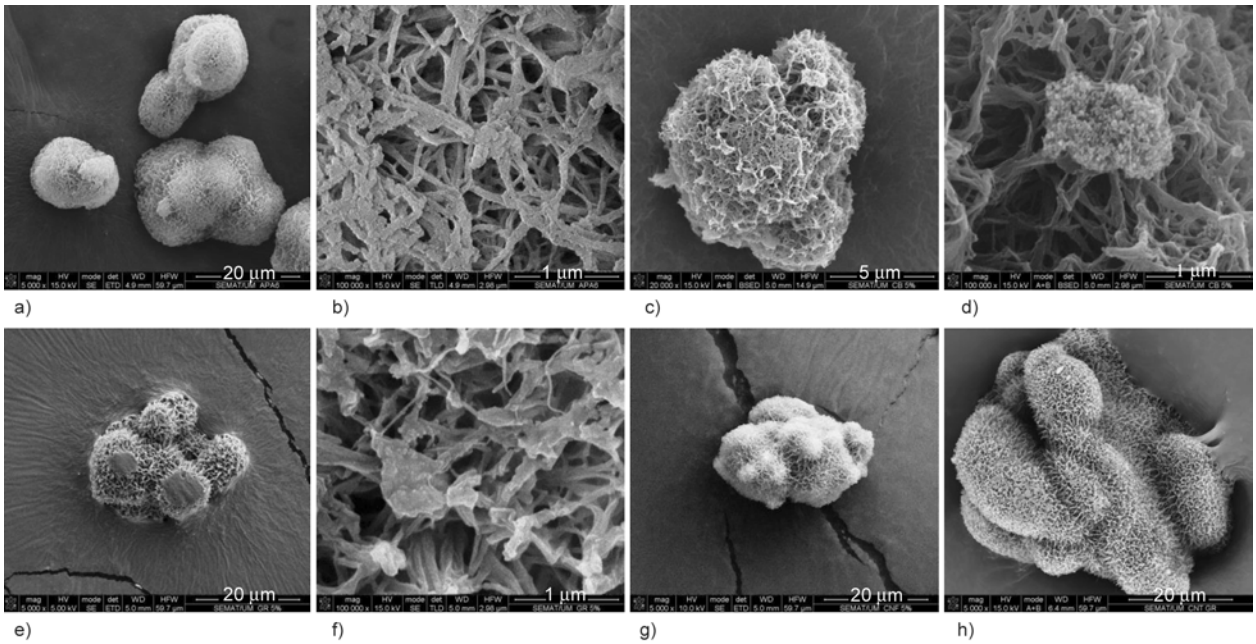


**Figure 3.** Selected SEM micrographs of PAMC: (a) – PA6; (b) – magnification of (a); (c) – PA6/CB-6%; (d) – magnification of (c); (e) – PA6/GR-6%; (f) – magnification of (e); (g) – PA6/CNF-6%; (h) – PA6/CNT-GR 5+5%. For sample designation see Table 1.

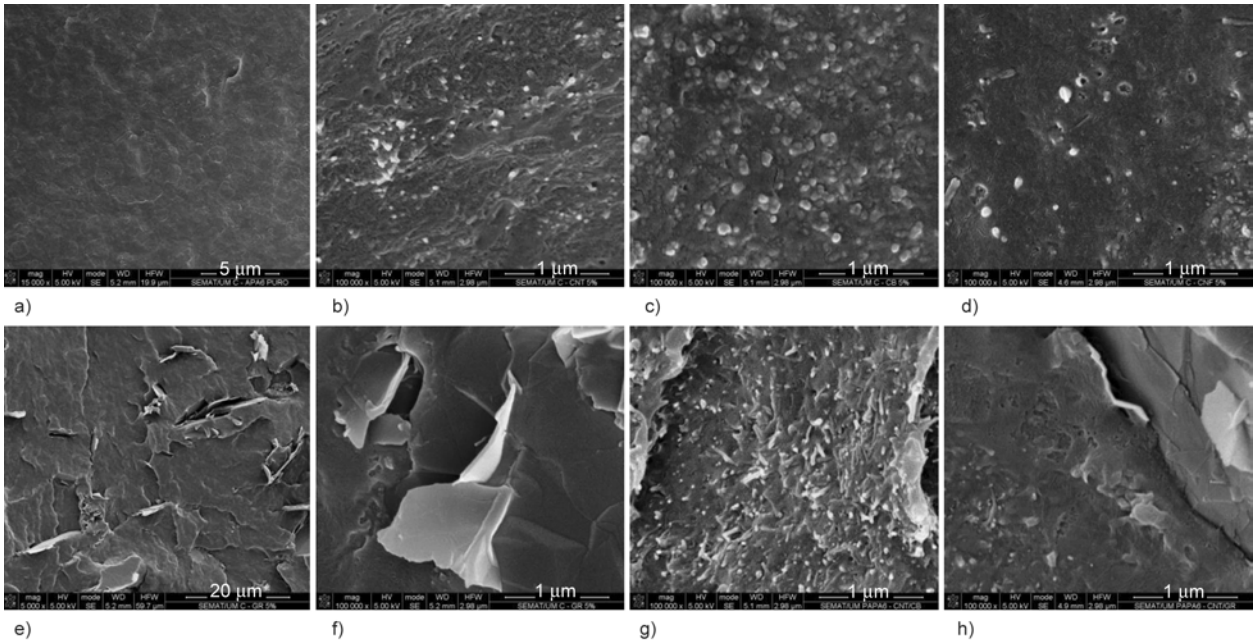


**Figure 4.** Selected SEM micrographs of compression molded plates obtained from PAMC: (a) – PA6; (b) – PA6/CNT 6%; (c) – PA6/CB-6%; (d) – PA6/CNF 6%; (e) – PA6/GR-6%; (f) – magnification of (e); (g) – PA6/CNT-CB 5+5%; (h) – PA6/CNT-GR 5+5%. For sample designation see Table 1.

tallization peaks suggesting the coexistence of $\alpha$- and $\gamma$-PA6 polymorphs. During the second DSC scan (Figure 5c) the small difference in $T_m$ for neat and carbon-loaded PAMC is preserved, whereby the melting peaks of loaded PAMC (especially those of CNF and GR-containing samples) show a shoulder at lower temperature typical of the $\gamma$-PA6 polymorph [45]. In general, all PAMC samples display $T_m$ values with 15–20 °C lower than the hydrolytic or bulk anionic PA6 with similar $M_v$ with $T_m$ = 225 °C.

Figure 6 and Table 2 display the thermal behavior of the composite plates prepared by compression molding of PAMC at 230ºC, *i.e.*, well above their $T_m$. As expected, the differences between the $T_m$ values of the samples during the 1st (Figure 6a) and 2nd (Figure 6b) DSC scans are quite negligible, preserving the higher temperatures of dynamic crystallization of the C-loaded composites.

From Table 2 it can also be seen that, as a rule, the crystallinity index $X_c$ of PAMC measured during the

**Table 2.** DSC data comparison between PAMC and the respective compression molded composites (plate)

| Sample | | 1st DSC scan | | 2nd DSC scan | | Recrystallization* |
|---|---|---|---|---|---|---|
| | | $T_m$ [°C] | $X$ [%] | $T_g$ [°C] | $X$ [%] | $T_c$ [°C] |
| PA6 | PAMC | 211.3 | 35.0 | 34.4 | 20.6 | 151.1 |
| | plate | 212.8 | 24.2 | 46.8 | 21.8 | 159.8 |
| PA6/CB-6 | PAMC | 201.2 | 28.9 | 37.4 | 24.6 | 174.3 |
| | plate | 206.9 | 27.6 | 46.9 | 27.6 | 173.3 |
| PA6/CNT-6 | PAMC | 207.0 | 39.4 | 33.2 | 23.0 | 169.7 |
| | plate | 209.3 | 26.5 | 45.8 | 26.5 | 168.8 |
| PA6/GR-6 | PAMC | 206.1 | 37.9 | 42.9 | 22.8 | 165.8 |
| | plate | 206.6 | 28.8 | 45.5 | 26.8 | 167.4 |
| PA6/CNF-6 | PAMC | 206.2 | 38.1 | 39.2 | 22.5 | 163.3 |
| | plate | 208.6 | 29.1 | 45.8 | 26.8 | 169.0 |
| PA6/CNT-GR 5 + 5 | PAMC | 198.0 | 32.4 | 51.4 | 27.6 | 171.4 |
| | plate | 203.1 | 23.4 | 55.6 | 28.6 | 173.3 |
| PA6/CNT-CB 5 + 5 | PAMC | 206.9 | 30.9 | 41.5 | 21.7 | 171.4 |
| | plate | 200.9 | 30.6 | 42.3 | 25.9 | 173.0 |
| PA6/GR-CB 5+5 | PAMC | 207.9 | 41.4 | 42.1 | 26.7 | 172.9 |
| | plate | 206.3 | 26.8 | 44.6 | 26.5 | 172.9 |

*Determined after 1st DSC scan under fast cooling down.

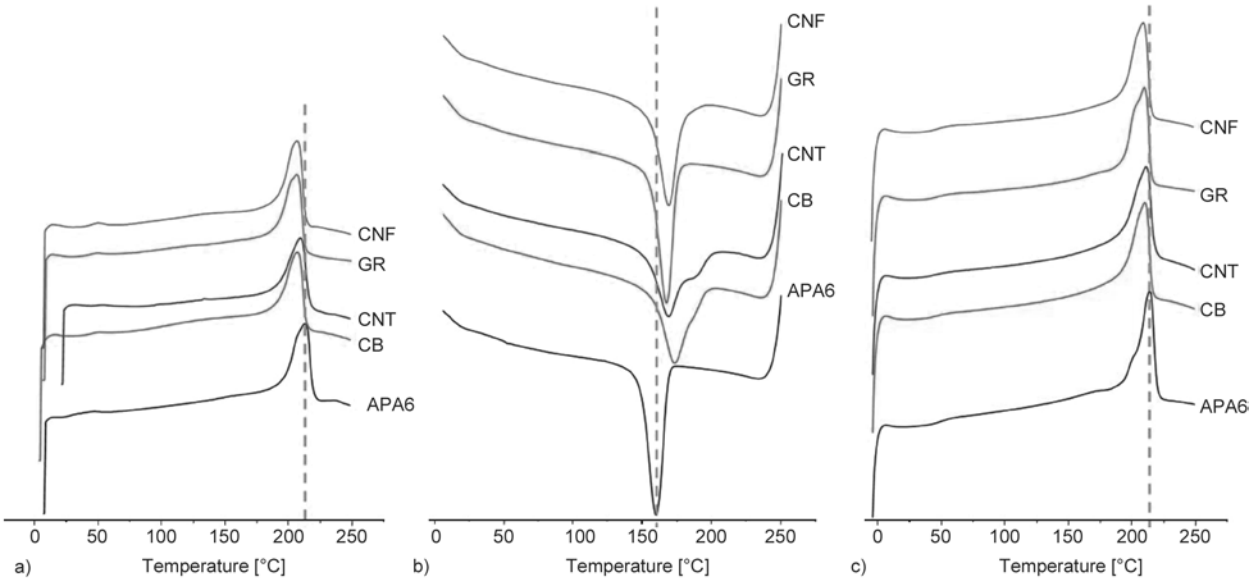


**Figure 5.** DSC traces of loaded PAMC containing 6% of the indicated allotrope: (a) – first DSC scan; (b) – cooling down to 30 °C after 1st scan; (c) – 2nd DSC scan

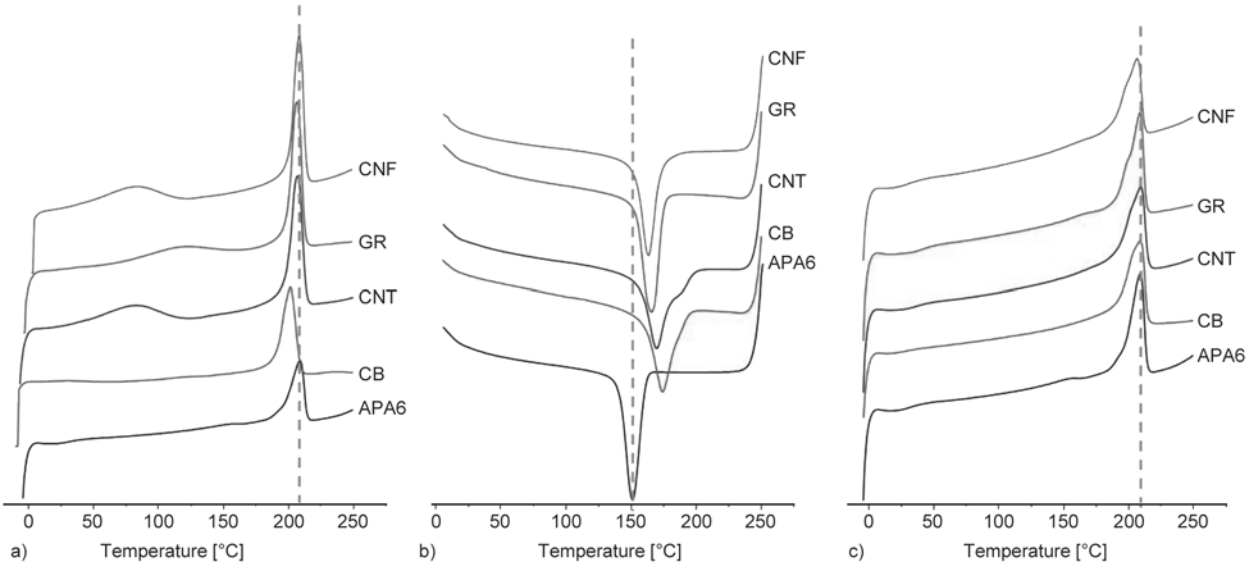


**Figure 6.** DSC traces of compression molded composite plates containing 6% of the indicated allotrope: (a) – first DSC scan; (b) – fast cooling down to 30 °C after 1st scan; (c) – 2nd DSC scan

1st scan is higher than that of the respective compression molded composite. The difference depends on the C-filler and can reach 12–15 °C % as in PA6/GR-CB and PA6/CNT-6 compositions, as well as for the neat PAMC/PA6 plate pair. This difference equalizes after the 2nd scan in the range of 3–4° % for all samples. This observation confirms the previously established fact that the thermal history of the PA6 sample is of prime importance for the crystallinity index [45, 46]. During AAROP, the PAMC samples were synthesized and crystallized at isothermal conditions (~135 °C for one hour) and then cooled gradually to room temperature *i.e.*, no melting occurred. The molded plates were obtained after melting at 230 °C and cooling down with ca. 20 °C/min to room temperature. That is why the second DSC scan of PAMC and the first scan of plates show similar crystallinities. Another comparison based on the data in Table 2 can be made between the glass-transition temperatures $T_g$ of loaded PAMC and their molded composites. The microcapsules show lower $T_g$ values related to a higher segmental mobility, this difference being best expressed in the empty PAMC/neat PA6 pair and in that with composition PA6/CNT-6.

The purpose of the TGA studies of PAMC shown in Figure 7 is to establish the thermal stability of the samples as a function of: (i) carbon load type, (ii) its amount and (iii) the presence of two-component

filler system. The determination of the real C-filler content in the basis of the carbonized residue at 600 °C was discussed previously. Figure 7 shows that all hybrid PAMC display improved thermal stability. In the empty PAMC the thermal degradation starts at $T_S$ = 295 °C and the maximum degradation rate is reached at $T_{MDR}$ = 339 °C, whereas with the best performing PA6/GR-6 microcapsules these values are 316 and 364 °C, respectively. The respective temperatures of the CNT, CNF and CB-loaded PAMC are within ca. 20 °C difference. Increasing the amount of CNT from 2 to 10% (Figure 7b) did not change either $T_S$ or $T_{MDR}$ however a second degradation process was registered with $T_{MDR}$ = 370 °C. The PAMC with two fillers (Figure 7c) displayed better thermostability because of the higher filler content. Notably, PAMC containing the CNT-CB mixture displayed $T_S$ and $T_{MDR}$ values of 310 and 400 °C *i.e.*, 60–65 °C higher than the empty PAMC. This synergism in PAMC with mixed fillers can be interesting in tailoring the thermal stability of PA6/C-allotrope composite materials. The TGA traces of PAMC in Figure 7 do not show significant weight losses at low temperatures typical for the presence of ECL monomer or oligomer products. Together with the average $M_v$ values in Table 1, this is an indication that all PAMC are practically made of high molecular weight PA6.

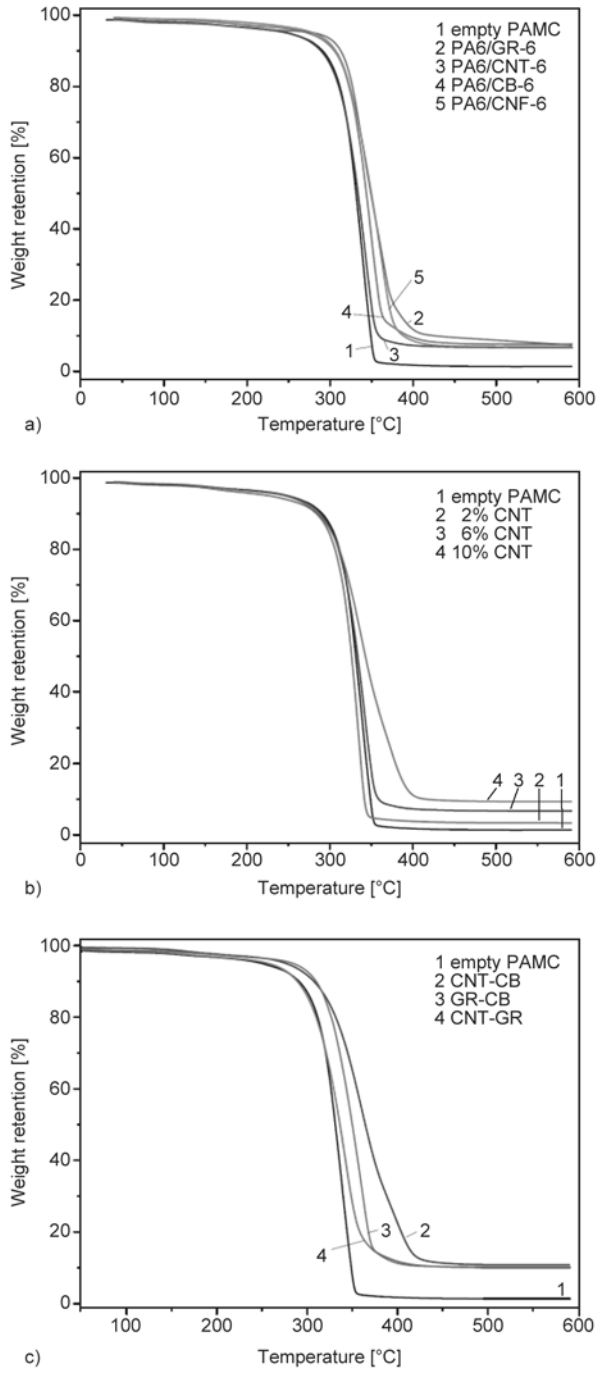


**Figure 7.** TGA traces of PAMC samples (in $N_2$ atmosphere at 10°·min$^{-1}$ heating rate): (a) – as a function of the C-filler type, (b) – as a function of the percentage of CNT, (c) – PAMC with mixed fillers, 5+5%

The crystalline structure of PAMC and the molded plates was additionally studied by XRD (Figure 8, Table 3). As seen from Figure 8a, neat CNT, GR and CNF are crystalline materials that contain clear diffraction peaks, while CB was unable to produce coherent scattering at wide angles and therefore should be considered amorphous. The two reflections at $2\theta$ = 16–17 and 27–28° in CNT correspond to the (002) and (100) crystalline planes. In these same two ranges GR displays multiple and narrower reflections for the (002), (101) and (102)/(003) crystalline planes, which is a proof of more perfect crystallites. With the CNF fillers the (002) and (101) peaks are shifted at slightly lower $2\theta$ positions and are accompanied by diffuse scattering which is an indication of lower and imperfect crystallinity.

The diffraction curves of PAMC with the same amount of C-fillers are presented in Figure 8b and show a clear predominance the monoclinic $\alpha$-PA6 polymorph with its two characteristic reflections at $2\theta$ = 13.2 and 15.6°. They correspond to the $\alpha$200 and $\alpha$002/202 crystal planes formed between adjacent chains by van der Waals forces and H-bonds, respectively. Judging from the slightly lower intensity of the former peak, it seems that in all PAMC the crystal growth along the direction of the van der Waals forces is impeded. The patterns of the compression molded plates with the same composition (Figure 8c) also display the presence of $\alpha$-polymorph however the appearance of a weak shoulder at 9–10°

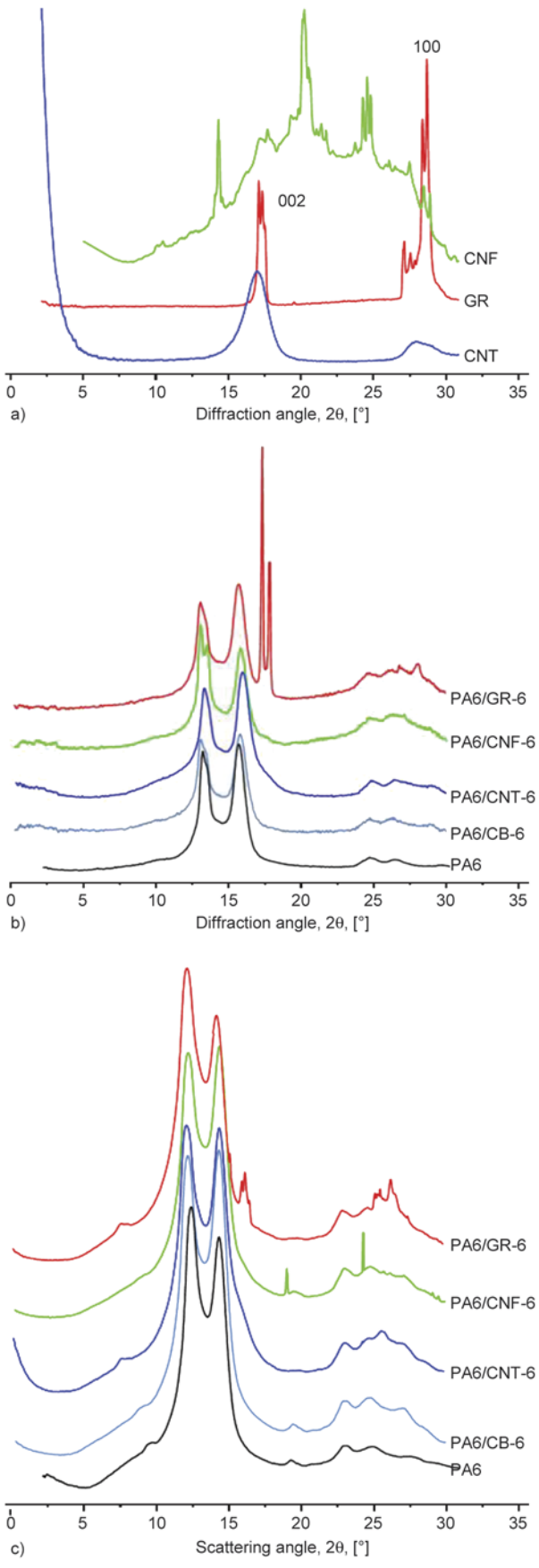


**Figure 8.** Linear WAXS profiles of: (a) – crystalline pure C-allotropes; (b) – PAMC; (c) – molded plates

corresponding to the $\gamma$020 reflection verifies a larger amount of $\gamma$-PA6. Analyzing the intensity of the two $\alpha$-reflections, it seems that only in the GR-containing composite the crystal growth has a preferred direction, which is the H-bond direction. In the CNT, CB and CNF composites it seems that compression molding equalizes the crystal growth in both directions.

Table 3 summarizes the polymorph content, the crystallinity index and the d-spacings of the $\alpha$- and $\gamma$-PA6 polymorphs in the as-prepared PAMC and the respective compression molded plates. These data were obtained by peak-fitting the linear diffraction profiles as previously indicated [47]. Judging by the $\alpha/\gamma$ ratio, it can be concluded that the as-prepared PAMC are up to 3–4 times richer in $\alpha$-PA6 as compared to the molded plates with the same composition, the largest difference being found in the GR-containing samples. The polymorph ratio becomes closer to unity after melt processing which was established in earlier studies on PA6 obtained by bulk AAROP [44]. The analysis of the d-spacings shows that within the PAMC or molded plates datasets the C-filler does not change the unit cell dimension, whereas the transitions from PAMC to molded plates results in an observable increase of these parameters.

Table 4 displays the mechanical properties in tension of the composites produced from PAMC loaded with different amounts and types of carbon fillers. All composites display higher Young's modulus values. The improvement factor *IF* calculated according to Equation (2) is always positive and increases with 25–40% for samples with 10% carbon loads – individual or mixed. The stress at break $\sigma_{br}$ values seems to depend much stronger on the C-filler type. Thus, the samples with 6 and 10 wt% CB as well as the systems with CNT-CB and GR-CB modification showed lower tensile strength as compared to the matrix PA6. The rest of the carbon fillers and notably the multi-walled CNT increased the strength with up to 27%. As expected, the elongation at break $\varepsilon_{br}$ as a rule drops abruptly even with the lowest filler content passing from ductile (neat PA6) to brittle failure. The only exception is the composite with 2% of GR. From all C-fillers only CB affects negatively (alone or in combination with other C-fillers) the composite's tensile strength (Table 4). This might be related to the particulate morphology of

**Table 3.** Polymorph content, WAXS crystallinity and long spacing data extracted from the WAXS profiles in Figure 8

| Sample | | $\alpha$ [%] | $\gamma$ [%] | $X_c$ [%] | $\alpha/\gamma$ | $d_{\alpha(200)}$ [Å] | $d_{\alpha(002)/(202)}$ [Å] | $d_{\gamma(020)}$ [Å] | $d_{\gamma(001)}$ [Å] | $d_{\gamma(200)}$ [Å] |
|---|---|---|---|---|---|---|---|---|---|---|
| PA6 | PAMC | 39.4 | 11.7 | 51.1 | 3.37 | 4.14 | 3.56 | – | 4.12 | 3.81 |
| | plate | 25.9 | 18.5 | 44.4 | 1.40 | 4.48 | 3.89 | 5.86 | 4.46 | 4.21 |
| PA6/CB-6 | PAMC | 34.9 | 8.7 | 43.6 | 4.00 | 4.19 | 3.57 | – | 4.13 | 3.68 |
| | plate | 24.8 | 23.3 | 48.1 | 1.06 | 4.52 | 3.91 | 5.72 | 4.50 | 4.07 |
| PA6/CNT-6 | PAMC | 27.4 | 9.2 | 46.5* | 2.98 | 4.17 | 3.56 | – | 4.11 | 3.89 |
| | plate | 25.5 | 20.5 | 52.1* | 1.24 | 4.50 | 3.89 | 6.42 | 4.44 | 4.17 |
| PA6/GR-6 | PAMC | 32.2 | 5.4 | 59.3* | 6.15 | 4.21 | 3.59 | – | 4.06 | 3.86 |
| | plate | 29.6 | 21.4 | 53.2* | 1.38 | 4.58 | 3.91 | 6.43 | 4.47 | 4.23 |

*For the samples containing GR and CNT, $X_c > \alpha + \gamma$, the difference accounting for the crystalline peaks of the fillers.

**Table 4.** Mechanical properties of composite plates compression molded from loaded PAMC

| Sample designation | Load [wt%] | Young's modulus, $E$ [GPA] | $IF^*$ [%] | Tensile strength, $\sigma_{br}$ [MPa] | $IF^*$ [%] | Deformation at break, $\varepsilon_{br}$ [%] |
|---|---|---|---|---|---|---|
| PA6 | – | 1.72±0.09 | – | 71.8±4.3 | – | 19.2±1.5 |
| PA6/CB | 2 | 2.03±0.15 | 18.0 | 73.1±3.5 | 1.81 | 4.3±0.2 |
| | 6 | 2.27±0.03 | 32.0 | 53.3±3.9 | –25.8 | 2.6±0.3 |
| | 10 | 2.37±0.13 | 37.8 | 60.0±4.5 | –16.4 | 3.6±0.6 |
| PA6/CNT | 2 | 2.09±0.02 | 21.5 | 81.3±1.6 | 13.2 | 9.3±1.8 |
| | 6 | 2.24±0.11 | 30.2 | 91.3±1.3 | 27.1 | 7.3±1.5 |
| | 10 | 2.31±0.10 | 34.3 | 87.2±4.9 | 21.5 | 6.2±1.3 |
| PA6/GR | 2 | 2.01±0.04 | 16.9 | 80.1±1.3 | 11.6 | 19.4±2.9 |
| | 6 | 2.30±0.02 | 33.7 | 84.7±1.7 | 18.0 | 8.6±0.6 |
| | 10 | 2.43±0.08 | 41.3 | 76.9±2.6 | 7.1 | 6.8±1.3 |
| PA6/CNF | 2 | 2.13±0.04 | 23.8 | 74.0±1.5 | 3.1 | 5.6±2.0 |
| | 6 | 2.11±0.11 | 22.7 | 77.3±4.3 | 7.7 | 4.9±0.6 |
| | 10 | 2.14±0.06 | 24.4 | 74.4±4.3 | 3.6 | 4.3±0.4 |
| PA6/CNT-GR | 5 + 5 | 2.33±0.05 | 35.5 | 84.9±2.1 | 18.3 | 6.3±0.2 |
| PA6/CNT-CB | 5 + 5 | 2.38±0.11 | 38.4 | 67.3±3.4 | –6.3 | 3.4±0.3 |
| PA6/GR-CB | 5 + 5 | 2.36±0.13 | 37.2 | 59.1±3.9 | –17.7 | 2.9±0.2 |

*Determined according to Equation (2).

All data are for samples conditioned for more than 10 days at room temperature and 65% relative humidity.

CB and its amorphous structure, whereas CNT, GR and CNF are crystalline materials organized as platelets or fibers with significant aspect ratio.

The d.c. electrical conductivity $\sigma$, the permittivity $\varepsilon'$, the dielectric loss $\varepsilon''$ and the loss factor $\tan\delta = \varepsilon''/\varepsilon'$ were determined for all composites produced from compression molded PAMC (Figure 9, Table 5) using Equation (3) and (4). As expected, neat PA6 is insulator with $\sigma$ values of above $10^{-10}$ S/m. The well-dispersed according to SEM data CB and CNT nanofillers with effective loads of 6–10 wt% result in a notable growth of $\sigma$ with 8–9 decades reaching values characteristic of semiconductors. Mixtures of carbon allotrope fillers such GR/CNT and especially CB/CNT 5 + 5 wt% also result in $\sigma$ values of ca. $10^{-1}$ S/m, which is an indication that a part of the expensive CNTs can be substituted by the much cheaper GR or CB maintaining the good conductivity values. Similar synergism related to conductivity

**Table 5.** Electrical properties of PA6 hybrid composites obtained by compression molding of loaded PAMC. For more details see the text.

| Sample designation | Load [%] | Conductivity, $\sigma$ [S·m$^{-1}$] | Permitivity, $\varepsilon'$ | Loss factor, $\tan\delta$ |
|---|---|---|---|---|
| PA6 | – | $6.21\cdot10^{-10}$ | $6.50\cdot10^{0}$ | $5.31\cdot10^{-2}$ |
| PA6/CB | 2 | $4.57\cdot10^{-9}$ | $1.11\cdot10^{1}$ | $8.39\cdot10^{-2}$ |
| | 6 | $1.99\cdot10^{-5}$ | $5.38\cdot10^{1}$ | $4.19\cdot10^{-1}$ |
| | 10 | $2.02\cdot10^{-2}$ | $5.32\cdot10^{2}$ | $1.97\cdot10^{0}$ |
| PA6/CNT | 2 | $6.58\cdot10^{-5}$ | $1.53\cdot10^{1}$ | $1.64\cdot10^{-1}$ |
| | 6 | $1.17\cdot10^{-2}$ | $3.48\cdot10^{1}$ | $2.90\cdot10^{-2}$ |
| | 10 | $1.26\cdot10^{-1}$ | $3.93\cdot10^{2}$ | $1.19\cdot10^{2}$ |
| PA6/GR | 2 | $5.97\cdot10^{-9}$ | $7.27\cdot10^{-2}$ | $6.99\cdot10^{-2}$ |
| | 6 | $3.42\cdot10^{-9}$ | $9.60\cdot10^{0}$ | $1.01\cdot10^{-1}$ |
| | 10 | $3.51\cdot10^{-9}$ | $1.23\cdot10^{1}$ | $1.13\cdot10^{-1}$ |
| PA6/CNF | 2 | $3.07\cdot10^{-9}$ | $8.77\cdot10^{0}$ | $9.51\cdot10^{-2}$ |
| | 6 | $6.55\cdot10^{-6}$ | $2.90\cdot10^{1}$ | $3.72\cdot10^{-1}$ |
| | 10 | $1.13\cdot10^{-6}$ | $3.95\cdot10^{1}$ | $3.23\cdot10^{-1}$ |
| CNT/GR | 5 + 5 | $2.22\cdot10^{-2}$ | $4.80\cdot10^{1}$ | $1.89\cdot10^{1}$ |
| CNT/CB | | $1.16\cdot10^{-1}$ | $1.42\cdot10^{3}$ | $5.53\cdot10^{0}$ |
| GR/CB | | $3.12\cdot10^{-9}$ | $3.10\cdot10^{1}$ | $2.20\cdot10^{-1}$ |

was reported recently by Socher *et al*. for of CNT and CB fillers in PA12 matrices [3]. The CNF filler alone produced only a slight increase of $\sigma$ (3 decades

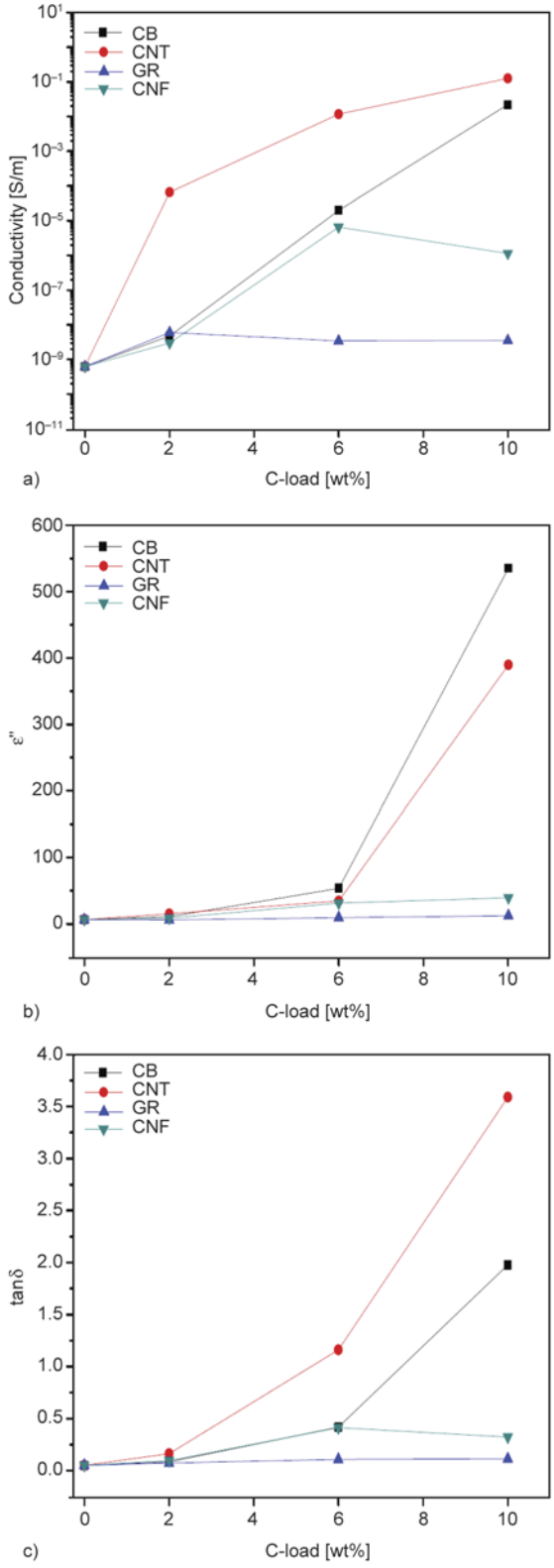


**Figure 9.** Electrical properties of molded PA6/C-filler composites as a function of composition: (a) – conductivity, $\sigma$ [S/m]; (b) – permittivity, $\varepsilon'$; (c) – loss factor tan$\delta$

at 10 wt% load), while GR conveyed no additional conductivity to the matrix material even at the highest loads (Table 5). As seen from Figure 9a, the slope of the semi-logarithmic curves $\log_{10}(\sigma) = f$[C-content] depends on the type of the filler being the steepest with CNT. Relating these results to the observation of morphology of CNT, CB and CNF hybrids in Figure 4, it can be inferred that the nanometric size of the load particles and their homogeneous distribution within the PA6 matrix are important factors enhancing the electrical conductivity. Apparently, the aspect ratio of the carbon particles being the highest in the CNT seems also to contribute to the increase. As regards the $\varepsilon'$ and tan$\delta$ values (Figures 9b and 9c, Table 5) they can be controlled by changing appropriately the C-filler type and concentration. Thus, PA6/CB-10 wt% and PA6/CNT-CB samples possess high conductivity and high permittivity combined with relatively low loss factor, while in the PA6/CNT-10 wt% sample the loss factor is 100 times larger at a similar conductivity and permittivity values, allowing in this way to tailor composite electrical properties for specific applications.

## 4. Conclusions

A one-step *in-situ* process was used to synthesize porous PAMC loaded with four different C-fillers based on suspension AAROP of ECL in a 1:1 toluene/xylene mixed solvent. The PAMC formation most probably passes through entrapping of the load particles into initially formed viscous aggregates of growing macromolecules followed by coalescence and crystallization. This novel method is characterized by short polymerization times of ca. 60 min, low polymerization temperatures (~135 °C) and high, reproducible conversion to high molecular weight PAMC. It can introduce high loads of one or more powdered C-fillers into PAMC, and is suitable for scale-up to industrial production. Transforming these loaded PAMC into composites by conventional compression molding produces good homogenization of the conductive filler without the need of its functionalization. This results in improved mechanical properties of the hybrid composite even at high filler loads. There are all indications that preparing PAMC with mixed C-loads could be a way to manipulate the whole set of electric and dielectric properties of the molded composites adjusting them to different target applications.

## Acknowledgements

The authors gratefully acknowledge the financial support of the Portuguese Foundation for Science and Technology (FCT) by the Strategic Project LA25/2013-2014, the post-doctoral grant SFRH/BPD/45252/2008 and the grant by the MiNaXS beamline of DESY – Hamburg, Germany. This work was also supported by FEDER through the COMPETE Program and by the FCT in the framework of the Strategic Project PEST-C/FIS/UI607/2013. P. Martins thanks FCT for the SFRH/BPD/96227/2013 grant.

## References

[1] György I.: Conducting polymers: A new era in electrochemistry. Springer-Verlag, Berlin (2008).

[2] Hoppe H., Sariciftci N. S.: Organic solar cells: An overview. Journal of Materials Research, **19**, 1924–1945 (2004).
DOI: 10.1557/JMR.2004.0252

[3] Socher R., Krause B., Hermasch S., Wursche R., Pötschke P.: Electrical and thermal properties of polyamide 12 composites with hybrid fillers systems of multiwalled carbon nanotubes and carbon black. Composites Science and Technology, **71**, 1053–1059 (2011).
DOI: 10.1016/j.compscitech.2011.03.004

[4] Popov C.: Nanostructured carbon materials. in 'Functional properties of nanostructured materials' (eds.: Kassing R., Petkov P., Kulish W., Popov C.) Springer, Dordrecht, 387–398 (2006).
DOI: 10.1007/1-4020-4594-8_34

[5] Liu H., Hou L., Peng W., Zhang Q., Zhang X.: Fabrication and characterization of polyamide 6-functionalized graphene nanocomposite fiber. Journal of Materials Science, **47**, 8052–8060 (2012).
DOI: 10.1007/s10853-012-6695-5

[6] Steurer P., Wissert R., Thomann R., Mülhaupt R.: Functionalized graphenes and thermoplastic nanocomposites based upon expanded graphite oxide. Macromolecular Rapid Communications, **30**, 316–327 (2009).
DOI: 10.1002/marc.200800754

[7] Tsubokawa N.: Functionalization of carbon black by surface grafting of polymers. Progress in Polymer Science, **17**, 417–470 (1992).
DOI: 10.1016/0079-6700(92)90021-P

[8] Mitchell C. A., Bahr J. L., Arepalli S., Tour J. M., Krishnamoorti R.: Dispersion of functionalized carbon nanotubes in polystyrene. Macromolecules, **35**, 8825–8830 (2002).
DOI: 10.1021/ma020890y

[9] Bahr J. L., Tour J. M.: Covalent chemistry of single-wall carbon nanotubes. Journal of Materials Chemistry, **12**, 1952–1958 (2002).
DOI: 10.1039/B201013P

[10] Dyke C. A., Tour J. M.: Solvent-free functionalization of carbon nanotubes. Journal of the American Chemical Society, **125**, 1156–1157 (2003).
DOI: 10.1021/ja0289806

[11] Socher R., Krause B., Müller M. T., Boldt R., Pötschke P.: The influence of matrix viscosity on MWCNT dispersion and electrical properties in different thermoplastic nanocomposites. Polymer, **53**, 495–504 (2012).
DOI: 10.1016/j.polymer.2011.12.019

[12] Bae W-S., Kwon O. J., Kim B. C., Chae D. W.: Effects of multi-walled carbon nanotubes on rheological and physical properties of polyamide-based thermoplastic elastomers. Korea-Australia Rheology Journal, **24**, 221–227 (2012).
DOI: 10.1007/s13367-012-0027-9

[13] Arboleda L., Ares A., Abad M. J., Ferreira A., Costa P., Lanceros-Mendez S.: Piezoresistive response of carbon nanotubes-polyamides composites processed by extrusion. Journal of Polymer Research, **20**, 1–11 (2013).
DOI: 10.1007/s10965-013-0326-y

[14] Krause B., Ritschel M., Täschner Ch., Oswald S., Gruner W., Leonhardt A., Pötschke P.: Comparison of nanotubes produced by fixed bed and aerosol-CVD methods and their electrical percolation behaviour in melt mixed polyamide 6.6 composites. Composites Science and Technology, **70**, 151–160 (2010).
DOI: 10.1016/j.compscitech.2009.09.018

[15] Krause B., Pötschke P., Häußler L.: Influence of small scale melt mixing conditions on electrical resistivity of carbon nanotube-polyamide composites. Composites Science and Technology, **69**, 1505–1515 (2009).
DOI: 10.1016/j.compscitech.2008.07.007

[16] Ferreira T., Paiva M. C., Pontes A. J.: Dispersion of carbon nanotubes in polyamide 6 for microinjection moulding. Journal of Polymer Research, **20**, 301–309 (2013).
DOI: 10.1007/s10965-013-0301-7

[17] Leer C., van Hattum F. W. J., Gaspar-Cunha A., Carneiro O. S., Bernardo C. A.: Tailored shear extrusion of carbon nanofibre/polyamide composites and its effect on electrical percolation threshold. Plastics, Rubber and Composites, **35**, 268–275 (2006).
DOI: 10.1179/174328906X146531

[18] Coleman J. N., Khan U., Blau W. J., Gun'ko Y. K.: Small but strong: A review of the mechanical properties of carbon nanotube–polymer composites. Carbon, **44**, 1624–1652 (2006).
DOI: 10.1016/j.carbon.2006.02.038

[19] Salmoria G. V., Paggi R. A., Lago A., Beal V. E.: Microstructural and mechanical characterization of PA12/MWCNTs nanocomposite manufactured by selective laser sintering. Polymer Testing, **30**, 611–615 (2011).
DOI: 10.1016/j.polymertesting.2011.04.007

[20] Brosse A-C., Tencé-Girault S., Piccione P. M., Leibler L.: Effect of multi-walled carbon nanotubes on the lamellae morphology of polyamide-6. Polymer, **49**, 4680–4686 (2008).
DOI: 10.1016/j.polymer.2008.08.003

[21] Koysuren O., Yesil S., Bayram G.: Effect of composite preparation techniques on electrical and mechanical properties and morphology of nylon 6 based conductive polymer composites. Journal of Applied Polymer Science, **102**, 2520–2526 (2006).
DOI: 10.1002/app.24654

[22] Pinto G., López-González C., Jimenez-Martín A.: Polymer composites prepared by compression molding of a mixture of carbon black and nylon 6 powder. Polymer Composites, **20**, 804–808 (1999).
DOI: 10.1002/pc.10404

[23] Tchoudakov R., Breuer O., Narkis M., Siegmann A.: Conductive polymer blends with low carbon black loading: Polypropylene/polyamide. Polymer Engineering and Science, **36**, 1336–1346 (1996).
DOI: 10.1002/pen.10528

[24] Socher R., Krause B., Boldt R., Hermasch S., Wursche R. Pötschke P.: Melt mixed nano composites of PA12 with MWNTs: Influence of MWNT and matrix properties on macrodispersion and electrical properties. Composites Science and Technology, **71**, 306–314 (2011).
DOI: 10.1016/j.compscitech.2010.11.015

[25] Wu X., Qiu J., Liu P., Sakai E.: Preparation and characterization of polyamide composites with modified graphite powders. Journal of Polymer Research, **20**, 284–291 (2013).
DOI: 10.1007/s10965-013-0284-4

[26] Kim S. R., Poostforush M., Kim J. H., Lee S. G.: Thermal diffusivity of *in-situ* exfoliated graphite intercalated compound/polyamide and graphite/polyamide composites. Express Polymer Letters, **6**, 476–484 (2012).
DOI: 10.3144/expresspolymlett.2012.50

[27] Gong L., Yin B., Li L-P., Yang M-B.: Nylon-6/graphene composites modified through polymeric modification of graphene. Composites Part B: Engineering, **73**, 49–56 (2015).
DOI: 10.1016/j.compositesb.2014.12.009

[28] Chou A., Böcking T., Singh N. K., Gooding J. J.: Demonstration of the importance of oxygenated species at the ends of carbon nanotubes for their favorable electrochemical properties. Chemical Communications, **7**, 842–844 (2005).
DOI: 10.1039/B415051A

[29] Lellinger D., Xu D., Ohneiser A., Skipa T., Alig I.: Influence of the injection moulding conditions on the in-line measured electrical conductivity of polymer–carbon nanotube composites. Physica Status Solidi (B), **245**, 2268–2271 (2008).
DOI: 10.1002/pssb.200879619

[30] O'Neill A., Bakirtzis D., Dixon D.: Polyamide 6/graphene composites: The effect of *in situ* polymerisation on the structure and properties of graphene oxide and reduced graphene oxide. European Polymer Journal, **59**, 353–362 (2014).
DOI: 10.1016/j.eurpolymj.2014.07.038

[31] Kelar K.: Polyamide 6 modified with fullerenes, prepared via anionic polymerization of ε-caprolactam. Polimery, **51**, 415–424 (2006).

[32] Zuev V. V., Ivanova Y. G.: Mechanical and electrical properties of polyamide-6-based nanocomposites reinforced by fulleroid fillers. Polymer Engineering and Science, **52**, 1206–1211 (2012).
DOI: 10.1002/pen.22188

[33] Dencheva N., Gaspar H., Filonovich S., Lavrova O., Busani T., Bernardo G., Denchev Z.: Fullerene-modified polyamide 6 by *in situ* anionic polymerization in the presence of PCBM. Journal of Materials Science, **49**, 4751–4764 (2014).
DOI: 10.1007/s10853-014-8174-7

[34] Zuev V. V., Shlikov A. V.: Polyamide 12/fullerene C60 composites: Investigation on their mechanical and dielectric properties. Journal of Polymer Research, **19**, 9925/1–9925/6 (2012).
DOI: 10.1007/s10965-012-9925-2

[35] Zuev V. V., Kostromin S. V., Shlykov A. V.: Mechanics of polymer nanocomposites modified with fulleroid nanofillers. Polymer Science Series A, **52**, 532–536 (2010).
DOI: 10.1134/S0965545X10050081

[36] Denchev Z., Dencheva N.: Polyamide microcapsules and method to produce the same. Portuguese Patent 107879, Portugal (2014)

[37] Dencheva N., Denchev Z., Lanceros-Méndez S., Sanz T. E.: One-step *in situ* synthesis of polyamide microcapsules with inorganic payload and their transformation into responsive thermoplastic composite materials. Macromolecular Materials and Engineering, in press (2015).
DOI: 10.1002/mame.201500194

[38] Rusu Gh., Ueda K., Rusu E., Rusu M.: Polyamides from lactams by centrifugal molding via anionic ring-opening polymerization. Polymer, **42**, 5669–5678 (2001).
DOI: 10.1016/S0032-3861(01)00059-3

[39] Roda J.: Polyamides. in 'Handbook of ring-opening polymerization' (eds.: Dubois P., Coulembier O., Raquez J-M.) Wiley-VCH, Weinheim, 165–196 (2009).
DOI: 10.1002/9783527628407.ch7

[40] Dan F., Vasiliu-Oprea C.: Anionic polymerization of caprolactam in organic media. Morphological aspects. Colloid and Polymer Science, **276**, 483–495 (1998).
DOI: 10.1007/s003960050270

[41] Vasiliu-Oprea C., Dan F.: On the relation between synthesis parameters and morphology of anionic polycaproamide obtained in organic media. II. Influence of the Na [O $(CH_2)_2OCH_3]_2AlH_2$/aliphatic diisocyanates catalytic systems. Journal of Applied Polymer Science, **64**, 2575–2583 (1997).
DOI: 10.1002/(SICI)1097-4628(19970627)64:13<2575::AID-APP11>3.0.CO;2-Z

[42] Dan F., Vasiliu-Oprea C.: On the relationship between synthesis parameters and morphology of the anionic polycaproamide obtained in organic media. III. Macroporous powders obtained using $CO_2$ and carbodiimides as activating compounds. Journal of Applied Polymer Science, **67**, 231–243 (1998).
DOI: 10.1002/(SICI)1097-4628(19980110)67:2<231::AID-APP5>3.0.CO;2-V

[43] Dencheva N., Denchev Z.: Clay distribution and crystalline structure evolution in polyamide 6/montmorillonite composites prepared by activated anionic polymerization. Journal of Applied Polymer Science, **130**, 1228–1238 (2013).
DOI: 10.1002/app.39274

[44] Dencheva N., Denchev Z., Pouzada A. S., Sampaio A. S., Rocha A. M.: Structure–properties relationship in single polymer composites based on polyamide 6 prepared by in-mold anionic polymerization. Journal of Materials Science, **48**, 7260–7273 (2013).
DOI: 10.1007/s10853-013-7546-8

[45] Fornes T. D., Paul D. R.: Crystallization behavior of nylon 6 nanocomposites. Polymer, **44**, 3945–3961 (2003).
DOI: 10.1016/S0032-3861(03)00344-6

[46] Pesetskii S. S., Jurkowski B., Olkhov Y. A., Bogdanovich S. P., Koval V. N.: Influence of a cooling rate on a structure of PA6. European Polymer Journal, **41**, 1380–1390 (2005).
DOI: 10.1016/j.eurpolymj.2004.12.009

[47] Dencheva N., Nunes T., Oliveira M. J., Denchev Z.: Microfibrillar composites based on polyamide/polyethylene blends. 1. Structure investigations in oriented and isotropic polyamide 6. Polymer, **46**, 887–901 (2005).
DOI: 10.1016/j.polymer.2004.11.105

*eXPRESS Polymer Letters Vol.10, No.2 (2016) 176–186*
*Available online at www.expresspolymlett.com*
*DOI: 10.3144/expresspolymlett.2016.16*

# Biocomposites based on poly(lactic acid)/willow-fiber and their injection moulded microcellular foams

*M. T. Zafar[1], N. Zarrinbakhsh[2,3], A. K. Mohanty[2,3], M. Misra[2,3], S. N. Maiti[1], A. K. Ghosh[1*]*

[1]Centre for Polymer Science and Engineering, Indian Institute of Technology Delhi, 110 016 New Delhi, India
[2]Bioproducts Discovery and Development Centre, Department of Plant Agriculture, Crop Science Building, University of Guelph, Guelph, ON, N1G 2W1, Canada
[3]School of Engineering, Thornbrough Building, University of Guelph, Guelph, ON, N1G 2W1, Canada

*Received 29 July2015; accepted in revised form 28 September 2015*

**Abstract.** Natural fiber reinforced biocomposites have recently attracted many researchers because of their biodegradability, cost effectiveness and ecofriendliness. The present study investigates the properties of willow-fiber reinforced poly(lactic acid) based composites and their foam processability. Microcellular foams of the composites were prepared by foam injection moulding using nitrogen gas as the blowing agent. The effects of willow-fiber addition on the morphology, mechanical properties, thermal stability, crystallization, and heat deflection temperature (HDT) were studied. At 30 weight percent [wt%] willow-fiber content, unfoamed composites showed good improvement in specific tensile and flexural moduli. Addition of willow-fiber increased crystallinity and the rate of crystallization and yielded narrow crystallite size distribution as observed by differential scanning calorimetry (DSC). Scanning electron microscopy (SEM) results of the foamed composites revealed that increase in willow-fiber content caused smaller average cell size and higher cell density. Specific notch impact strength of foamed composites at both 20 and 30 wt% willow-fiber content showed increasing trend compared to that of their unfoamed counterparts.

***Keywords:*** *biopolymers, biocomposites, reinforcements, foam injection moulding, microcellular foam*

## 1. Introduction

Poly(lactic acid) (PLA), a biobased polymer, has properties comparable to that of petroleum based plastics but has limited commercial applications due to its higher cost and narrow processing window [1–4]. As the main drawbacks associated with PLA are low toughness, low impact strength, low crystallinity, and slower crystallization rate: preparation of biocomposites using natural fibers followed by foaming can be an efficient way to overcome these drawbacks of PLA. Nowadays technology based on the reinforcement of the polymer matrix using natural fibers is focusing on creating lightweight materials with lower cost, higher modulus and higher crystallinity. However, this cost effectiveness is achieved at the loss of other valuable properties as the incorporation of cellulosic natural fibers makes the polymer matrix brittle and also decreases the impact strength [5]. As a possible solution, foaming of these biocomposites is expected to improve the impact strength and toughness.

Foamed materials show specific properties, such as lightweight, low thermal conductivity, high surface area, etc. There are several techniques available for creating porous structure in the polymer matrix e.g. – salt leaching, freeze drying, gas foaming, etc. Among all, gas foaming is the simplest and most commonly used method to prepare porous polymeric materials [6]. During the gas foaming process, initially the gas is incorporated inside the polymer

*Corresponding author, e-mail: anupkghosh@gmail.com

matrix which later on releases and leaves micro cells inside the matrix. Polymeric foams can be open or close cell type. In open cell structure, the neighboring cells are interconnected while in closed cell structure all cells are well separated by cell walls. Open cell foams are generally more flexible than closed-cell foams. The blowing agents used for the foaming are either physical or chemical blowing agents. Chemical blowing agents undergo thermal decomposition reactions and evolve the foaming gases while physical blowing agents are themselves the gases [7]. Foaming reduces the brittleness and increases the impact resistance of the biocomposites along with significant improvement in the expansion ratio and weight reduction. The high expansion ratio of the foamed biocomposites helps in reducing the material cost in mass production of plastic parts. The expansion ratio, which is a function of the cell-size and cell-density, is the crucial factor in controlling the mechanical performance of the foamed biocomposites. The increase in cell-size beyond a limit causes reduction in the mechanical properties. Therefore the optimization between the cell-size i.e. the expansion ratio and the mechanical properties is a challenging task and offers a huge potential for the research activities.

The microcellular injection moulding process utilizes physical blowing agents – mainly $N_2$ or $CO_2$. These gases are used as supercritical fluid to produce microcells. There are a lot of challenges in working with microcellular injection moulding process because of the dynamic nature of the procedure. Most of the time it becomes difficult to get the desired cell morphology (i.e. high cell density and small average cell size) and often large and non-uniform cell size results due to the lack of control on the process [8].

Willow biomass is abundantly found in moist soils in cold temperate regions of the northern hemisphere. It is an energy crop which grows very fast and harvested using advanced agricultural tools. The easy availability, abundance and fast growing capability makes the willow-fiber most prominent cellulosic filler to meet the growing demand of the biocomposites in commodity and industrial applications. Even then the area of biodegradable polymer biocomposites based on willow-fiber is almost unexplored. Therefore, the present research work unravels the potential of the willow-fiber as a natural fiber reinforcement as well as heterogeneous nucleating agent in the foaming process of biocomposites.

The present research work comprises of two stages: 1) Processing of biocomposites using extruder and 2) injection molding of the prepared biocomposites by two separate processes – one by conventional injection molding without foaming module and other with the foaming module on the same injection molding machine to prepare unfoamed and foamed samples respectively, which were further characterized by various techniques.

## 2. Experimental

### 2.1. Materials

Poly(lactic acid) (PLA) 3001D was procured from NatureWorks® LLC, USA. As per the material data sheet it had specific gravity of 1.24 and melt flow index of 22 g/10 min (210 °C, 2.16 kg). The glass transition temperature was 60–63 °C and melting temperature was 170 °C. Willow-fiber (biomass-willow) were harvested in December 2009 at the Guelph Turf Grass Institute (GTI), Guelph, ON, Canada, and pelletized at the Crosswood Farm without using any additive and was used as received.

### 2.2. Composite processing

Before processing, PLA was dried at 70 °C under vacuum for 24 hours. Willow-fiber was dried by keeping them inside the hot air drier at 80 °C for 48 hours. PLA and willow-fiber were then compounded in a co-rotating twin screw extruder from Lab Tech Engineering Company Ltd., Thailand, with $L/D$ = 32, and screw diameter = 26 mm. The screw speed was 100 rpm. PLA and willow-fiber were fed through different feeders (feeder-1 and feeder-2) and the feeder speeds were calibrated in order to get the desired percentage of PLA and willow-fiber. The extruder temperature was set in accordance with predetermined temperature profile (zone 1–zone 8: 140, 160, 180, 190, 200, 200, 200, 200 °C). After extrusion, composite strands were chopped into small pellets by a pelletizer and dried in a vacuum oven for 24 hours at 80 °C. PLA/willow-fiber composites at willow-fiber content of 20 and 30 wt% and virgin PLA as a reference material were extruded.

### 2.3. Preparation of unfoamed and foamed samples

Samples of the composites, extruded PLA and virgin PLA were injection moulded using an Arburg Allrounder 370 S, 77 tons injection moulding machine equipped with Mucell® module from Trexel Inc.

**Table 1.** Processing conditions used for the Injection moulding process

| Conditions | Conventional injection moulding | Mucell® (foam) injection moulding |
|---|---|---|
| Injection pressure | 1000 bar | 1000 bar |
| Injection temperature | 200 °C | 200 °C |
| Injection speed | 35–45 mm/sec | 35–45 mm/sec |
| Packing pressure | 700 bar | – |
| Packing time | 9.25 sec | – |
| Mould temperature | 24 °C | 24 °C |
| Cooling time | 55 sec | 55 sec |
| Supercritical fluid (SCF) | – | 0.69 [%] |
| SCF flow rate | – | 0.19 kg/hrs |
| SCF delivery pressure | – | 2800 Psi |
| SCF injection time | – | 3.5sec |

Before moulding, all materials were dried properly in order to remove the moisture. The samples were moulded at the processing conditions indicated in Table 1. While working with Mucell® process to form the foamed samples, $N_2$ gas was used as the supercritical fluid and inserted inside the barrel during the screw recovery process. After moulding, packing pressure was eliminated to allow the nucleation and subsequent cells growth expands the parts and provides the essential pressure to pack it out against the mould walls [9]. With conventional injection moulding no $N_2$ gas was used and after the moulding, packing pressure was applied. A mould of ASTM standard for tensile, flexural and impact test bars was used.

## 2.4. Characterization techniques

### 2.4.1. Scanning electron microscopy (SEM)

Cryogenically fractured foamed and unfoamed samples surfaces were studied by SEM (Inspect S-570) (FEI Company) and Zeiss EVO 18 instruments. Prior to scanning the fractured surfaces were gold coated. Obtained images were analyzed by ImageJ software.

### 2.4.2. Characterization of microcellular foamed samples

Density measurements of foamed ($\rho_f$) and unfoamed ($\rho_u$) samples were performed using Alfa Mirage Electronic Densimeter (MD-300S) in which distilled water was used as the reference fluid. For each sample in order to minimize the error density measurement was conducted at least five times and average values were taken. In order to determine the density reduction or void fraction ($V_f$) Equation (1) was used while Equation (2) was used to determine the volume expansion ratio ($\phi$) [3, 5, 6, 10]:

$$V_f[\,\%\,] = \frac{\rho_u - \rho_f}{\rho_u} \cdot 100 \tag{1}$$

$$\phi = \frac{\rho_u}{\rho_f} = \frac{1}{1 - V_f} \tag{2}$$

Equation (3) was used to calculate the Foam cell density ($N_f$) [6, 10]:

$$N_f = \left(\frac{n}{A}\right)^{3/2} \cdot \phi \tag{3}$$

where $A$ (in $cm^2$) is the area taken from the SEM images and $n$ represents the number of the cells.

### 2.4.3. Mechanical properties

Tensile test of all the samples were performed according to the ASTM D638 test procedure at the cross head speed of 5 mm/min on Instron 3382 instrument. Flexural testing of all compositions were also completed on the same instrument following ASTM D790 test method at the cross head speed of 14 mm/min. Impacts testing of all the samples were completed as per the ASTM D256 test method on an impact tester ((TMI) model 43-02-01). In order to calculate the specific flexural strength, specific flexural modulus, specific tensile strength, specific tensile modulus, and specific impact strength, the tested flexural strength, flexural modulus, tensile strength, tensile modulus and impact properties were divided by the densities of the respective samples.

### 2.4.4. Thermogravimetric analysis (TGA)

The TGA study was done at 30–600 °C on TA Instruments (TGA Q-500) analyzer at the rate of 20 °C·min$^{-1}$ in a nitrogen atmosphere.

### 2.4.5. Differential scanning calorimetry (DSC)

DSC studies of all foamed and unfoamed injection moulded samples were performed with a TA Instrument (DSC Q-200) analyzer at 10 °C/min scan rate and the values from the 1st heating cycle were reported. The glass transition temperature ($T_g$), cold crystallization peak temperature ($T_{cc}$), melting temperature ($T_m$), and enthalpy of melting ($\Delta H_m$), were analyzed for all the samples using Universal Analysis software from TA Instruments. Percentage crystallinities of all the samples were calculated using Equation (4):

$$X_c = \frac{\Delta H_m - \Delta H_{cc}}{\Delta H_{m^\circ}} \cdot \frac{100}{W_f} \tag{4}$$

where $X_c$ is the crystallinity [%], $\Delta H_m$ the heat of melting, $\Delta H_{cc}$ the heat of cold crystallization, $\Delta H_{m^\circ}$ heat of melting of 100% crystalline PLA samples (considered as $\Delta H_{m^\circ}$ = 93 J/g), and $W_f$ the PLA weight fraction in the composite [11, 12]. From the DSC cold crystallization peak, slope of the peak ($S_p$) (at lower temperature side) as a measure of rate of crystallization and peak width at a half height ($\Delta W_d$) as a measure of crystallite size distribution were also calculated. A schematic, representing parameters evaluated from DSC cold crystallization peak is presented in Figure 1 [13].

#### 2.4.6. Heat deflection temperature (HDT)

In order to determine the HDT of all foamed and unfoamed samples dynamic mechanical analyzer of the TA instrument (DMA Q-800) was used. The samples were prepared in the form of rectangular bars of dimensions 50×3.2×12.8 mm$^3$. The tests were conducted at three point bending mode using a load of 66 psi (0.455 MPa). During the test samples were heated from 30 to 70 °C at a rate of 2 °C/min. HDT is the temperature at which deflection of 0.25 mm occurred for a given sample at specified conditions as per ASTM D648 test method [14].

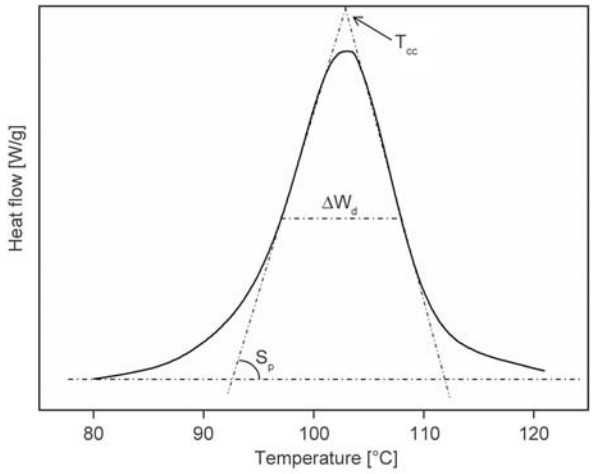


**Figure 1.** Schematic representation of DSC cold crystallization peak parameters

## 3. Results and discussion

### 3.1. Morphology study by SEM

#### 3.1.1. Microstructure of the composites

The SEM images of the willow-fiber are shown in Figure 2. It can be observed from the figure that the willow-fiber are in the form of bundles of small fibers with dimension ranging between 500–2000 μm in length and 250–300 μm in diameter with rough surface morphology. The fractured surfaces of the composites were viewed to analyze the mechanism of failure and the possible interaction between PLA matrix and willow-fiber.

The fractured surfaces of PLA/willow-fiber (80/20) and (70/30) composites are shown in Figure 3. SEM images revealed uniform distribution of fibers in both the composites. Many voids inside the matrix as well as spaces between willow-fiber and polymer matrix were observed. Voids inside the matrix might have been generated because of the removal of the willow-fiber at the time of cryogenic fracture of the samples. Both observations, voids inside the matrix and spaces between willow-fiber and PLA matrix suggest insufficient bonding between the surface of willow-fiber and PLA matrix [15].

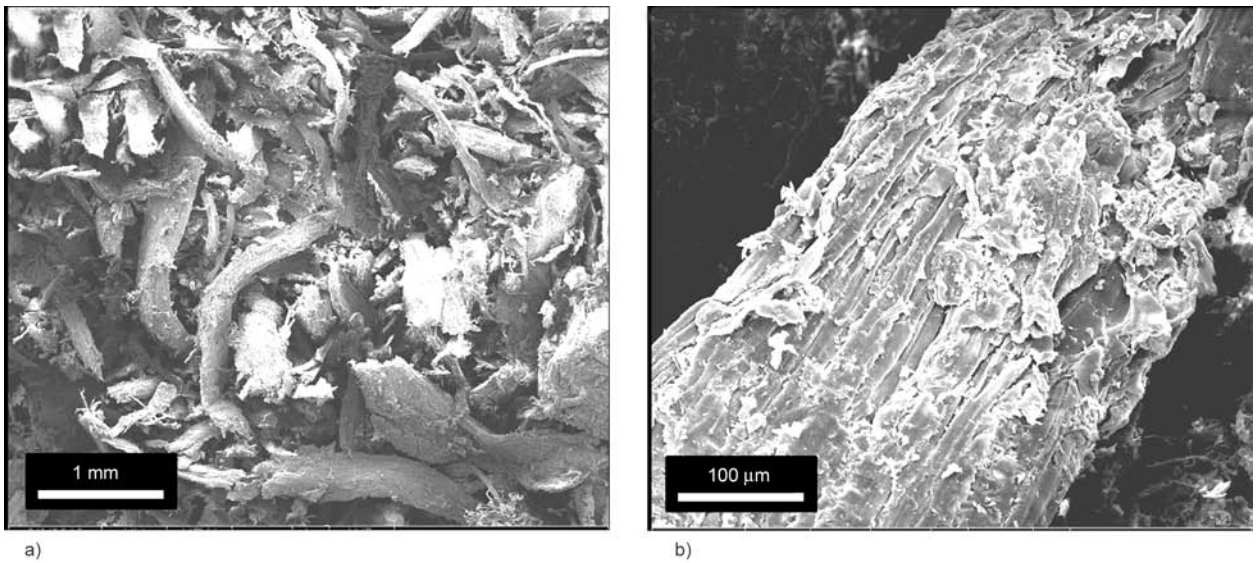


**Figure 2.** Structure and appearance of willow-fiber: (a) overview; (b) detailed view

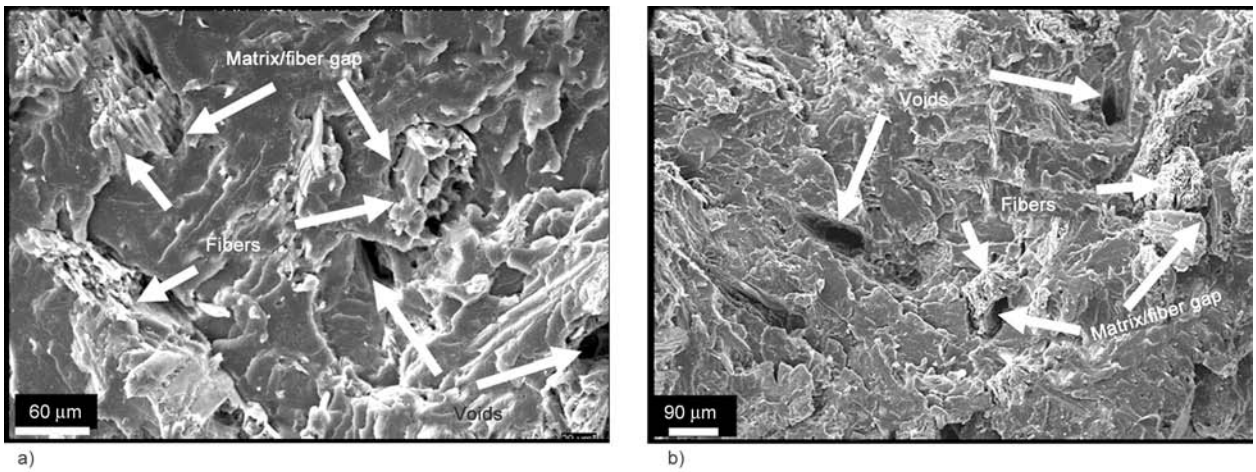


**Figure 3.** SEM images of the cryogenically fractured unfoamed composite surfaces: (a) PLA/willow-fiber (80/20); (b) PLA/willow-fiber (70/30)

### 3.1.2. Morphology of microcellular foamed samples

SEM images of the microcellular foam structure of PLA and composites are shown in Figure 4. Morphology analysis of the microcellular foams was done by imageJ software. Foamed samples of all composites samples show cells with the finer average sizes in comparison to those of virgin and extruded PLA. Figure 5 shows the comparison of cell size and cell densities of these foamed samples. The cell-size reduced in case of extruded PLA as compared to virgin PLA and thereafter further reduced on addition of willow-fiber. The cell-density increased in case of foamed samples of extruded PLA as compared to those of virgin PLA. It further enhanced in case of composites as the willow-fiber content increased.

As the PLA was extruded, its DSC data (Table 2) show that crystallinity [%] increased but crystallite sized reduced and distribution narrowed down in comparison to neat PLA. This in turn gave rise to increased preferable sites for the nucleation at the interface of the crystallites for foaming. As a result the nucleation density increased significantly leading to higher cell density. But since nucleation density was higher, average cell size reduced due to less space available for the expansion.

In case of composites the heterogeneous nucleation increased the nucleation sites resulting in the enhanced cell-density. However, due to increased melt viscosity of the matrix, on increasing the willow-fiber content, the composite turned stiffer than the unfilled PLA. Therefore, the cell-growth became difficult which led to the reduced average cell size. Resistance in the cell growth due to increased melt viscosity and stiffness of matrix after adding the wood-flour/cellulose-fibers has also been reported elsewhere [3, 16–20].

Figure 6 illustrates the variations of void fraction (Equation (1)) and expansion ratio (Equation (2)) of the foamed samples. The void fraction and the expansion ratio of the extruded PLA increased in comparison of virgin PLA significantly. This may be explained on the basis of higher nucleation density leading to higher cell density and reduced average cell size as discussed above. The cumulative effect of both the factors is exhibited in the form of increased void fraction and expansion ratio.

On the contrary, the void fraction and expansion ratio decreased in the case of composites on increasing the filler content. This trend may be expected as the volume expansion ratio and the void fraction during the foaming process is controlled by not only the number of the nucleated cells but also the amount of gas dissolved in the matrix [3, 16–20] . Previous studies have established that increasing the filler content results in the decrease of the volume fraction of the matrix in composites [21]. As a result the amount of gas absorbed in composites noticeably lowered in comparison of neat PLA. Hence the decreasing trend in the void fraction and the volume expansion ratio is resulted.

## 3.2. Mechanical properties

In Figure 7 the specific flexural strength and specific flexural modulus while in Figure 8, specific tensile strength and specific tensile modulus are shown.

Figure 7a and 8a, exhibited that addition of willow-fiber caused reduction in specific flexural strength and in specific tensile strength of all unfoamed

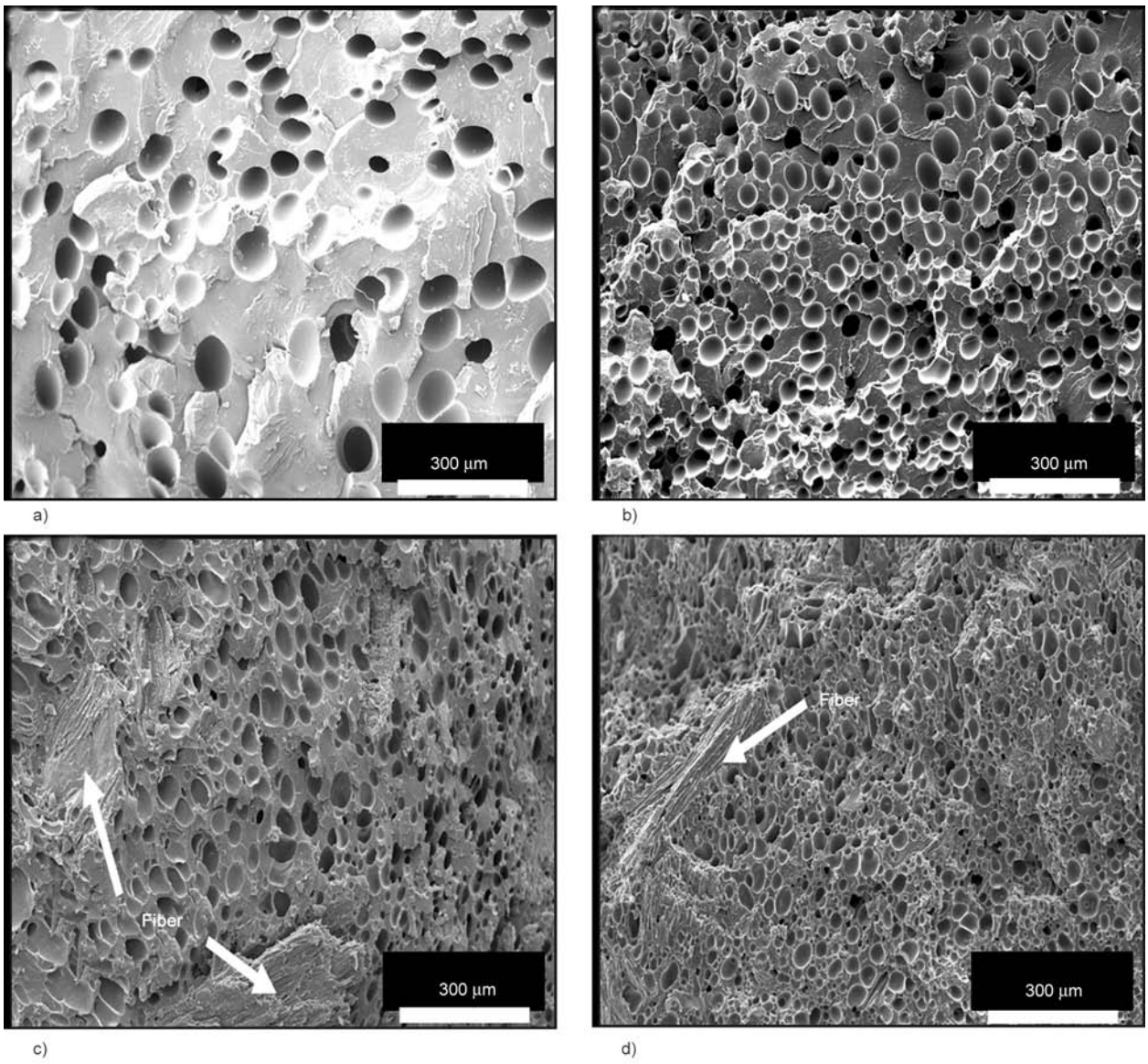


**Figure 4.** Scanning electron microscopy (SEM) image of foamed samples: (a) virgin PLA; (b) extruded PLA; (c) PLA/willow-fiber (80/20); (d) PLA/willow-fiber (70/30)

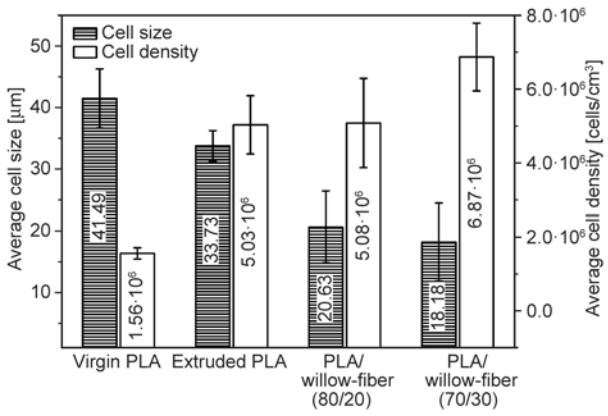


**Figure 5.** Effect of willow-fiber content on the cell size and cell density of foamed PLA and composites

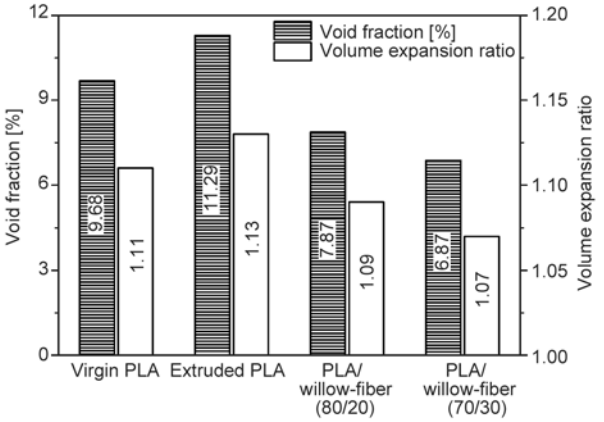


**Figure 6.** Effect of willow-fiber content on the void fraction and volume expansion ratio of foamed PLA and composite

**Table 2.** DSC data of PLA and PLA based foamed and unfoamed composites

| Sample name | Sample type | $S_p$ [W/(g·°C)] | $\Delta W_d$ [°C] | $T_g$ [°C] | $T_{cc}$ [°C] | $H_{cc}$ [J/g] | $T_m$ [°C] | $H_m$ [J/g] | $X_c$ [%] |
|---|---|---|---|---|---|---|---|---|---|
| Virgin PLA | Unfoamed | 0.014 | 20.56 | 62.98 | 104.87 | 28.83 | 169.10 | 45.50 | 17.92 |
| | Foamed | 0.045 | 10.58 | 62.60 | 103.05 | 27.02 | 169.68 | 45.86 | 20.26 |
| Extruded PLA | Unfoamed | 0.017 | 14.55 | 62.49 | 98.26 | 26.82 | 169.17 | 48.26 | 23.05 |
| | Foamed | 0.039 | 10.76 | 62.85 | 98.06 | 24.11 | 169.14 | 49.17 | 26.95 |
| PLA/willow-fiber (80/20) | Unfoamed | 0.054 | 8.50 | 66.29 | 96.59 | 25.68 | 169.54 | 43.97 | 24.58 |
| | Foamed | 0.073 | 7.98 | 64.45 | 95.00 | 24.30 | 169.07 | 45.80 | 28.90 |
| PLA/willow- fiber (70/30) | Unfoamed | 0.058 | 8.10 | 66.41 | 95.38 | 21.89 | 168.81 | 40.61 | 28.76 |
| | Foamed | 0.066 | 7.86 | 64.15 | 95.17 | 19.87 | 168.55 | 41.32 | 32.95 |

PLA/willow-fiber composites. This reduction in strength of unfoamed composites may be due to the poor stress transfer across the fiber-matrix interphase which suggested weak interfacial bonding between willow-fiber and PLA matrix. Similar observation was reported elsewhere [22]. Further, the foamed composites showed decreased specific flexural strength and specific tensile strength in every instance when compared with their unfoamed counterparts. This decrease in specific flexural strength and in specific tensile strength of the foamed composites might be because of the presence of cells inside the matrix. Presumably, these cells become points of stress concentration which decreased the strength of the foamed composites. Similar observation has also been reported earlier [8]. The results of specific flexural modulus and specific tensile modulus (Figure 7b and 8b) indicate that the addition of willow-fiber increased the modulus of the unfoamed composites. The specific flexural modulus

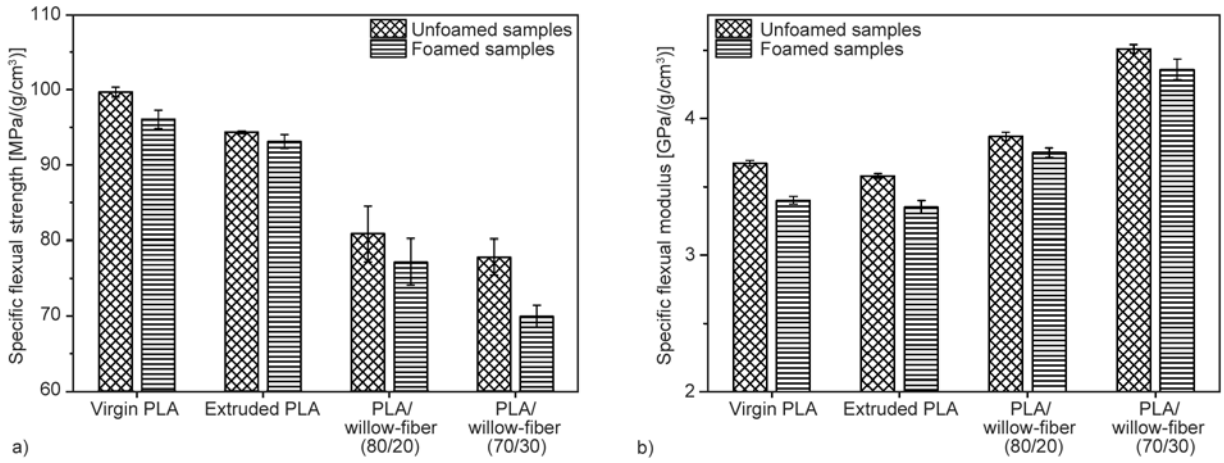


**Figure 7.** Mechanical properties of the foamed and unfoamed PLA and composites: (a) specific flexural strength; (b) specific flexural modulus

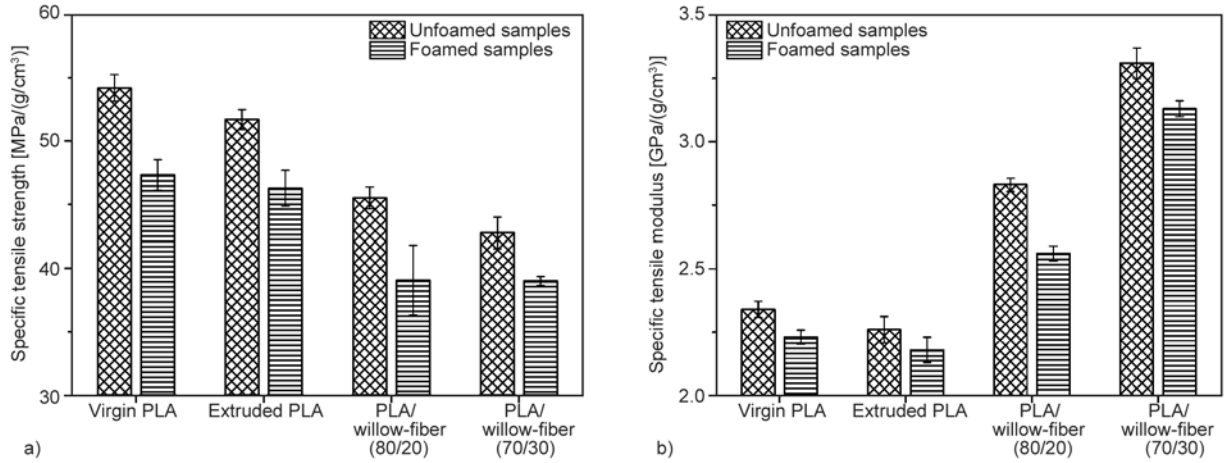


**Figure 8.** Mechanical properties of the foamed and unfoamed PLA and composites: (a) specific tensile strength; (b) specific tensile modulus

of unfoamed PLA/willow-fiber (80/20) and (70/30) composites increased by 11.5 and 30%, respectively, whereas the specific tensile modulus of unfoamed PLA/willow-fiber (80/20) and (70/30) composites increased by 21 and 41.4%, respectively, in comparison to unfoamed PLA samples. This increase in the modulus of unfoamed composites may be due to enhanced crystallinity and differential thermal shrinkage. Thus although there may not be good adhesion between willow-fiber and matrix, the modulus increase is shown since the parameters are evaluated at low strains where weakness in the composites structure does not have time to take effect [15, 22, 23].

Further, the specific flexural modulus and specific tensile modulus of the foamed composite reduced slightly in comparison to their unfoamed counterparts. This might be due to the presence of voids or microcells inside the matrix.

The observed decrease in the mechanical properties of unfoamed extruded PLA in comparison to the unfoamed virgin PLA might be because of the molecular weight degradation of extruded PLA during extrusion by shear and thermal exposure. Decrease in molecular weight during extrusion and hence a decrease in mechanical properties has also been reported by some other researchers [1, 24].

Figure 9 shows the specific notched impact strength of the foamed and unfoamed samples. As shown, incorporation of willow-fiber decreased the specific notched impact strength of the unfoamed composites. The decrease in specific notched impact strength of unfoamed composites might be because of the increased brittleness of the composites due to the addition of the cellulosic fiber [15, 25, 26]. The specific notched impact strength of the foamed composites show increasing trend when compared with their unfoamed counterparts. There are 15.9 and 45.5% increment in specific notched impact strength of foamed PLA/willow-fiber (80/20) and (70/30) composites, respectively, in comparison to their unfoamed counterparts. This increment in the specific notched impact strength of the foamed composites was due to the presence of micro cells which help in preventing the crack propagation process and absorb the energy thus increased the total energy required to propagate the crack. Further it may be assumed that during crack propagation cell walls of the foams also absorbed the energy and thus total impact strength increased [5].

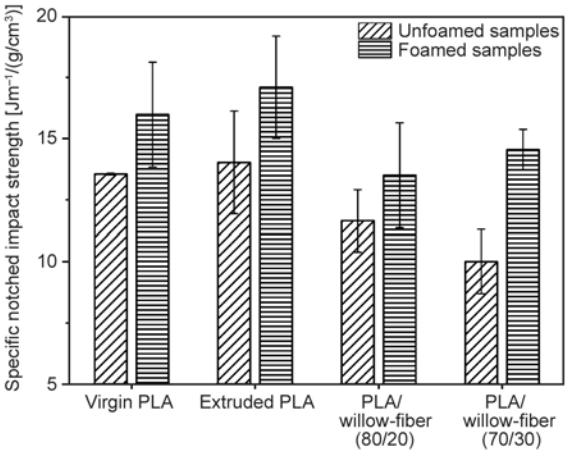


**Figure 9.** Specific notched impact strength of the foamed and unfoamed PLA and composites

### 3.3. Thermogravimetric analysis (TGA)

TGA was done to study the effect of temperature on the stability of foamed and unfoamed PLA and the composites. The results are shown in Table 3. The TGA curve of willow-fiber shows slight degradation near 100 °C due to moisture loss followed by severe single stage degradation starting at 310 °C. From the TGA results it is evident that addition of willow-fiber decreases the thermal stability of the composites which might be due to the decrease in the relative molecular mass of PLA after adding the willow-fiber [27]. When the thermal stability of the foamed samples are compared with their unfoamed counterparts, it is observed that in case of virgin and extruded PLA foamed samples have almost the same thermal stability as the unfoamed samples. In case

**Table 3.** TGA data of PLA and PLA based foamed and unfoamed composites

| Sample name | Onset temperature [°C] | | Inflection temperature [°C] | | End temperature [°C] | |
|---|---|---|---|---|---|---|
| | Unfoamed | Foamed | Unfoamed | Foamed | Unfoamed | Foamed |
| Willow-fiber | 310 | | 365 | | 381 | |
| Virgin PLA | 335 | 336 | 352 | 353 | 362 | 363 |
| Extruded PLA | 334 | 335 | 352 | 353 | 363 | 364 |
| PLA/Willow-fiber (80/20) | 329 | 313 | 349 | 335 | 362 | 347 |
| PLA/Willow-fiber (70/30) | 313 | 303 | 330 | 320 | 344 | 337 |

of the composites, foamed samples show lower thermal stability than the corresponding unfoamed samples which might be due to the decrease in the interfacial bonding between fibers and matrix during the foaming.

### 3.4. Crystallization study by DSC

Crystallization studies were carried out on foamed and unfoamed samples of PLA and the composites by DSC and the data obtained there from are shown in Table 2. The crystallinity [%] of the extruded PLA increased in comparison to virgin PLA. The slope of the cold crystallization peak indicated the increase in the rate of crystallization ($S_p$) in case of extruded PLA as compared to virgin PLA while width of peak at half height ($\Delta W_d$) showed the narrowing down the crystallites size distribution in the former one in comparison to the latter. This happened due to decrease in molecular weight because of thermal degradation and chain scission during extrusion process [1].

The $T_g$ and $T_m$ of the PLA (virgin and extruded) and the composite samples were not appreciably changed, however, the percentage crystallinity increased on increasing the willow-fiber content. The rate of cold crystallization also increased on increasing willow-fiber content as revealed by the slope of the cold crystallization peak. Higher slope denoted higher rate of crystallization while lower slope signified the lower rate of crystallization [13]. The cold crystallization peak was shifted towards left on increasing willow-fiber content showing the decrease in $T_{cc}$. The area of cold crystallization peak was also decreased in the similar manner on increasing willow-fiber content, which implies that $X_c$ [%] increases on increasing willow-fiber content. The $\Delta W_d$ of cold crystallization curve decreased on increasing willow-fiber content showing narrowing down of the crystallite size distribution. The above observations clearly indicate that willow-fiber provided crystallization surfaces and enhanced the $X_c$ [%] in PLA composites. Increased number of crystallites did not allow the crystallites to grow further, however, the resultant crystallinity was increased. As a result the average crystallite size was smaller and more uniform in composites in comparison to those in neat samples.

When unfoamed samples were compared to their foamed counterparts the total crystallinity [%] was found to increase in all foamed samples and the amont of increase was almost similar in all the samples, indicating that the addition of willow-fiber is acting in the similar manner in unfoamed and foamed samples. However, the crystallinity increased in the foamed samples may be due to strain induced alignment of the PLA chains during the cell growth process. Wang *et al*. [28] have also reported improvement in the crystallinity of PLA due to the extension associated with the cell growth during foaming.

### 3.5. Heat deflection temperature (HDT)

HDT of PLA and PLA based foamed and unfoamed composites are shown in Table 4. HDT is the short term thermal characteristic which is the measure of the thermal sensitivity and stability of polymeric materials. The results show that addition of willow-fiber increased HDT of the unfoamed composites. On addition of 20% willow-fiber, HDT increased to 58.7 °C, while on addition of 30% willow-fiber the same was increased to 60.3 °C. This improvement in HDT is due to reinforcing effect of willow-fiber in PLA matrix as well as due to increased crystallinity (Table 2). Huda *et al*. [29] also studied the similar improvement in HDT while studying the reinforcement of PLA using wood-fiber at 30 and 40 wt% loading.

HDT of foamed samples are found to be the same to their unfoamed counterparts which indicates no effect of foaming on HDT.

Although the increase in HDT depends upon the crystallinity and reinforcement effect of the filler, yet the improvement in HDT, in present study, is not as much as speculated, which may because of insufficient interfacial interactions between PLA and willow-fiber as obvious from SEM image (Figure 3). Still the improvement in HDT values on addition of willow-fiber can be regarded as an important achievement which indicates the increased upper working temperature limit of the composites.

**Table 4.** HDT data of PLA and PLA based foamed and unfoamed composites

| Samples name | HDT [°C] | |
|---|---|---|
| | Unfoamed sample | Foamed sample |
| Virgin PLA | 56.5±0.10 | 56.2±0.11 |
| Extruded PLA | 56.7±0.14 | 56.5±0.25 |
| PLA/willow-fiber (80/20) | 58.7±0.22 | 58.7±0.14 |
| PLA/willow-fiber (70/30) | 60.3±0.14 | 60.1±0.25 |

## 4. Conclusions

The PLA/willow-fiber biocomposites were prepared in twin screw extruder and subsequently injection molded by two separate processes; one by conventional injection molding without foaming module and the other with the foaming module on the same injection molding machine. The key findings are as below:

- The morphology study shows voids inside the matrix and weak phase interaction between PLA matrix and willow-fiber. SEM images of the foamed sample show that the addition of willow-fiber in the PLA matrix decreased the cell size with increase in the cell density.
- Adding willow-fiber caused a reduction in specific flexural strength and in specific tensile strength of all foamed and unfoamed PLA/willow-fiber composites. However, addition of willow-fiber increased the specific tensile modulus and specific flexural modulus of the unfoamed composites which were found maximum at 30 wt% willow-fiber content. Specific notched impact strength of the foamed composites show increasing trend. Foamed PLA/ willow-fiber (80/20) and (70/30) composites shows 15.9 and 45.5% improvement in specific notched impact strength respectively compared to their unfoamed counterparts.
- Thermogravimetric analysis shows that the addition of willow-fiber as well as foaming decreased the thermal stability of the composites. DSC results show that addition of willow-fiber in the PLA matrix increased the crystallinity [%] and crystallization rate while decreased the cold crystallization peak temperature and gave narrower crystallite size distribution. Crystallization properties of the foamed samples were found similar to their unfoamed counterparts.
- HDT improved by 2.2 °C on addition of 20% willow-fiber while the same was increased by 3.8 °C on adding 30% willow-fiber. Foamed composites show HDT similar to their unfoamed counterparts.

## Acknowledgements

The authors thank the Department of Foreign Affairs and International Trade Canada (DFAIT) and Canadian Bureau for International Education (CBIE) for Providing Fellowship under Canadian Commonwealth Exchange Program, Asia–Pacific (Formerly GSEP) 2011-2012 to Mohammad Tahir Zafar. The Council of Scientific and Industrial Research (CSIR), New Delhi, India (File No.09/086(0913)/2008-EMR-I) is acknowledged for providing a senior research fellowship (SRF) to Mohammad Tahir Zafar. The authors are also thankful to the Ontario Research Fund Round 4; Highly Qualified Personnel (HQP) Scholarship from Ontario Ministry of Agriculture, Food and Rural Affairs (OMAFRA), 2009, Ontario, Canada to Nima Zarrinbakhsh; OMAFRA-Alternative Renewable Fuels Plus Research Program, 2008, Ontario, Canada. Authors also gives thank to Dr. Naresh V Thevathasan, University of Guelph and Dr. Andrew Gordon, University of Guelph for providing willow-fiber samples.

## References

[1] Carrasco F., Pagès P., Gámez-Pérez J., Santana O. O., Maspoch M. L.: Processing of poly(lactic acid): Characterization of chemical structure, thermal stability and mechanical properties. Polymer Degradation and Stability, **95**, 116–125 (2010). DOI: 10.1016/j.polymdegradstab.2009.11.045

[2] Lim L-T., Auras R., Rubino M.: Processing technologies for poly(lactic acid). Progress in Polymer Science, **33**, 820–852 (2008). DOI: 10.1016/j.progpolymsci.2008.05.004

[3] Matuana L. M., Faruk O.: Effect of gas saturation conditions on the expansion ratio of microcellular poly(lactic acid)/wood-flour composite. Express Polymer Letters, **4**, 621–631 (2010). DOI: 10.3144/expresspolymlett.2010.77

[4] Zhang Q., Shi L., Nie J., Wang H., Yang D.: Study on poly(lactic acid)/natural fibers composites. Journal of Applied Polymer Science, **125**, E526–E533 (2012). DOI: 10.1002/app.36852

[5] Matuana L. M.: Solid state microcellular foamed poly (lactic acid): Morphology and property characterization. Bioresource Technology, **99**, 3643–3650 (2008). DOI: 10.1016/j.biortech.2007.07.062

[6] Kohlhoff D., Ohshima M.: Open cell microcellular foams of polylactic acid (PLA)-based blends with semi-interpenetrating polymer networks. Macromolecular Materials and Engineering, **296**, 770–777 (2011). DOI: 10.1002/mame.201000371

[7] Anne B., Benezet J. C.: Natural fibre-reinforced biofoams. International Journal of Polymer Science, **2011**, 569871/1–569871/14 (2011). DOI: 10.1155/2011/569871

[8] Kramschuster A., Gong S., Turng L-S., Li T., Li T.: Injection-molded solid and microcellular polylactide and polylactide nanocomposites. Journal of Biobased Materials and Bioenergy, **1**, 37–45 (2007). DOI: 10.1166/jbmb.2007.004

[9] Gong S., Yuan M., Chandra A., Kharbas H., Osorio A., Turng L. S.: Microcellular injection molding. International Polymer Processing, **20**, 202–214 (2005). DOI: 10.3139/217.1883

[10] Hwang S-S., Hsu P. P., Yeh J-M., Chang K-C., Lai Y-Z.: The mechanical/thermal properties of microcellular injection-molded poly-lactic-acid nanocomposites. Polymer Composites, **30**, 1625–1630 (2009). DOI: 10.1002/pc.20736

[11] Tábi T., Égerházi A. Z., Tamás P., Czigány T., Kovács J. G.: Investigation of injection moulded poly(lactic acid) reinforced with long basalt fibres. Composites Part A: Applied Science and Manufacturing, **64**, 99–106 (2014). DOI: 10.1016/j.compositesa.2014.05.001

[12] Battegazzore D., Bocchini S., Frache A.: Crystallization kinetics of poly(lactic acid)-talc composites. Express Polymer Letters, **5**, 849–858 (2011). DOI: 10.3144/expresspolymlett.2011.84

[13] Sewda K., Maiti S. N.: Crystallization and melting behavior of HDPE in HDPE/teak wood flour composites and their correlation with mechanical properties. Journal of Applied Polymer Science, **118**, 2264–2275 (2010). DOI: 10.1002/app.30551

[14] Zarrinbakhsh N., Misra M., Mohanty A. K.: Biodegradable green composites from distiller's dried grains with solubles (DDGS) and a polyhydroxy (butyrate-*co*-valerate) (PHBV)-based bioplastic. Macromolecular Materials and Engineering, **296**, 1035–1045 (2011). DOI: 10.1002/mame.201100039

[15] Mathew A. P., Oksman K., Sain M.: Mechanical properties of biodegradable composites from poly lactic acid (PLA) and microcrystalline cellulose (MCC). Journal of Applied Polymer Science, **97**, 2014–2025 (2005). DOI: 10.1002/app.21779

[16] Matuana L. M., Park C. B., Balatinecz J. J.: Processing and cell morphology relationships for microcellular foamed PVC/wood-fiber composites. Polymer Engineering and Science, **37**, 1137–1147 (1997). DOI: 10.1002/pen.11758

[17] Li Q., Matuana L. M.: Foam extrusion of high density polyethylene/wood-flour composites using chemical foaming agents. Journal of Applied Polymer Science, **88**, 3139–3150 (2003). DOI: 10.1002/app.12003

[18] Mengeloglu F., Matuana L. M.: Foaming of rigid PVC/wood-flour composites through a continuous extrusion process. Journal of Vinyl and Additive Technology, **7**, 142–148 (2001). DOI: 10.1002/vnl.10282

[19] Matuana L. M., Mengeloglu F.: Manufacture of rigid PVC/wood-flour composite foams using moisture contained in wood as foaming agent. Journal of Vinyl and Additive Technology, **8**, 264–270 (2002). DOI: 10.1002/vnl.10373

[20] Matuana L. M., Li Q.: Statistical modeling and response surface optimization of extruded HDPE/wood-flour composite foams. Journal of Thermoplastic Composite Materials, **17**, 185–199 (2004). DOI: 10.1177/0892705704035404

[21] Matuana-Malanda L., Park C. B., Balatinecz J. J.: Characterization of microcellular foamed PVC/cellulosic-fibre composites. Journal of Cellular Plastics, **32**, 449–469 (1996). DOI: 10.1177/0021955X9603200503

[22] Bledzki A. K., Gassan J.: Composites reinforced with cellulose based fibres. Progress in Polymer Science, **24**, 221–274 (1999). DOI: 10.1016/S0079-6700(98)00018-5

[23] Hedenberg P., Gatenholm P.: Conversion of plastic/cellulose waste into composites. I. Model of the interphase. Journal of Applied Polymer Science, **56**, 641–651 (1995). DOI: 10.1002/app.1995.070560601

[24] Żenkiewicz M., Richert J., Rytlewski P., Moraczewski K., Stepczyńska M., Karasiewicz T.: Characterisation of multi-extruded poly(lactic acid). Polymer Testing, **28**, 412–418 (2009). DOI: 10.1016/j.polymertesting.2009.01.012

[25] Mohanty A. K., Misra M., Hinrichsen G.: Biofibres, biodegradable polymers and biocomposites: An overview. Macromolecular Materials and Engineering, **276–277**, 1–24 (2000). DOI: 10.1002/(sici)1439-2054(20000301)276:1<1::aid-mame1>3.0.co;2-w

[26] Ahmad F., Choi H. S., Park M. K.: A review: Natural fiber composites selection in view of mechanical, light weight, and economic properties. Macromolecular Materials and Engineering, **300**, 10–24 (2015). DOI: 10.1002/mame.201400089

[27] Yu T., Li Y., Ren J.: Preparation and properties of short natural fiber reinforced poly(lactic acid) composites. Transactions of Nonferrous Metals Society of China, **19**, s651–s655 (2009). DOI: 10.1016/S1003-6326(10)60126-4

[28] Wang J., Zhu W., Zhang H. Park C. B.: Continuous processing of low-density, microcellular poly(lactic acid) foams with controlled cell morphology and crystallinity. Chemical Engineering Science, **75**, 390–399 (2012). DOI: 10.1016/j.ces.2012.02.051

[29] Huda M. S., Drzal L. T., Misra M., Mohanty A. K.: Wood-fiber-reinforced poly(lactic acid) composites: Evaluation of the physicomechanical and morphological properties. Journal of Applied Polymer Science, **102**, 4856–4869 (2006). DOI: 10.1002/app.24829